UH University of Houston

Department of Civil and Environmental Engineering
Houston, Texas 77204-4791
(713) 749-4481
FAX: (713) 749-2559

Cullen College of Engineering

January 6, 1992

Mr. Michael Adams
Federal Highway Administration
HNR-30
6300 Georgetown Pike
McLean, VA 22101

Dear Mr. Adams,

Per our phone conversation of January 6, I enclose a copy of the results of the study that we performed for Minerals Management Service and other sponsors entitled "Response of Tension Piles to Simulated Seismic Motion in Saturated Fine Sand." This study was oriented mainly toward TLP applications but should provide useful information for any piles that are loaded in tension during seismic events.

I believe Charles Smith told you that the second study, which we hope to start this spring, will involve investigation of the effects of both hydraulic overpressures and small values of cohesion in the soil, as well as the investigation of existing mathematical models for predicting pile extraction vis-a-vis our experimental data.

Thank you for your support of our research. I look forward to seeing you next week at TRB.

Sincerely,

Michael W. O'Neill
Professor and Chairman

encl (report)

c: Charles E. Smith
U.S. Dept. of the Interior
Technology Assessment & Research Branch
381 Elden Street, MS647
Herndon, Virginia 22070-4817

RESPONSE OF TENSION PILES TO SIMULATED SEISMIC MOTION IN SATURATED FINE SAND

by

Michael W. O'Neill
Cumaraswamy Vipulanandan
Mauricio Ochoa

December 1990

Final Report

for

Minerals Management Service
U.S. Army Engineer Waterways Experiment Station
Exxon Production Research Company
Unocal, S & T Division

Department of Civil and Environmental Engineering
University of Houston
Report No. UHCEE 90-09

RESPONSE OF TENSION PILES TO SIMULATED SEISMIC MOTION IN SATURATED FINE SAND

by

Michael W. O'Neill
Cumaraswamy Vipulanandan
Mauricio Ochoa

December 1990

Final Report

for

Minerals Management Service
U.S. Army Engineer Waterways Experiment Station
Exxon Production Research Company
Unocal, S & T Division

Department of Civil and Environmental Engineering
University of Houston
Report No. UHCEE 90-09

DISCLAIMER

This report presents research results developed by the authors. Neither the University of Houston nor the authors accepts any responsibility for the application of these research results by others.

PREFACE / ACKOWNLEDGEMENTS

This study was performed by the Department of Civil and Environmental Engineering, at the University of Houston, under contract to the Minerals Management Service; U.S. Army Engineer Waterways Experiment Station; Exxon Production Research Company; and Unocal, S &T Division.

The authors wish to express their appreciation to the sponsors of this project. The completion of this study was made possible only by the contributions of many at the University of Houston. Special thanks are due:

Roy Henson, Martin Kowis and Joe Thomas, Civil and Environmental Engineering technicians, for their help during the testing set up,

Mike Irwin, for his help during the programing of the testing machine, and

The Engineering Media Center, for painstakingly preparing many of the figures.

CONVERSION FACTORS, U. S. CUSTOMARY TO METRIC (SI) UNITS OF MEASUREMENT

U. S. customary units of measurement used in this report can be converted to metric (SI) units as follows:

Multiply	By	To Obtain
Angstroms	0.0000001 (10^{-7})	millimetres
inches	2.54	centimetres
feet	0.3048	metres
miles (U. S. statute)	1.609344	kilometres
square inches	0.00064516	square metres
square feet	0.09290304	square metres
cubic feet	0.02831685	cubic metres
cubic yards	0.7645549	cubic metres
grams	0.001	kilograms
pounds (mass)	0.4535924	kilograms
tons (2000 pounds)	907.1847	kilograms
pounds (mass) per cubic foot	16.01846	kilograms per cubic metre
pounds (mass) per cubic yard	0.59327631	kilograms per cubic metre
pounds (force)	4.448222	newtons
pounds (force) per square inch	6894.757	pascals
pounds (force) per square foot	4.882428	kilograms per square metre
miles per hour	1.609344	kilometres per hour
degrees (angle)	0.01745329	radians
Fahrenheit degrees	5/9	Celsius degrees or Kelvins*

* To obtain Celsius (C) temperature readings from Fahrenheit (F) readings, use the following formula: $C = (5/9)(F - 32)$. To obtain Kelvin (K) readings, use: $K = (5/9)(F - 32) + 273.15$.

ABSTRACT

A laboratory experimental study of tension piles subjected to simulated seismic loading through the soil was conducted. The objective of the study was to assess the magnitude of biased tension load that can be sustained by displacement-type piles driven into loose to medium dense saturated sand. The prototype characteristics modeled in this study consisted of a closed-ended, or plugged, impact-driven pipe pile, 15 to 30 in. in diameter, 20 to 40 ft in length (or top 20 to 40 ft of a longer pile). An acceleration record for particular Magnitude 5.8 seismic event, the Oceanside earthquake of 1986, measured at an offshore (California) deep soil site, 74 km from the epicenter, was selected for detailed study and scaled to higher magnitudes (e.g., Magnitudes of 7.0, 7.5 and 8.0) to simulate more severe earthquake loading conditions on the pile.

A 21 in. high by 20 in. diameter pressure chamber was used to contain the saturated soil and to simulate isotropic effective stresses and drainage conditions. The model test pile, was an instrumented steel closed-ended cylinder, 1 in. in diameter and 16 in. long. Pile-head movement, load vs. depth and pore water pressures in the soil were measured throughout the experiments. The simulated seismic records were applied through the base of the chamber, while the biased tension load was applied simultaneously and continuously through a one-degree-of-freedom weight and spring system to model a simple superstructure. Both the simulated seismic record and/or soil permeability were scaled to model the effect of drainage distance and its effect on pore water pressure generation and dissipation.

Contour plots of stability, mobility and failure conditions for the model pile were developed. The effect of distance between the pile and event epicenter on stability was also considered. For the scaled earthquake studied, the ultimate shaft resistance between pile and soil to applied uplift loads was not affected by the action of the vertical component of the simulated seismic event. For the horizontal component of event magnitudes of 7.0 and 7.5, 74 km from the epicenter, stability was preserved for biased loads of 70% of the static capacity, whereas, for an event of Magnitude 8.0, the condition of stability was reduced to a biased loads of no more than 55% of the static capacity. For piles that did not fail during the simulated seismic event, losses in static capacity of 0 - 15% occurred.

TABLE OF CONTENTS

	Page
DISCLAIMER	ii
PREFACE / ACKNOWLEDGMENTS	iii
SI CONVERSION	iv
ABSTRACT	v
TABLE OF CONTENTS	vi
LIST OF TABLES	ix
LIST OF FIGURES	x
CHAPTER I - INTRODUCTION	1
Lateral Response	2
Axial Response	2
Liquefaction	3
Summary	5
CHAPTER II - OVERVIEW OF RESEACH PROGRAM	7
Objectives	10
Research Approach	11
CHAPTER III - DESCRIPTION OF TESTING SYSTEM	15
Testing Chamber / Loading System	15
Test Pile	27
Soil Instruments	29
Drop Hammer	32
Data Acquisition Systems	32
Dynamic Data Acquisition System	32
Static Data Acquisition System	36
Sand Placement	37
Calibration Procedures	42
Pile Axial Strain Gages	42
Miniature Pore Water Pressure Transducers (PDCR 81)	42
Applied Boundary Pressures	44

TABLE OF CONTENTS (Cont'd)

Page

Vertical Motion 46
Horizontal Motion 46

CHAPTER IV - SAND PROPERTIES 51
Grain-Size Distribution 51
Minimum and Maximum Densities 53
Permeability 53
Triaxial Compression 54
Interface Shear 54

CHAPTER V - SCALING PROCEDURES 62
Earthquake Scaling 62
Scaling of the Vertical (Z) Component of Motion 66
Scaling of the Horizontal (Combined X and Y) Component of Motion 73
Model to Prototype Scaling... 88
Static Scaling 88
Dynamic Scaling 89
Dynamic Time Scaling 89
Dynamic Diffusion Scaling 90
Selection of Time Scaling Factor for the Experimental Study .. 90
Induced Pressures in the Water Mass due to Vertical Seismic Excitation 92

CHAPTER VI - ANALYSIS OF TEST RESULTS, VERTICAL MOTION 94
Induced Pore Water Pressure During Impact Driving 94
Relation Between Penetration Resistance and Uplift Static Capacities 98
Comparison of Measured and Target Spectra 101
Static Behavior 101
Static Uplift Capacities 101
Static Unit Load Transfer Characteristics 108
Pile and Soil Response During the Simulated Seismic Event 115
Post-Shaking Static Capacities after Simulated Seismic Event 128
Dynamic Load Transfer Characteristics 133

TABLE OF CONTENTS (Cont'd)

Page

CHAPTER VII - ANALYSIS OF RESULTS, HORIZONTAL AND COMBINED HORIZONTAL AND VERTICAL MOTIONS 135
Comparison of Measured and Target Spectra 135
Pile and Soil Response During the Horizontal Component of the Simulated Seismic Event 138
Effect of Combined Horizontal and Vertical Motions on Pile Response 157
Effect of Fundamental Period of Model Superstructure 161
Post-Shaking Static Capacities After Simulated Seismic Event 161
Dynamic Load Transfer Characteristics 167

CHAPTER VIII - CONCLUSIONS AND RECOMMENDATIONS 174
Summary 174
Conclusions 181
Recommendations 184

REFERENCES 185
APPENDIX A GENERAL SOIL LOG AT SEMS UNIT SITE 190
APPENDIX B CALIBRATION EQUATIONS 191
APPENDIX C MODEL TO PROTOTYPE SIMILITUDE 194
APPENDIX D INDUCED PRESSURE DUE TO VERTICAL WATER MASS EXCITATION 197
APPENDIX E LOAD-DEPTH RELATIONSHIPS 200
APPENDIX F TIME HISTORY MEASUREMENTS DURING DYNAMICS TESTS, VERTICAL MOTION (Raw Data) 208
APPENDIX G BASIC AXIAL WAVE PROPAGATION ANALYSIS IN A FINITE ROD 241
APPENDIX H SPECTRA, ACCELERATION, VELOCITY AND DISPLACEMENT TIME HISTORIES FOR MAGNITUDE 7.0 AND 7.5 (HORIZONTAL MOTION) 246
APPENDIX I SOIL PROPERTIES FOR SHAKE ANALYSIS 257
APPENDIX J TIME HISTORY MEASUREMENTS DURING DYNAMIC TESTS, HORIZONTAL MOTION (Raw Data) 258

LIST OF TABLES

		Page
Table 2.1.	Testing Sequence, Phase 1 (Vertical Component of Motion)	13
Table 2.2.	Testing Sequence, Phase 2 (Horizontal and Combined Vertical and Horizontal Motions)	14
Table 4.1.	Permeability Test Results	53
Table 6.1.	Driving Blow Count and Static Capacity for All Static Tests	95
Table 6.2.	Summary of Dynamic Test Program Results, Vertical Motion	96
Table 7.1.	Summary of Dynamic Test Program Results, Horizontal and Combined Horizontal and Vertical Motions	136
Table 7.2.	Post-Test Loss of Static Uplift Capacity (Conf. Pressure = 2.5 psi, Rel. Density = 55%)	171
Appendix B		
Table B.1.	Pore Water Transducer (PDCR 81) Calibration Equations	193
Table B.2.	Test Chamber Calibration	193
Appendix C		
Table C.1.	Model Test Scaling Factors [Modified After Fuglsand and Ovesen (1988)]	196

LIST OF FIGURES

Page

Fig. 2.1. Idealization of Induced Stress Waves During a Seismic Event for an Offshore TLP 8

Fig. 2.2. Idealization of Induced Stress Waves During a Seismic Event for a Hydraulic Structure 9

Fig. 3.1. Overall Testing Arrangement 16

Fig. 3.2. Schematic of Testing Arrangement 17

Fig. 3.3. Schematic Elevation of Test Chamber (Vertical Motion) 18

Fig. 3.4. Idealization of Waves in Test Chamber (Vertical Motion) 20

Fig. 3.5. Schematic Elevation of Test Chamber (Rotational Motion) 21

Fig. 3.6. Idealization of Waves in Test Chamber (Rotational Motion) 23

Fig. 3.7. Plan Schematic View of Chamber, Indicating Conversion of Rotational Motion into Modelled Horizontal Translational Motion 24

Fig. 3.8. Articulated Arm Display 25

Fig. 3.9. Overall Testing Arrangement with Stiff Spring 26

Fig. 3.10. Longitudinal Cross-Sectional View of Test Pile 28

Fig. 3.11. Dimensions of Miniature Pore Water Pressure Transducer 30

Fig. 3.12. Placement of Pore Water Pressure Transducer into Sand 31

Fig. 3.13. Schematic of Drop Hammer 33

Fig. 3.14. Pile Installation Display 34

Fig. 3.15. Schematic of Dynamic Data Acquisition System 35

Fig. 3.16. Schematic of Static Data Acquisition System 38

Fig. 3.17. Cyclic Stress Ratio versus Number of Cycles for Different Compaction Procedures [After Mulilis et al. (1975)] 39

Fig. 3.18. Schematic of Sand Placement Arrangement 41

Fig. 3.19. Test Pile Calibration Arrangement 43

LIST OF FIGURES (Cont'd)

		Page
Fig. 3.20.	Pore Water Pressure Response versus Applied Confining Pressure (Ventilation Ports Closed)	45
Fig. 3.21.	Display of Insertion of Accelerometers in Dry Sand for Strain Measurements	47
Fig. 3.22.a	Measured Strain-Time History (Dry Sand) During Simulated Scaled Magnitude-8.0 Oceanside Event (Horizontal Motion) (Uncorrected Baseline)	48
Fig. 3.22.b	Measured Strain-Time History (Dry Sand) During Simulated Scaled Magnitude-8.0 Oceanside Event (Horizontal Motion) (Corrected Baseline)	48
Fig. 3.23.	Computed Strain-Time Histories in the Free Field on the Prototype Soil During Period of Strong Shaking for Loose and Medium Dense Conditions	50
Fig. 4.1.	Grain Size Distribution for Sands Selected for the Study	52
Fig. 4.2.	Results of Consolidated-Drained Triaxial Compression Tests for SJR Sand at 60% Relative Density	55
Fig. 4.3.	Failure Envelope for Triaxial Compression Test on p'-q Diagram on SJR Sand	52
Fig. 4.4.	Results of Direct Interface Shear Tests for SJR Sand at 60% Relative Density	58
Fig. 4.5.	Failure Envelope for Direct Interface Shear Test on SJR Sand	59
Fig. 4.6.	Results of Direct Interface Shear Tests for Micro-fine Sand at 60% Relative Density	60
Fig. 4.7.	Failure Envelope for the Direct Interface Shear Test on Micro-fine Sand at 60% Relative Density	61
Fig. 5.1.	Location of SEMS Unit [After Sleefe and Engi (1987)]	63
Fig. 5.2.	Seismic Record of Vertical, or Z, Component of Oceanside Earthquake	64
Fig. 5.3.	Seismic Record of Horizontal, or X, Component of Oceanside Earthquake	65
Fig. 5.4.	Seismic Record of Horizontal, or Y, Component of Oceanside Earthquake	65
Fig. 5.5.	Frequency Spectrum of Unfiltered Z-Component Record	67

LIST OF FIGURES (Cont'd)

		Page
Fig. 5.6.	Frequency Spectrum of Filtered (A = 0.70) Z - Component Record	68
Fig. 5.7.	Phase Angles of Filtered Z-Component Record	69
Fig. 5.8.	Functions a(T), b(T), c(T), d(T), and e(T) for use in Eq. 5.2 [After Trifunac (1979)]	71
Fig. 5.9.	Vertical (v=1) Fourier Amplitude Spectra for MMI = IV - XII, for s = 0 and s = 2, and for p = 0.50 [After Trifunac (1979)]	72
Fig. 5.10.	Rate of Decay of MMI with Distance, R, and Magnitude, M [After Trifunac (1979)]	74
Fig. 5.11.	Original (Filtered A = 0.7), Target and Computed (Scaled) Spectra (Vertical Motion)	75
Fig. 5.12.	Acceleration Time History of Scaled (M=8.0) Vertical Component of Oceanside Earthquake	76
Fig. 5.13.	Displacement Time History of Scaled (M = 8.0) Vertical Component of Oceanside Earthquake	77
Fig. 5.14.	Combined X and Y Components of Oceanside Earthquake (M = 5.8)	79
Fig. 5.15.	Horizontal (v=0) Fourier Amplitude Spectra for MMI = IV-XII, for s = 0 and s = 2, and for p = 0.50 [After Trifunac (1979)]	80
Fig. 5.16.	Original, Target and Computed (Scaled, M = 8.0) Spectra (Horizontal Motion)	81
Fig. 5.17.	Combined Scaled (M = 8.0) Horizontal Record of Oceanside Earthquake	82
Fig. 5.18.	Extended Scaled (M = 8.0) Horizontal Record of Oceanside Earthquake	84
Fig. 5.19.	Velocity Time History of Extended Scaled (M = 8.0) Horizontal Component of Oceanside Earthquake	85
Fig. 5.20.	Displacement Time History of Extended Scaled (M = 8.0) Horizontal Component of Oceanside Earthquake	86
Fig. 5.21.	Attenuation of Peak Horizontal Accelerations with Distance for Different Soils During Loma Prieta Earthquake [After Plafker and Galloway (1989)], and for Oceanside Earthquake (M = 7.0, Epic. Distance = 74 km, in Alluvium Site)	87
Fig. 5.22.	Assumed Conditions for Analysis of Induced Pressures in Water Mass Subjected to Vertical Seismic Motion	92

LIST OF FIGURES (Cont'd)

		Page
Fig. 5.23.	Window for Induced Pore Water Pressure Analysis During a Simulated Vertical Seismic Event	93
Fig. 6.1.	Induced Pore Water Pressure due to Impact Driving, Test A3 and Test F, (σ_c' = 5 psi)	97
Fig. 6.2.	Schematic Comparison of Baseline Static Capacities from Controlled Displacement (CD) and Controlled Load (CL) Tests	99
Fig. 6.3.	Penetration Resistance (Blows/in.) versus Static Capacity (lbs) for all Static Tests	100
Fig. 6.4.	Measured Spectrum versus Target Spectrum, Test H2	102
Fig. 6.5.	Load-Movement Curves, Tests A1, A2, A3, F, O1, O2	103
Fig. 6.6.	Load-Movement Curves, Tests B1, B2, P	104
Fig. 6.7.	Load-Movement Curve, Test C	105
Fig. 6.8.	Load-Movement Curve, Test D	106
Fig. 6.9.	Load-Movement Curve, Tests E1, E2, Q	107
Fig. 6.10.	Relationships of f versus w, Tests A1, A2, A3, F , O1, O2	110
Fig. 6.11.	Relationships of f versus w, Tests B1, B2, P	111
Fig. 6.12.	Relationships of f versus w, Test C	112
Fig. 6.13.	Relationships of f versus w, Test D.....	113
Fig. 6.14.	Relationships of f versus w, Tests E1, E2, Q	114
Fig. 6.15.	Time History Measurements of Dynamic Load on Pile, Test H1	116
Fig. 6.16.	Time History Measurements of Near and Far Field Pore Water Pressures, Test H1, [m = milli]	117
Fig. 6.17.	Time History Measurements of Pile Head Movement, Test H1, [m = milli]	118
Fig. 6.18.	Time History Measurements of Dynamic Load on Pile, Test I2	119
Fig. 6.19.	Time History Measurements of Near and Far Field Pore Water Pressures, Test I2, [m = milli]	120
Fig. 6.20.	Time History Measurements of Pile Head Movement, Test I2, [m = milli]	121

LIST OF FIGURES (Cont'd)

		Page
Fig. 6.21.	Time History Measurements of Pile Head Movement and Near Field Pore Water Pressure, Test I2, [m = milli]	122
Fig. 6.22.	Time History Measurements of Dynamic Load on Pile, Test K	123
Fig. 6.23.	Time History Measurements of Near and Far Field Pore Water Pressures, Test K, [m = milli]	124
Fig. 6.24.	Time History Measurements of Pile Head Movement, Test K, [m = milli]	125
Fig. 6.25.	Time History Measurements of Pile Head Movement and Near Field Pore Water Pressure, Test K, [m = milli]	126
Fig. 6.26.	Load-Movement Curves, Tests A3, I1, N2	129
Fig. 6.27.	Load-Movement Curves, Tests F, M1, M2	130
Fig. 6.28.	Load-Movement Curves, Tests E1, E2, L2	131
Fig. 6.29.	Load-Movement Curves, Tests I1, M2	132
Fig. 6.30.	Top and Bottom Time Histories of Normalized Unit Load Transfer, Tests H1, H2	134
Fig. 7.1.	Measured Spectrum versus Target Spectrum, Horizontal Motion	137
Fig. 7.2.	Time History Measurements of Dynamic Load on Pile, Test R2	139
Fig. 7.3	Time History Measurements of Near and far Field Pore Water Pressures, Test R2, [m = milli]	141
Fig. 7.4.	Time History Measurements of Pile Head Movement, Test R2, [m = milli]	142
Fig. 7.5.	Time History Measurements of Dynamic Load on Pile, Test S4	143
Fig. 7.6.	Time History Measurements of Near and Far Field Pore Water Pressures, Test S4, [m = milli]	144
Fig. 7.7.	Time History Measurements of Pile Head Movement, Test S4, [m = milli]	145
Fig. 7.8.	Time History Measurements of Pile Head Movement and Near Pore Water Pressure, Test S4, [m = milli]	146
Fig. 7.9.	Time History Measurements of Dynamic Load on Pile, Test U1	148
Fig. 7.10.	Time History Measurements of Near and Far Field Pore Water Pressures, Test U1, [m = milli]	149

LIST OF FIGURES (Cont'd)

		Page
Fig. 7.11.	Time History Measurements of Pile Head Movement, Test U1, [m = milli]	150
Fig. 7.12.	Time History Measurements of Dynamic Load on Pile, Test U3	151
Fig. 7.13.	Time History Measurements of Near and Far Field Pore Water Pressures, Test U3, [m = milli]	152
Fig. 7.14.	Time History Measurements of Pile Head Movement, Test U3, [m = milli]	153
Fig. 7.15.	Time History Measurements of Near Field and Far Field Pore Water Pressures, and Pile Head Movement, Test U3, [m = milli]	154
Fig. 7.16.	Display of Liquefaction Around the Pile, Test U3	156
Fig. 7.17.	Time History Measurements of Dynamic Load on Pile, Test T1	158
Fig. 7.18.	Time History Measurements of Near and Far Field Pore Water Pressures, Test T1, [m = milli]	159
Fig. 7.19.	Time History Measurements of Pile Head Movement, Test T1, [m = milli]	160
Fig. 7.20.	Time History Measurements of Dynamic Load on Pile, Test T2	162
Fig. 7.21.	Time History Measurements of Near and Far Field Pore Water Pressures, Test T2, [m = milli]	163
Fig. 7.22.	Time History Measurements of Pile Head Movement, Test T2, [m = milli]	164
Fig. 7.23.	Load-Movement Curves, Tests R1, S3, U3	165
Fig. 7.24.	Load-Movement Curves, Tests R2, S4	166
Fig. 7.25.	Load-Movement Curves, Tests S1,T1,T2	168
Fig. 7.26.	Load-Movement Curves, Tests U1,U2,U3	169
Fig. 7.27.	Load-Movement Curves, Tests U3, V1, W1	170
Fig. 7.28.	Top and Bottom Time Histories of Normalized Unit Load Transfer, Tests R1, U3	173
Fig. 8.1.	Contour Plot of Stability, Mobility and Failure Conditions Under Horizontal Earthquake Loading (Confining Pressure = 2.5 psi, Relative Density = 55%)	177

LIST OF FIGURES (Cont'd)

Page

Fig. 8.2. Contour Plot of Stability and Mobility Conditions Under Horizontal Earthquake Loading (Confining Pressure = 2.5 psi, Relative Density = 70%) 178

Fig. 8.3. Contour Plot of Stability and Mobility Conditions Under Horizontal Earthquake Loading (Confining Pressure = 5.0 psi, Relative Density = 55%) 179

Fig. 8.4. Contour Plot of Stability and Mobility Conditions Under Horizontal Earthquake Loading with Distance to Epicenter (Confining Pressure = 5.0 psi,Relative Density = 55%) 180

Appendix B

Fig. B.1. Strain Gage Calibration Equations 192

Appendix E

Fig. E.1. Load-Depth Relationships, Test A1 201

Fig. E.2. Load-Depth Relationships, Test A2..... 201

Fig. E.3. Load-Depth Relationships, Test A3 202

Fig. E.4. Load-Depth Relationships, Test B1 202

Fig. E.5. Load-Depth Relationships, Test B2 203

Fig. E.6. Load-Depth Relationships, Test C 203

Fig. E.7. Load-Depth Relationships, Test D 204

Fig. E.8. Load-Depth Relationships, Test E1 204

Fig. E.9. Load-Depth Relationships, Test E2 205

Fig. E.10. Load-Depth Relationships, Test F 205

Fig. E.11. Load-Depth Relationships, Test O1 206

Fig. E.12. Load-Depth Relationships, Test O2 206

Fig. E.13. Load-Depth Relationships, Test P 207

Fig. E.14. Load-Depth Relationships, Test Q 207

LIST OF FIGURES (Cont'd)

Page

Appendix F

Fig. F.1. Time History Measurements of Dynamic Load on Pile, Test G 209

Fig. F.2. Time History Measurements of Near and Far Field Pore Water Pressures, Test G, [m = milli] 210

Fig. F.3. Time History Measurements of Pile Head Movement, Test G, [m = milli] 211

Fig. F.4. Time History Measurements of Dynamic Load on Pile, Test H2 212

Fig. F.5. Time History Measurements of Near and Far Field Pore Water Pressures, Test H2, [m = milli] 213

Fig. F.6. Time History Measurements of Pile Head Movement, Test H2, [m = milli] 214

Fig. F.7. Time History Measurements of Dynamic Load on Pile, Test I1 215

Fig. F.8. Time History Measurements of Near and Far Field Pore Water Pressures, Test I1, [m = milli] 216

Fig. F.9. Time History Measurements of Pile Head Movement, Test I1, [m = milli] 217

Fig. F.10. Time History Measurements of Pile Head Movement and Near Field Pore Water Pressure, Test I1, [m = milli] 218

Fig. F.11. Time History Measurements of Dynamic Load on Pile, Test J 219

Fig. F.12 Time History Measurements of Near and Far Field Pore Water Pressures, Test J, [m = milli] 220

Fig. F.13. Time History Measurements of Pile Head Movement, Test J, [m = milli] 221

Fig. F.14. Time History Measurements of Dynamic Load on Pile, Test L1 222

Fig. F.15 Time History Measurements of Near and Far Field Pore Water Pressures, Test L1, [m = milli] 223

Fig. F.16. Time History Measurements of Pile Head Movement, Test L1, [m = milli] 224

Fig. F.17. Time History Measurements of Dynamic Load on Pile, Test L2 225

Fig. F.18. Time History Measurements of Near and Far Field Pore Water Pressures, Test L2, [m = milli] 226

LIST OF FIGURES (Cont'd)

Page

Fig. F.19. Time History Measurements of Pile Head Movement, Test L2, [m = milli] 227

Fig. F.20. Time History Measurements of Pile Head Movement and Near Field Pore Water Pressure, Test L2, [m = milli] 228

Fig. F.21. Time History Measurements of Dynamic Load on Pile, Test M1 229

Fig. F.22. Time History Measurements of Near and Far Field Pore Water Pressures, Test M1, [m = milli] 230

Fig. F.23. Time History Measurements of Pile Head Movement, Test M1, [m = milli] 231

Fig. F.24. Time History Measurements of Dynamic Load on Pile, Test M2 232

Fig. F.25. Time History Measurements of Near and Far Field Pore Water Pressures, Test M2, [m = milli] 233

Fig. F.26. Time History Measurements of Pile Head Movement, Test M2, [m = milli] 234

Fig. F.27. Time History Measurements of Dynamic Load on Pile, Test N1 235

Fig. F.28. Time History Measurements of Near and Far Field Pore Water Pressures, Test N1, [m = milli] 236

Fig. F.29. Time History Measurements of Pile Head Movement, Test N1, [m = milli] 237

Fig. F.30. Time History Measurements of Dynamic Load on Pile, Test N2 238

Fig. F.31. Time History Measurements of Near and Far Field Pore Water Pressures, Test N2, [m = milli] 239

Fig. F.32. Time History Measurements of Pile Head Movement, Test N2, [m = milli] 240

Appendix H

Fig. H.1. Original, Target and Computed (Scaled, M = 7.0) Spectra (Horizontal Motion) 247

Fig. H.2. Combined Scaled (M = 7.0) Horizontal Record of Oceanside Earthquake 248

Fig. H.3. Extended Scaled (M = 7.0) Horizontal Record of Oceanside Earthquake 249

LIST OF FIGURES (Cont'd)

		Page
Fig. H.4.	Velocity Time History of Extended and Scaled (M = 7.0) Horizontal Component of Oceanside Earthquake	250
Fig. H.5.	Displacement Time History of Extended and Scaled (M = 7.0) Horizontal Component of Oceanside Earthquake	251
Fig. H.6.	Original, Target and Computed (Scaled, M = 7.5) Spectra (Horizontal Motion)	252
Fig. H.7.	Combined Scaled (M = 7.5) Horizontal Record of Oceanside Earthquake	253
Fig. H.8.	Extended Scaled (M = 7.5) Horizontal Record of Oceanside Earthquake	254
Fig. H.9.	Velocity Time History of Extended and Scaled (M = 7.5) Horizontal Component of Oceanside Earthquake	255
Fig. H.10.	Displacement Time History of Extended and Scaled (M = 7.5) Horizontal Component of Oceanside Earthquake	256
Appendix J		
Fig. J.1.	Time History Measurements of Dynamic Load on Pile, Test R1	259
Fig. J.2.	Time History Measurements of Near and Far Field Pore Water Pressures, Test R1, [m = milli]	260
Fig. J.3.	Time History Measurements of Pile Head Movement, Test R1, [m = milli]	261
Fig. J.4.	Time History Measurements of Dynamic Load on Pile, Test S1	262
Fig. J.5.	Time History Measurements of Near and Far Field Pore Water Pressures, Test S1, [m = milli]	263
Fig. J.6.	Time History Measurements of Pile Head Movement, Test S1, [m = milli]	264
Fig. J.7.	Time History Measurements of Dynamic Load on Pile, Test S2	265
Fig. J.8.	Time History Measurements of Near and Far Field Pore Water Pressures, Test S2, [m = milli]	266
Fig. J.9.	Time History Measurements of Pile Head Movement, Test S2, [m = milli]	267
Fig. J.10.	Time History Measurements of Dynamic Load on Pile, Test S3	268
Fig. J.11.	Time History Measurements of Near and Far Field Pore Water Pressures, Test S3, [m = milli]	269

LIST OF FIGURES (Cont'd)

		Page
Fig. J.12.	Time History Measurements of Pile Head Movement, Test S3, [m = milli]	270
Fig. J.13.	Time History Measurements of Dynamic Load on Pile, Test U2	271
Fig. J.14.	Time History Measurements of Near and Far Field Pore Water Pressures, Test U2, [m = milli]	272
Fig. J.15.	Time History Measurements of Pile Head Movement, Test U2, [m = milli]	273
Fig. J.16.	Time History Measurements of Dynamic Load on Pile, Test V1	274
Fig. J.17.	Time History Measurements of Near and Far Field Pore Water Pressures, Test V1, [m = milli]	275
Fig. J.18.	Time History Measurements of Pile Head Movement, Test V1, [m = milli]	276
Fig. J.19.	Time History Measurements of Dynamic Load on Pile, Test V2	277
Fig. J.20.	Time History Measurements of Near and Far Field Pore Water Pressures, Test V2, [m = milli]	278
Fig. J.21.	Time History Measurements of Pile Head Movement, Test V2, [m = milli]	279
Fig. J.22.	Time History Measurements of Dynamic Load on Pile, Test W1	280
Fig. J.23.	Time History Measurements of Near and Far Field Pore Water Pressures, Test W1, [m = milli]	281
Fig. J.24.	Time History Measurements of Pile Head Movement, Test W1, [m = milli]	282
Fig. J.25.	Time History Measurements of Dynamic Load on Pile, Test W2	283
Fig. J.26.	Time History Measurements of Near and Far Field Pore Water Pressures, Test W2, [m = milli]	284
Fig. J.27.	Time History Measurements of Pile Head Movement, Test W2, [m = milli]	285
Fig. J.28.	Illustration of Effect of Pulley Lag on Axial Force on Pile During Horizontal Tests	286

CHAPTER I

Introduction

The dynamic response of axially loaded piles has been the focus of considerable research, both analytical and experimental, for several years. Mathematical models that treat the supporting soil as linear, viscoelastic media are presently in use [Novak and Aboul-Ella (1979); Roesset (1980); Dobry and Gazetas (1985)], although most applications have been in the area of machine foundations. However, nonlinear solutions more suitable to the analysis of piles during seismic events have been developed recently. One class of such models considers radiational damping through the soil in a generally rigorous way [Nogami and Konagai (1986)], while another class requires that assumptions be made regarding radiation damping but which models near-field hysteretic damping accurately based on time series response of nonlinear uncoupled unit load transfer curves [Foo et al. (1977)]. In the latter class, it is possible to replicate seismic events through specified time-history motion of the free-field soil (physically, motion of the supports for the nonlinear springs that model the uncoupled soil unit load transfer curves). However, effects of losses in pile-soil shearing, net passive and base resistance during the event due to cyclic loading must be supplied by the user of the method and hence are presumed to be at least approximately predictable. The primary use of the mathematical models described in Nogami and Konagai (1986) and Foo et al. (1977) has been to model problems in which dynamic load is applied through the pile head and/or where assumed degradation models have been applied to the soil undergoing seismic excitation. The objectives of these analyses have generally been to develop dynamic response curves for foundations in order to permit analysis of the superstructure and not specifically to model the capacity of the pile during loading.

Some experimental data exist against which to test the mathematical models, but most of the experiments have not simulated earthquake loading or have not included one or more important variables. The most reliable data are those developed under conditions in which the effective stresses simulate those found in situ, that is, either full-scale field tests or tests conducted in a centrifuge. For example, full-scale experimental studies of piles subjected to harmonic dynamic loads large enough to impart nonlinear behavior have been reported [Blaney et al. (1987); Muster and O'Neill (1986); Scott et al. (1982); Hall (1984)], and recent attempts have been made toward applying measured soil base motion response to piles and pile groups in dry sand in the centrifuge [Finn (1987)].

LATERAL RESPONSE

A study by Scott et al. (1982), which involved only lateral pile-head excitation, indicated that liquefaction (and instantaneous reduction in lateral soil reaction) may have been induced by pile-head loading in a saturated fine sand. Except for this study, none of the referenced studies was conducted to loads large enough to produce significant degradation of capacity.

AXIAL RESPONSE

An important source of data are laboratory and field tests that have been performed on piles to a sufficient magnitude of combined cyclic load and static bias load to produce failure. Most of these tests have been conducted under a slow rate of loading. The results may be misleading regarding their application to earthquake problems, because rapid, high-amplitude, cyclic axial loading tends to produce two counteracting effects: (a) loss of capacity, principally in skin friction [Poulos (1984); Poulos (1982); Lambson and Craig (1988)], and (b) increase in capacity due to viscoelastic effects [Bea (1980); Briaud and Terry (1986); Poulos (1981)]. Studies show, however, that net capacity loss (i.e., degradation) occurs in both cohesive soils [Holmquist and Matlock (1976); Karlsrud et al. (1986)] and cohesionless soils [Poulos (1982)]. Studies have also indicated that relative motions between the pile and soil required to initiate cyclic degradation are approximately equal to the relative displacement required to initiate side shear failure in static loading [Poulos (1984); Lambson (1988)].

Holmquist and Matlock (1976) determined from slow cyclic tests in soft clay that one-way loading produced less severe degradation than two-way loading and recommended an envelope unit load transfer curve that terminated at 0.67 times the static ultimate capacity for one-way loading and at 0.33 times the static capacity for two-way loading. Karlsrud et al. (1986) independently arrived at similar conclusions for piles in overconsolidated clay in the field and further observed that large-amplitude, post-failure loading produced additional degradation in available side shear to about 30% of its static value. In low-plasticity, overconsolidated, cohesive glacial till, McAnoy et al. (1982) observed that piles tested with a tensile bias of 40% of the static uplift capacity and a superimposed cyclic load of 40% of the static uplift capacity produced a degradation of about 20% in average ultimate unit side shear after application of over 500 cycles of load.

With lower amplitudes of either static bias or cyclic load, insignificant loss of capacity occurred with in excess of 13000 cycles of applied load.

In sands, Poulos [Poulos (1982); Poulos (1984)] found that short, stiff piles suffer degradation sooner and degrade more severely than long, flexible piles, and that degradation of skin friction in calcareous sands tends to be more severe than in siliceous sands (in the range of 25% loss of capacity in siliceous sands and 50% loss in calcareous sands). Poulos (1984) also found that neither the soil modulus nor the ultimate base bearing capacity appeared to be seriously affected by cyclic loading. Chang and Hanna (1980) performed one-way cyclic loading tests on laboratory model piles in dry medium dense sand to a large number of cycles. They found that pile behavior was highly dependent on the magnitude of the repeated load and that pile failure could occur with cyclic loads of as little as 30% of the ultimate static load. They also found that one of the effects of repeated loading was to cause a redistribution of loads from the shaft to the base.

Separate sources of data providing information about the effects of capacity gain due to rate-of-loading effects [Bea (1980); Briaud and Terry (1986)] suggest that axial pile capacity increases by about 5% per log cycle decrease in total time to failure in clay, suggesting that load excursions at primary earthquake frequencies could produce capacity increases, relative to static capacity, of perhaps 20 to 30% in the absence of cyclic degradation. In sands, the effect appears to be slightly less pronounced [Briaud and Terry (1986)].

Since the data from slow cyclic tests suggest losses due to cyclic degradation of from 20 to 70% of static capacity, and data from rate-of-loading studies suggest that viscous loading effects will independently produce gains in capacity of 20 to 30%, it would appear that, if the result of the two type of studies can be superimposed, earthquake frequency loading could produce a net loss of capacity, provided that the induced amplitude of relative pile to soil displacement during the seismic events exceeds perhaps 1% of pile diameter, the approximate value required to initiate static side shear failure.

LIQUEFACTION

Other factors, however, also appear to be relevant when considering the response of axially loaded piles to seismic excitation. Stress waves in a saturated granular soil can produce either liquefaction or cyclic mobility in the free field which, when superimposed

on the effects of cyclic pile motion described above, may further reduce the capacity of the pile enough to produce foundation failure. Physical evidence of the severity of the damage to foundation piles due to liquefaction-induced ground displacement has been reported in Japan [Hamada (1989)]. Liquefaction and cyclic mobility phenomena have been extensively investigated during the last two decades [e.g., Seed (1976); Castro and Poulos (1976); Finn (1985)]. Liquefaction denotes a condition where soil will undergo continued deformation at a constant low residual resistance or with no residual resistance, due to the build-up and maintenance of high pore water pressures which reduce the effective confining pressures to a very low value. Cyclic mobility denotes a condition in which cyclic shear application produces a condition of initial liquefaction and subsequent cyclic stress applications cause limited strains to develop either because of the remaining resistance of the soil to deformation or because the soil dilates, which causes the pore water pressure to drop, and the soil to stabilize under the applied loads. Liquefaction has been observed in situ on many occasions [e.g., Seed (1967); Seed and Idriss (1967)], and it has been reproduced in the laboratory [e.g., Castro (1969); Seed and Peacock (1970)]. Generally, liquefaction appears not to occur when shear strains (γ) induced by loading are less than 0.01 per cent [Dobry et al. (1982)]. An experimental study [Veyera (1990)] conducted on shock-loaded saturated soils under undrained conditions indicated that above a threshold compressive strain of about 0.005 percent, residual excess pore-water pressure increases could be induced, while below this value no excess pore-water pressures were observed. Stokoe and Nazarian (1985) observed the sites of recent earthquakes in California and found that sands do not liquefy when v_s (shear wave velocity) is greater than 550 ft/sec and do liquefy when v_s is less than 450 ft/sec. Based on 130 liquefied and non liquefied sites during 19 Japanese earthquakes, Midorikawa et. al. (1988) concluded that the occurrence of soil liquefaction is better correlated with the peak ground velocity (PGV) during a seismic event than with the peak ground acceleration (PGA), which has often been suggested in the past. They estimated that liquefaction is likely to occur when the peak ground velocity exceeds 6 in./sec. In laboratory undrained cyclic tests (triaxial, direct simple shear) on saturated sand, cyclic mobility has been observed to develop and to result in large strains [Casagrande (1975); Lee and Seed (1967)]. A laboratory study conducted on artificially cemented sand [Saxena et al. (1988)] showed that small amount of cohesion increased significantly the cyclic strength of uncemented sand increasing, therefore, the liquefaction resistance. The effect of the multidirectional loading has been studied by Ishihara and Yamakasi (1980) concluding that liquefaction resistance under multidirectional shaking becomes as much as 25 to 40% smaller than would be expected under unidirectional loading.

Available computer programs, such as SHAKE [Schnabel et al. (1972)], can be used to evaluate the dynamic response of a soil deposit . In SHAKE, the soil deposit is modelled as a system of homogeneous, visco-elastic layers of infinite horizontal extent subjected to vertically propagating shear waves. A computer program APOLLO [Martin and Seed (1978)] can be used for the analysis of generation and dissipation of pore pressures with time in horizontal sand layers during cyclic or earthquake loading. DCHARM [Idriss et al. (1988)], a nonlinear ground response computer program (that allows modification of material properties with time due to increase in pore water pressure or remolding), can be used for assessing the dynamic response of sites underlain by soft clay sediments. The evaluation of liquefaction potential of the free-field soil can also be accomplished by using the simplified procedure (cyclic stress approach) developed by Seed and Idriss (1971). A convenient closed-form expression for earthquake-induced shear stress magnitude and its phase shift with respect to the ground acceleration has also been derived analytically [Harrop-Williams (1988)]. An alternative approach, the cyclic strain approach [Dobry et al. (1982)], for evaluating the buildup of excess pore water pressures and the potential for liquefaction of level sandy sites during earthquakes has also been proposed. Using state-of-the-practice design procedures, for instance, in a nonlinear seismic response analysis of a jacket platform founded in liquefiable soil in the Adriatic sea, Vanzini, et al. (1988) evaluated the soil-pile interaction behavior by considering the free-field and the near-field liquefaction potentials separately, and subsequently incorporated them into the soil-pile-structure interaction analyses. Very few attempts have been made to study how liquefaction and/or cyclic mobility interact with cyclic degradation due to relative pile-soil movement to affect pile capacity, especially in uplift. In one experimental study, De Alba (1983) reported that the capacity of piles in small scale (either single or within groups) in saturated sand during simulated strong seismic motion in the laboratory was reduced in proportion to the ratio of induced pore water pressure to the initial effective stress in the sand mass when the sand was loaded horizontally. No attempt was made to scale length or to model the seismic signature of a specific event or class of events.

SUMMARY

It would appear that any serious experimental study of the seismic axial response of piles in granular soils should include the effects of pile-soil degradation due to both relative pile-soil movement and to the build-up of excess pore water pressures in the free field that are generated by the seismic motion. These effects could best be simultaneously

modelled by conducting tests in which the soil, and not the pile, is excited. Such is the manner in which the experiments described herein were conducted.

The response of the pile to soil-induced excitation depends on the characteristics of the ground motion, the dynamic characteristics of the pile and the superstructure that the pile supports and, possibly, to the direction and magnitude of any biased load on the pile. Some modern offshore structures (such as tension leg platforms (TLP's) and compliant tower frames) and hydraulic structures require that piles be designed with biased quasi-static uplift loads [e.g., Bradshaw et al. (1984)]. The fundamental periods of framed structures are usually in the range of 0.2 to 0.5 sec. (rotational motion producing push-pull action in the piles) [Bea (1980)], while those for TLP's are somewhat higher. Components of ground motion having similar periods are present in most seismic events, particularly where deep deposits of soil exist above a rock base [Seed and Idriss (1969)]. The presence of these components may produce magnification of structural loads that can potentially feed back into the pile and affect its response. However, Tazoh et al. (1987) have recently published a study of measured response of piles supporting a large bridge in Japan to real seismic events. They concluded, through back-analysis of the data, that while superstructure feedback influenced pile response, the response of the piles was governed more significantly by direct ground motion. These results suggest that the present study should focus on excitation of the pile through the soil and that simulation of the soil motion only, independent of the specific details of the superstructure feedback response, is a reasonable testing condition for the pile. Superstructure feedback for this study was simulated in a very simple and generic manner by applying the biased tension load through a dead weight-spring system having a natural period of approximately 1.0 sec.

CHAPTER II

Overview of Research Program

This study addresses the problem of dynamic response of axially loaded piles with tension bias under vertical and horizontal components of earthquake loading. Of specific concern are (a) whether the pile loses capacity during the period of strong ground motion and thereby either fails or operates under a lower-than-desirable factor of safety, and (b) if the pile loses capacity, whether that loss is permanent or whether it is regained after the conclusion of the seismic event. While mathematical models exist that can provide computations for these phenomena, very little experimental data are known to exist against which to test these models.

The problem has been studied experimentally using physical modelling techniques. The response of axially loaded piles with uplift biases has been simulated as accurately as possible under a given set of controlled conditions in the laboratory. Such behavior has been studied for an impact-driven pile in saturated fine sands of varying permeabilities and subjected to the scaled vertical and horizontal components of a seismic soil motion that has been measured on the seafloor during the Oceanside earthquake (offshore California) of July 13, 1986. Principles of scaling an earthquake to a higher magnitude, and scaling relationships between model and prototype, similar to those applied to centrifuge models, have been utilized in an attempt to simulate the problem realistically.

At a offshore seismic site (Fig. 2.1), vertical and horizontal components of seismic motion at the bedrock level produce primarily compression (p) and shear (s) waves which propagate upwards. Some compression waves may propagate up through the mooring lines of a tension leg platform (TLP) and excite the floating structure, inducing additional dynamic pullout forces into the foundation piles (superstructure feedback). In addition, the seismic waves may also induce changes in the soil, such as far-field induced liquefaction, near-field induced liquefaction, and near-field pile capacity degradation without liquefaction (the latter two cases as a product of the relative motion between the pile and the surrounding soil mass). Soil supporting pile foundations for hydraulic structures, such as piles beneath Tainter gate monoliths, Fig. 2.2, may also experience similar conditions. Therefore, it is essential to understand whether the potential loss of axial capacity of a pile developed from excess pore water pressures and effective stress changes in the soil due to

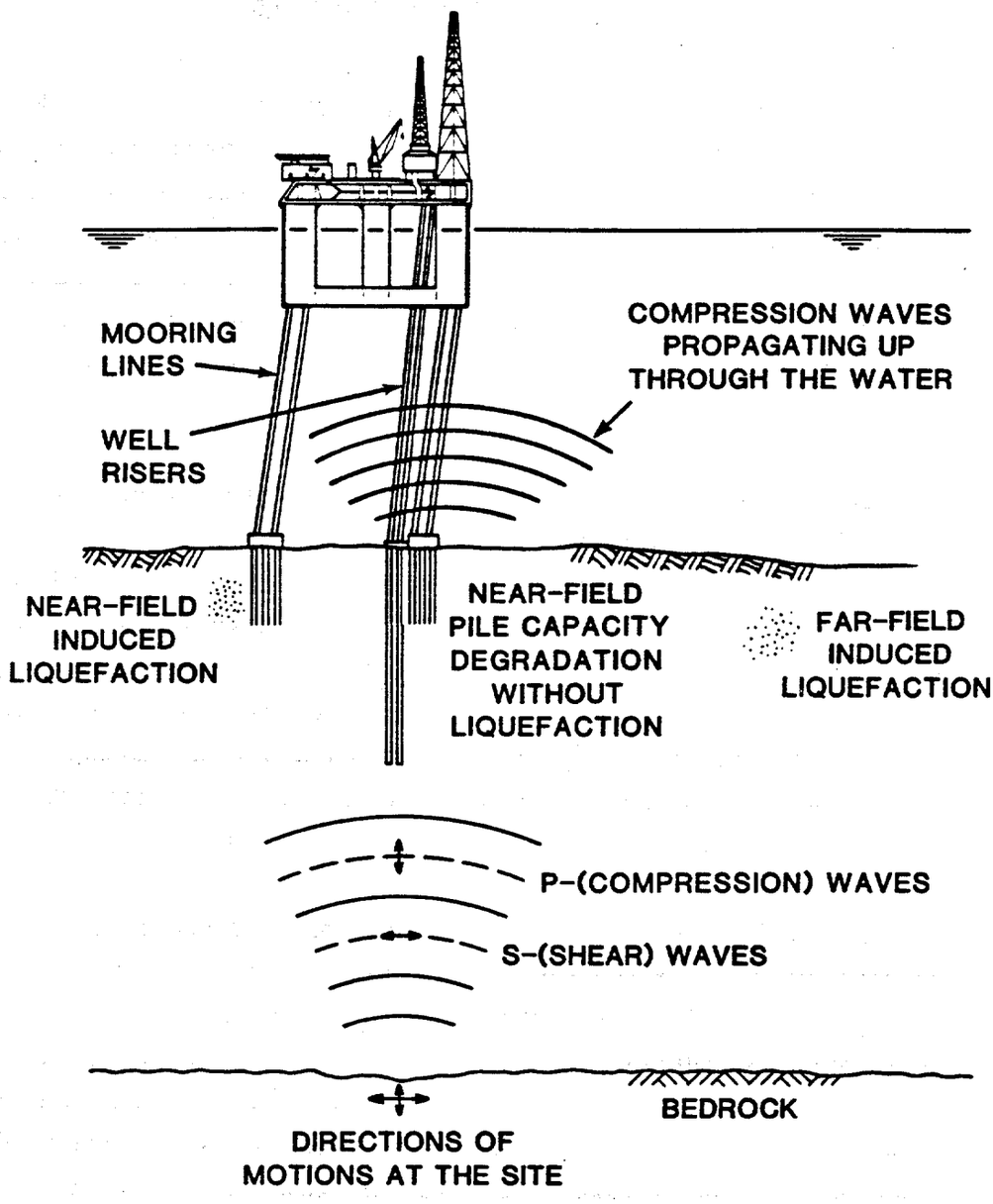

Fig. 2.1. Idealization of Induced Stress Waves During a Seismic Event for an Offshore TLP.

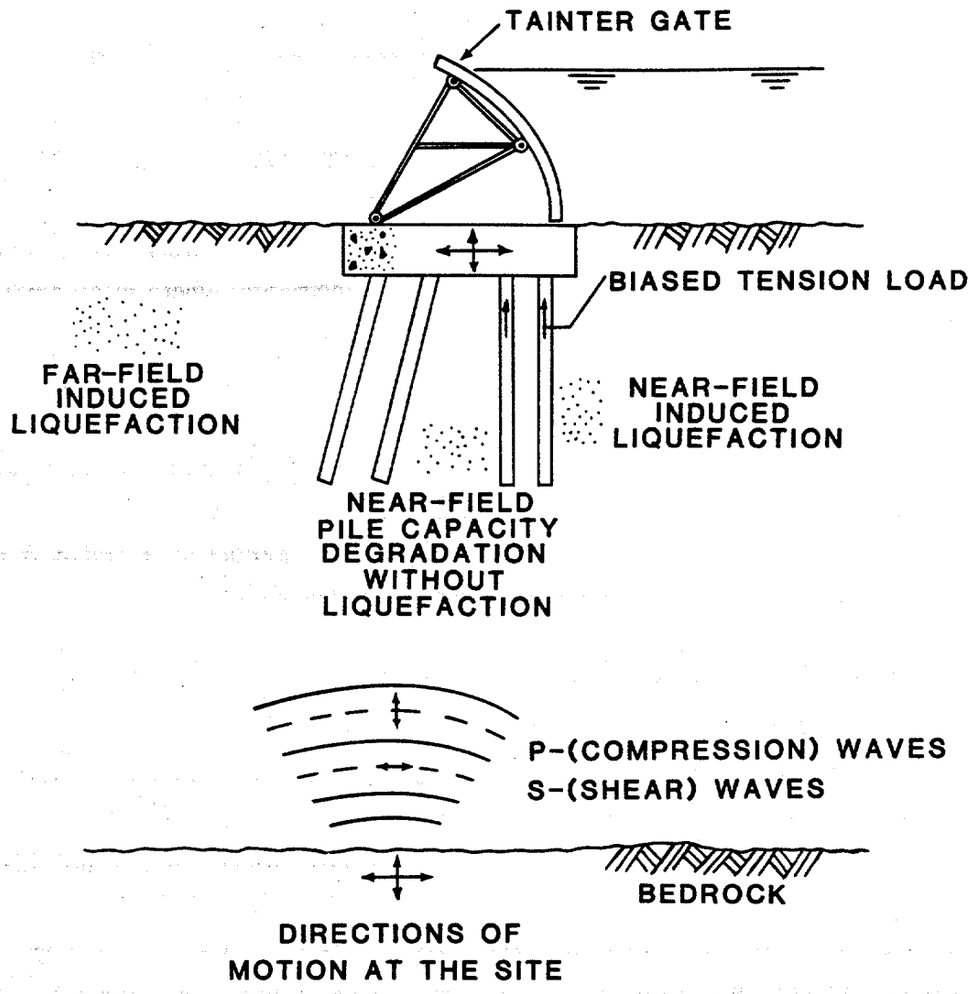

Fig. 2.2. Idealization of Induced Stress Waves During a Seismic Event for a Hydraulic Structure.

the components of relative pile-soil motion should be considered, or whether such interaction can be effectively neglected. This study provides insight into that issue by defining the magnitude of the effects of vertical and horizontal soil motions on a pile in a saturated sand under biased tension loading.

OBJECTIVES

A laboratory experimental study has been conducted in order to evaluate the effect of several parameters affecting the capacity of axially loaded piles subjected to biased uplift loads in a saturated sand deposit that is subjected to simulated vertical and horizontal components of seismic excitation. Generally the zone of greatest susceptibility to loss of side shear capacity is the upper 40 ft of pile penetration, where mean ambient effective stresses in most offshore sand deposits are 5 psi or less. In that zone soil stress waves can produce pore water pressures that are a significant percentage of the in-situ effective stresses (inducing near-field and/or free-field liquefaction). Therefore, this study is focused on simulation of pile-soil interaction in that zone, which has been accomplished by placing a pile segment in an isotropically pressurized chamber in which mean initial effective stresses of 2.5 and 5.0 psi (corresponding to pile penetrations of 20 and 40 ft, respectively) were applied. The pile segment to be tested simulates only that portion of the pile in the zone of interest.

The particular event chosen for this study was the Oceanside event of July 13, 1986, a Richter Magnitude 5.8 earthquake whose epicenter was 74 km southeast of the instrumentation site from which the data were acquired, known as the "SEMS" site. This moderate event appeared to produce a typical record for an offshore California earthquake. The SEMS unit was a three-dimensional accelerometer buried in sediments 5 feet below the mudline off the coast of Long Beach, California. The site is a deep, soft soil site, as characterized in Appendix A. Low peak accelerations of the vertical and horizontal components (3-4 milli-g's and 20-25 milli-g's, respectively) suggested no loss of pile capacity. Therefore, the actual earthquake was scaled to higher magnitudes, i.e., Richter Magnitude 8.0 for the vertical component of motion, and Richter Magnitudes 7.0, 7.5 and 8.0 for a resultant horizontal component of motion. Furthermore, scaling effects for model to prototype were employed.

The specific parameters investigated are listed below:

(1) Magnitude of mean initial effective pressure in the sand (prior to pile driving),

(2) Ratio of static uplift bias load to peak static uplift capacity,

(3) Relative density of the sand,

(4) Earthquake magnitude, and

(5) Type of static loading tests (controlled displacement test or controlled load test).

In order to scale the effect of drainage distance and its effect on pore water pressure generation and dissipation, both the simulated seismic record (acceleration and/or time axis) and soil permeability were also scaled in some tests with vertical motion and for all tests with horizontal motion.

Components of behavior that were investigated are as follows:

(a) Dynamic uplift capacity of the pile during simulated seismic motion for selected combinations of the above parameters (i.e., under what conditions does the pile fail by pullout during the simulated seismic event?), and

(b) Residual static uplift capacity of the pile after the simulated seismic event (i.e., capacity under monotonic uplift loading).

The information developed should provide practical guidance concerning the permissible tension bias loads that can be sustained by piles in fine saturated sand under vertical and horizontal excitation for Magnitude 7.0, 7.5 and 8.0 California-type seismic events.

RESEARCH APPROACH

The response of piles loaded in biased uplift to vertical and horizontal components of Magnitude 7.0, 7.5 and 8.0 seismic events was studied systematically using experimental techniques. The testing sequence was divided in two phases. Phase 1 involved investigation of the behavior of the driven pile subjected to a simulated vertical seismic soil motion, while Phase 2 was focused on studying the behavior of the driven pile subjected to simulated horizontal motion and combined horizontal and vertical motion of the soil in which it was embedded. The in-situ soil stresses were simulated in a saturated pressure chamber under various parametric conditions. The controls (nonvariables) were (a) length (embedment) of the pile segment, (b) degree of saturation of the test sand (100%), (c) pile segment shape (circular steel pile with closed end, uniform diameter and wall thickness), and (d) method of pile insertion (impact driving). Relative densities of the soil considered in this study ranged between 55% (loose sand) and 70% (medium dense sand). Relative

densities lower than 55% are not expected to be found in areas with seismic activity. The general sequence of testing was as follows. A given set of soil conditions was duplicated within the pressurized test chamber. Several static uplift load tests were conducted on piles driven into the saturated soil in the chamber under these conditions to develop a consistent relationship between penetration rate (blow count per inch) and static pullout capacity. This step allowed close estimation of static capacity for the next step (dynamic tests) from the blow count record to drive the pile.

Dynamic tests were then conducted in which the pile was driven into the pressurized chamber and its static uplift capacity evaluated from the penetration rate. A given ratio of static biased load to evaluated static capacity was then applied to the pile through a one-degree-of freedom weight and spring system to model a long-period structure (e.g., a TLP) to which the pile was secured, and the simulated earthquake was applied to the base of the chamber through a servo-controlled testing machine. The weight-spring system represented the effects of superstructure feedback. If the pile failed during the simulated earthquake, no further testing was done. If the pile did not fail, additional static load was applied at the conclusion of the dynamic test to determine whether the post-earthquake static capacity was reduced from the static capacity that was inferred from the driving rate. In this manner the ratio of biased load that could be present on the pile to the pile's static capacity without producing failure during the seismic event could be determined.

The remaining chapters in this document describe the details of the testing apparatus, sand properties, scaling procedures, test results and the conclusions developed from this study. The testing sequence performed to achieve the stated objectives are shown in Table 2.1 and Table 2.2. A relatively large number of baseline (static) tests (A1-F, O1-Q) were conducted to confirm the repeatability of the static uplift capacity, for different relative density and mean effective stress in the soil mass. In order to investigate static failure criteria, both controlled load (CL) and controlled displacement (CD) tests were conducted during the static phase of testing. The dynamic tests (G-N2, R1-W2) were then performed under conditions identical to those that existed in the static tests. Dynamic tests T1 and T2 were also performed with combined horizontal and vertical motions with simple sinusoidal motion for the vertical simulated component. In Test T2, a stiffer spring was used to assess the effect of fundamental vertical period of the superstructure modeled by spring-weight system.

Table 2.1. Testing Sequence, Phase 1 (Vertical Component of Motion)

Test No.	Type of Test: Static (Base Line)/ Dynamic	Type of Static Loading: CD/CL[e]	Condition: Dr(%)/σ_c (psi) / % of Inferred Static Capacity
A1	Static	CD	55 / 5 / -
A2	Static	CD	55 / 5 / -
A3	Static	CL	55 / 5 / -
B1	Static	CD	70 / 5 / -
B2	Static	CL	70 / 5 / -
C	Static	CD	78 / 5 / -
D	Static	CD	85 / 5 / -
E1	Static	CD	55 / 2.5 / -
E2	Static	CL	55 / 2.5 / -
F	Static [a]	CL	55 / 5 / -
G	Dynamic	CD	55 / 5 / 25
H1	Dynamic	CL	55 / 5 / 50
H2	Dynamic	CL	55 / 5 / 70
I1	Dynamic	CL	55 / 5 / 90
I2	Dynamic	CL	55 / 5 / 90
J	Dynamic	CL	70 / 5 / 75
K	Dynamic	CL	70 / 5 / 90
L1	Dynamic	CD	55 / 2.5 / 60
L2	Dynamic	CL	55 / 2.5 / 90
M1	Dynamic [a,c,d]	CL	55 / 5 / 60
M2	Dynamic [a,c,d]	CL	55 / 5 / 90
N1	Dynamic [c]	CL	55 / 5 / 60
N2	Dynamic [c]	CL	55 / 5 / 90

a. Tests conducted with micro-fine sand[b]. Other static tests conducted with standard test sand (SJR sand).

b. Sand with a coefficient of permeability approximately 0.12 times that of SJR sand (standard test sand) to scale drainage distance.

c. Time scaled by a factor of 0.14 in the acceleration record to scale drainage distance and other length factors.

d. Accelerations scaled by a factor of 7 in the acceleration record.

e. CD refers to a controlled displacement test. CL refers to a controlled load test.

Table 2.2. Testing Sequence, Phase 2 (Horizontal and Combined Vertical and Horizontal Motions)

Test No.	Type of Test[a,b]: Static (Base Line)/ Dynamic	Simulated Earthquake Magnitude, M	Condition: Dr(%)/σ_c (psi) / % of Inferred static Capacity
O1	Static	-	55 / 5 / -
O2	Static	-	55 / 5 / -
P	Static	-	70 / 5 / -
Q	Static	-	55 / 2.5 / 0
R1	Dynamic	7.0	55 / 2.5 / 75
R2	Dynamic	7.0	55 / 2.5 / 90
S1	Dynamic	7.5	55 / 2.5 / 60
S2	Dynamic	7.5	55 / 2.5 / 60
S3	Dynamic	7.5	55 / 2.5 / 75
S4	Dynamic	7.5	55 / 2.5 / 90
T1	Dynamic[c]	7.5	55 / 2.5 / 60
T2	Dynamic[c,d]	7.5	55 / 2.5 / 60
T3	Dynamic[e]	7.5	55 / 5.0 / 90
T4	Dynamic[e]	7.5	70 / 2.5 /90
U1	Dynamic	8.0	55 / 2.5 / 45
U2	Dynamic	8.0	55 / 2.5 / 60
U3	Dynamic	8.0	55 / 2.5 / 75
V1	Dynamic	8.0	55 / 5 / 75
V2	Dynamic	8.0	55 / 5 / 90
W1	Dynamic	8.0	70 / 2.5 / 75
W2	Dynamic	8.0	70 / 2.5 / 90

a. All static tests were controlled load test (CL) and all tests were conducted with micro-fine sand.

b. Dynamic tests conducted with time scaled by a factor of 0.14 and acceleration scaled by a factor of 7 in the acceleration record.

c. Combined horizontal and vertical motions with simple sinusoidal motion for vertical component.

d. Conducted with stiffer spring to scale the fundamental period of superstructure.

e. Modified tests in which only applied bias load and displacement were measured.

CHAPTER III

Description of Testing System

The complete testing system described in this chapter includes the test chamber / loading system, test pile, soil instruments, drop hammer, data acquisition system, sand placement methods and calibration constants. Fig. 3.1 provides a picture of the testing arrangement, which is shown in schematic form in Fig. 3.2.

TEST CHAMBER / LOADING SYSTEM

The test chamber, consisting of three separate pieces (3/4-in.-thick top and bottom plates and a 1/4-in.-thick containment cylinder, all made of aluminum) is shown in Fig. 3.3, configured for uplift testing under pure vertical soil excitation. The assembled test chamber was 22.2 in. in height and 24 in. in diameter. Top and bottom plates were attached to the containment cylinder by eight equally-spaced, 1/2-in-diameter threaded rods. A rubber membrane, 1/8-in. thick, folded to the inside of the cylinder and sealed to the outside by hose clamps, provided uniform lateral confinement to the soil inside the chamber, while a separate pressure membrane (pancake bladder), affixed to the underside of the top plate, provided the vertical confinement. Teflon sheets were placed on the inside of the lateral membrane and underneath the top bladder to reduce the friction between the sand and membranes. Appropriate sealing was obtained when the cylinder (with the folded membrane) was inserted in a 1/2-in. groove in each end plate and the bolts tightened. A perforated metal diffusion ring at the base of the chamber was used to flush the sand with carbon dioxide immediately after it was placed in the dry. Such flushing reduces the concentration of nitrogen in the soil pores, which tends to form air bubbles in the soil pores when the soil is saturated. Once this process had been completed, deaired water was introduced into the specimen through the same ring. It was allowed to rise slowly within the soil column until the specimen was saturated.

Two quick connectors were placed through small holes on opposite sides of the chamber to serve as pressure ports for the lateral membrane. As the soil was placed into the chamber, the membrane remained collapsed, allowing the chamber wall to retain the

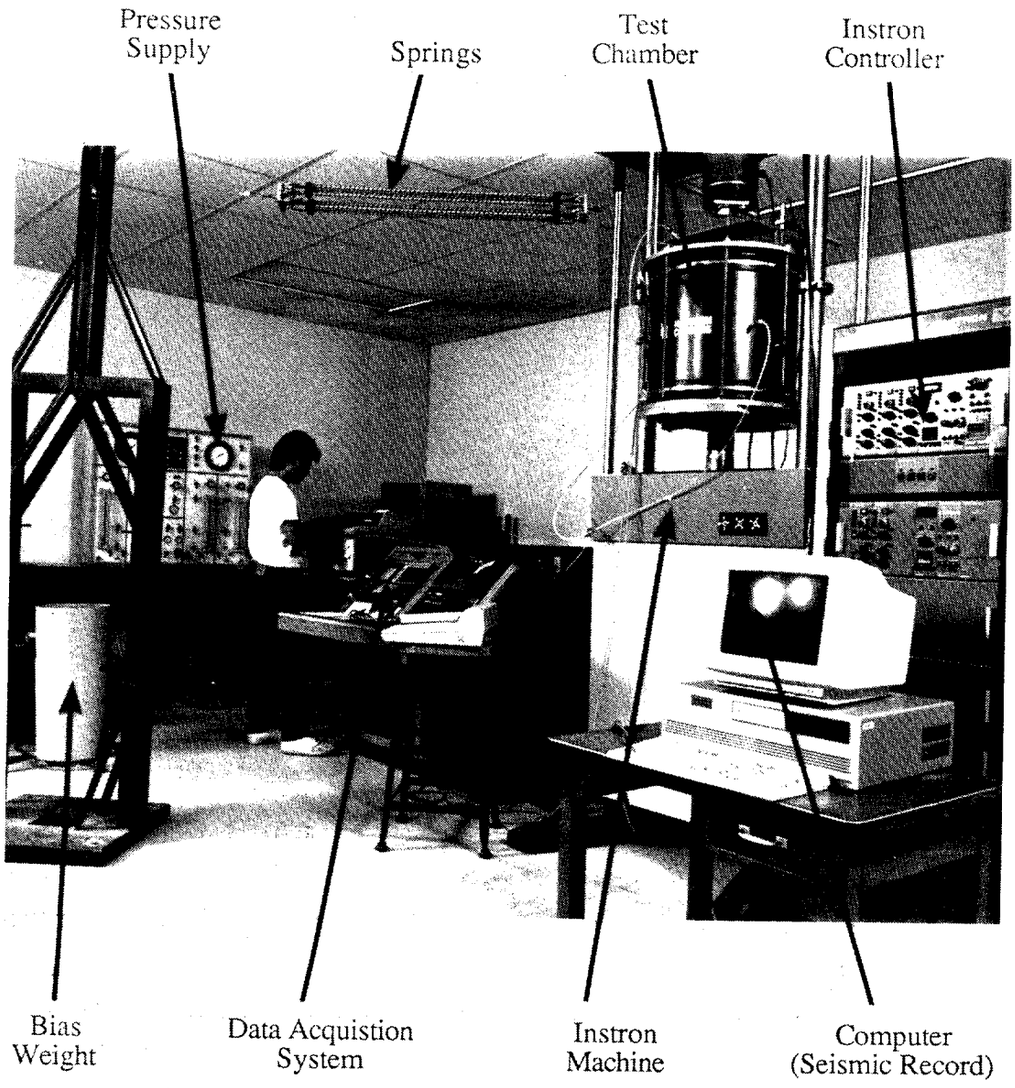

Fig. 3.1. Overall Testing Arrangement.

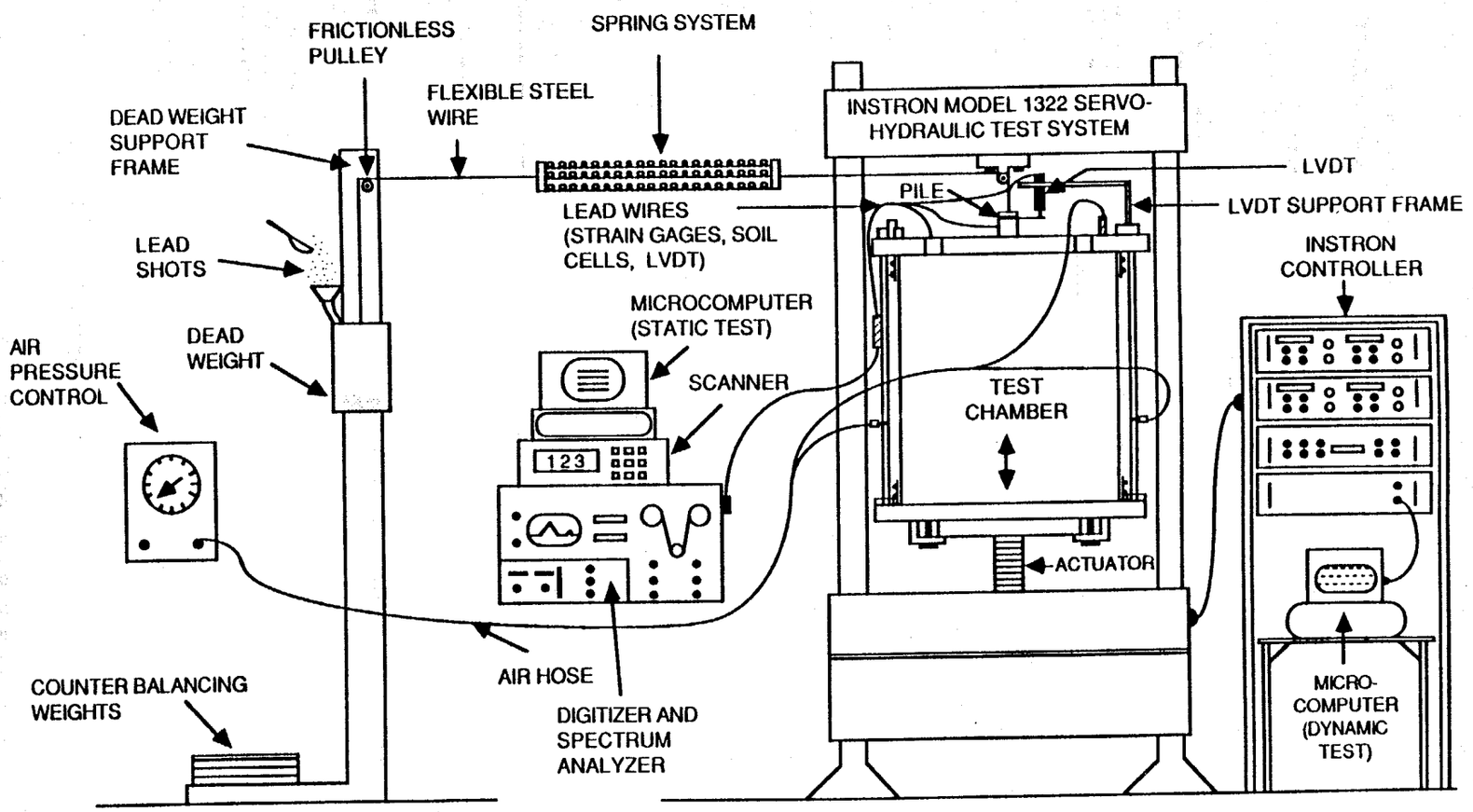

Fig. 3.2. Schematic of Testing Arrangement

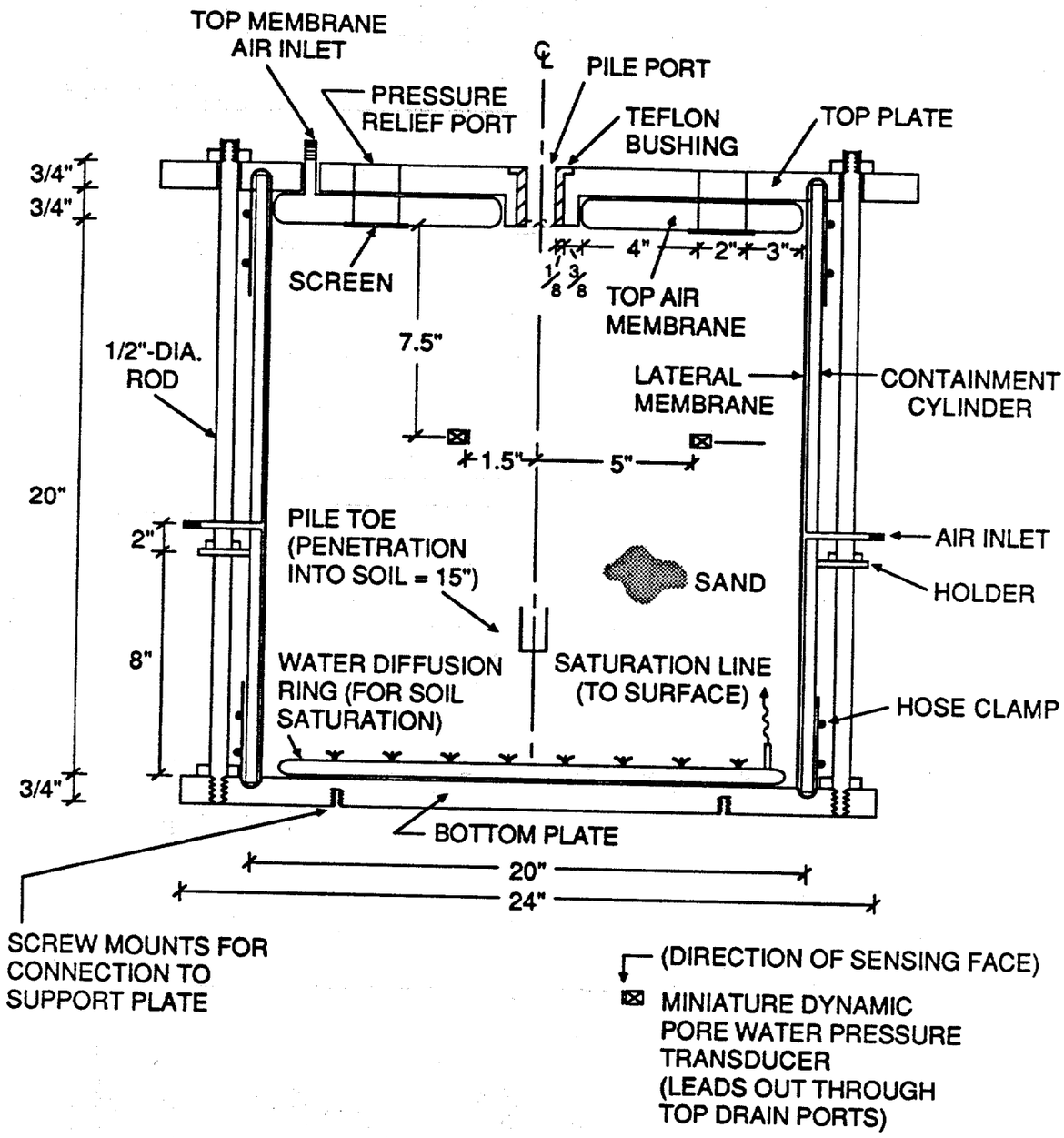

Fig. 3.3. Schematic Elevation of Test Chamber (Vertical Motion).

deposited soil with zero lateral strain, thus preventing changes in the density in the soil mass during deposition. Once the chamber was charged and saturated, air pressure was applied to the lateral membrane that allowed it to lift slowly off the sides of the chamber a distance sufficient to produce a controlled total stress condition at the lateral boundary during subsequent testing.

The top of the chamber, and the top of the soil column, was drained by means of six ports in the top plate: four drainage ports, one port for the pile (which was not pressure tight) and one port that allowed for passthrough of the single air valve for the top membrane. A one-inch-diameter model pile, as indicated in Fig. 3.3, can be accommodated in the chamber.

Dynamic loading was applied to the base of the chamber containing the biased-tension-loaded pile through an Instron (TM) servo-controlled testing machine that was programmed to follow a prescribe deflection time history, defined by the scaled earthquake of interest. The boundary conditions for the internal surface of the test chamber can be summarized as follows:

Top: Controlled effective stress, with drainage;
Sides: Controlled total stress, no drainage; and
Base: No drainage, no relative soil chamber motion.

The condition of upward flow of water through the soil pores during simulated seismic activity (an important factor in liquefaction in loose soils) was permitted.

Fig. 3.4 provides a simplified schematic of the types of waves that can be expected in the soil with the existing test system and imposed vertical motion (Phase 1). The imposed vertical base motion produces upward-propagating compression waves, which, in turn, serve both to excite the pile and potentially to generate excess pore water pressures in the free-field soil. Relative motion is allowed to develop between the pile and the soil, which produces radially propagating shear waves (primarily) which may further produce excess pore water pressures and otherwise degrade the pile/soil resistance. The ratio of chamber radius to pile radius of 10 and the presence of a flexible lateral membrane minimize the effects of boundary reflections.

For Phase 2 (horizontal component of simulated seismic record), the test chamber was reconfigured as shown in Fig. 3.5. The pile was installed by driving it into the

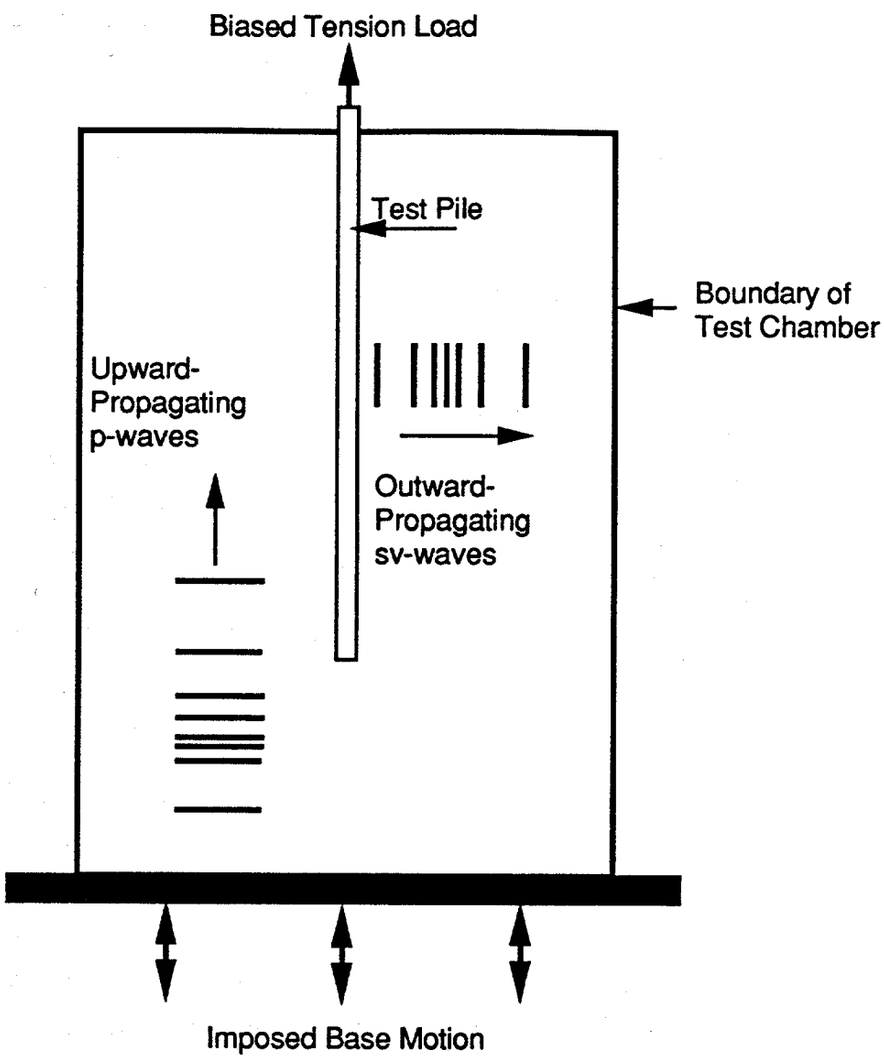

Fig. 3.4. Idealization of Waves in Test Chamber (Vertical Motion).

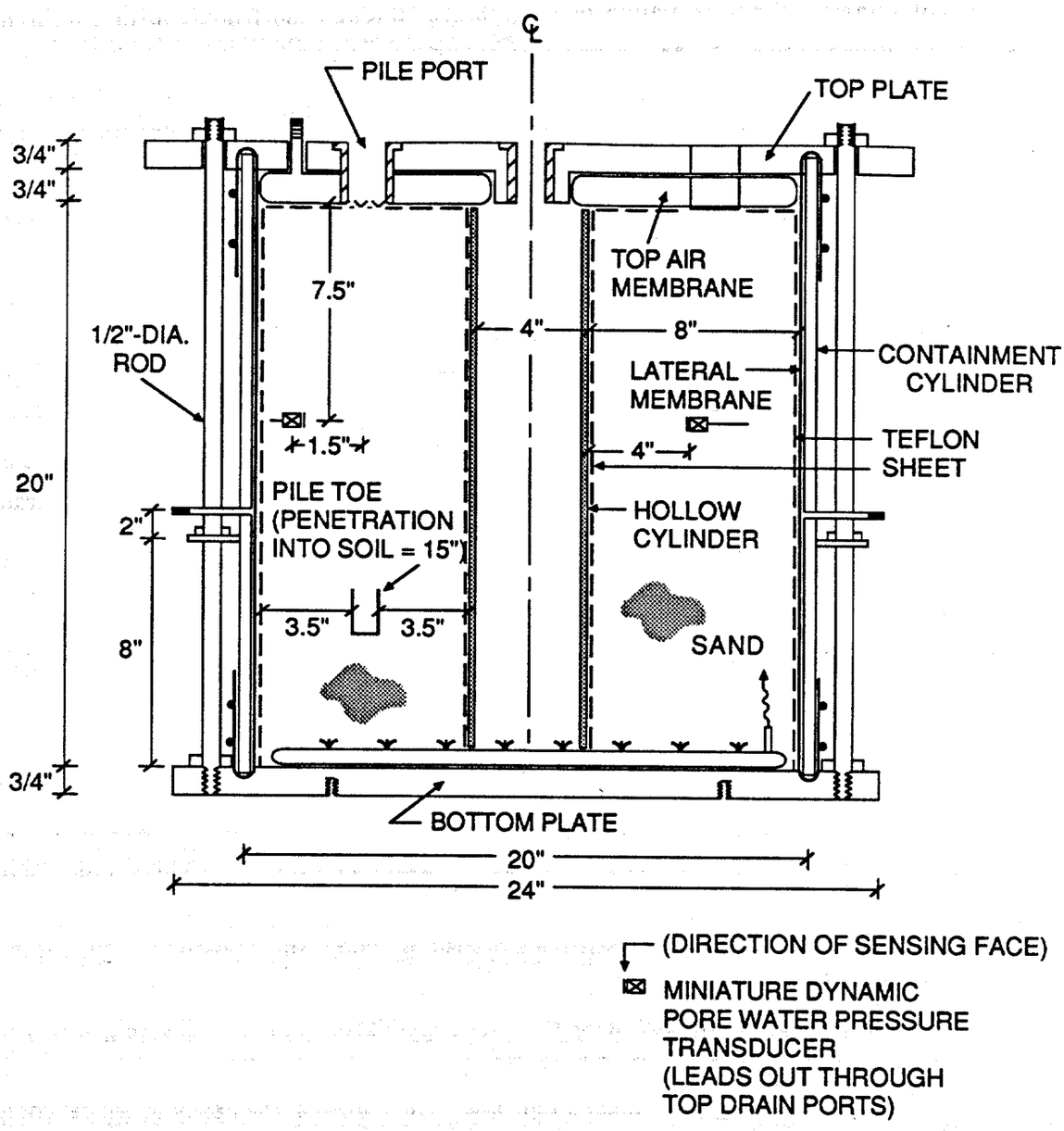

Fig. 3.5. Schematic Elevation of Test Chamber (Rotational Motion).

chamber off center, so that the programmed horizontal seismic motion can be applied through torsional excitation of the chamber through the Instron testing machine. As indicated in Fig. 3.6, the torsional motion produces upward propagating shear (s) waves in the chamber, which can cause the pile to deflect laterally and set up secondary waves that propagate outward toward the boundary of the chamber, which simulates in-situ conditions reasonably well. The sand was placed by dry raining into the annulus between the chamber walls and a central hollow cylinder, as indicated schematically in Figs. 3.5 and 3.7, with the pile equidistant from the inner and outer boundaries. This arrangement was employed to minimize strain gradients radially outward from the axis of rotation and to simulate more directly linear motion (Fig. 3.7). The rotation of the chamber was controlled by a rotational potentiometer at the base of the chamber, programmed so that the linear time history of motion to be simulated was equivalent to the tangential time history of translation at the radial distance of the pile from the axis of the chamber. An articulated arm, shown in Fig. 3.8, was also employed as means to support the applied bias load during the duration of testing with the chamber configured as shown in Fig. 3.5.

The system for applying the biased load (Figs. 3.1 and 3.2) consisted mainly of a flexible high-strength cable, 1/16-in. thick, a threaded steel plug inserted into the pile head, a simple steel loading frame, a flexible spring system (need for the dynamic tests), two frictionless pulleys made of brass (one supported by the Instron's frame and the other supported by the loading frame), a plastic container, lead shots poured into the container acting as dead weight, and a funnel used to control the loading rate (16 lb/min). In the "CL" (controlled loading) static tests load was added until pile pullout was observed. Stability of the loading frame was assured by the presence of counterbalancing weights placed on an extended arm welded to the base plate of loading frame. Static post-shaking CL tests were performed by adding more weight (lead shots) into the plastic container until the pile failed. The ratio of spring constant in the static load application system to bias weight was always such that the natural period of the weight-spring system was 1-2 sec., which was selected because it is in the general range of the lowest fundamental frequency of typical compliant offshore structures. A stiffer spring was used in test T2 to scale, approximately, the fundamental period of a stiffer superstructure following the scaling rules between model and prototype. Such an arrangement for Test T2 is shown in Fig. 3.9. The natural period with this spring was 0.16 sec.

For the preliminary static "CD" (controlled displacement) tests, the pile head was affixed to the Instron's high capacity load cell and the actuator engaged to provide a

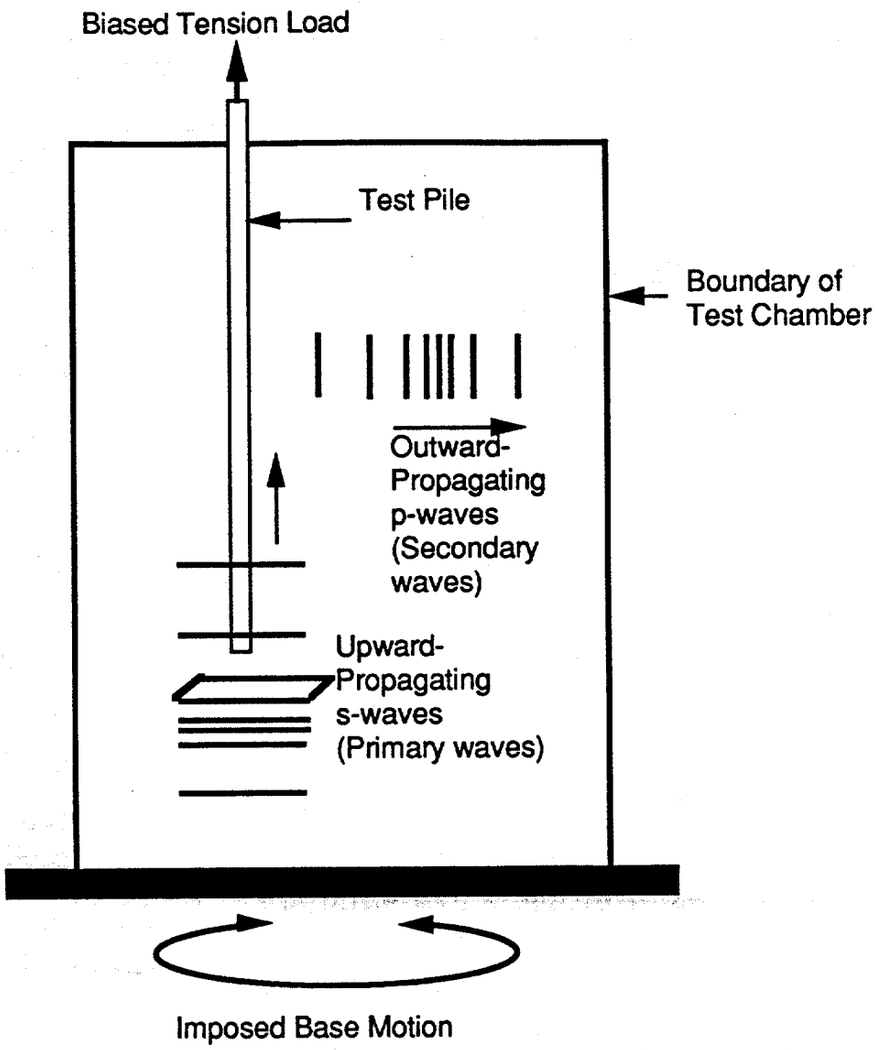

Fig. 3.6. Idealization of Waves in Test Chamber (Rotational Motion).

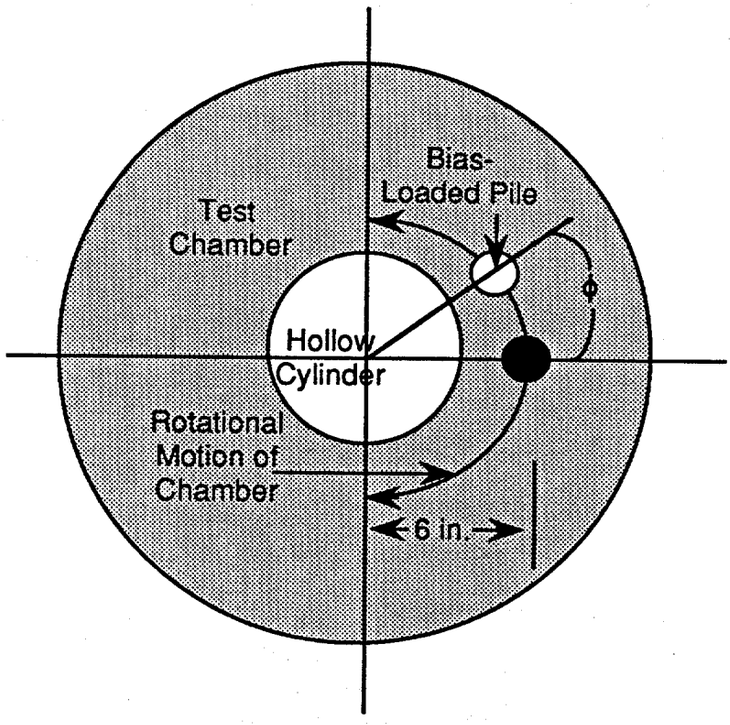

Linear Movement along Path AB Models Horizontal Soil Movement Recorded by SEMS Unit Scaled Appropriately to Magnitude 7, 7.5 and 8, Respectively, for Oceanside Event of July, 1986.

Hollow Cylinder Is Used to Produce Near-Uniform Strain Fields in the Vicinity of the Test Pile.

Fig. 3.7. Plan Schematic View of Chamber, Indicating Conversion of Rotational Motion into Modelled Horizontal Translational Motion.

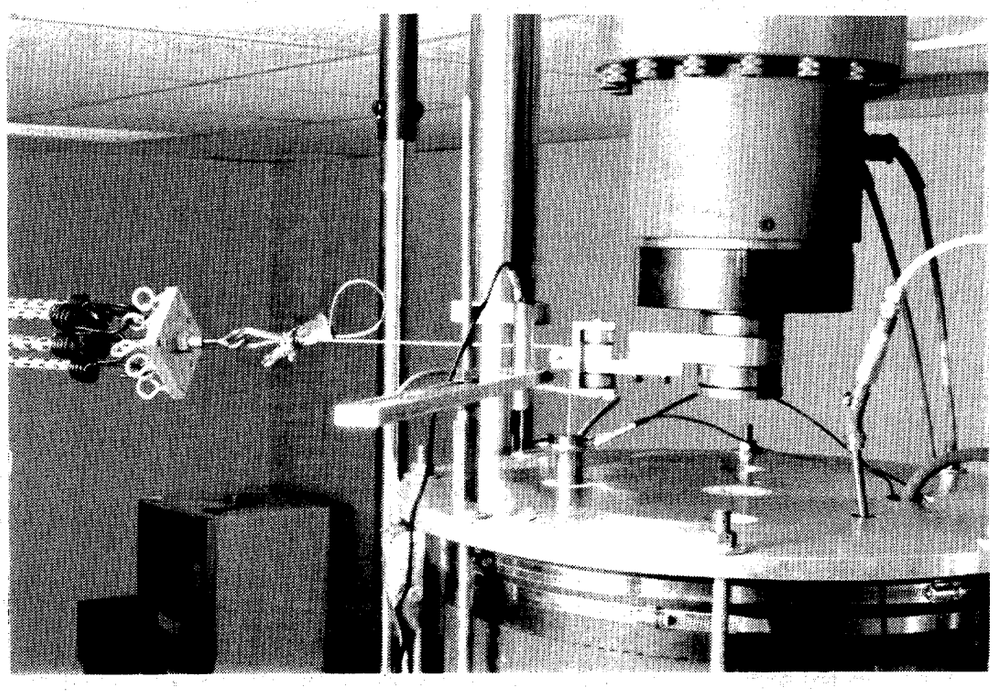

Fig. 3.8. Articulated Arm Display.

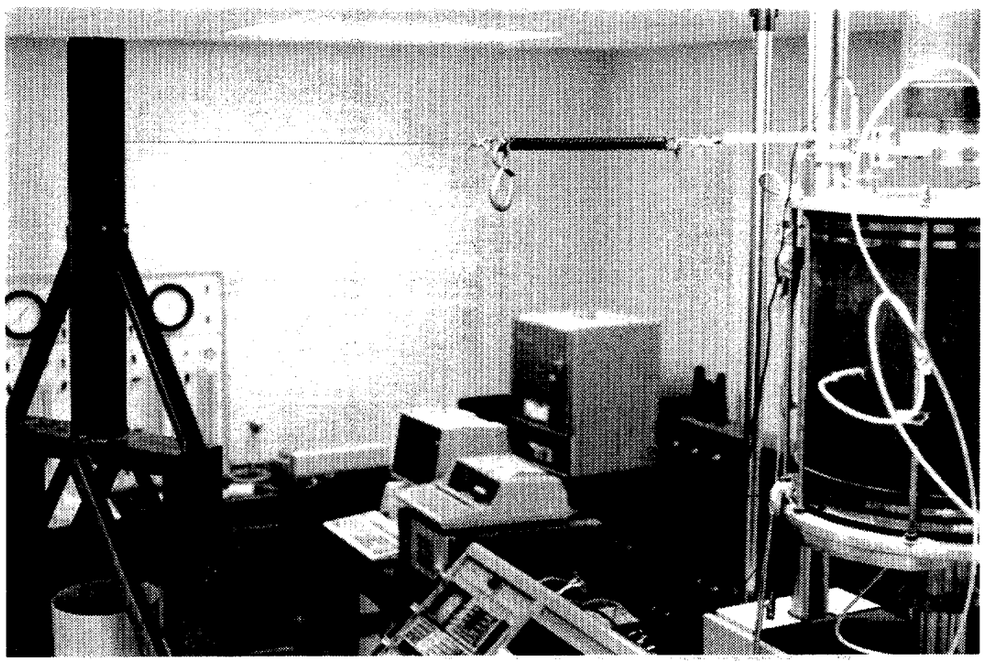

Fig. 3.9. Overall Testing Arrangement with Stiff Spring.

controlled displacement rate of 0.0033 in./min. For CD tests, conducted after dynamic tests, the bias load was applied by the dead-weight-spring system and held during the dynamic portion of the test, after which the Instron's actuator was used to apply the additional load to fail the pile in the post-shaking static test. The effects of CL testing versus CD testing are described later.

TEST PILE

This section describes the reusable model test pile that was employed during the study. The choice of the diameter of the pile and chamber represented a compromise between cost and minimizing scale effects between pile size and maximum sand particle size (which was 1 mm in the case of the coarsest sand used in the chamber tests, San Jacinto River Sand). Use of a minimum pile diameter-to-soil-particle-size ratio of 25 to reduce particle scale effects resulted in the choice of the 1.0-in.-diameter pile. The diameter of the test chamber containing the sand was limited by the presence of lateral supports of the Instron testing machine, resulting in a 20-in.-diameter test chamber and a test-chamber-to-pile diameter ratio of 20. With this test-chamber-to-pile diameter ratio, some boundary effects may have occurred in the chamber, although they would have been minimized by the flexible boundary (lateral membrane and teflon sheets) that was employed.

A longitudinal view of the closed-ended pile is shown in Fig. 3.10. The pile, 1.0 in. in diameter and having a 0.05-in. wall thickness, was constructed of drawn, seamless steel tubing. The pile was divided into four segments to facilitate the placement of the strain gages and then reassembled as a unit using the inside threads in every end of each segment. The threads in the uppermost segment (head) of the pile were used to attach a loading plug to a flexible cable from the loading system. The total length of the pile was 17.5 in., with an effective penetration into the soil of 15 in. A 1.5-in. section of the pile was in frictionless contact with a Teflon bushing in the top plate to assure the verticality of the pile during driving. The top 1.0 in. was encased within the anvil of the hammer during the driving operation and remained exposed above the chamber during a test. After every test, minor oil and rust deposits were removed from the outside wall of the pile by rubbing the pile with emery cloth impregnated with a degreasing substance to assure the consistency of the potential shear surface along the outside of the pile.

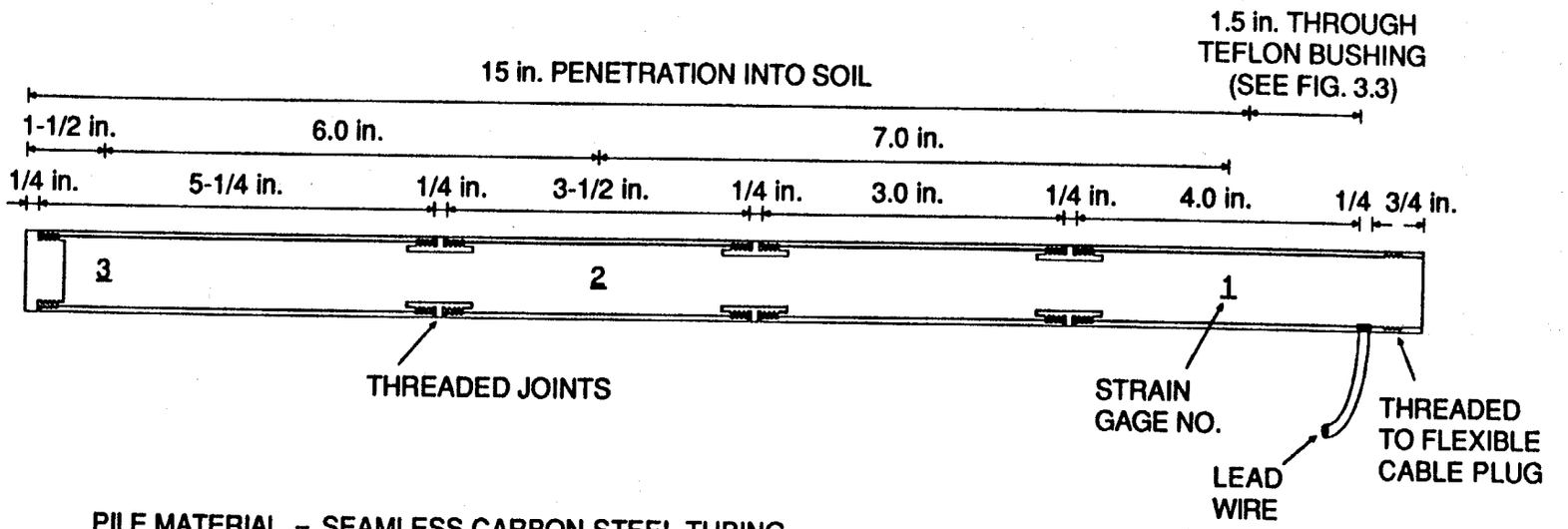

PILE MATERIAL = SEAMLESS CARBON STEEL TUBING GRADE 1018

TOTAL WEIGHT = 2.1 LBS

Fig. 3.10. Longitudinal Cross-Sectional View of Test Pile.

The pile instrumentation was placed permanently on the pile prior to the first test and remained on the pile throughout the entire study. Three levels of strain gages were placed in the pile wall, as shown schematically in Fig. 3.10. Each level was a full-bridge circuit. The levels are denoted by the numerals "1-3." All three levels were read before and during the pile installation, and during the static and dynamic tests to develop static and dynamic load transfer curves. At each gage level, two linear strain gages were epoxy-bonded to the inside of the pile wall and situated 180° apart. The two gages were wired as opposite, active gages in a Wheatstone bridge, permitting the cancellation of any bending stresses that might have been inadvertently applied to the pile and simultaneously doubling the sensitivity of the circuit to axial stress. The dummies for this bridge were precision resistors placed directly outside the test chamber to avoid differences in temperature with that of the active gages on the pile. Lead wires for the active gages were carried through the inside of the pile to a plug that could be connected with a mating plug from the data acquisition system. The bridge circuits were completed outside the pile using the external dummy resistors.

SOIL INSTRUMENTS

Two miniature pore water pressure transducers were embedded in the soil mass, one near the surface of the pile and one in an area influenced mainly by free-field effects, as shown in Figs. 3.3 and 3.5. These transducers, which had approximately the same mass as the soil they displaced, consisted of a simple crystal silicon diaphragm with a fully active strain gage bridge diffused into the surface. In order to resist the effective stress of the soil a ceramic porous plate was placed in front of the diaphragm. Dimensions of the miniature pore water pressure transducers are given in Fig. 3.11.

Since these instruments are required to be fully saturated at all times, the test chamber was filled to the level at which each of these instruments had to be placed (Figs. 3.3 and 3.5) and the soil saturated to that level. Soil deposition, density control and saturation procedures are described later in this chapter. Each instrument was then placed by hand slightly embedded in the saturated sand (Fig. 3.12) in its designated orientation (facing the pile). Some wet sand was then carefully placed and slowly tamped directly above the instruments to attempt to produce the same density at the recording faces of the instruments as existed in the general soil mass. Raining then continued followed by completion of saturation. Lead wires were brought directly to the side of the chamber and

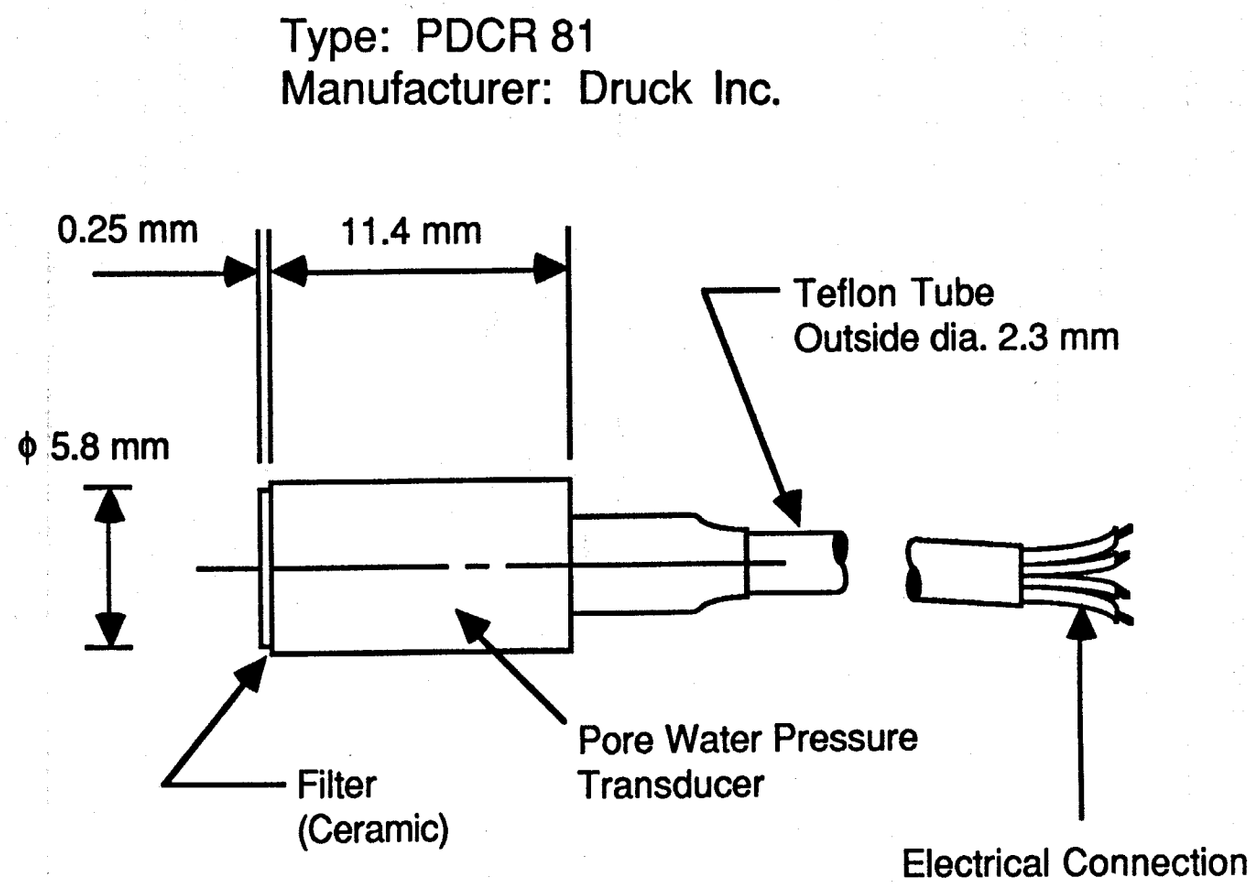

Fig. 3.11. Dimensions of Miniature Pore Water Pressure Transducer.

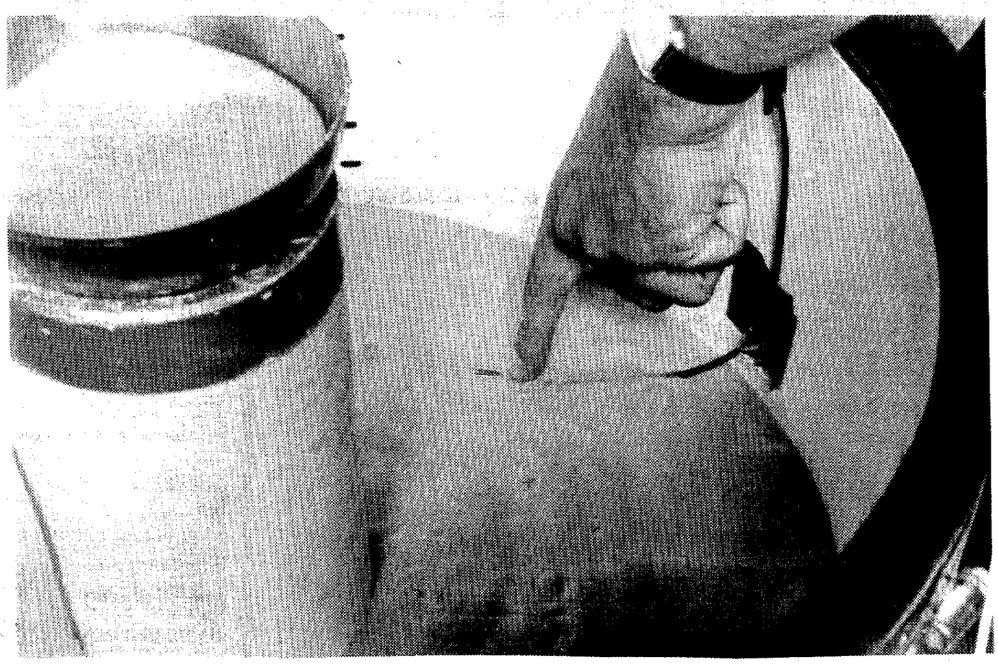

Fig. 3.12. Placement of Pore Water Pressure Transducer into Sand.

up the the inside surface of the chamber to the top, where they were brought out under the top plate and fed directly to the data acquisition system.

DROP HAMMER

A schematic of the hand-operated, single-acting drop hammer used to drive the test pile is given in Fig. 3.13. The hammer, consisted of an 11.2-lb ram, an aluminum cylinder to guide the ram, plywood cushions and an anvil. The free-fall distance of 15 inches produced an average rate of penetration of 8 blows per inch for a relative density of 55% and applied confining pressure of 5 psi. At full stroke the operating speed of hammer was approximately 25 blows per minute. Ventilation ports at top and bottom allowed the air to escape during the hammer operation. The cushions consisted of plywood sheets, 3/16-in. thick. The cushions in contact with the ram did not appear visually to have suffered crushing during driving. Cushions in contact with the pile were replaced about 4 times (about every 4 in.) during driving to protect the pile-head from damage. A photograph of the pile being installed with the pile-driving system is shown in Fig. 3.14.

DATA ACQUISITION SYSTEMS

Two separate data acquisition systems were used during testing: one for the acquisition of dynamic data during pile installation and the dynamic test, and one for the static uplift test and the static part of the dynamic test (monitoring of static bias load and static post-shaking test to failure).

Dynamic Data Acquisition System

The dynamic data acquisition system is shown in schematic form in Fig. 3.15. During the pile installation and simulated seismic events, the following time series data were recorded on an eight-channel analog magnetic tape recorder: top (pile head), middle and toe strain gage outputs in the pile, near-field and free-field pore water pressures, pile displacement (during shaking tests), and rate of penetration during driving and start/stop events during seismic tests (on the voice channel). Acoustic time marks were placed on the voice channel during pile driving. An observer indicated the passage of various depth marks on the pile past the top of the top plate of the test chamber, which tied the data on the other channels to a particular penetration into the chamber during driving. Acoustic time

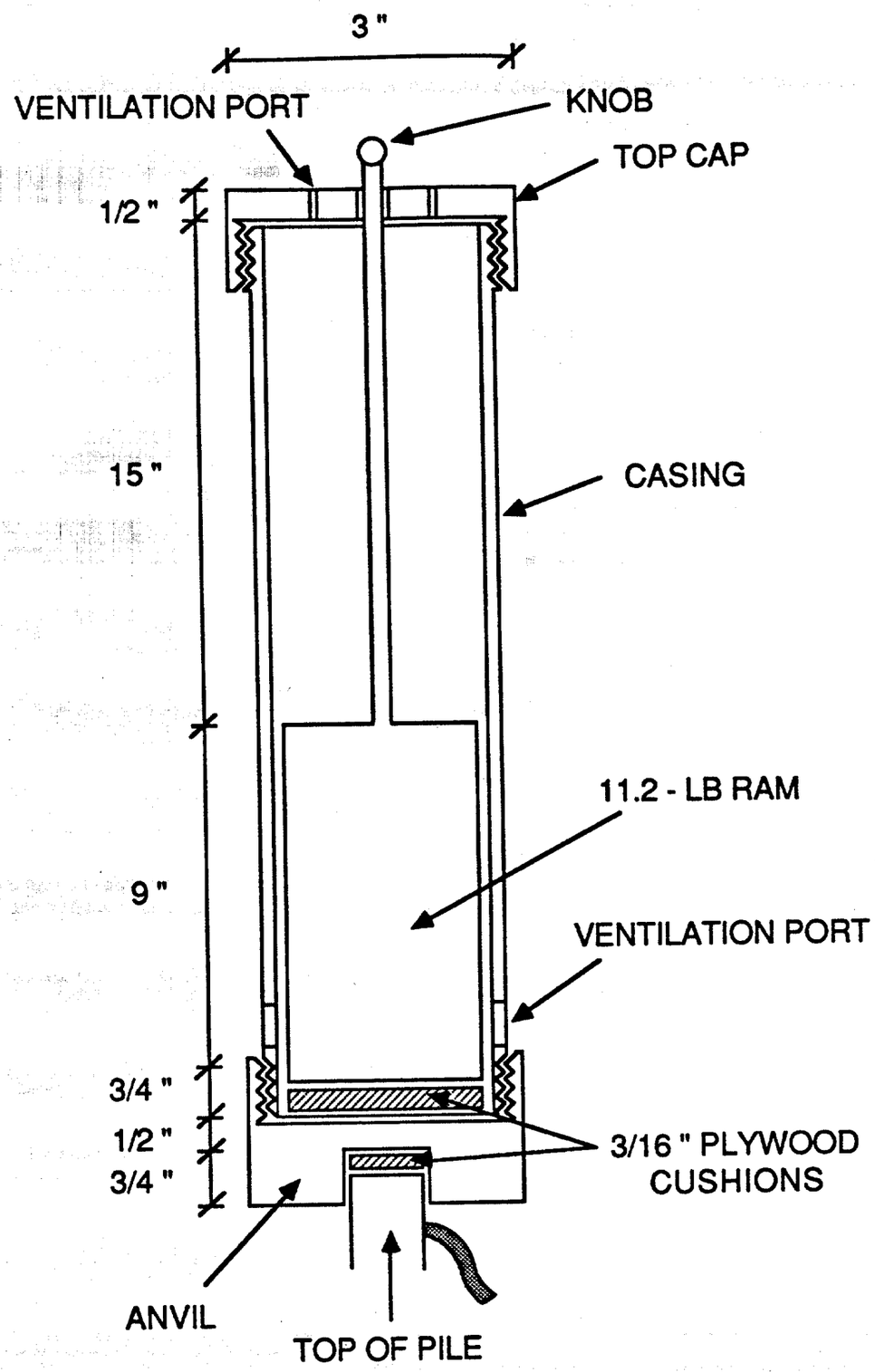

Fig. 3.13. Schematic of Drop Hammer.

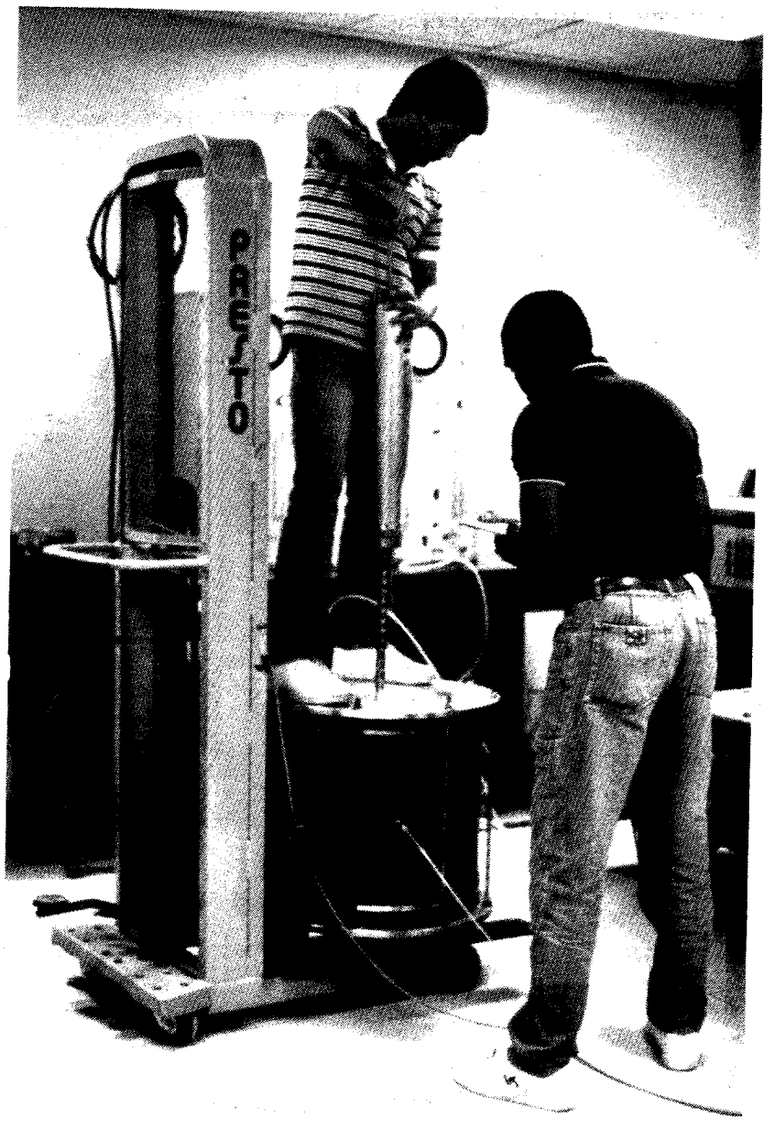

Fig. 3.14. Pile Installation Display.

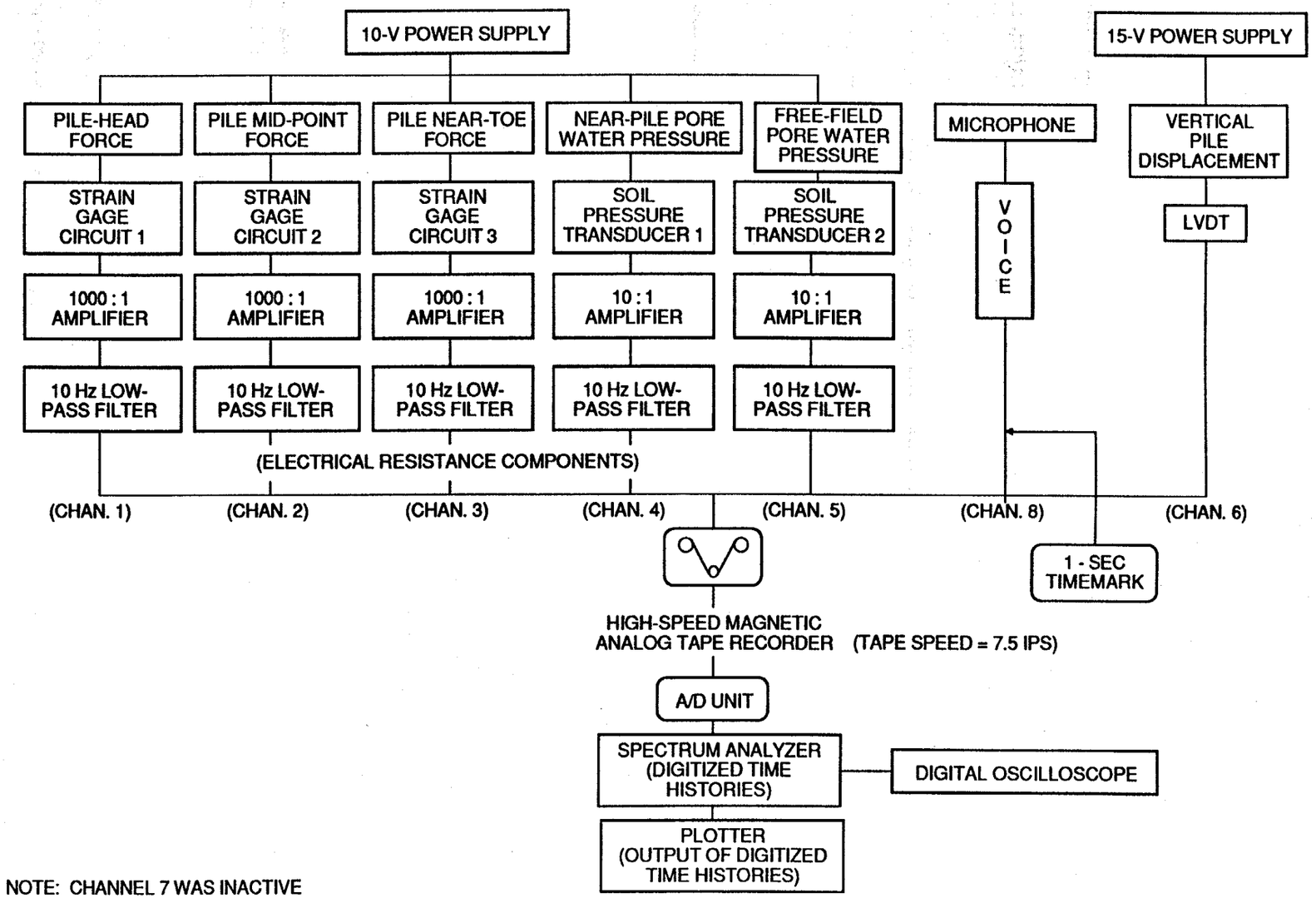

Fig. 3.15. Schematic of Dynamic Data Acquisition System.

marks were also employed during the seismic tests. The tape recorder was run continuously during every dynamic test, and during the pile installation in two tests.

The resulting data tapes are recordings of voltage outputs for the various instruments on the channels that are indicated in Fig. 3.15, and are valid for a tape speed of 7.5 in. per sec. The voltages that are recorded on those tapes were multiplied by the appropriate instrument calibration factors to obtain engineering units. The dynamic data on the analog tape was digitized off line at a rate that was appropriate to replicate the analog signals by an A/D converting unit that was coupled to the spectrum analyzer (Fig. 3.15). Digitized data were stored in the memory of the spectrum analyzer for further processing (simple multiplication by calibration factors) after which they were output to a pen plotter for interpretation. After every test, digitized data were reviewed for apparent correctness using the digital oscilloscope.

Electronic filtering was employed to remove the effects of frequency components of any signals that are of no importance in the analysis of the tests. Low-pass filters employed during the data acquisition process used 10-Hz (unscaled-record tests) and 60-Hz (scaled-record tests) rolloffs for the circuits for the pile strain gages and pore water pressure transducers (in which predominant frequencies of the simulated earthquake were of the order of 1 to 4 Hz and 4 to 25 Hz, respectively).

Although not explicitly shown in Fig. 3.15, each electrical resistance strain-gage-type circuit (pile strain gages and soil pressure cells) was connected to a shunting resistor to balance each circuit individually prior to each test. The strain gages were always zeroed with the test pile resting vertically on top of the chamber without the weight of the hammer resting on it. By this method it was possible to trace the true zero of the strain gages through the entire sequence of events during a test, even though data files were opened and closed many times (as they were on both the static and dynamic data acquisition systems), provided that the final reading before closing a file was taken under identical conditions as the opening reading of the next file. In this manner, residual stresses in the pile during driving could be included in the evaluation of load-transfer.

Static Data Acquisition System

The data acquisition system that was used during the static load tests and during the static parts of the dynamic tests (application of static bias load and static post-seismic test to

failure) is shown in Fig. 3.16. Data from seven channels (plus the power supply) were acquired on command from the microcomputer, which was manually operated. Readings of data from all channels were made at intervals of applied pile-head load of 5 lbs, resulting in about 40 readings during the loading phase of a test. Keying the computer sent a command to the scanner to read each channel serially (requiring about 2.0 sec.). The digital voltmeter used with the scanner permitted acquisition of five digits of significant data. The digitized voltages were sent to a buffer from which they were read immediately by the microcomputer. Physically, all of the system shown within the dashed boundary in Fig. 3.16 was contained in one unit.

The computer then performed simple mathematical operations (multiplying the voltage on each channel by the appropriate calibration factor) and wrote the resulting output (in engineering units) to both paper tape and a magnetic tape cassette. The hard copies (paper tapes) have been archived as permanent records of the static tests, and further used to develop load transfer curves and load-movement curves. As with the dynamic data acquisition system, the various strain gage circuits in the static system were balanced while the pile was stress free (sitting vertically on the top of the chamber). These zero conditions were used for the static load tests (i.e., no rebalancing was done once pile installation started), so that the stresses reported for static load tests contain the effects of any residual stresses that were induced in the pile during installation. Since a data file was also opened before each static event (i.e., initial static loading, post-seismic test static loading), all readings in such a file were subtracted from the first reading (datum) to obtain the true applied load at that particular moment, allowing the top strain gage readings to be used to compute the load-movement curves for the static pre- and post-seismic tests.

SAND PLACEMENT

It was judged that sand densities of practical interest for this study would be those in the medium dense to dense range (relative densities of approximately 55% to 85%), which is representative of offshore California deposits and other continental shelf deposits outside of pro-delta regions. The relative density of 55% is the value of greatest practical interest since liquefaction problems are most likely to occur in looser soil. Experimental results [Mulilis et al. (1975)] showing the significance of the method of sample preparation on liquefaction characteristics of a saturated sand are displayed in Fig. 3.17. As seen in Fig. 3.17, pluviation (dry raining) through air ("pluviatile compaction") exhibited more suceptibility to liquefy than any other compaction method. In a separate lab study

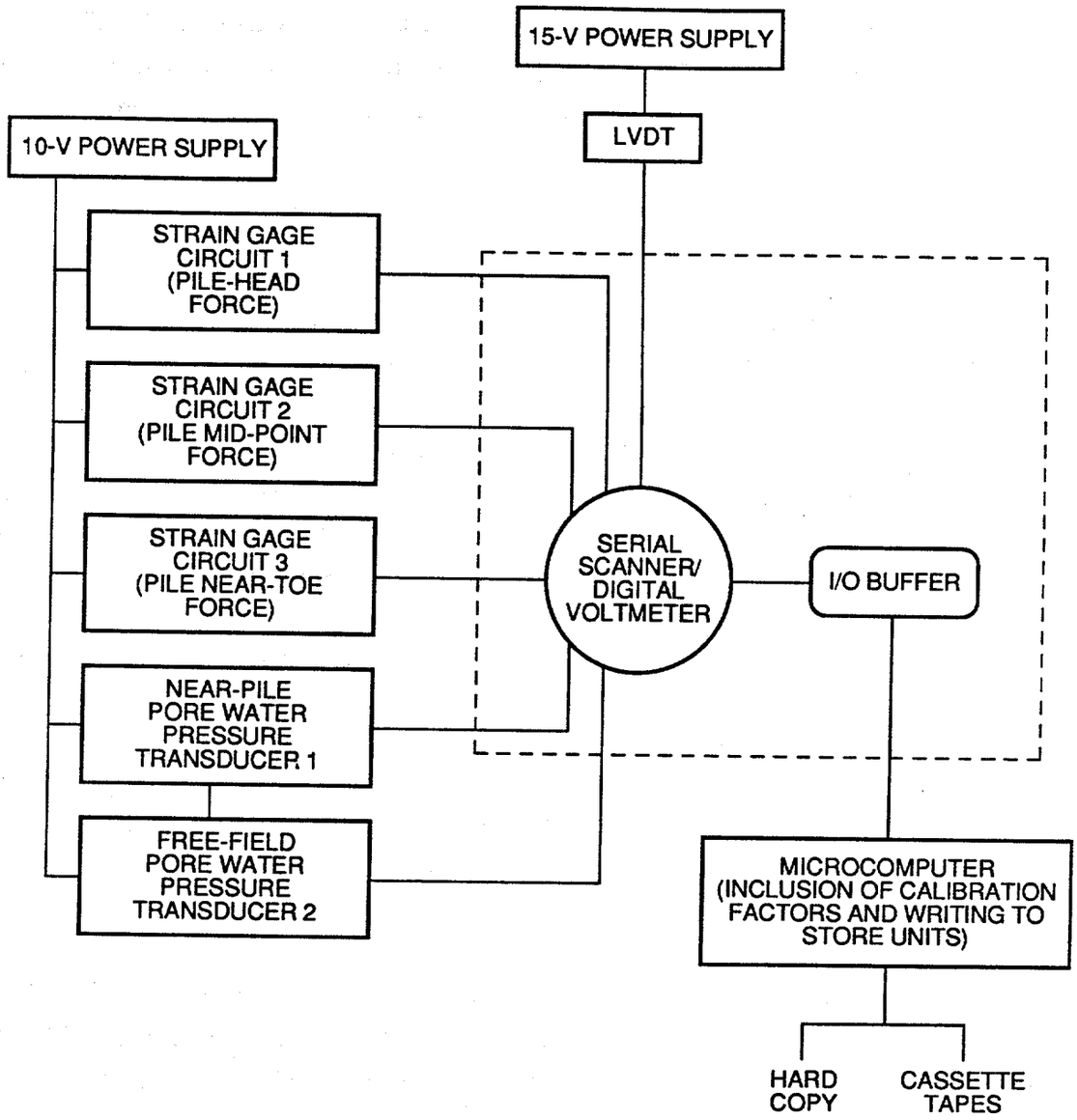

Fig. 3.16. Schematic of Static Data Acquisition System.

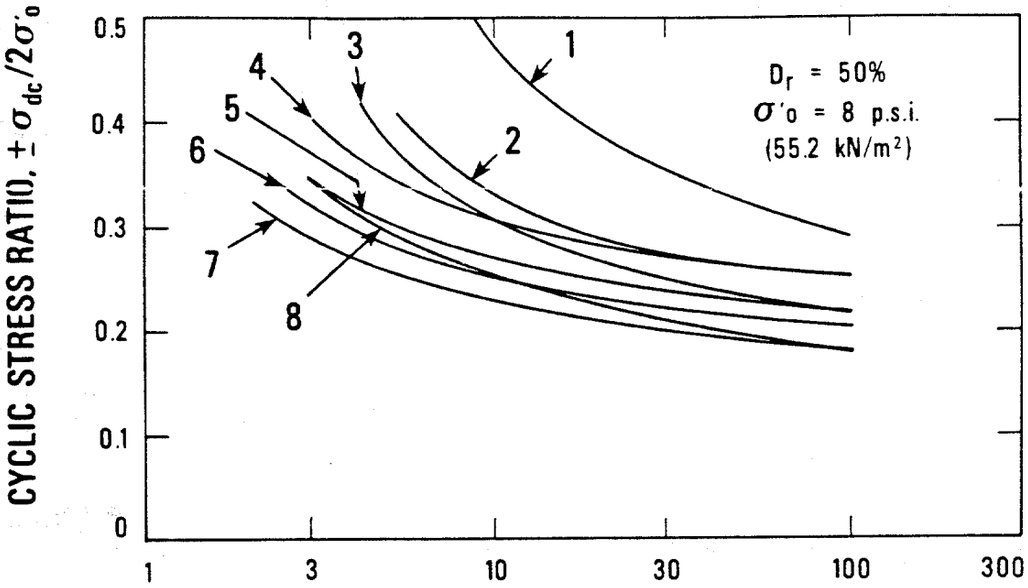

Curve No.	Method of Compaction
1	High frequency vibrations on moist samples
2	Moist tamping
3	Moist rodding
4	Low frequency vibrations on dry samples
5	High frequency vibrations on dry samples
6	Pluviated-water
7	Pluviated-air
8	Dry rodding

Fig. 3.17. Cyclic Stress Ratio versus Number of Cycles for Different Compaction Procedures [After Mulilis et al. (1975)].

[DeGregorio (1990)], dry pluviated specimens also displayed a greater peak pore-water pressure response than specimens prepared by either of two moist methods (moist tamping and moist vibration). Based on those findings, the method of pluviatile compaction (providing the most critical condition for liquefaction) was chosen for the sand placement in this study.

A schematic diagram of the raining system used for deposition of the two sands employed in the study (fine SJR sand and micro-fine sand) in all density states is given in Fig. 3.18. Prior to the beginning of the sand raining process, a water diffusion ring and riser were placed at the bottom of the test chamber. In air pluviation techniques, the relative density achieved is very much dependent on the drop height [Vaid and Negussey (1984)]. Therefore, the drop height was carefully adjusted depending upon the particular target relative density. Drop heights for each relative density were determined before the testing program started by placing aluminum sampling cans (standard laboratory moisture sample cans, two in. in diameter and 1.5 in. in height) inside the chamber and proceeding with the raining in 2-in. lifts from a known height. Each sample can was then carefully removed and the overburden properly trimmed. The weight of the dry soil within the sample can (which had a known volume) was measured, the dry unit weight calculated and the relative density determined based upon the known minimum and maximum index densities (Chapter IV). This procedure was repeated with different drop heights and for a given drop height until repeatability of the relative density for a particular drop height was achieved.

Once the drop height was properly set, the sand was rained continuously, moving the funnel from the outside of the chamber to the inside in a circular pattern. Adjustments of the nozzle elevation were made to keep the drop height constant as the soil surface raised. The raining was then interrupted at the level of the soil instruments (mid-height of chamber). The soil was then flushed with carbon dioxide and saturated with deaired water, and the pressure transducers were placed. The raining continued until the sand surface reached the top of the chamber, after which the remainder of the sand column was saturated very slowly since flushing with carbon dioxide was not possible. The top membrane, followed by the top plate, was then placed and the bolts properly tightened. Equal confining pressure was then applied to the membranes. On average, the time required to saturate the SJR sand was 1 hour, while for the micro-fine sand saturation took about 24 hours.

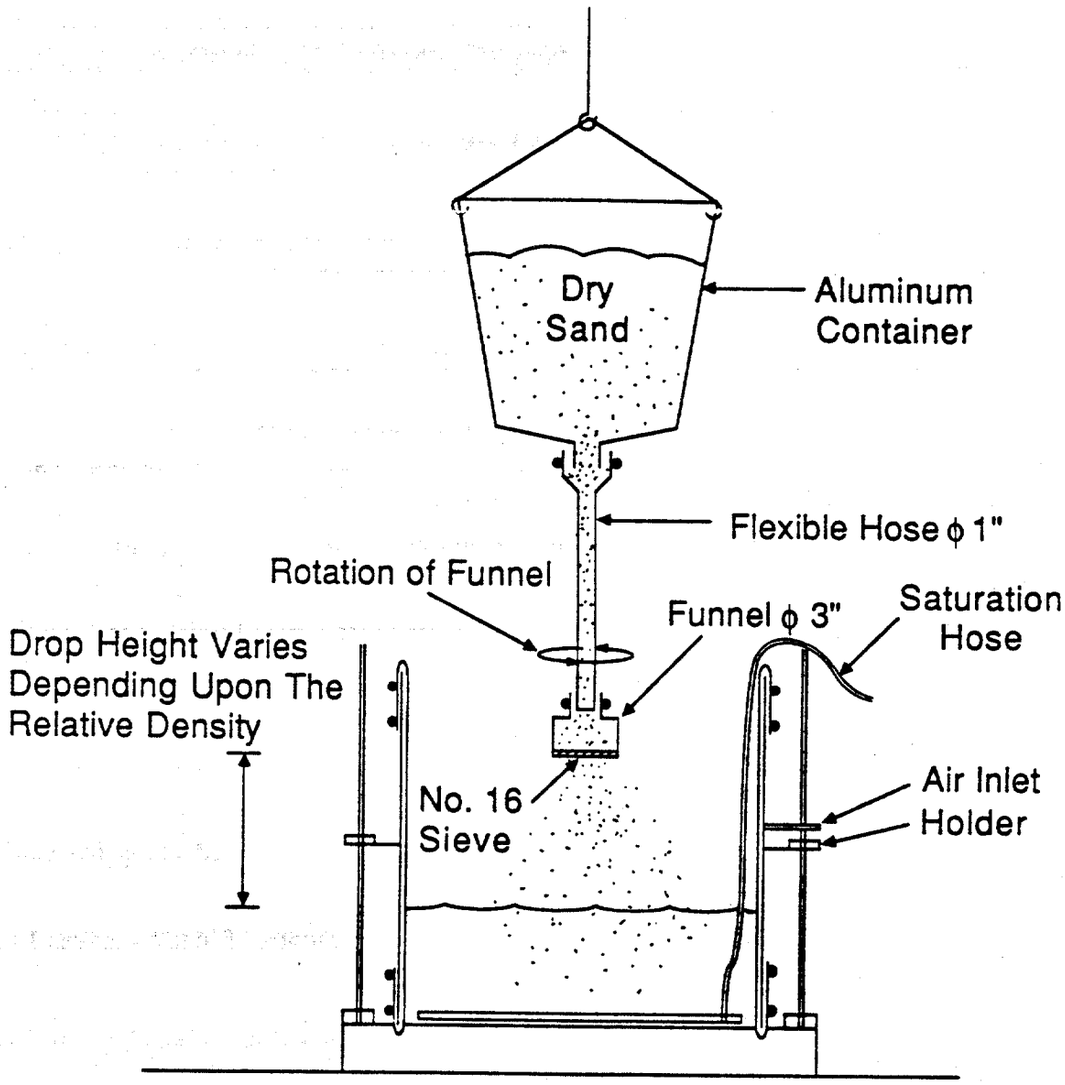

Fig. 3.18. Schematic of Sand Placement Arrangement.

Following the completion of a given test, the chamber was depressurized and the pile extracted. The top cap and top membrane were then removed, and the moist sand shovelled out. Soil instruments were also carefully removed during this process. The moist sand was then placed in a forced-air convection oven for drying. The oven-dry sand was then placed back into the stockpile bin for reuse in future tests. The drying process required about 24 hours and 48 hours for the 4 cubic ft of SJR sand and the micro-fine sand, respectively.

CALIBRATION PROCEDURES

Pile Axial Strain Gages

The test pile was calibrated in tension to a load of 500 lbs prior to the beginning of the testing program. Fig. 3.19 shows the pile calibration arrangement. The calibration procedure was as follows: The pile was initially placed in a standard loading frame commonly used for triaxial tests in the laboratory. A calibrated load cell was then inserted between the pile head and a reaction beam to sense the applied load. A tension load was then applied by means of a hand-operated wheel engaged to a system of gears assembled in a particular configuration. Loading (tension) and unloading cycles to 100 lbs were repeated five times in order to exercise the pile and mitigate the effects of existing residual stresses in the steel. The pile was then loaded in increments of 50 lbs, and each strain gage circuit along with the calibrated load cell and power supply were read using the static data acquisition system and bridge completion circuit that was used during the testing program. Graphical depictions of strain gage circuit output as a function of load for gages 1 to 3 are given in Appendix B.

Miniature Pore Water Pressure Transducers (PDCR 81)

The calibration constants used during testing were provided by the manufacturer (Druck, Inc.) and are given in Appendix B. A check was performed by submerging the instruments in a water tank to different levels of known hydrostatic pressure and sensing the voltage output response of each instrument using a voltmeter. Such a procedure verified that calibration constants given by the manufacturer were correct.

Fig. 3.19. Test Pile Calibration Arrangement.

Applied Boundary Pressures

The effective confining pressure applied to the soil mass through the 1/8-in.-thick rubber membranes was checked. Two large calibrated electrical resistance pressure cells were embedded in the dry soil mass within the chamber, which was then pressurized through its membranes to a known value of pressure. Location and orientation of the sensing faces were different for both instruments to sense, approximately, the pressure distribution within the soil mass. It can be concluded from a table of known applied pressure versus the pressure response obtained from the pressure cells (Appendix B) that the "membrane effect" in the chamber membranes was negligible for the ranges of pressure considered in this study.

Degree of Saturation

A laboratory study conducted by Yoshimi et al. (1989) concluded that liquefaction resistance increased significantly with a decrease in the degree of saturation to such an extent that liquefaction resistance at 70% saturation was about three times that at full saturation. Based on that finding, the degree of saturation was checked ('B' parameter test) on the micro-fine sand to verify 100% saturation of the soil, a condition typical of an offshore or river bottom site. The 'B' parameter check was accomplished by embedding one of the miniature pore water pressure transducers in saturated micro-fine sand (following the same technique implemented during the sand placement and saturation procedure), closing all ventilation and pile ports, and increasingly applying confining pressure up to 2.5 psi (applied mean confining pressure during testing program for most tests conducted with micro-fine sand). As shown in Fig. 3.20, for an applied pressure of 2.5 psi (at the air panel gage), the induced pore water pressure (subtracting the small zero offset value) was 2.4 psi (B = 0.96), indicating essentially full saturation in the soil mass.

Dynamic Strains

It was considered essential that the chamber produce amplitudes of shearing strain in the soil essentially equivalent to those that would occur in the column of prototype soil modelled in the chamber. Since shearing strains were not measured at the SEMS site or in the model tests, it was necessary to evaluate prototype and model strains analytically.

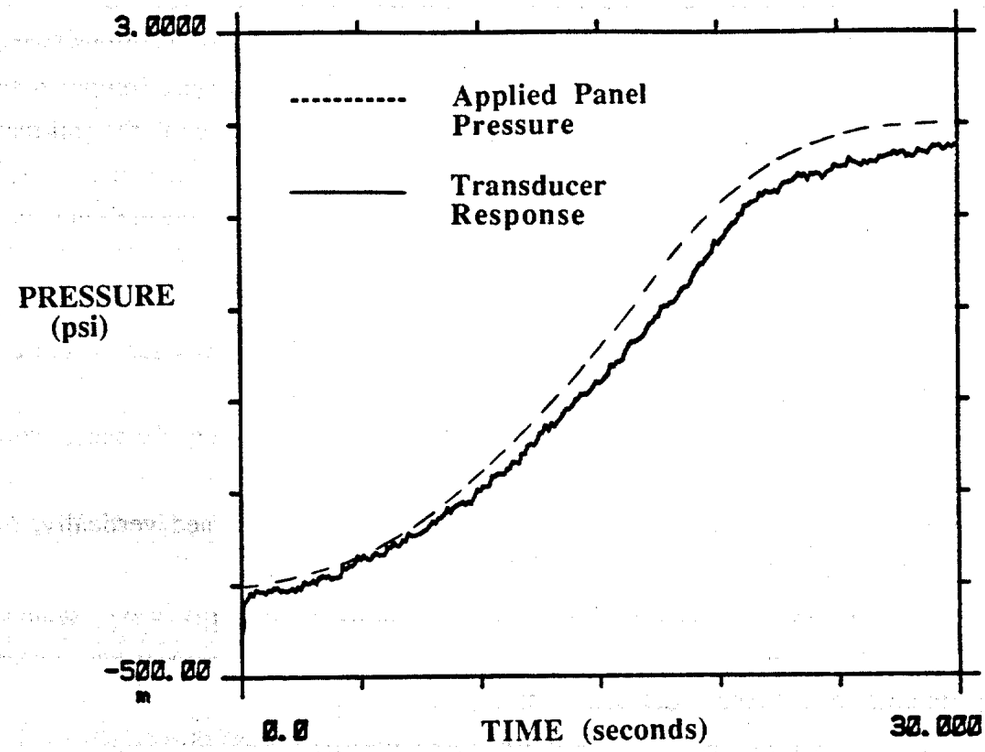

Fig. 3.20. Pore Water Pressure Response versus Applied Confining Pressure (Ventilation Ports Closed).

Vertical Motion. A mathematical analysis of maximum shearing strain of the soil in the chamber, induced by the vertical component of the simulated seismic motion, has been performed based upon the principles of axial wave propagation in a uniform bar. For simplicity, the soil and the test chamber were modeled as a column of soil which is excited at one end by a known displacement function and is free at the other end. Complete derivations and computations are given in Appendix G. The magnitude of maximum shearing strain, obtained from two sinusoidal displacement-time functions (window of displacement-time history of a Magnitude 8.0 event, Fig. 5.23) were computed and then added together to obtain the approximate maximum shearing strain in the soil mass. The computed value of shearing strain was in the order of 10^{-4} %, a value normally insufficient to induce liquefaction in the free field. This analysis is to be confirmed in the test results given in Chapter VI.

Horizontal Motion. Measurements of shear strains of the soil in the chamber induced by the horizontal component of the simulated seismic event were performed. Dynamic shearing strains were obtained by numerical integration of the acceleration-time histories of two low-g accelerometers embedded in dry sand (as shown in Fig. 3.21) with a chamber pressure of 2.5 psi. These accelerometers were aligned vertically, oriented horizontally, and were separated 10 in. from each other. The chamber was subjected to a simulated scaled (scaling rules explained in Chapter V) Magnitude 8.0 seismic event (record used during testing program, Tests U1-W2). Shearing strain was interpreted as the difference in horizontal displacement of the two accelerometers divided by vertical separation (10 in.) at any given time step. Shearing strain time history is shown in Fig. 3.22. Fig. 3.22.a shows the measured, uncorrected shear strain time history, in which an obvious baseline drift appears, possibly because one or both accelerometers translated or rotated permanently during the test, aggravated by inertia effects in the accelerometers, which weighed slightly more than the weight of the soil displaced. The baseline has been corrected visually in Fig. 3.22.b, which can be compared to the analytical solution for shear strain vs. time to asses whether the shear strain amplitudes produced in the chamber were realistic for the event magnitude that was being modelled. The order of magnitude of the dynamic shearing strains are large enough to induce buildup of pore water pressure and, possibly, to cause liquefaction for the test sand in saturated conditions [Dobry et al. (1982)].

A mathematical analysis of the strain developed in the free field by the horizontal component of a Magnitude 8.0 seismic event was also computed using the program

Fig. 3.21. Display of Insertion of Accelerometers in Dry Sand for Strain Measurements.

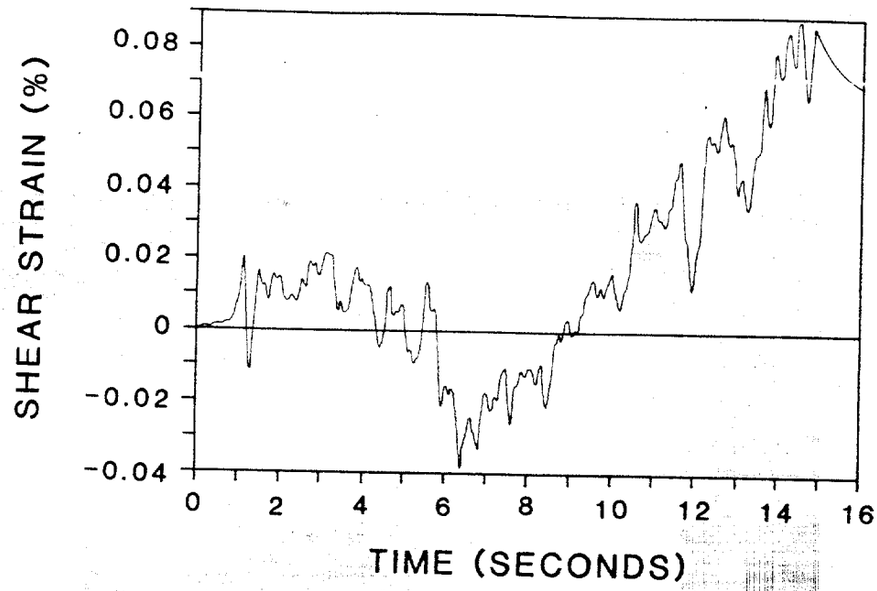

Fig. 3.22.a Measured Strain-Time History (Dry Sand) During Simulated Scaled Magnitude-8.0 Oceanside Event (Horizontal Motion) (Uncorrected Baseline)

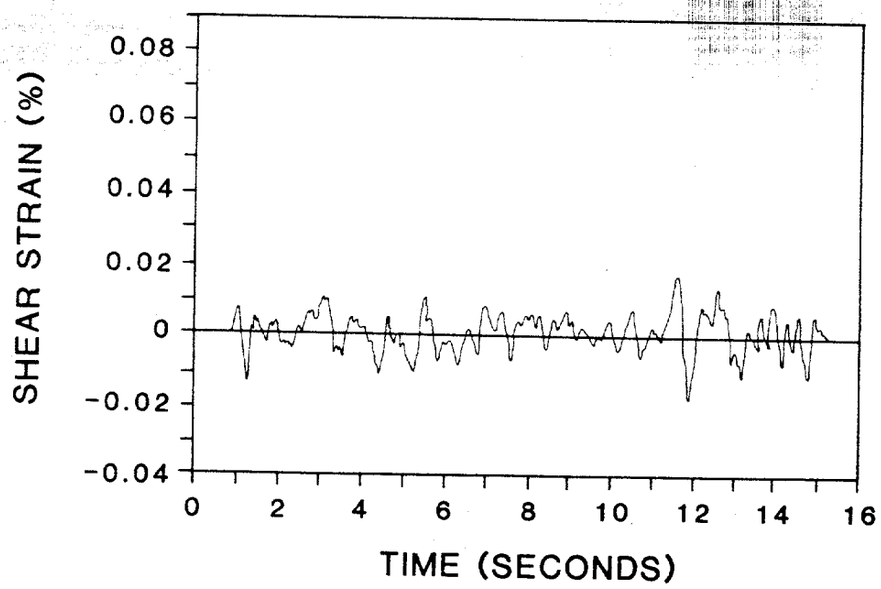

Fig. 3.22.b Measured Strain-Time History (Dry Sand) During Simulated Scaled Magnitude-8.0 Oceanside Event (Horizontal Motion) (Corrected Baseline)

SHAKE [Schnabel et al. (1972)] for the range of assumed soil characteristics at the SEMS site given in Appendix I (loose and medium dense). The time window for the input motion corresponds to the period of strong shaking (between 20 and 40 seconds) of the scaled Magnitude-8.0 record of the Oceanside earthquake shown in Fig. 5.17. The input motion was applied at the middle of layer 2 (9 ft below ground surface). Computed shear strain time histories for loose and medium dense conditions at the level of applied motion are shown in Fig. 3.23. A reasonable agreement can be seen between the measured strains in the test chamber and those predicted in the free-field prototype soil using SHAKE.

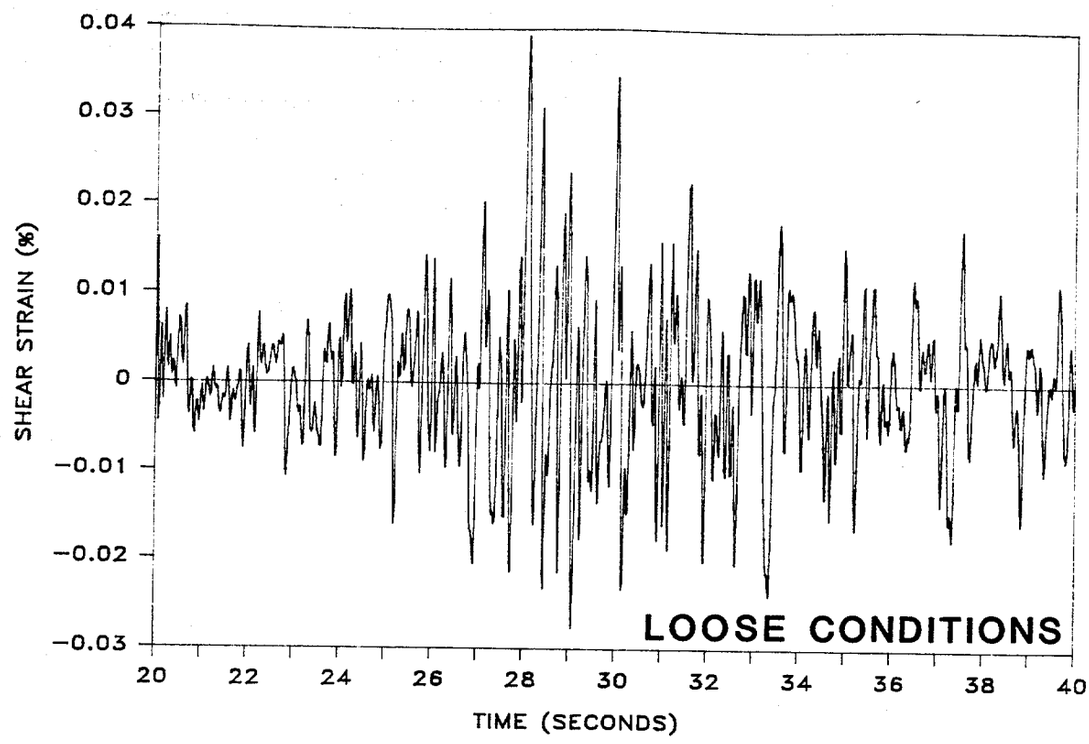

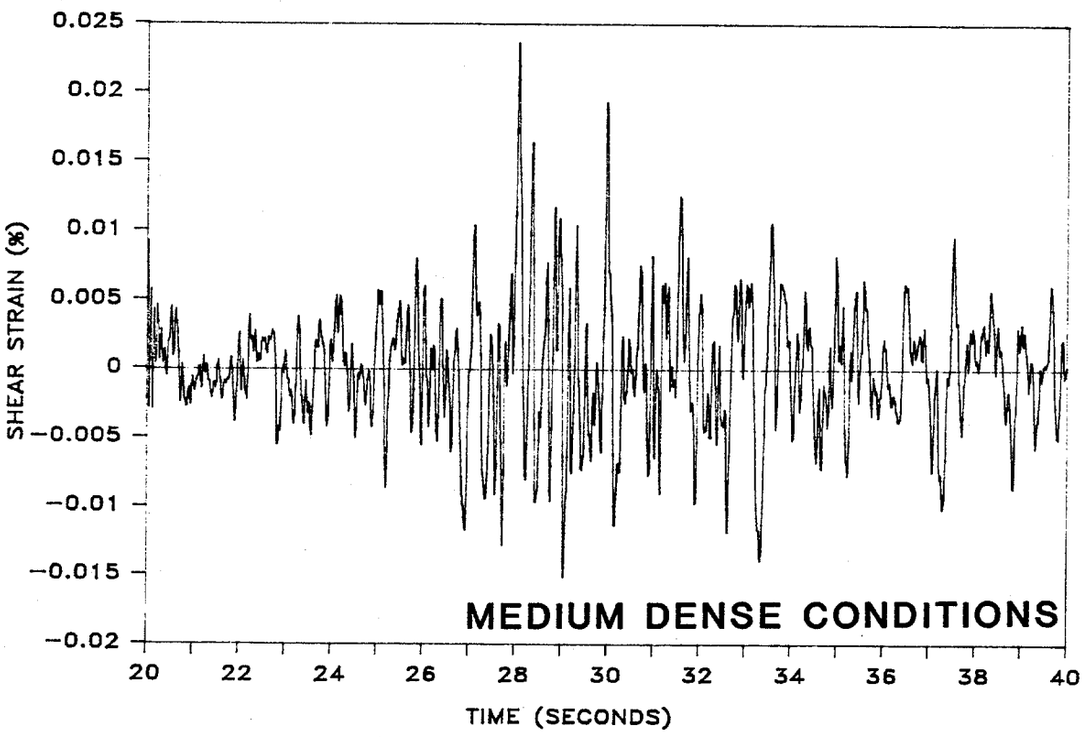

Fig. 3.23. Computed Strain-Time Histories in the Free Field of the Prototype Soil During Period of Strong Shaking for Loose and Medium Dense Soil Conditions.

CHAPTER IV

Sand Properties

Laboratory tests were conducted to characterize the two sands that were employed, SJR sand and micro-fine sand. The tests performed were as follows: Grain-size distribution (sieve analysis), minimum and maximum index densities, permeability, triaxial compression, and interface shear. Although these tests do not necessarily represent the stress paths to which the sand was subjected in the test chamber during pile driving, static testing and dynamic testing, they provide information on the mechanical properties of the sands. In selecting effective pressures in the chamber, it was assumed that the soil stresses for penetrations up to 40 ft could be simulated within a reasonable approximation by applying an isotropic effective stress within the test chamber equal to the ground stress that could occur at the middepth of the pile if K_o in the soil deposit being simulated were 1.0. The in-situ isotropic effective stress levels of interests were in the range of 2.5 to 5 psi. This selection is discussed further in Chapter V. Pile tests were conducted with initial isotropic effective chamber pressure of 2.5 and 5 psi. However, the mean effective stress in the soil mass during and after installation would be expected to increase considerably above the initial in-situ value due to the cavity expansion around the pile. Therefore, laboratory strength tests were conducted with confining pressures of 10, 20 and 40 psi.

GRAIN-SIZE DISTRIBUTION

Two types of sand were used in the study: a fine, uniform siliceous sand, San Jacinto River (SJR) sand, represented the prototype sand, and a mixture of a very fine siliceous sand ("Blasting Sand No. 5") and finely ground glass beads, termed "micro-fine sand," was used as the model sand for tests in which permeability was modelled. The grain-size distributions for the two test sands are shown in Fig. 4.1. For the SJR sand, the effective grain size, d_{10}, is 0.2 mm, and the coefficient of uniformity, C_u, is 1.74. From visual inspection the typical shape of the grains was observed to be subrounded, and the SJR sand can be classified according to the Unified Soil Classification System as "SP," or a poorly graded fine sand. For the micro-fine sand, the effective grain size, d_{10}, is 0.06 mm,

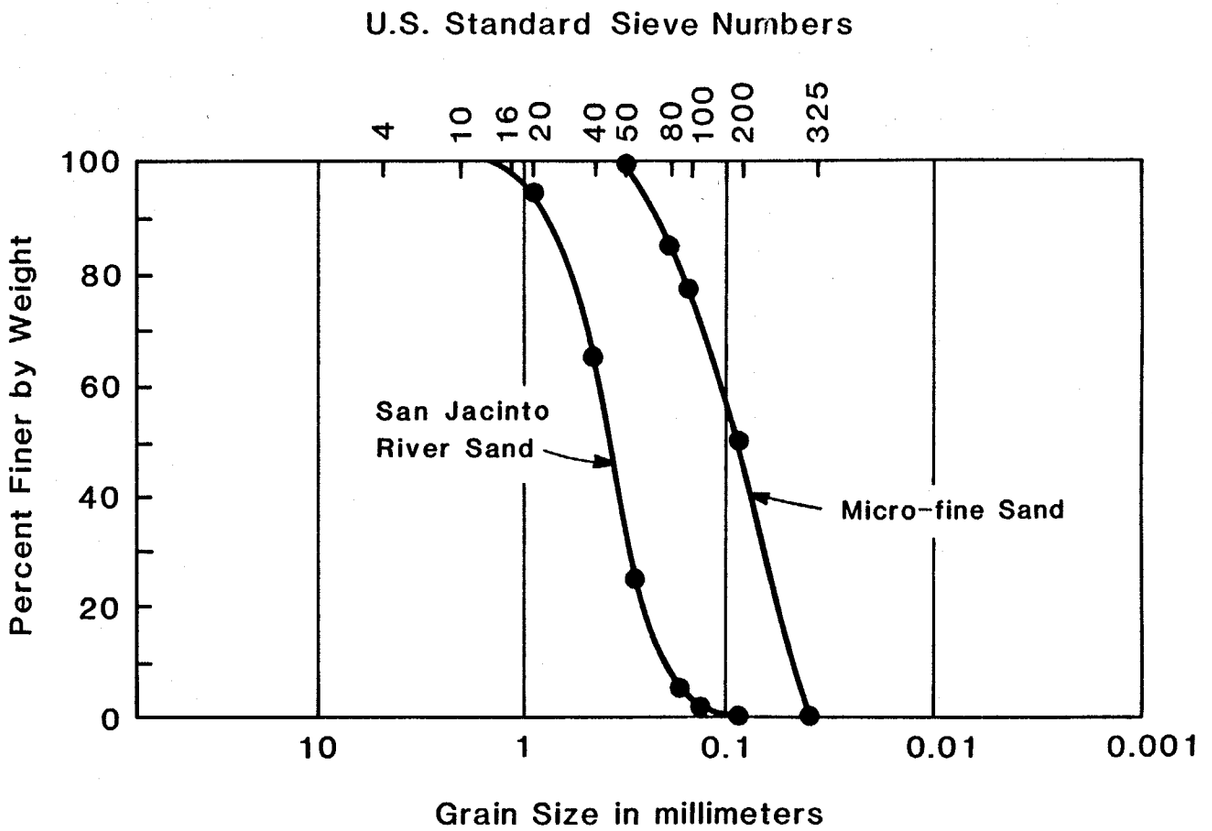

Fig. 4.1. Grain Size Distributions for Sands Selected for the Study

the coefficient of uniformity, C_u, is 1.66, and it can be classified as "SM," a very fine silty sand to sandy silt.

MINIMUM AND MAXIMUM DENSITIES

Volume-change characteristics of the sand are considered to be one of the factors influencing the behavior of the pile-soil system under load. The volume-change characteristics are complex functions of the effective stresses and initial relative density of the sand. In order to control the actual density required for the attainment of target values of relative density, it was necessary to determine the minimum and maximum densities as defined by ASTM standards D 4253 and D 4254 [Annual Book of ASTM Standards (1988)]. The values of the maximum and minimum index densities were 110.4 pcf and 94.2 pcf for the SJR sand and 112.9 pcf and 96.6 pcf for the micro-fine sand.

PERMEABILITY

Falling-head permeability tests were conducted on both sands deposited with a relative density of 55%. Tests were conducted by depositing oven-dry soil by raining through air into rigid-wall cylinders, three in. in diameter and six in. in height, and saturating the samples very slowly with deaired water from bottom to top to simulate, approximately, the procedure that was used to deposit and saturate both sands in the test chamber. Coefficients of permeability for each sand are summarized in Table 4.1. It is observed that SJR sand (the coarser of the two test sands) is about eight times more permeable than the micro-fine sand.

Table 4.1. Permeability Test Results

Sand	Coefficient of Permeability (cm/sec)
San Jacinto River	1.00×10^{-2}
Micro-fine Sand	1.21×10^{-3}

TRIAXIAL COMPRESSION

Consolidated-drained triaxial compression tests were conducted on saturated samples of medium dense (60% nominal relative density) SJR sand, which was near the relative density of 55% employed in most chamber tests. These tests were conducted to provide information on stress-strain properties and shear strength, as characterized by the angle of internal friction. The samples were prepared by raining of oven-dry sand, as per the permeability test. After gravity saturation (and verification of saturation by measurement of the B-parameter), the 1.5-in.-diameter by 3.0-in.-high specimens were consolidated isotropically and then loaded to failure by increasing the major (vertical) principal stress at a constant displacement rate of 0.23 mm/min. During the application of load, volume change was measured by recording the amount of water that flowed into or out of the specimen from a calibrated burette that communicated with the pores of the specimens. The stress-strain and volume-strain response are shown in Fig. 4.2. Volumetric changes are expressed as volumetric strain (change in volume / initial volume, as a percent). The results for the medium dense conditions (relative density of 60%) indicate that SJR sand contracts initially upon shearing, with the magnitude of contraction depending on the value of the confining pressure, and then dilates after shear failure begins.

A plot of mean effective normal stress versus maximum shear stress ("p'-q diagram") is shown in Fig. 4.3. The angle of internal friction, ϕ, can be derived from the slope of this relation,

$$\phi = \sin^{-1} [\tan \xi] , \qquad (4.1)$$

where ξ is the slope of the line in Fig. 4.3. The measured value of the angle of internal friction, ϕ, is about 39°.

INTERFACE SHEAR

It was also considered important to investigate the interface shear strength properties of both sands and the material comprising the outer wall of the pile. In order to study this effect, interface shear tests were conducted in a direct shear apparatus. Sand was deposited by raining the soil in a dry state at an approximate relative density of 60% onto a prepared flat steel plate in the bottom half of a circular direct shear box, 3 in. in diameter. In order to represent the pile surface closely, the steel plate was made of the same material as the pile

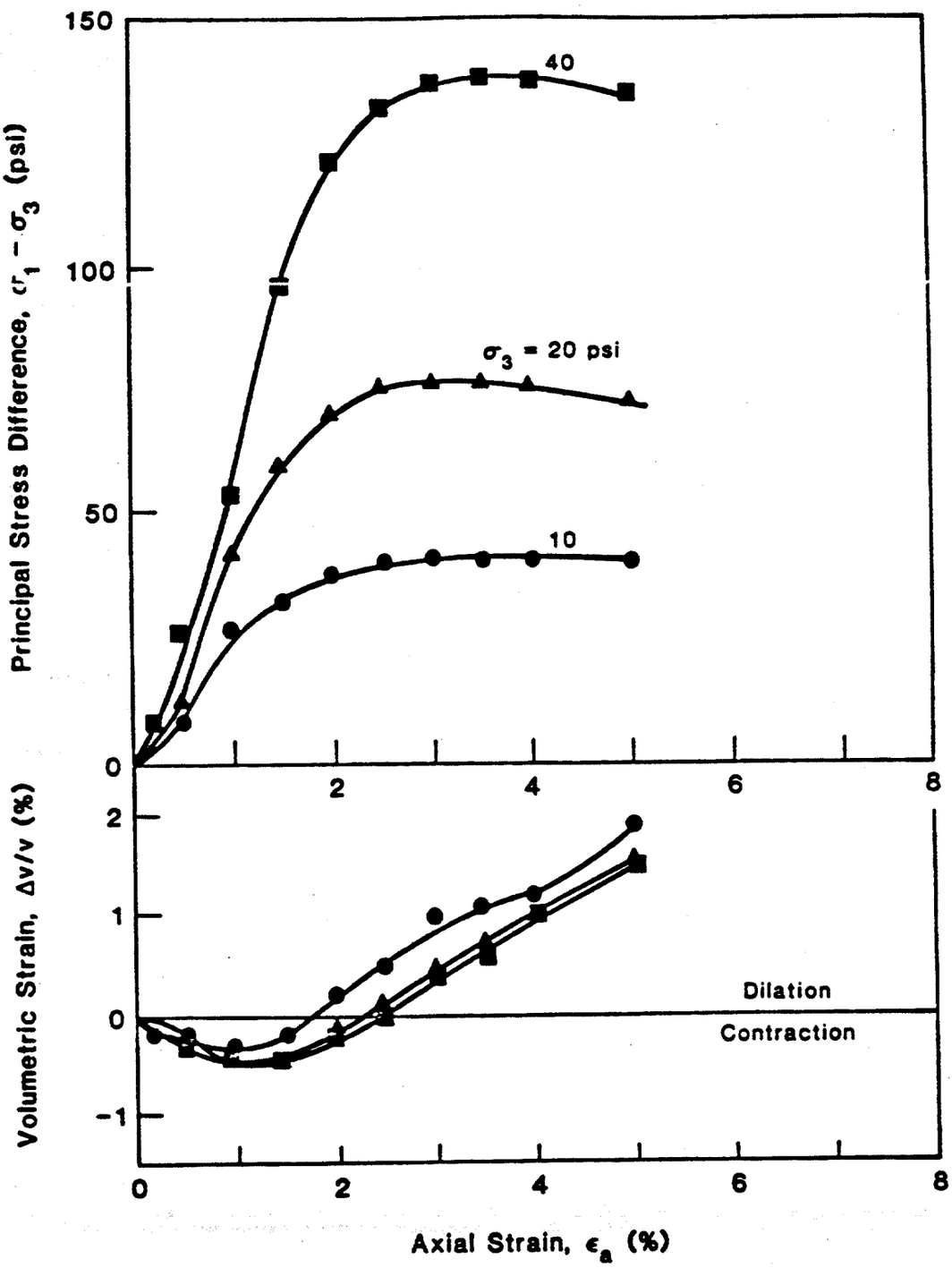

Fig. 4.2. Results of Consolidated-Drained Triaxial Compression Tests for SJR Sand at 60% Relative Density

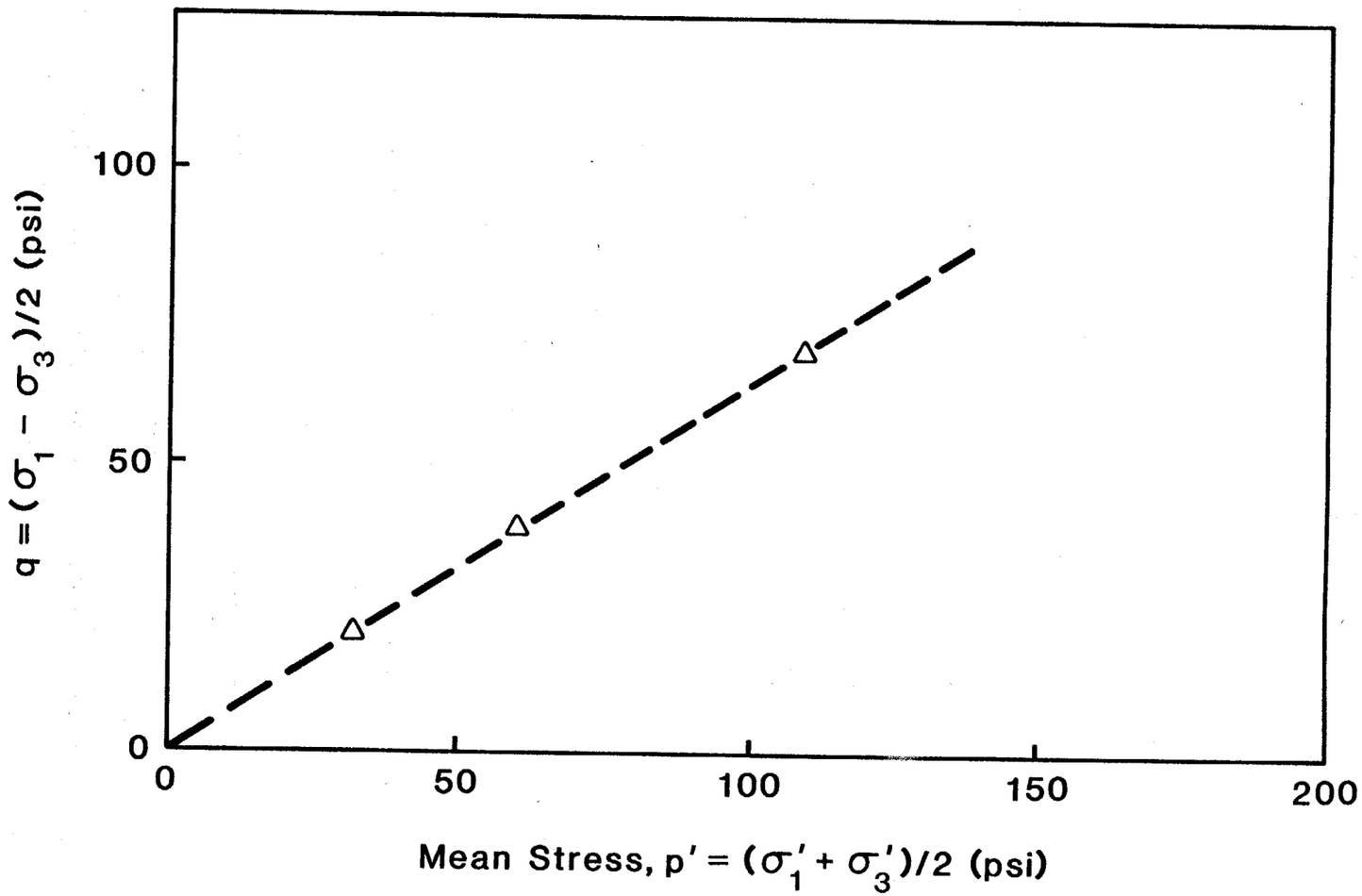

Fig. 4.3. Failure Envelope for Triaxial Compression Test on p'-q Diagram on SJR Sand

and was given the same finish as that on the pile by lightly machining it with an end mill and rubbing it with an emery cloth prior to depositing the sand. After placement, the sand was saturated and tested in a consolidated-drained mode under normal interface stresses of 10, 30 and 50 psi for SJR sand, and 11, 22 and 45 psi for micro-fine sand. Both shear stress-displacement and vertical-horizontal-displacement relations are given in Figs. 4.4 and 4.6. The contractive behavior of both sands placed at 60% relative density can be observed for different normal pressures.

The interface frictional failure envelopes are shown in Figs. 4.5 and 4.7. The interface friction angles were 27° and 22° for SJR sand and micro-fine sand, respectively. It is noted that the interface friction angle of the SJR sand is considerably lower than the angle of internal friction obtained from triaxial compression tests corresponding to peak principal stress differences.

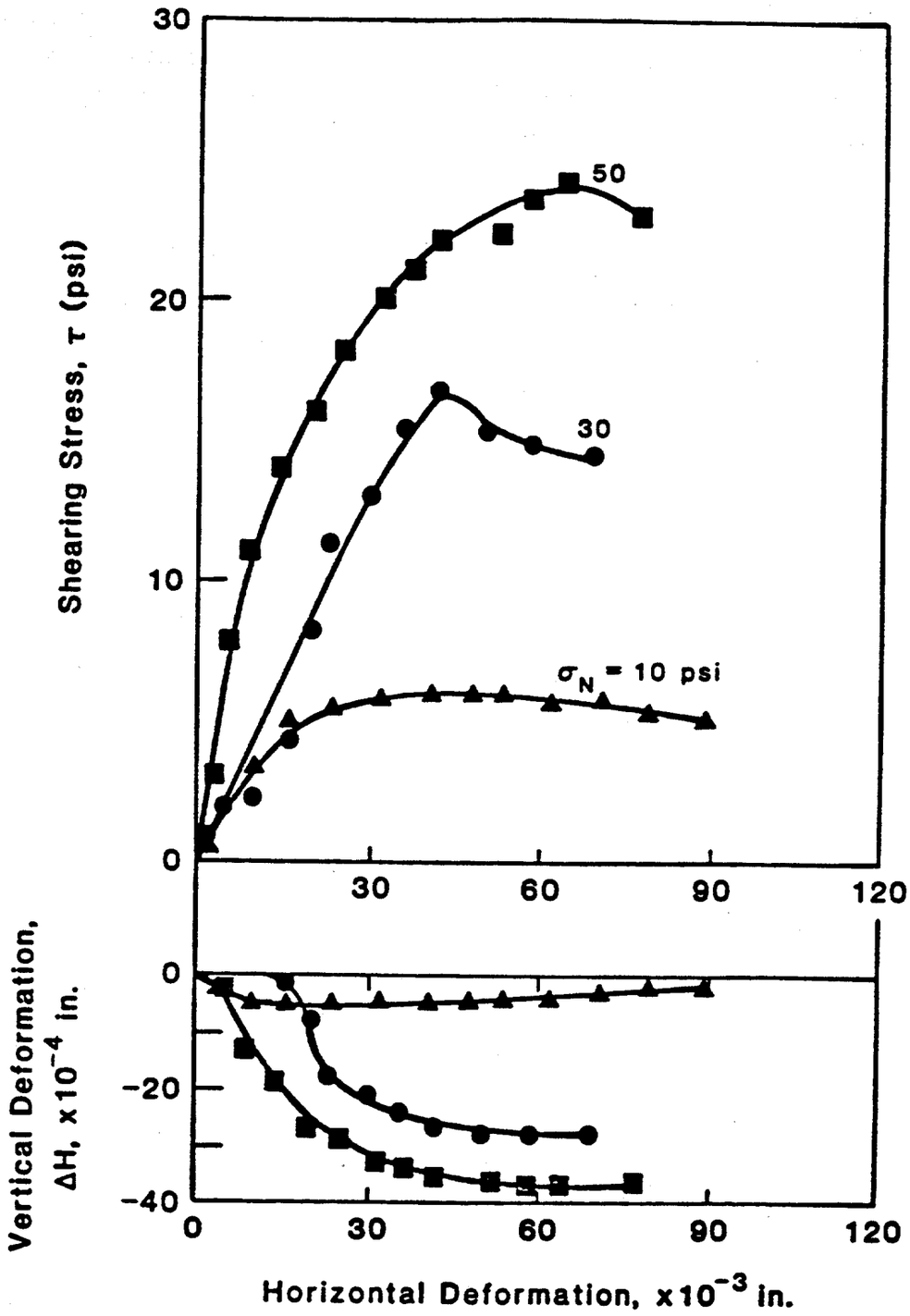

Fig. 4.4. Results of Direct Interface Shear Tests for SJR Sand at 60% Relative Density

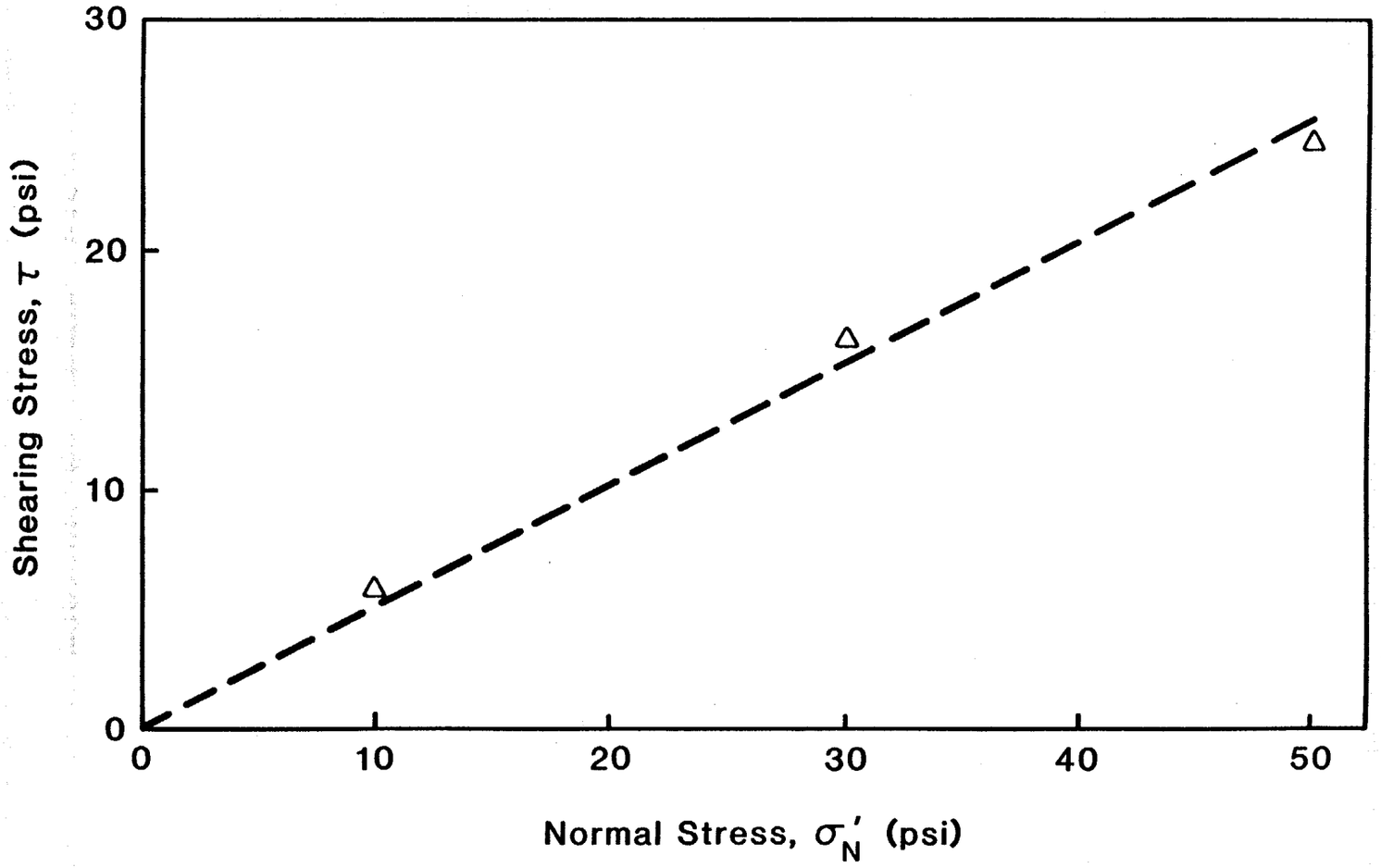

Fig. 4.5. Failure Envelope for the Direct Interface Shear Test on SJR Sand at 60% Relative Density

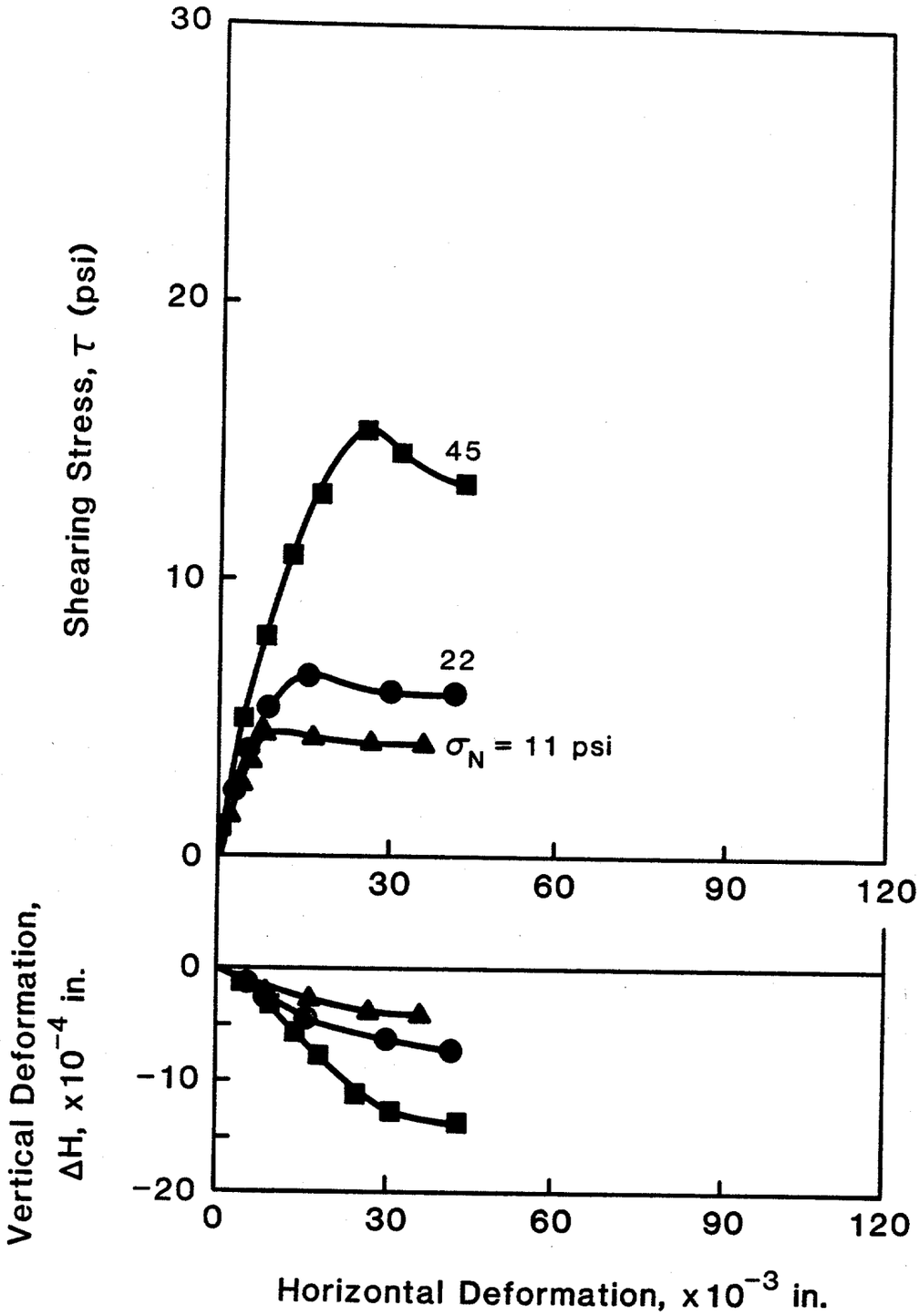

Fig. 4.6. Results of Direct Interface Shear Tests for Micro-fine Sand at 60% Relative Density

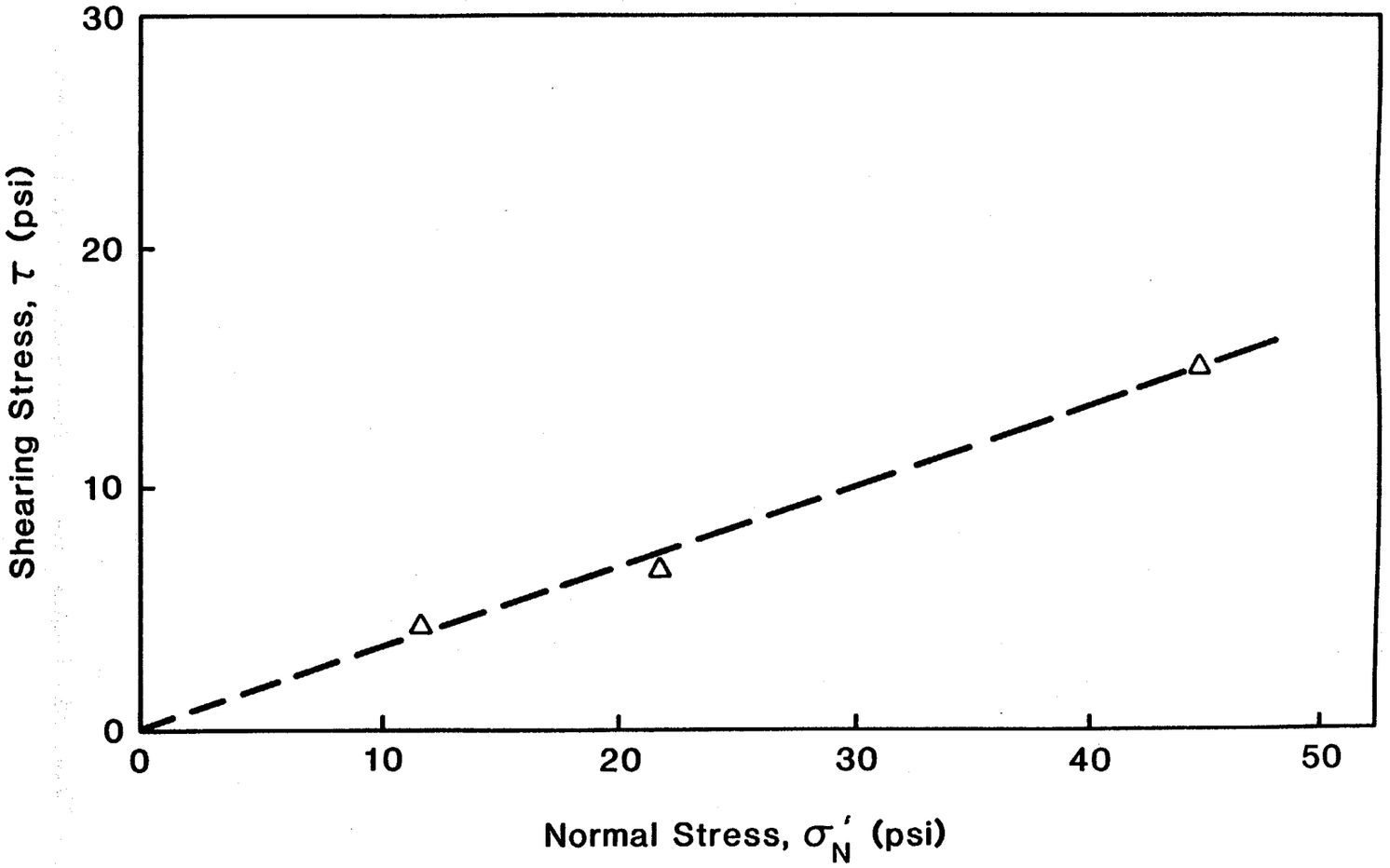

Fig. 4.7. Failure Envelope for the Direct Interface Shear Test on Micro-fine Sand at 60% Relative Density

CHAPTER V

Scaling Procedures

The site that was chosen for simulation was the SEMS (Seafloor Earthquake Measurement System) site off Long Beach, California, a deep soil site at which strong-motion seismic records were recorded in three dimensions during two seismic events in 1986 [Sleefe and Engi (1987)]. The particular event chosen for this study was the Oceanside event of July 13, 1986, a Ritcher Magnitude 5.8 earthquake whose epicenter was 74 km southeast of the instrumentation site. Epicentral distance, time of first motion, depth of focus, location of the instrumentation site and orientation of the horizontal (X and Y) accelerometers are shown in Fig. 5.1.

The recorded vertical, or Z, and horizontal, X and Y, components of motion are shown in Figs. 5.2, 5.3 and 5.4. Peak vertical and horizontal accelerations were of the order of only 3 - 4 milli-g's and 20 - 28 milli-g's, respectively, with an approximate duration of strong shaking of 25 sec. Experience and intuition suggested that tension pile response to such an event (low values of peak acceleration) would not produce any measurable loss of pile capacity. Therefore, a scaling procedure was used to scale upward the Z component from a Magnitude 5.8 to an event Magnitude 8.0 and the combined components of horizontal motion (X and Y) to event Magnitudes of 7.0, 7.5 and 8.0, for an epicentral distance of 74 km. Two scaling problems are evident. The first involves scaling of the earthquake magnitude, and the second involves scaling the model to the prototype. These two aspects of scaling are discussed in order in the following sections.

EARTHQUAKE SCALING

Simple scaling of earthquakes can be performed either in the time domain or in the frequency domain. In the time domain, the time axis and/or the acceleration axis of the seismic record are multiplied by respective ratios (scaling factors) computed by comparing the significant characteristics (maximum acceleration amplitude, predominant frequency, and duration of strong motion) of existing and desired earthquake records. An example of this is the simplified procedure proposed by Seed et al. (1969) for scaling rock motions. In

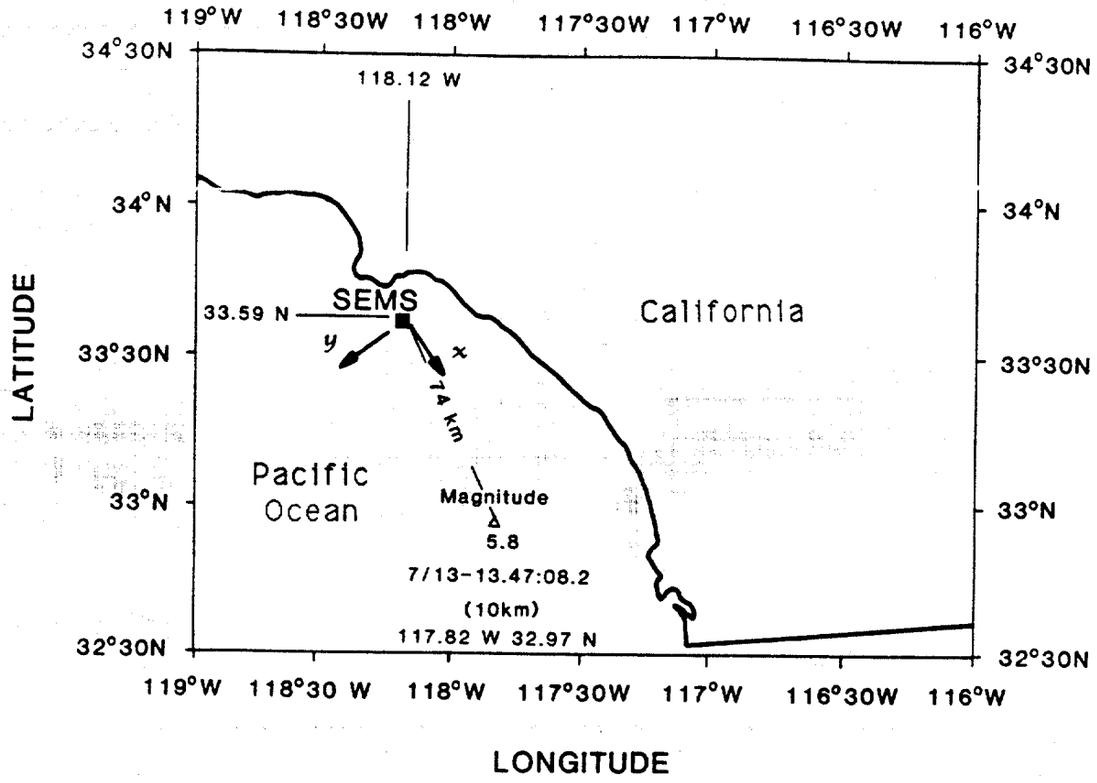

Fig. 5.1. Location of SEMS Unit [After Sleefe and Engi (1987)].

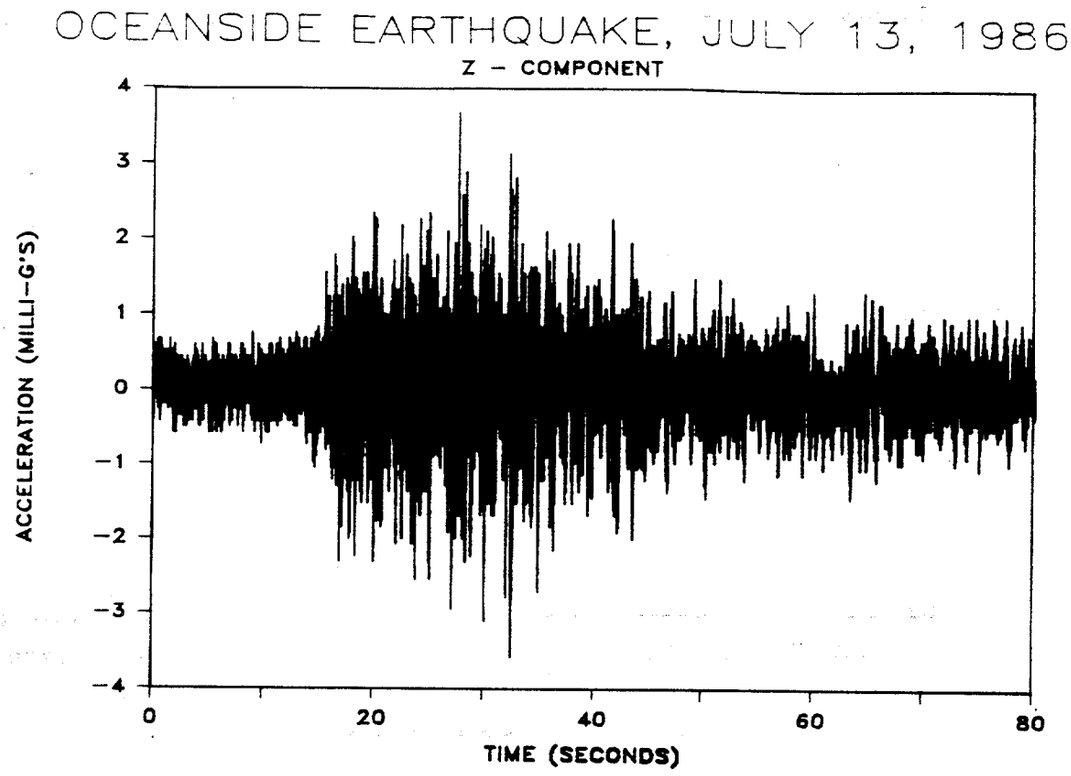

Fig. 5.2. Seismic Record of Vertical, or Z, Component of Oceanside Earthquake.

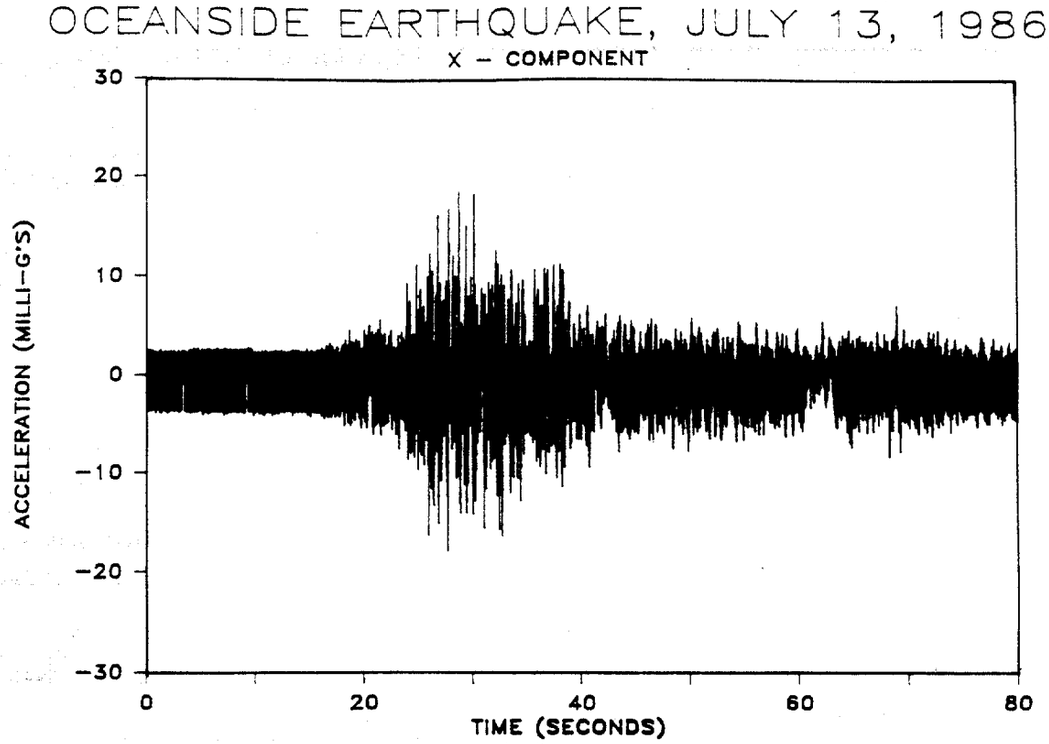

Fig. 5.3. Seismic Record of Horizontal, or X, Component of Oceanside Earthquake.

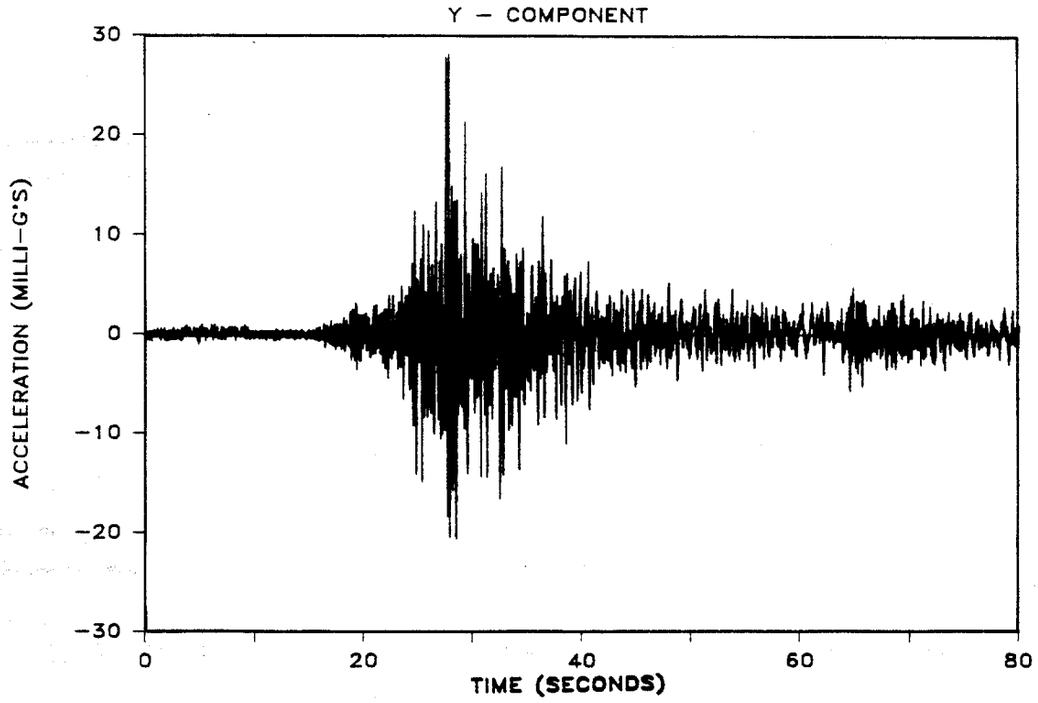

Fig. 5.4. Seismic Record of Horizontal, or Y, Component of Oceanside Earthquake.

the frequency domain approach (chosen for this study), the scaling procedure involves transforming the time history into the frequency domain, scaling to a spectrum that would represent a higher magnitude event (for instance, Magnitude 8.0), termed the target spectrum, and deconvolving back into the time domain while maintaining the same phase relationship (to preserve the same earthquake source mechanism) that existed in the original unscaled record. A step-by-step description of the frequency-domain scaling procedure for the components of the Oceanside earthquake follows.

Scaling of the Vertical (Z) Component of Motion

First, the frequency content of the acceleration versus time record of the Z-component of the earthquake in Fig. 5.2 is computed using the 'Fast Fourier Transform' (FFT) algorithm , developed by Cooley and Tukey (1965). This algorithm makes the involved computations feasible for use in microcomputers. The frequency content of the Z-component is given in Fig. 5.5. After analyzing frequency content and considering the low acceleration values of the original record, it was judged necessary to filter some of the undesirable high frequencies, the result of recording instrumentation noise. In order to do so, a recursive type of low-pass digital filter [Chakrabarti et al. (1986)] was used, which is characterized by the following equation,

$$Y_n = (1 - A)\, X_n + Y_{n-1} \ , \qquad (5.1)$$

where

Y = Filtered value of acceleration,

X = Original, unfiltered value of acceleration,

A = Parameter indicating the degree of filtering (A = 0 corresponds to no filtering; A = 1 corresponds to maximum filtering), and

n = Time step designator.

The original record was filtered using a value for A (selected by initial inspection of the frequency spectrum) of 0.7, which resulted in unfiltered predominant frequency content between 1 and 4 Hz, a characteristic range for strong seismic events at deep soil sites. The frequency content of the filtered signal is given in Fig. 5.6. For completeness, Fig. 5.7 displays the phase angles of the filtered but unscaled seismic record.

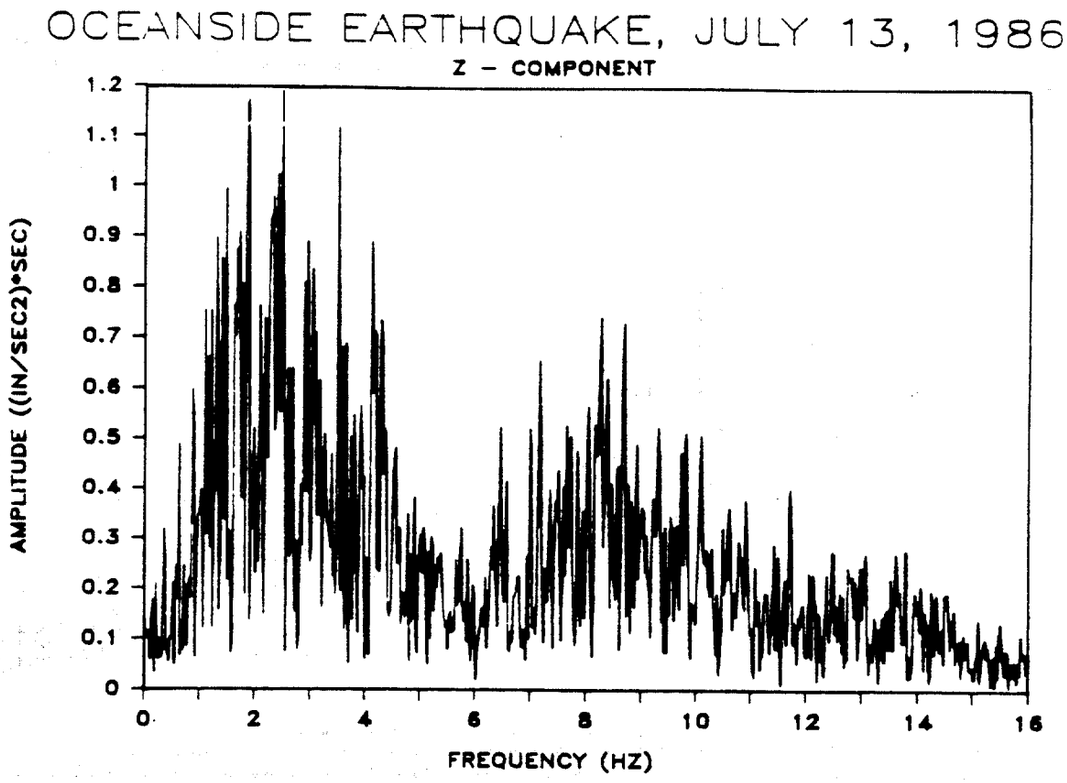

Fig. 5.5. Frequency Spectrum of Unfiltered Z-Component Record.

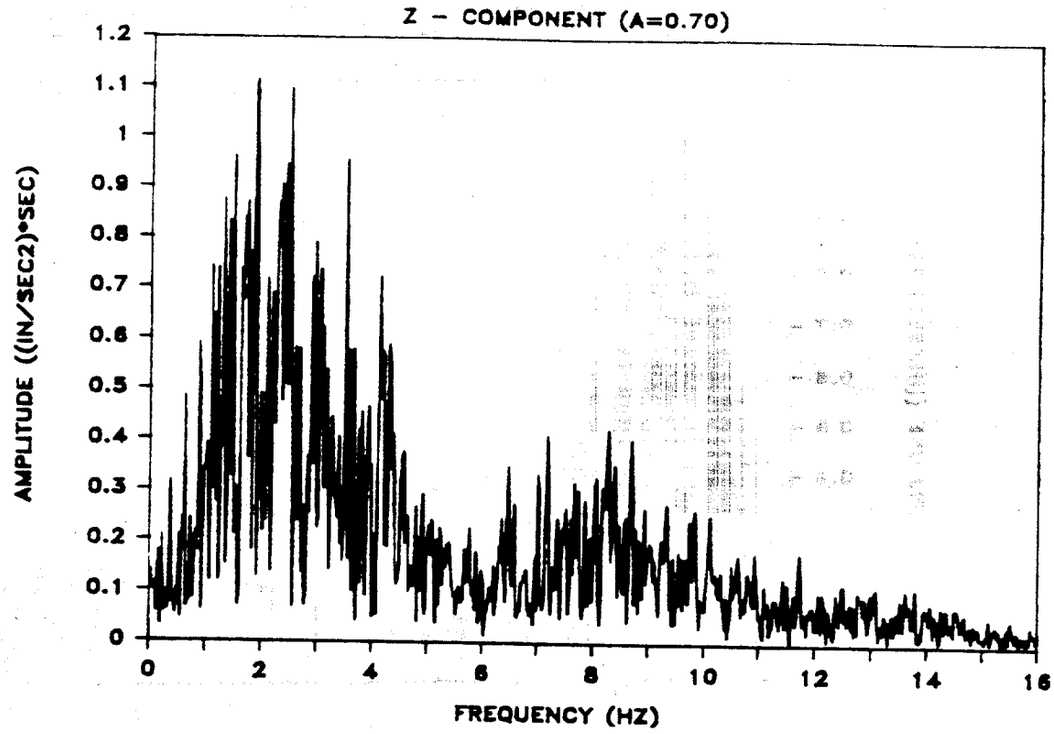

Fig. 5.6. Frequency Spectrum of Filtered (A = 0.7) Z-Component Record.

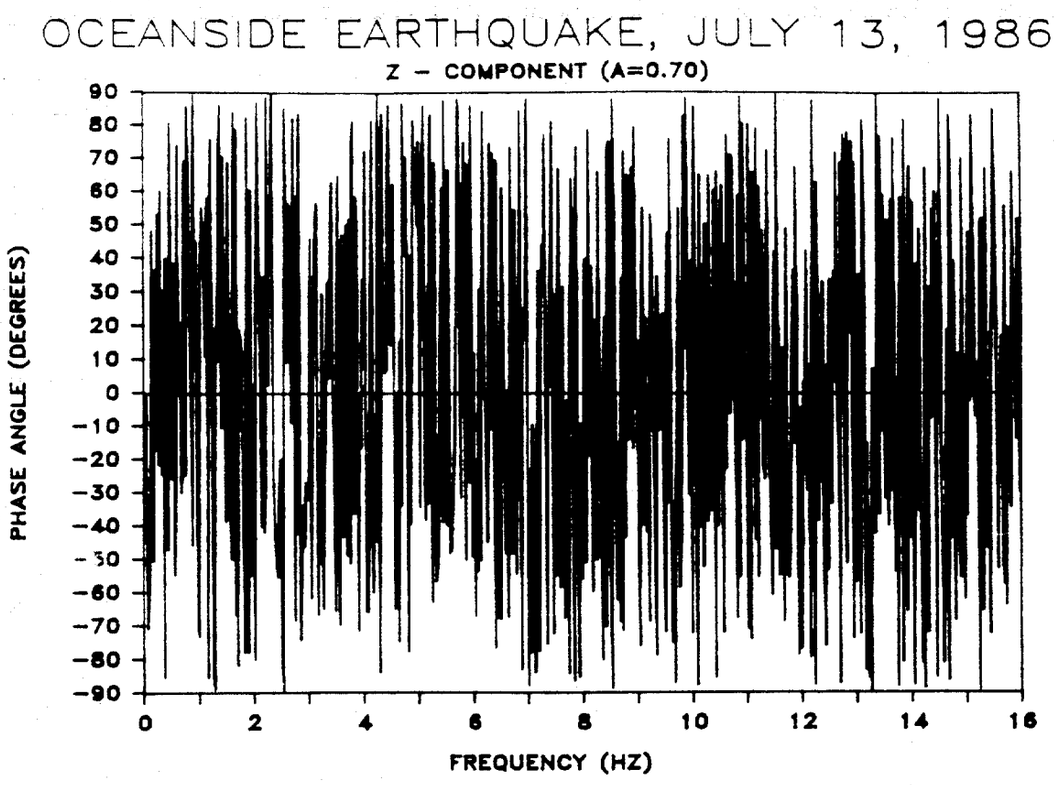

Fig. 5.7. Phase Angles of Filtered Z-component Record.

The second step is to establish an appropriate 'target' spectrum. In the development of scaling accelerograms for use in earthquake-resistant design, it is common practice to utilize some type of standard response spectrum shape, often scaled by an engineering estimate of the appropriate peak acceleration. Response spectra represent the maximum response (in acceleration, velocity and displacement) as a function of frequency, for a given damping ratio, of a single-degree-of-freedom system subjected to a time-dependent excitation. This approach can be justified for those applications where engineering judgment is most conveniently anchored to the methodology of the response spectrum approach. From a physical point of view, however, when it is required to estimate actual strong motion accelerations for given or assumed characteristics (parameters) describing the strong shaking, the approach based on scaling accelerograms in terms of Fourier amplitude spectra is more direct and better defined. Fourier amplitude spectra directly defining spectral parameters as functions of the Modified Mercalli Intensity (MMI), distance from epicenter, period (T), soil conditions, and direction of components (vertical and horizontal) of the strong motion have been derived by Trifunac (1979). The data base for Trifunac's analysis resulted from recording 57 earthquakes with Magnitudes between 3.0 and 7.7, and consisted of 186 records. Trifunac's proposed model is as follows,

$$\text{Log}_{10}[FS(T),p] = a(T)p + b(T)I_{MM} + c(T) + d(T)s + e(T)v\,, \qquad (5.2)$$

where

$FS(T),p$ = Estimate of the Fourier spectrum amplitude at the period of vibration, T, which is larger than the p fraction (confidence level) of all the data so far recorded under the same conditions,

$a(T), ..., e(T)$ = Regression coefficients (given in Fig. 5.8.),

I_{MM} = Level of intensity at a given site in terms of the Modified Mercalli Intensity,

s = Approximate site soil conditions (s = 0 for alluvial soil sites, s = 2 for rock sites, and s = 1 for intermediate sites), and

v = 0 for horizontal (X,Y) components and 1 for vertical (Z) component.

Vertical motion Fourier amplitude spectra computed from Eq. (5.2) for p = 0.50 and different levels of MMI are shown in Fig. 5.9.

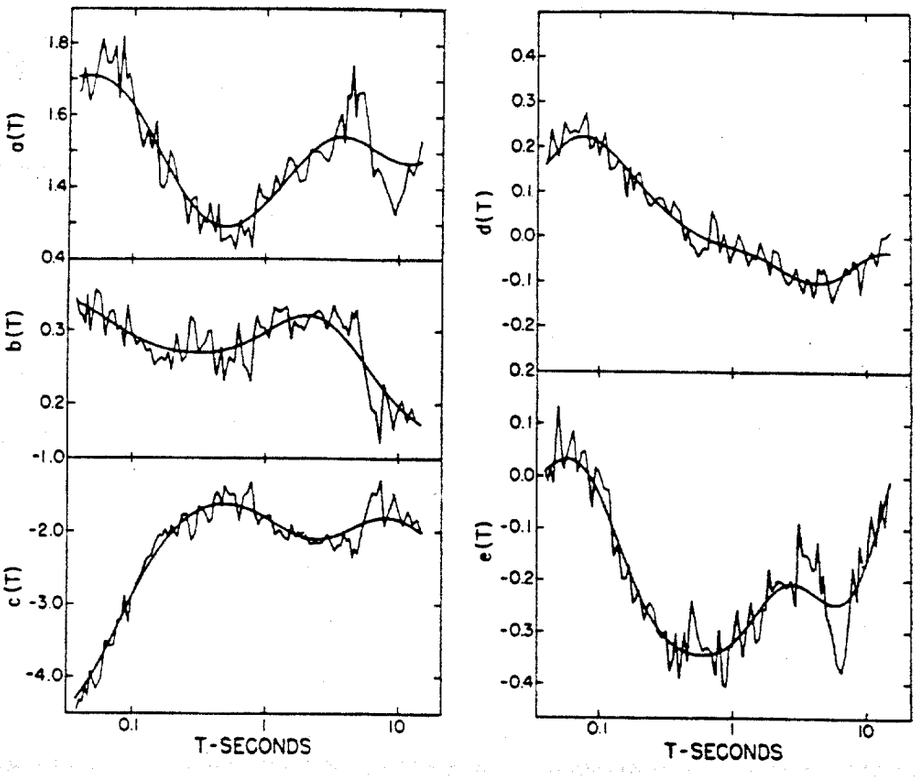

Fig. 5.8. Functions a(T), b(T), c(T), d(T), and e(T) for use in Eq. 5.2 [After Trifunac (1979)].

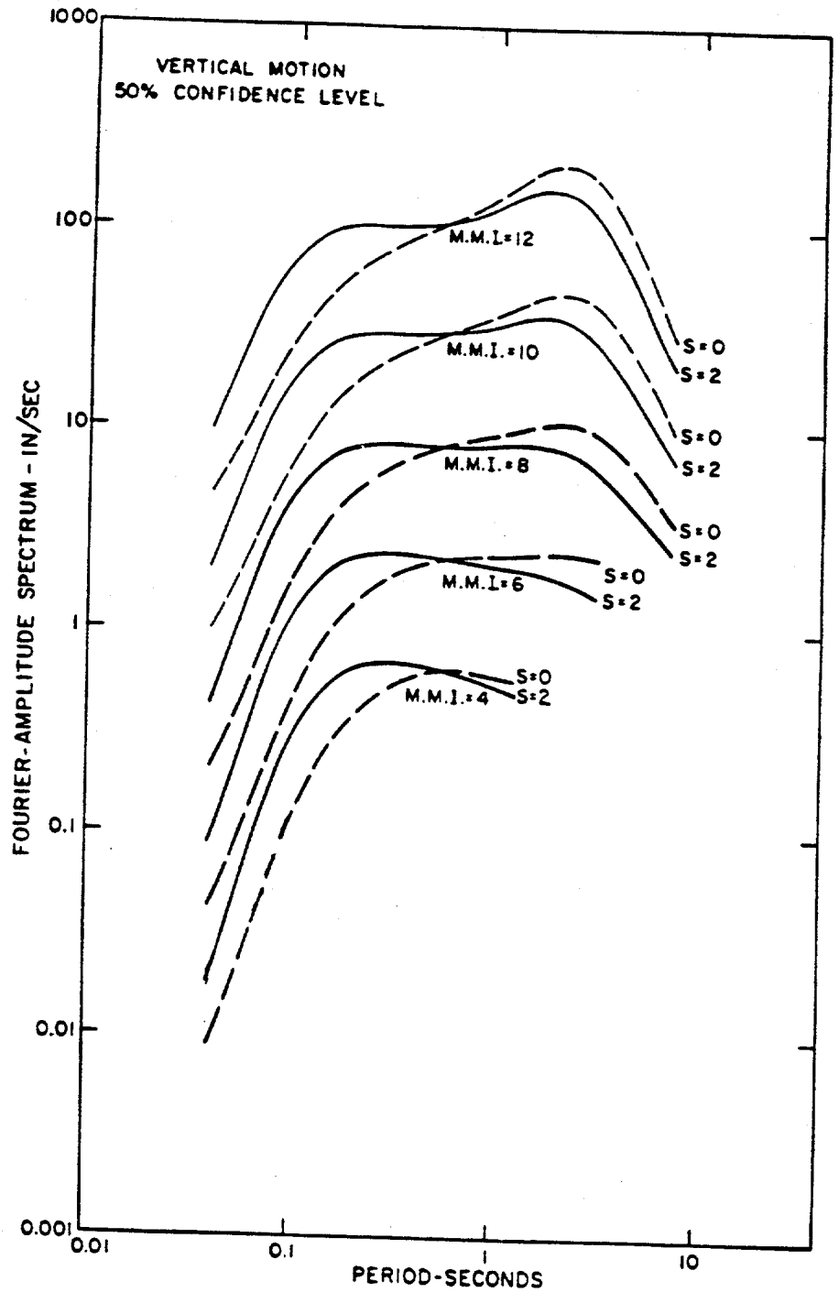

Fig. 5.9. Vertical (v = 1) Fourier Amplitude Spectra for MMI = IV-XII, for s = 0 and s = 2, and for p = 0.50 [After Trifunac (1979)].

Based on the same 186 earthquake records, Trifunac (1979) performed an analysis of the rate of decay of MMI with epicentral distance and correlated this decay with earthquake magnitude. Such correlations are depicted in Fig. 5.10. For this study, for an epicentral distance of 74 km and a Magnitude 8.0 earthquake the corresponding value of MMI is, approximately, 8.5. Interpolated values of the Fourier amplitude spectrum for MMI of 8.5 can be obtained from Fig. 5.9, for later use in scaling. Factor s = 0 for sites such as the SEMS site.

The third step in the scaling procedure consisted of scaling upward the spectrum of the original seismic record to match the target spectrum. This can be accomplished by multiplying the real and imaginary parts of the Fourier amplitude spectrum, at a particular frequency, by the same constant (phase relationship is not altered) to match the target spectrum. The value of the multiplying constant changes from frequency to frequency. It was judged that frequencies lower than 0.1 Hz and higher than 10 Hz would not be scaled up since their contribution to the strong motion is minimum. The original spectrum (after being filtered), the target spectrum [from Fig. 5.9, for MMI = 8.5 (M= 8.0, epicentral distance = 74 km)], and the computed spectrum after scaling are shown in Fig. 5.11.

The fourth, and last, step is to deconvolve the computed (scaled) spectrum back into the time domain while maintaining the same phase relationships (angles) that existed in the unscaled filtered record. For that purpose, the Inverse Fast Fourier Transform [Cooley and Tukey (1965)] was implemented to generate the time history of the new scaled accelerogram (Fig. 5.12) which was used in the testing program (peak accelerations of the order of 70 milli-g's). The displacement versus time record of the new filtered and scaled accelerogram was then obtained by double integration of the acceleration time history, as shown in Fig. 5.13. This time history was supplied to the chamber containing the bias-loaded pile.

Scaling of the Horizontal (Combined X and Y) Component of Motion

The X and Y components of motion of the seismic record were combined to provide the time history of the motion to be scaled up to Magnitudes 7.0, 7.5 and 8.0 and later used in Phase 2 of the testing program. After analyzing the frequency content and considering the signal-to-noise ratio, it was judged not to filter the original signals of the horizontal components of motion. The procedure for combining the two components of motion was based upon the three-dimensional stochastic model proposed by Penzien and Watabi

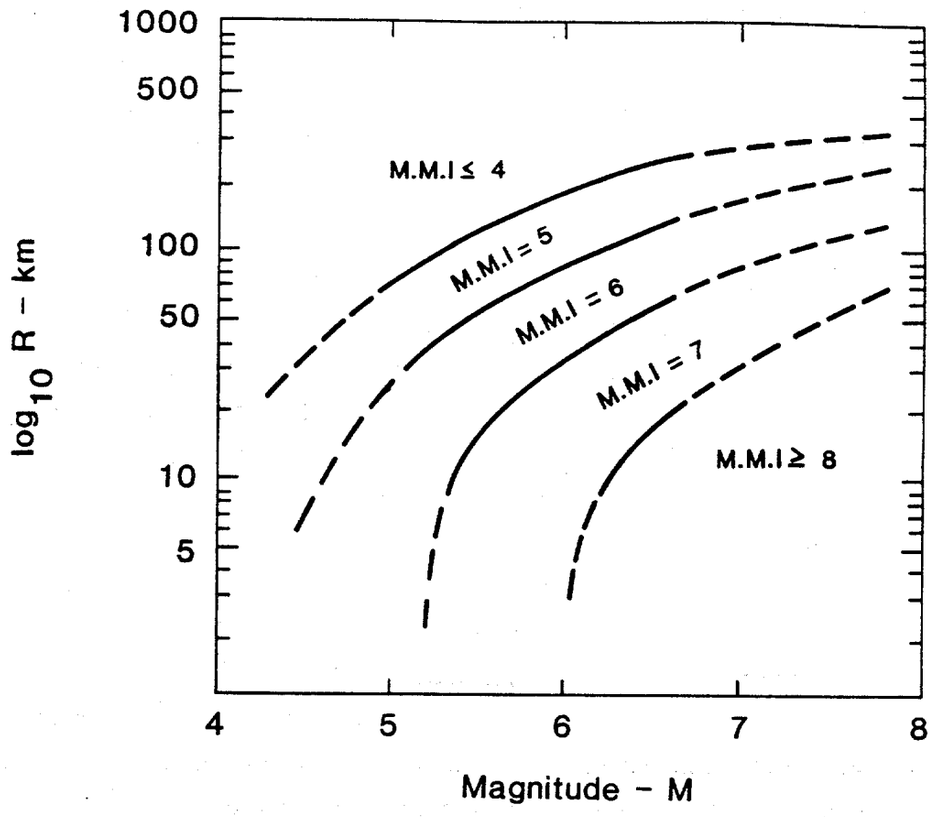

Fig. 5.10. Rate of Decay of MMI with Distance, R, and Magnitude, M [After Trifunac (1979)].

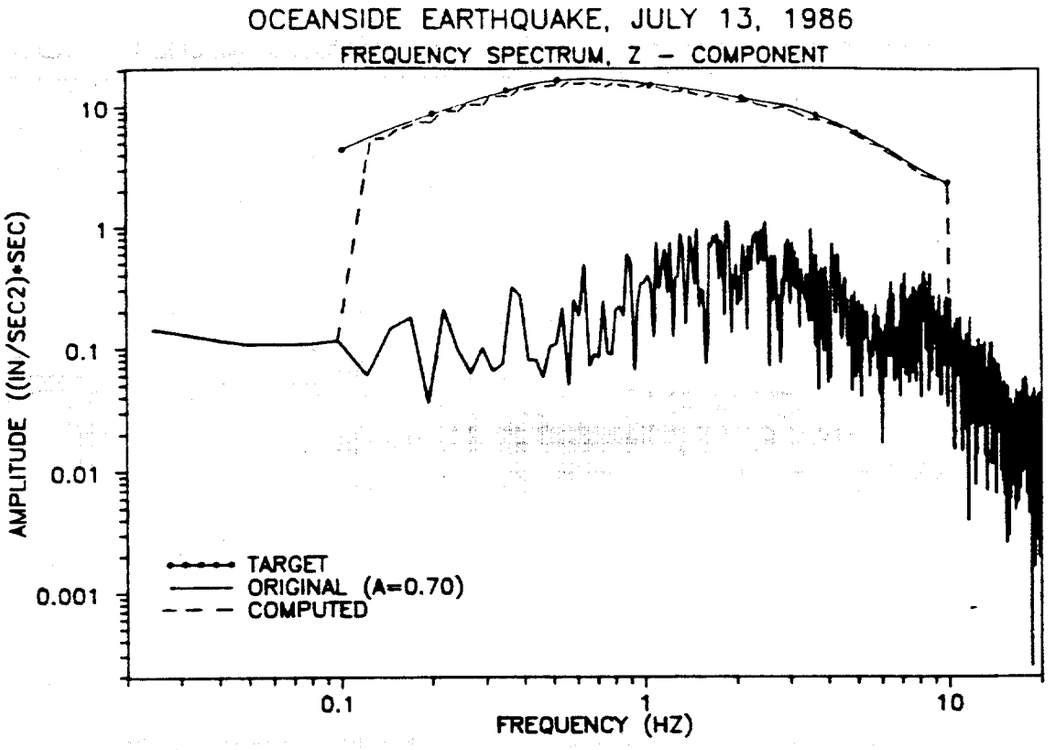

Fig. 5.11. Original (Filtered A = 0.7), Target and Computed (Scaled) Spectra (Vertical Motion).

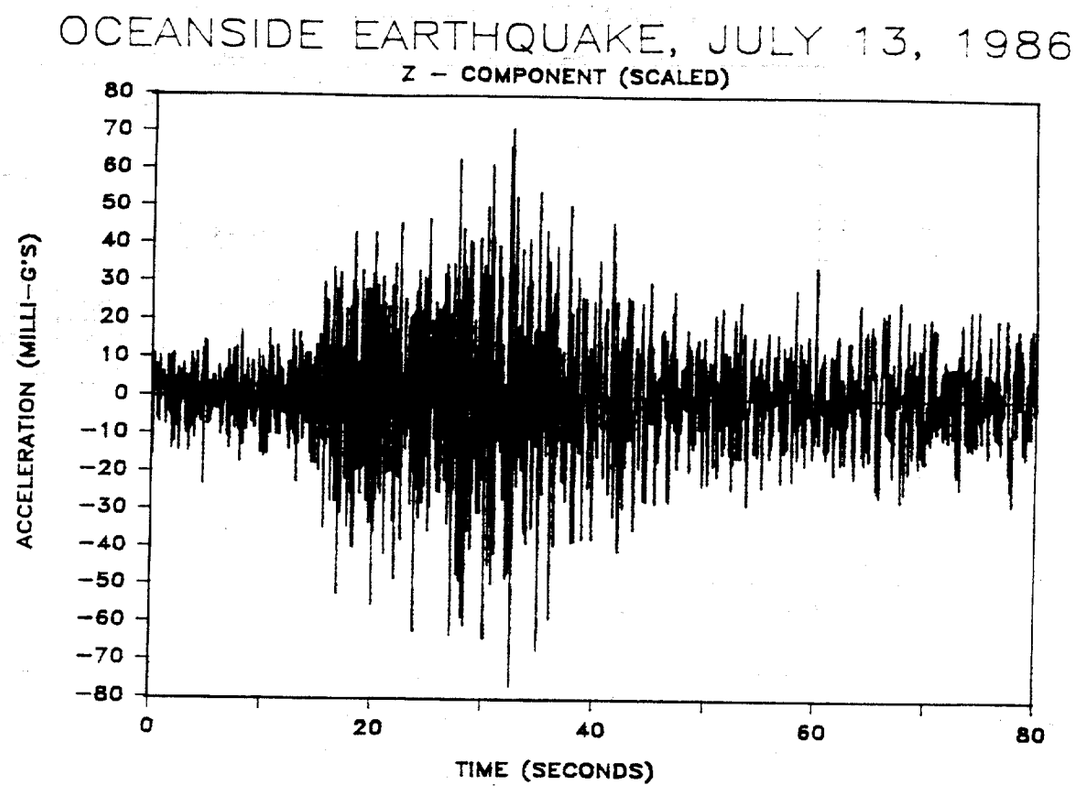

Fig. 5.12. Acceleration Time History of Scaled (M=8.0) Vertical Component of Oceanside Earthquake.

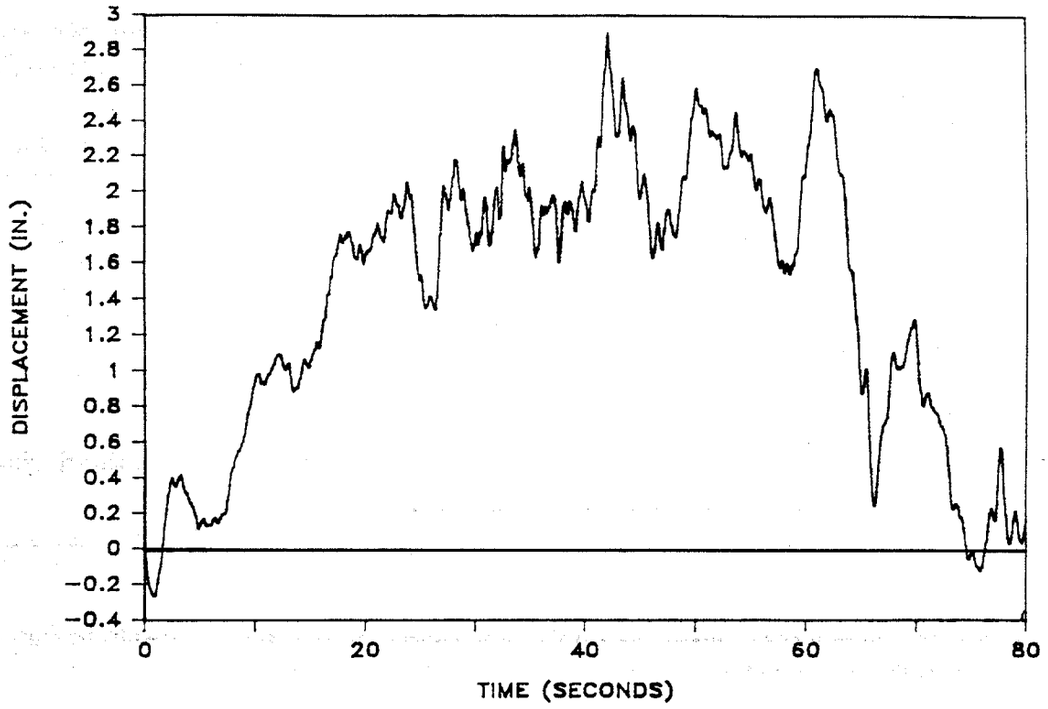

Fig. 5.13. Displacement Time History of Scaled (M=8.0) Vertical Component of Oceanside Earthquake.

(1975). The analytical treatment of such an approach uses the concept of principal axes of ground motion through an orthogonal transformation, completely analogous to the well-known transformation of stress. The vertical component of the recorded event was considered separately and, therefore, was not included in this analysis.

Covariances (μ_{ij}) of the recorded accelerations $a_x(t)$, $a_y(t)$ along the two accelerogram axes X and Y, respectively, were obtained using the relation [Penzien and Watabi (1975)],

$$\mu_{ij} = \langle [\, a_i(t) - A_i][\, a_j(t) - A_j] \rangle, \quad i, j = x, y \ , \tag{5.3}$$

where the time average (indicated by the triangular brackets) was taken over the interval,

$$t_1 = 20 \text{ sec} < t < t_2 = 40 \text{ sec} \ ,$$

(interval of strong shaking) but where mean values A_i and A_j were found by averaging $a_i(t)$ and $a_j(t)$ over the entire duration of motion. Expanding Eq. (5.3), principal variances (eigenvalues) of ground motion and their corresponding principal directions (eigenvectors) were then obtained. The computed principal direction (corresponding to the major principal variance) was then used to combine the accelerations of the X and Y records of motion giving as a result the acceleration time history (shown in Fig. 5.14) to be further scaled to higher magnitudes.

The same steps as those followed to scale up the vertical component of motion can be implemented for the case of the combined horizontal component of motion. In this case, the target spectrum may be chosen from those recommended by Trifunac (1979), for the case of horizontal motion (Fig. 5.15). The original spectrum of the combined horizontal component of motion, the target spectrum (From Fig. 5.15, for MMI= 8.5 (M= 8.0, epic. distance = 74 km)), and the computed spectrum after scaling are shown in Fig. 5.16. The time history of the new scaled accelerogram is given Fig. 5.17.

The duration of significant shaking is very much influenced by the magnitude of the earthquake, because shaking is likely to continue at least as long as fault rupture is occurring. The influence of earthquake magnitude on the duration of strong motion has been studied by several investigators [e.g., Housner (1965); Donovan (1973); Page et al. (1972)] . Based on Housner's estimations, the duration of strong shaking is expected to be 45 - 50 sec. for a Magnitude 8 earthquake. Since appropriate parts of the record may be

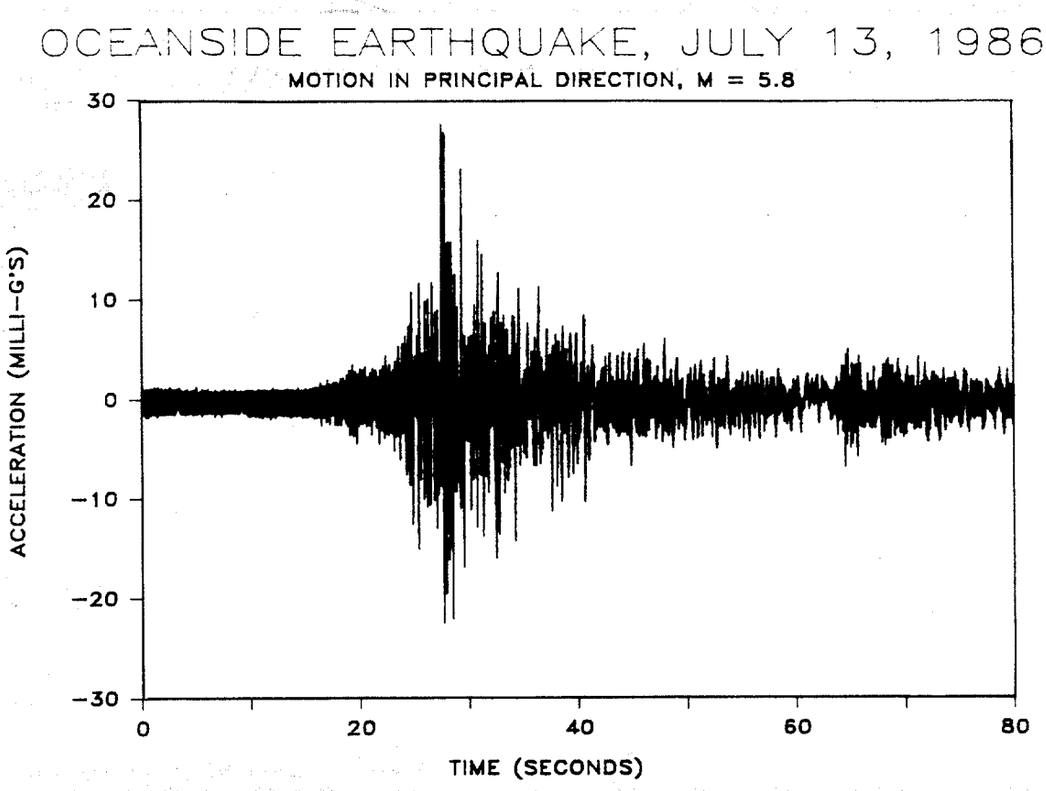

Fig. 5.14. Combined X and Y Components of Oceanside Earthquake (M=5.8).

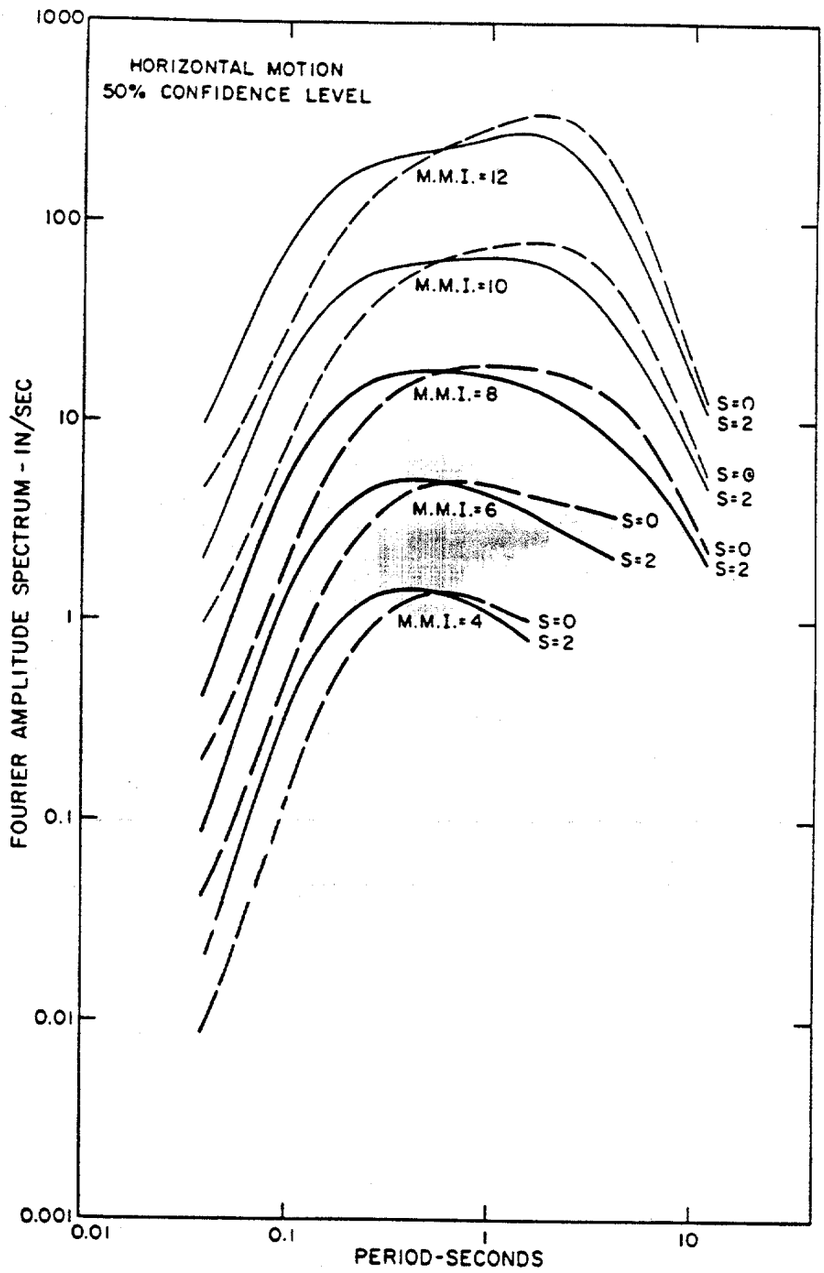

Fig. 5.15. Horizontal (v = 0) Fourier Amplitude Spectra for MMI = IV-XII, for s = 0 and s = 2, and for p = 0.50 [After Trifunac (1979)].

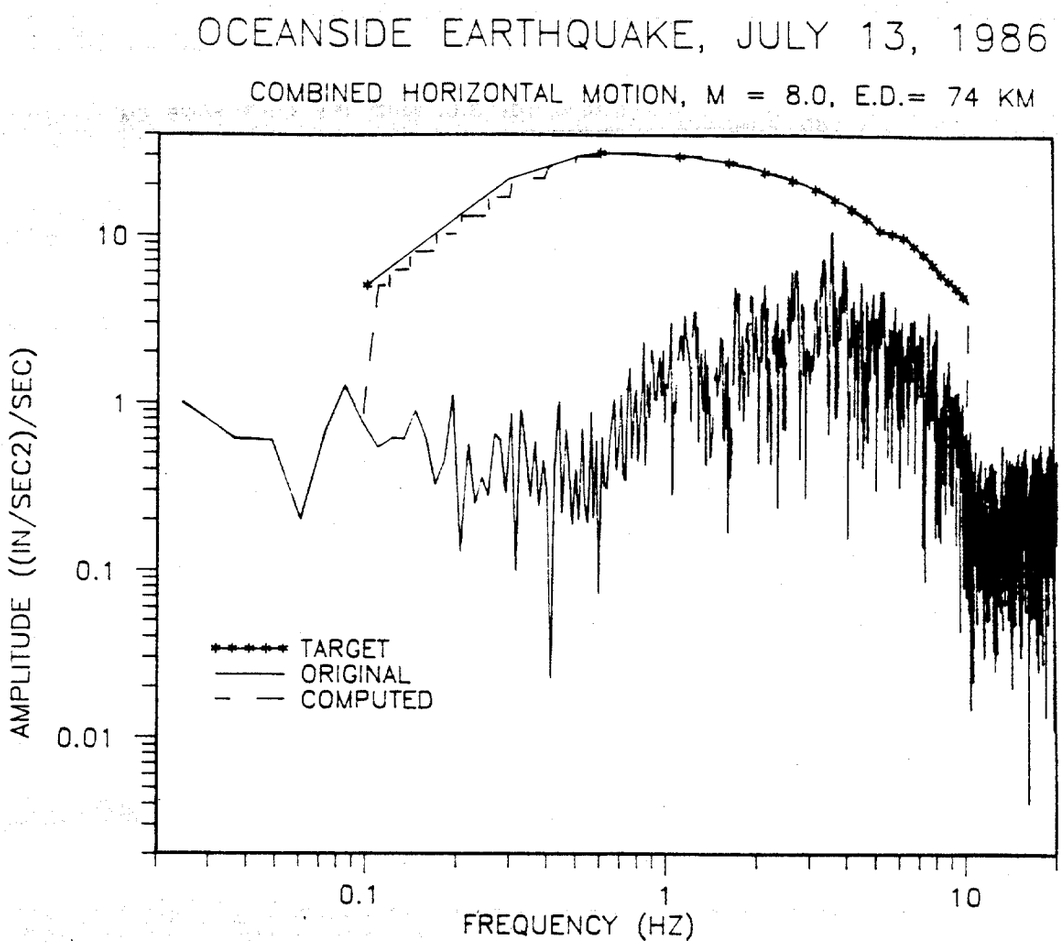

Fig. 5.16. Original, Target and Computed (Scaled, M=8.0) Spectra (Horizontal Motion).

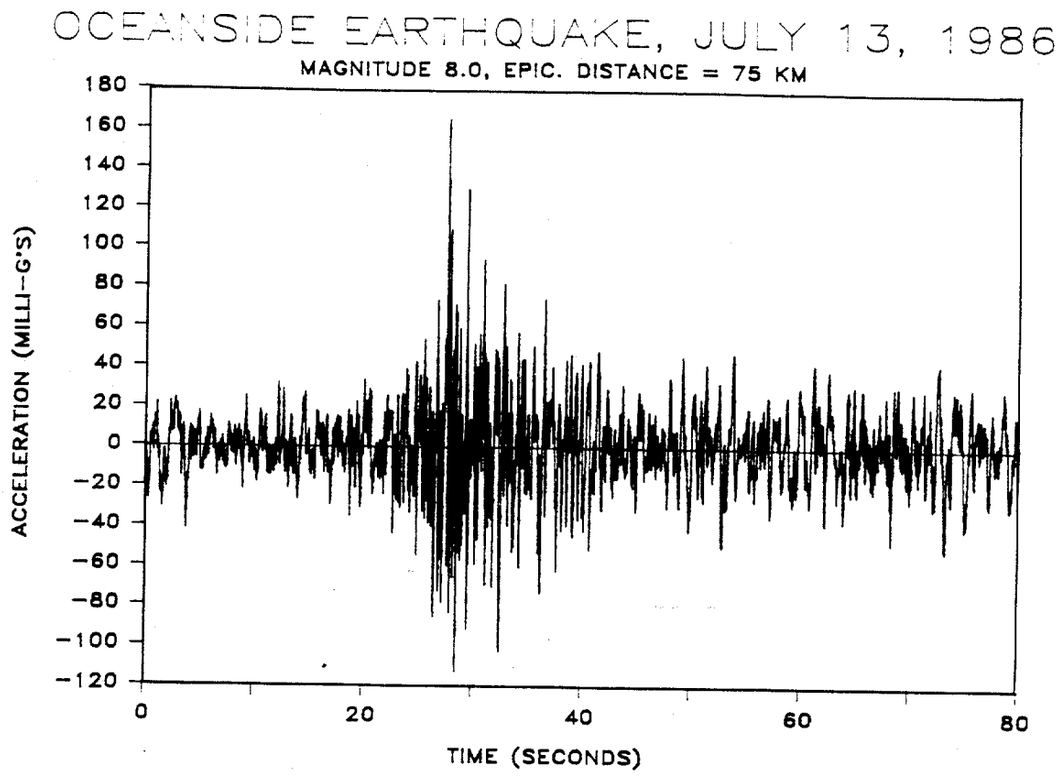

Fig. 5.17. Combined Scaled (M = 8.0) Horizontal Record of Oceanside Earthquake.

repeated as necessary to produce the desired duration [Seed et al. (1969)], the segment of the record (Fig. 5.17) between 25 and 40 sec. (period of strong shaking) was duplicated, as shown in Fig. 5.18, to produce an extended scaled time history for a Magnitude 8.0 event which was used in Phase 2 (horizontal motion) of the testing program (peak acceleration of the order of 170 milli-g's). The velocity and displacement versus time records, shown in Figs. 5.19 and 5.20, were obtained by single and double integration of the extended scaled acceleration time history, respectively. Original, target and computed spectra, scaled acceleration and extended scaled acceleration time histories, velocity and displacement time histories for Magnitudes 7.0 and 7.5 are given in Appendix H (Figs. H1 - H9). Threshold peak ground velocity (PGV) of 6 in./ sec needed to induce liquefaction [Mirodikawa et al. (1988)] suggests that liquefaction is expected to happen during the event Magnitude of 8.0. This fact will be verified in Chapter VII.

Comparisons of horizontal peak ground accelerations of the Oceanside earthquake, scaled to Magnitude 7.0 (Fig. H.3 in Appendix H), and the October 17, 1989, Loma Prieta earthquake (Magnitude 7.1) [Plafker and Galloway (1989)], recorded on alluvium and bay mud sites, are shown graphically in Fig. 5.21. Prediction using the widely used equation of Joyner and Boore (1988) has also been included for comparison. Some observations can be made regarding Fig. 5.21:

(1) For an alluvium site, except for one isolated point, horizontal peak accelerations of the Loma Prieta earthquake fall into a well defined band delimited by the dashed lines. Appreciable scattering can be observed for peak accelerations on bay mud sites.

(2) The attenuation equation of Joyner and Boore may be taken as the lower bound of peak accelerations for the Loma Prieta earthquake, for alluvium sites.

(3) Peak acceleration of the scaled Oceanside earthquake (75 milli-g's) for Magnitude 7.0 can be found to be within the limits of the Loma Prieta earthquake for alluvium sites, which is the site type of the SEMS site.

Based on those observations, peak ground accelerations of the Oceanside earthquake for Magnitudes 7.0, 7.5 and 8.0 (used during testing) can be expected to be in a realistic order of magnitude for real California earthquakes of Magnitudes 7.0, 7.5, and 8.0 about 74 km (46 miles) away from the causative fault.

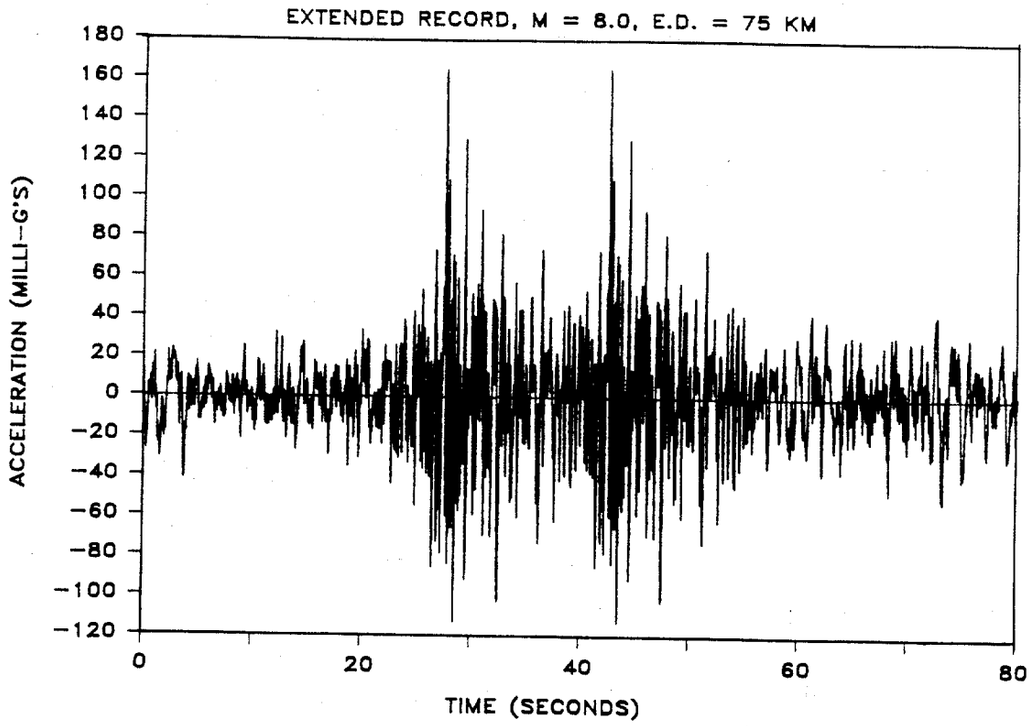

Fig. 5.18. Extended Scaled (M = 8.0) Horizontal Record of Oceanside Earthquake.

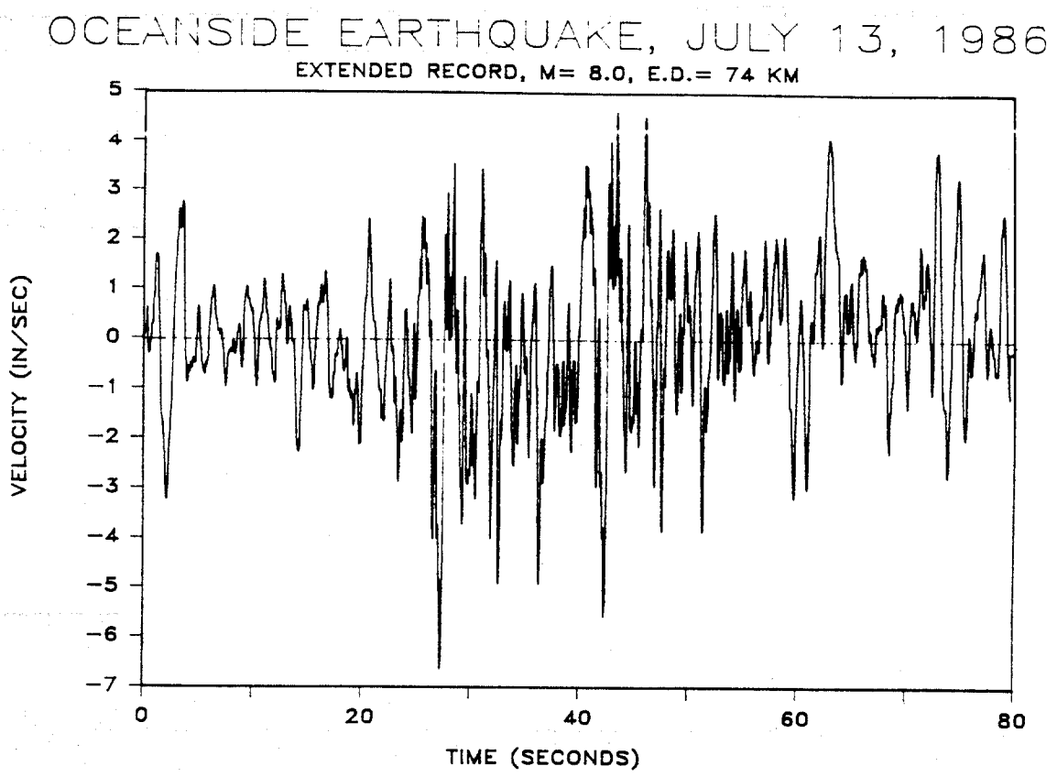

Fig. 5.19. Velocity Time History of Extended Scaled (M=8.0) Horizontal Component of Oceanside Earthquake.

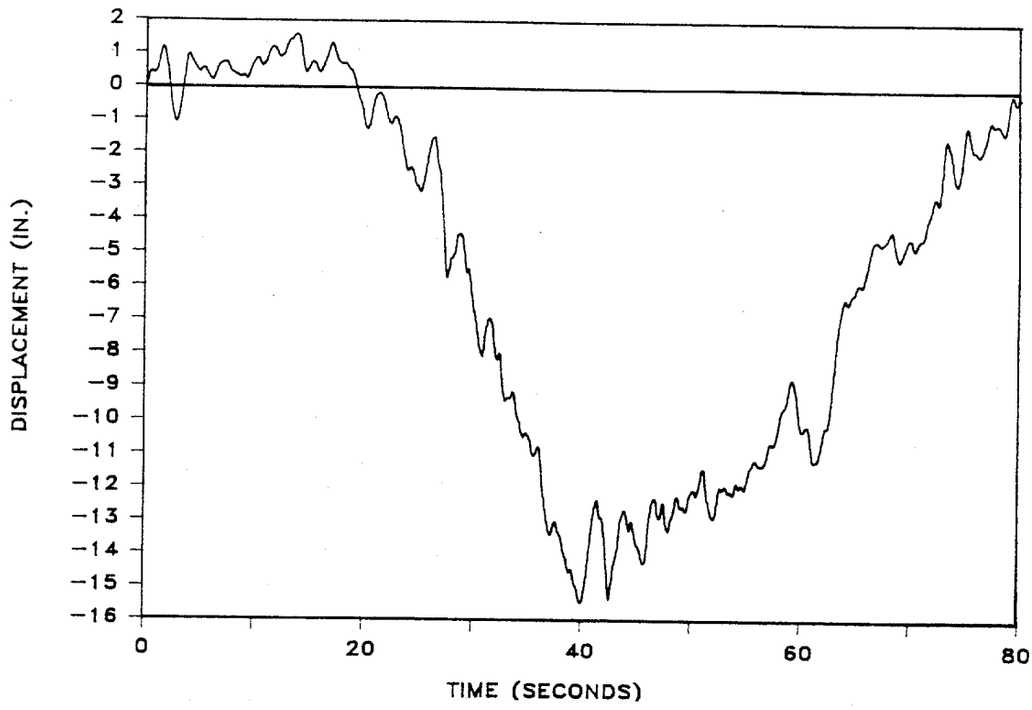

Fig. 5.20. Displacement Time History of Extended Scaled (M=8.0) Horizontal Component of Oceanside Earthquake.

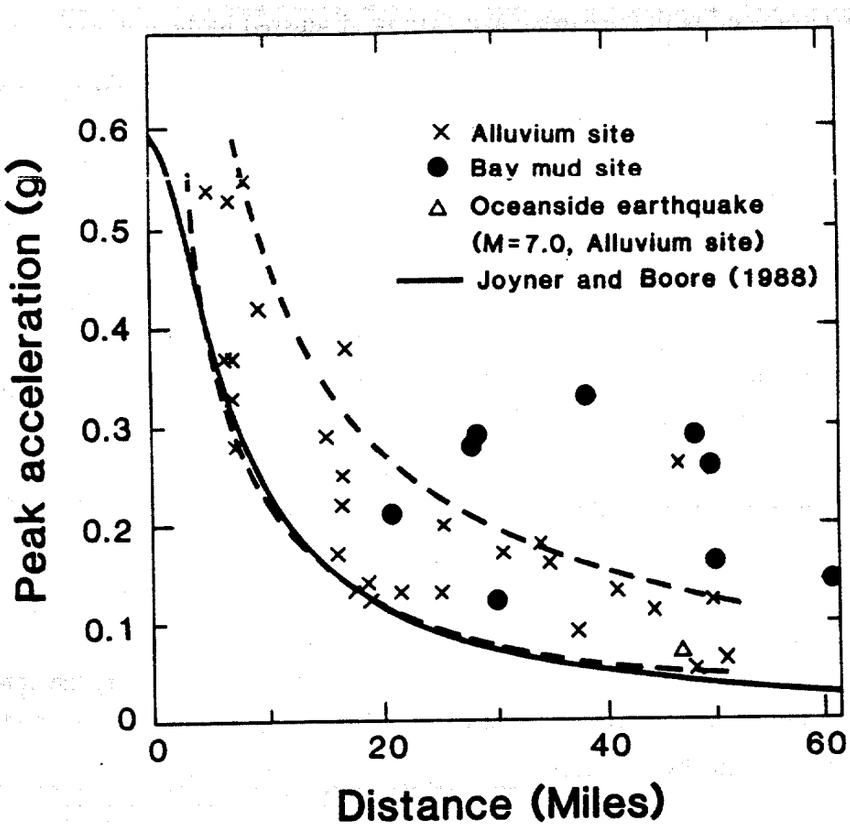

Fig. 5.21. Attenuation of Peak Horizontal Accelerations with Distance for Different Soils During Loma Prieta Earthquake [After Plafker and Galloway (1989)], and for Oceanside Earthquake (M=7.0, Epic. Distance = 74 km, in Alluvium Site).

MODEL-TO-PROTOTYPE SCALING

In addition to scaling the magnitude of the earthquake upward, it is also desirable to establish reasonable geometric scaling between the model and prototype. Such scaling is then combined with the earthquake scaling, discussed in the previous section, to produce similitude between the model tests and the response of a pile under biased tension loading during a strong seismic event at a deep soil site.

A straightforward analysis has been performed to establish geometric similitude rules based on the characteristic of the chamber that known isotropic effective stresses can be applied at the boundaries. This analysis includes both "static" and "dynamic" components. The static scaling rules relate the mean effective stress in a layer of prototype soil directly to the mean effective stress in the chamber, which gives a length scaling factor. Using this length scaling factor, it was then necessary to scale time and soil drainage characteristics in order to affect model-to-prototype similitude with respect to stress changes and pore water pressure diffusion rates during application of the modelled seismic event.

During most of the tests in Phase 1, the "dynamic" scaling rules were not observed. However, a few tests were conducted following these rules to verify the conclusions drawn from the majority of tests in Phase 1. However, in Phase 2, these scaling rules were followed for all shaking tests.

Static Scaling

A fundamental assumption underlying this testing program is that pile failure during an earthquake is likely to occur in side shearing resistance in the zone in which effective soil stresses are the lowest (i. e., nearest the ground surface). Similitude was established by controlling the effective stresses in the chamber such that they represented mean effective stresses in a submerged sand with K_o = 1.5 to depths of 20 and 40 ft. Extrapolation of the results to piles of greater penetration can be made by considering the 20 or 40 foot depth as representing the top 20 or 40 ft of the pile, or, conservatively by considering the results to represent the full length of pile, regardless of depth of penetration.

The computations establishing the relation of chamber pressure to depth are given in Appendix C. These computations use the principle that side shear in the pile is controlled by lateral effective stresses in the soil, the assumption that such stresses vary linearly in the prototype soil mass, and the fact that they are uniform in the pressure chamber (assuming weightless soil, as illustrated in Appendix C). Stresses in the model and prototype are made equal at the centroids of the respective lateral pressure diagrams, since static uplift capacity of the pile is proportional to the depth integrals of the lateral effective stresses against the piles, which are assumed in the establishment of scaling rules to have the same patterns as shown in Appendix C. Based on this background, Equation (C.1) is established. Recognizing that $K_o = 1$ in the model (isotropic stress conditions) and letting the prototype soil have $K_o = 1.5$ overconsolidated (medium to dense sand), the length scaling factor is derived in Appendix C to be 30 for effective chamber pressure of 5 psi. Thus, the 1.0-in.-diameter pile used in this study represents a 30-in.-diameter prototype, and the 15-in. (1.25-ft) penetration of the chamber employed in the model tests represented a 40-ft-log pile or top 40-ft segment of a pile. By a similar logic, the length scaling factor is 15 if the chamber pressure is 2.5 psi, and the model represents a prototype 15 in. in diameter and 20 ft long.

Dynamic Scaling

In order to model the stress changes in the soil and the build-up and dissipation of pore water pressure during the simulated seismic event, it is necessary to establish dynamic model-to-prototype similitude. This level of scaling results in an independent length scaling factor, which ideally should be identical to the length scaling factor derived above, and a time scaling factor. Scaling factors for modelling soil stresses in the test chamber and used in this modelling step are described in Table C.1 of Appendix C. The constraints employed are that the pore fluid in both model and prototype be identical (water), and that velocity similitude be preserved between model and prototype. The use of alternative pore fluid, e.g., oily water [Fuglsang and Ovesen (1988)], to manipulate the permeability may result in unknown and undesirable effects on the soil-pile interaction; therefore, this option was not implemented. Time scaling factors can then be established separately for stress changes and diffusion, as described below. It is recognized that other dynamic scale effects may also exist, but stress change and diffusion are clearly the most significant.

Dynamic Time Scaling. As shown by Relations 5, 10, and 13 in Table C.1 (Appendix C), similarity between model and prototype stress changes due to seismic

loading can be achieved if an n-scale model is subjected to accelerations n-times as large as the prototype's. This can be accomplished by applying a displacement-time record, with displacement amplitudes 1/n as large as those in the prototype record (Relation 1), in a time period 1/n as long as the prototype event (Relation 3). Therefore, both the time and displacement values in the time-displacement record for the scaled earthquake (i.e., Figs. 5.13 and 5.20 for M = 8.0, and corresponding records for M = 7.0 and 7.5) must be multiplied by 1/n to obtain the record to be applied to the model test chamber.

Dynamic Diffusion Scaling. It is impossible to model the effects of fluid inertia and diffusion simultaneously if the pore fluid is the same in the model as in the prototype. Since the decision was made that substitution of a viscous fluid in the model for water in the prototype could lead to ambiguous conclusions, it was decided not to model fluid inertia explicitly, but to model diffusion. Relation 16 in Table C.1 shows that the dimensionless time factor for diffusion (analogous to the time factor in linear consolidation theory) is scaled by $1/n^2$ rather than by 1/n. However, the diffusion scaling factor can be changed to 1/n, to make it compatible with the dynamic time scaling factor, if the factor N_{cv} in Relation 15 is adjusted to 1/n. This can be done by adjusting the hydraulic conductivity of the soil such that the model soil has a coefficient of Darcian permeability of 1/n times that of the prototype. That is, the model soil must be considerably finer than the prototype soil. This was the reason for using microfine sand to model SJR sand (Chapter IV).

Selection of Time Scaling Factor for the Experimental Study. The choice of the scaling factor for time (n) was conditioned simultaneously by two considerations: (1) The finest soil that could be found that did not possess cohesive characteristics and that could be saturated by gravity, as required by the design of the testing chamber, microfine sand (Chapter IV), had a coefficient of Darcian permeability approximately 1/8 that of SJR Sand (Table 4.1), so that the maximum value of n from this perspective was eight. (2) The available Instron closed-loop hydraulic testing machine could track the applied displacement time history at a minimum time step of 0.0014 sec. The minimum time step from the scaled time-displacement records for the seismic event required for replication of those records was approximately 0.01 sec. Therefore, the maximum scaling factor, n, from the perspective of the operation of the testing machine was 0.01/0.0014 = 7.

Since these two factors were approximately equal, it was judged that n = 7 was appropriate for testing, and that it was unnecessary to adjust the properties of microfine sand to obtain a permeability ratio of exactly seven.

The use of n = 7, however, leads to a basic incompatibility between dynamic and static scaling. In order to scale static conditions, controlled by the initial effective chamber pressure, the length scaling factor (n) was 15 to 30, such that the use of a one-in.-diameter pile in the model was equivalent to a 15- to 30-in.-diameter prototype pile. On the other hand, a time scaling factor n = 7 leads to prototype pile diameter = 7 in. Since both the physical constraints of modelling permeability by the use of microfine sand and the time-step limits of the machine precluded use of a time scaling factor larger than about seven, the modelling incompatibility was accepted.

The resulting model parameters were therefore as follows:

(1) Isotropic effective initial chamber pressures = 2.5 and 5.0 psi,

(2) Pile diameter = 1.0 in.; penetration of pile into chamber = 15 in.,

(3) Model soil is microfine sand with k = 1/8 k of the prototype sand (assumed to be SJR Sand),

(4) Time scale = 1/7 times the prototype time,

(5) Velocity = velocity of prototype, and

(6) Relative density of soil = relative density of prototype soil (no scaling). Model relative densities were 55 and 70%.

Criteria (4) and (5) lead to displacements 1/7 times those in the prototype and accelerations seven times those in the prototype.

The above scaling relations lead to the following prototype characteristics listed below:

(1) Pile diameter = 15 in. to 30 in., assuming that modelling Criterion (4), above, theoretically correct for 7 in. piles, is also relevant for 15 to 30 in. piles,

(2) Pile length = 20 to 40 ft (or concern is for the top 20 to 40 ft of a longer pile),

(3) Soil in which piles are driven is San Jacinto River Sand at relative density of about 55 to 70% with $K_o = 1$, and

(4) The pile is excited through the soil, with vertical feedback from the superstructure, by an earthquake represented by the Oceanside event of 1986 with a Richter Magnitude of 7 - 8. The earthquake epicenter is approximately 74 km from the site of the pile foundation.

Induced Pressures in the Water Mass due to Vertical Seismic Excitation.

In a prototype seismic event the vertical component of seafloor or river bottom motion will produce compression waves in the water, which could affect pore water pressure buildup in the soil, thus promoting pile failure more quickly than occurs in the model, which does not accommodate this phenomenon. It was therefore decided to conduct an analysis of this phenomenon in order to ascertain the magnitude of water pressure that could develop in the water mass at the soil line. In order that the analysis be conservative, the pile was assumed to be at an offshore location where the water depth is 1000 feet, as illustrated in Fig. 5.22. Derivations and numerical calculations are made in Appendix D. Only the period of strong shaking was used in the analysis, as shown in Fig. 5.23 (which is scaled to M = 8 but contains no time scaling effects). Two predominant frequencies can be observed: 1 Hz with 0.05-inch peak displacement; 0.12 Hz with 0.73-inch displacement. Using the superposition of these two sinusoidal displacement time histories at the base of a standing column of water, the magnitude of the "shock" pressure from the overlying water is computed to be slightly greater than the maximum effective pressure used in the chamber (5 psi). (See Appendix D.) The extent to which these pressures will be transferred into excess pore water pressure is unclear. If the entire water shock pressure is transferred into pore water pressure, shallow liquefaction of the soil could occur independent of the phenomena being modelled in the present study. It is assumed for design purposes, however, that the problem of liquefaction due to water overpressure can be decoupled from the problem of dynamic pile-soil interaction through seismic soil loading under study here.

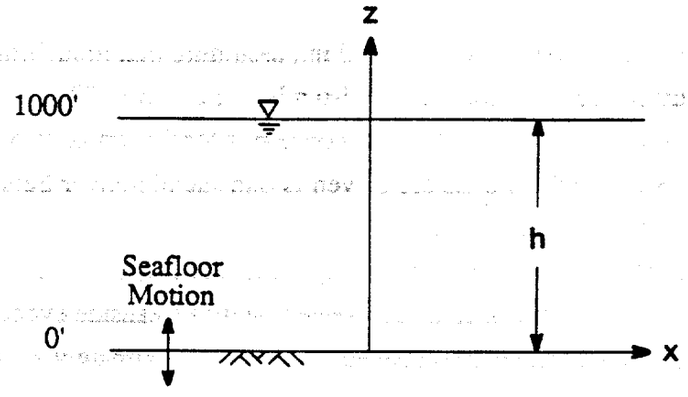

Fig. 5.22 . Assumed Conditions for Analysis of Induced Pressures in Water Mass Subjected to Vertical Seismic Motion.

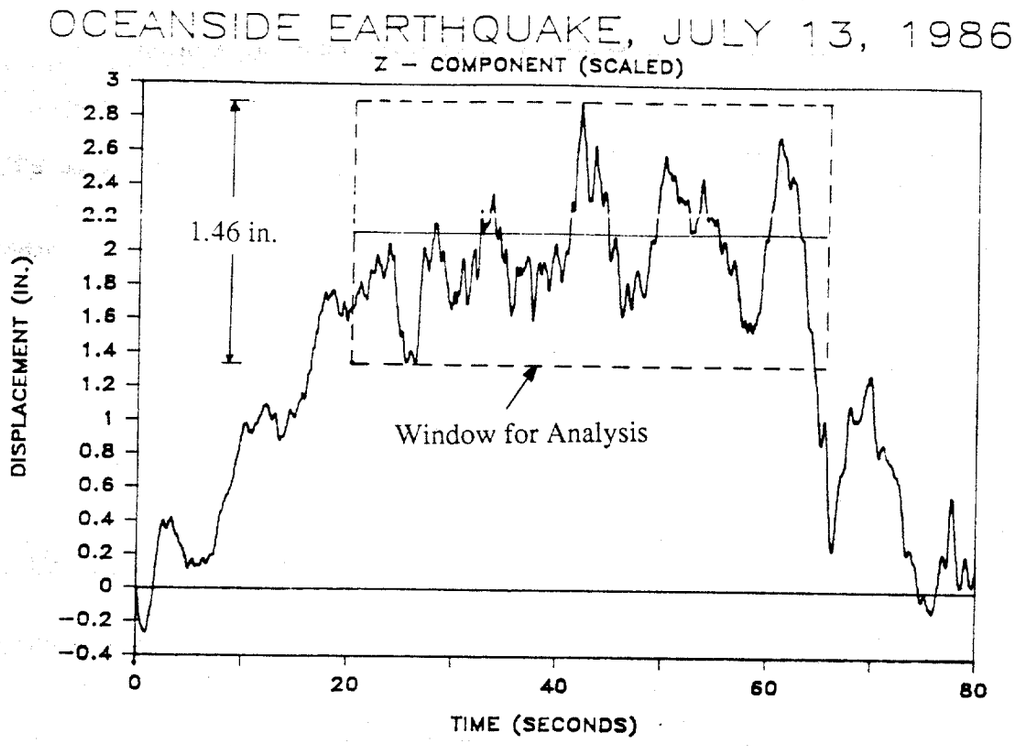

Fig. 5.23. Window for Induced Water Pressure Analysis During a Simulated Vertical Seismic Event.

CHAPTER VI

Analysis of Test Results, Vertical Motion

This chapter describes the analysis of relevant test data in order to develop a better understanding of the vertical dynamic response of axially loaded piles with tension bias under the vertical component of earthquake loading. The following aspects were investigated: (a) pore water pressure build-up during the impact driving of the pile (an indirect indication of the susceptibility of the test sand to pore water pressure generation during dynamic loading), (b) relationship between the penetration rate (blows/in.) and uplift static capacity, (c) comparisons between the vertical measured and target spectra, (d) ultimate uplift static capacities, (e) static load transfer characteristics, (f) pile and soil response during the vertical component of the simulated seismic event, (g) post-shaking static capacities after the seismic event, and (h) dynamic load transfer characteristics.

Summaries of the static and dynamic (vertical motion) test program results are given in Tables 6.1 and 6.2, respectively. The static tests (A1-F, O1-Q) represented, for further comparisons, the baseline for the remaining dynamic tests.

INDUCED PORE WATER PRESSURE DURING IMPACT DRIVING

Measurements of induced pore water pressures generated by the impact driving of the pile were performed by means of the miniature pore water pressure transducers embedded in the soil mass (Fig. 3.13). Calibrated outputs for the transducer placed one inch from the pile wall for two typical tests, Test A3 (SJR sand) and Test F (Micro-fine sand), are displayed graphically in Fig. 6.1. Some comments can be made regarding Fig. 6.1. First, the induced pore water pressure for the micro-fine sand (Test F) is doubled when compared with the induced pore water pressure values for the SJR sand (Test A3). Smaller particle sizes and, therefore, a reduced coefficient of permeability of the micro-fine sand may have impeded the flow of pore water, inducing higher pore water pressures. Second, the highest positive values of induced pore water pressures were measured when the pile toe was nearest the instrument level and were of the order of 20 - 40 % of the effective chamber pressure. Once the pile toe passed this point, negative pore water pressures were developed in the field around the instrument. Driving effects were negligible when the pile toe was

Table 6.1. Driving Blow Count and Static Capacity for All Static Tests

Test No.	Type of Static Loading: CD/CL[b]	Condition: Dr (%) / σ_c (psi)	Blow Count (blows/in.)[d]	Static Capacity[e] (lbs)
A1	CD	55 / 5	7.6	270
A2	CD	55 / 5	9.3	250
A3	CL	55 / 5	6.3	220
B1	CD	70 / 5	12.6	390
B2	CL	70 / 5	9.6	241
C	CD	78 / 5	19.6	560
D	CD	85 / 5	26.6	550
E1	CD	55 / 2.5	4.5	100
E2	CL	55 / 2.5	5.0	120
F[a]	CL	55 / 5	5.0	179
O1[a,c]	CL	55 / 5	7.4	204
O2[a,c]	CL	55 / 5	7.0	208
P[a,c]	CL	70 / 5	10.3	303
Q[a,c]	CL	55 / 2.5	4.7	117

a. Tests conducted with micro-fine sand. Other tests conducted with standard test sand (SJR sand).
b. CD refers to a controlled displacement test. CL refers to a controlled load test.
c. Pile driven off center.
d. Averaged blow count in the last 3 in. (3 diameters) of driving.
e. Static failure defined at load that produced initial interface slip, whether CD or CL test.

Table 6.2. Summary of Dynamic Test Program Results, Vertical Motion.

Test No.	Type of Test:	Type of Static Loading: CD/CL[e]	Condition: Dr(%) /σ_c (psi) / % of Inferred Static Capacity (Q bias (lb))	Static Capacity for Dynamic Test Inferred from Blow Count (lb)	Pullout Failure Observed ?	Static Capacity or Post-Shaking Static Capacity (lb)[f] (% of Inferred Static Capacity)
G	Dynamic	CD	55 / 5 / 24 (60)	251 (8.3 b/in.)	No	260 (103)
H1	Dynamic	CL	55 / 5 / 49 (123)	251 (8.3 b/in.)	No	229 (91)
H2	Dynamic	CL	55 / 5 / 60 (80)	135 (5.0 b/in.)	No	127 (94)
I1	Dynamic	CL	55 / 5 / 90 (156)	172 (6.0 b/in.)	Yes	-
I2	Dynamic	CL	55 / 5 / 92 (243)	260 (8.6 b/in.)	Yes	-
J	Dynamic	CL	70 / 5 / 75 (228)	303 (10 b/in.)	No	318 (104)
K	Dynamic	CL	70 / 5 / 93 (335)	359 (12 b/in.)	Yes	-
L1	Dynamic	CD	55 / 2.5 / 63 (184)	294 (9.7 b/in.)	No	264 (90)
L2	Dynamic	CL	55 / 2.5 / 90 (87)	96 (4.0 b/in.)	Yes	-
M1	Dynamic[a,c,d]	CL	55 / 5 / 58 (100)	172 (6.0 b/in.)	No	168 (97)
M2	Dynamic[a,c,d]	CL	55 / 5 / 92 (160)	172 (6.0 b/in.)	No	195 (112)
N1	Dynamic[c]	CL	55 / 5 / 53 (111)	207 (7.0 b/in.)	No	193 (93)
N2	Dynamic[c]	CL	55 / 5 / 96 (214)	217 (7.3 b/in)	No	239 (110)

a. Tests conducted with micro-fine sand[b]. Other tests conducted with standard test sand (SJR sand).
b. Sand with a coefficient of permeability approximately 0.12 times that of SJR sand (standard test sand) to scale drainage distance.
c. Time scaled by a factor of 0.14 in the acceleration record to scale drainage distance and other length factors.
d. Accelerations scaled by a factor of 7 in the acceleration record.
e. CD refers to a controlled displacement test. CL refers to a controlled load test.
f. Static failure (baseline or post-shaking loading tests) defined at load that produced initial interface slip, whether CD or CL test.

Notes:

1. Inferred static capacities for dynamic tests were obtained from the average blow count in the last 3 in. (3 diameters) of driving of the piles subjected to the dynamic test by comparing to relationship of measured static capacity to corresponding blow count (Tests A1 - F, O1 - Q).

2. Biased loads (Q_{bias}) were the pure static tension loads imposed on the piles before initiation of shaking. Due to the spring and mass biased loading system, some cyclic load was superimposed on this static bias during shaking. Consult measured time histories of loading for more details.

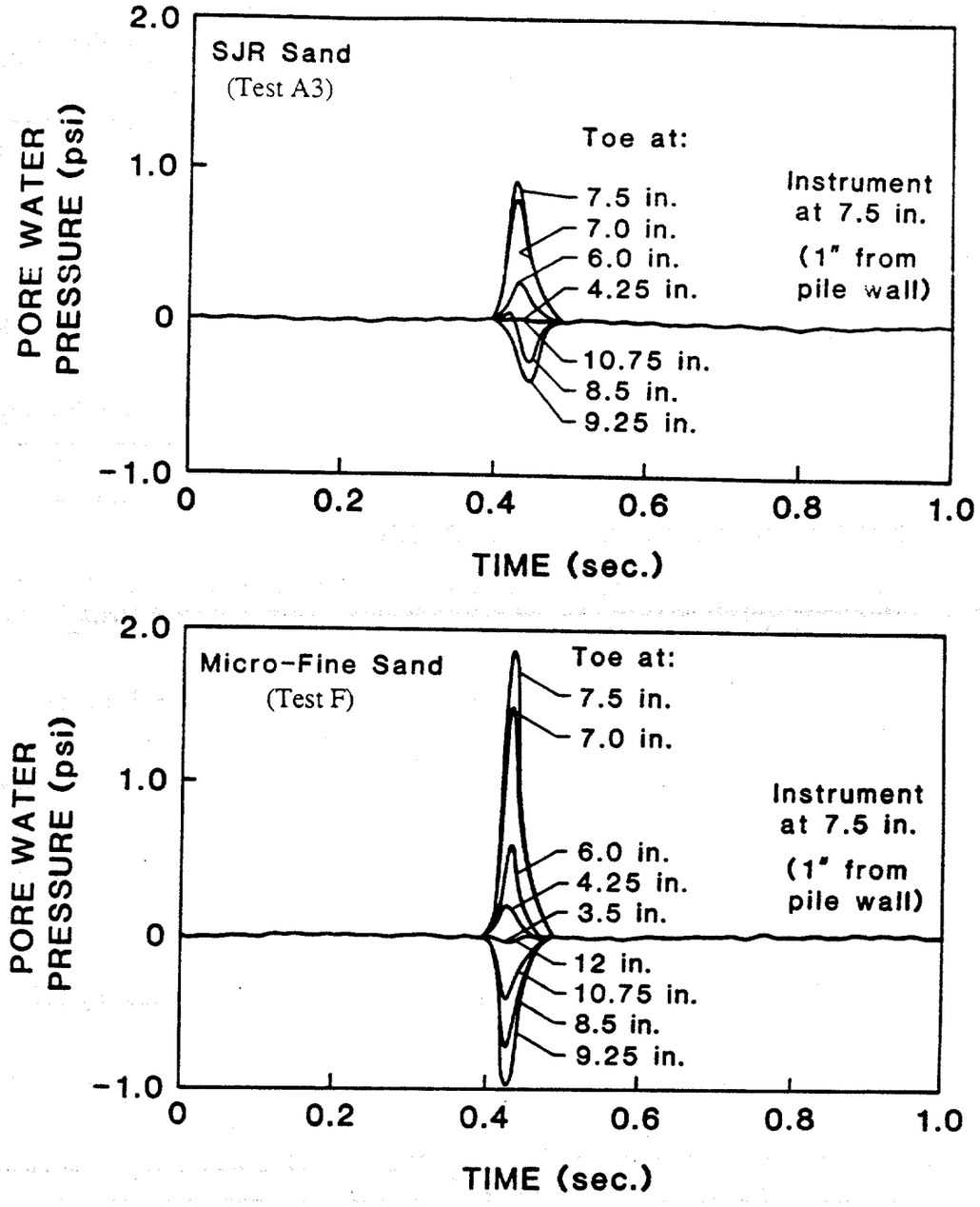

Fig. 6.1. Induced Pore Water Pressure due to Impact Driving, Test A3 and Test F, (σ_c' = 5 psi)

located 2.5 diameters and 4 diameters below the instrument level for SJR sand and micro-fine sand, respectively. Measurements with the far-field instrument were negligible, and therefore, are not shown here.

RELATION BETWEEN PENETRATION RESISTANCE AND UPLIFT STATIC CAPACITIES

Static uplift tests were conducted on the model pile driven into the chamber by controlled load (CL) and controlled displacement (CD) methods to develop blow-count-versus-uplift capacity relations. The definition of static failure load was not straightforward, and the mechanism of failure in static uplift had to be investigated. The fundamental problem is illustrated in Fig. 6.2. If a pile in the chamber is subjected to a static load test in which the load Q is applied under conditions of controlled displacement (CD), the load-movement relation on the left is produced. Initial slippage occurs when static friction first develops into sliding friction. But sliding friction is quickly arrested because the pile losses elastic energy and becomes less elongated, allowing static friction to once again develop, after which further frictional capacity is realized. This cycle is repeated perhaps several times, each of which results in a slight increase in uplift capacity following minute amounts of slippage. In a controlled load (CL) test, depicted on the right side of Fig. 6.2, no opportunity for arresting initial sliding friction exists, and pullout occurs at the time that initial sliding friction develops. The result of this behavior is that CL tests appear to produce lower capacities than those obtained from CD tests. The decision was made at the completion of the static tests to define failure in uplift for CD tests when the first slip occurred, while for CL (which may represent TLP and Tainter gate loading conditions better than the CD test) tests failure occurred when the pile was suddenly pulled out from the test chamber.

Penetration resistance records (average blow count in the last 3 diameters of driving) versus the ultimate capacity for all static tests of the testing program given in Table 6.1. The data have been fitted by a second-order polynomial equation, as shown in Fig. 6.3, which was used to infer the percentile of the static capacity corresponding to the applied bias load. For tests with similar confining pressures (σ_c' = 5 psi), an increasing trend of the static capacity with penetration resistance was observed, in which low and high values of penetration resistance corresponded to low and high values of relative density, respectively.

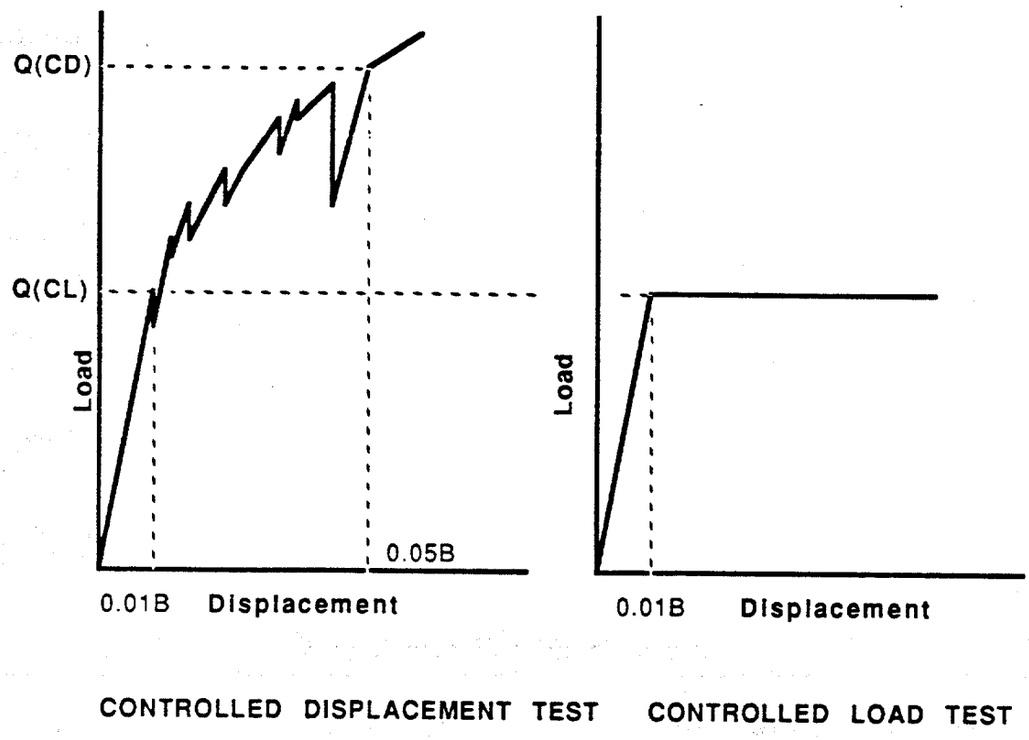

Fig. 6.2. Schematic Comparison of Baseline Static Capacities from Controlled Displacement (CD) and Controlled Load (CL) Tests.

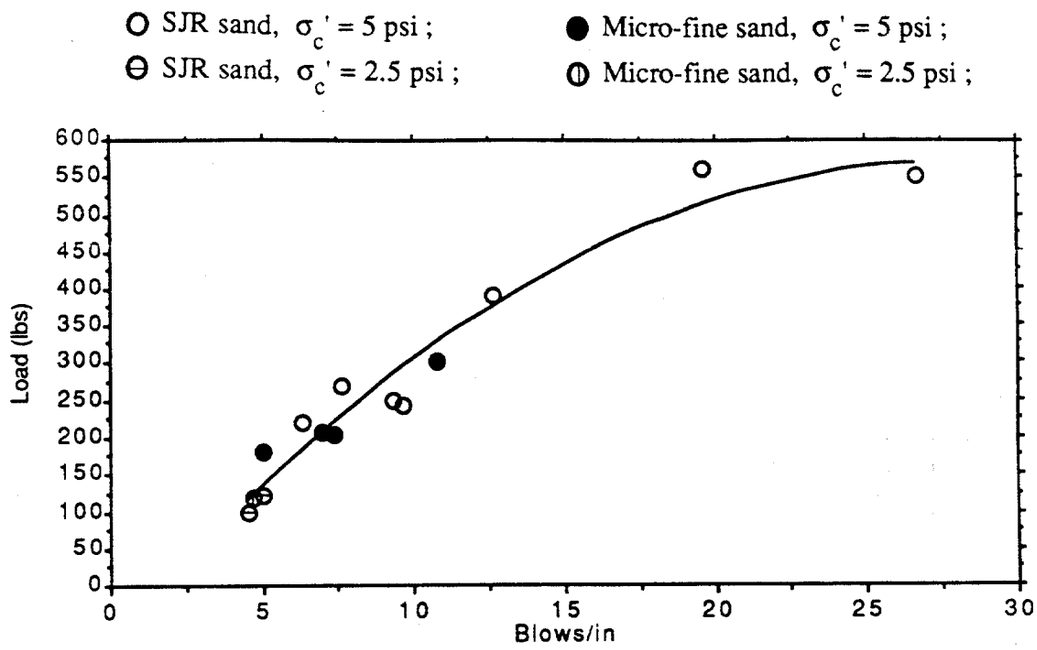

$$y = -74.007 + 45.934x - 0.819x^2$$

[y = load; x = bl / in., 27 b/ in. ≤ x ≤ 4 bl / in.]

Fig. 6.3. Penetration Resistance (Blows/in.) versus Static Capacity (lbs) for all Static Tests.

COMPARISON OF MEASURED AND TARGET SPECTRA

The actual vertical acceleration spectrum measured by means of a low-g accelerometer mounted underneath the chamber bottom plate in Test H2 is shown in Fig. 6.4. The resulting (measured) spectrum indicated a reasonable match between the target (scaled) spectrum and the applied motion below 3.5 Hz, but some loss of energy above 3.5 Hz, possibly due to the filtering caused by the limitation of the servo-hydraulic system of the Instron testing machine.

STATIC BEHAVIOR

Static Uplift Capacities

Graphical results of all static pull-out tests are shown in Figs. 6.5 - 6.9 in the following groupings:

(a) Tests at an effective chamber pressure of 5 psi and relative density of 55% (Fig. 6.5).

(b) Tests at an effective chamber pressure of 5 psi and relative density of 70% (Fig. 6.6).

(c) Test at an effective chamber pressure of 5 psi and relative density of 78% (Fig. 6.7).

(d) Test at an effective chamber pressure of 5 psi and relative density of 85% (Fig. 6.8).

(e) Tests at an effective chamber pressure of 2.5 psi and relative density of 55% (Fig. 6.9).

Several observations can be made from the load-movement results:

(a) The uplift load-movement response exhibited similar trends among tests of a given type (CD or CL).

(b) Controlled-Deformation (CD) tests produced higher capacities than those performed under Controlled-Load (CL) conditions.

(c) Similar behavior was observed for tests conducted with SJR sand and micro-fine sand. Slight differences in the ultimate static capacities can be attributed to variation in the blow count.

(d) The effect of the relative density on the static capacity is more pronounced at low relative densities than at high relative densities.

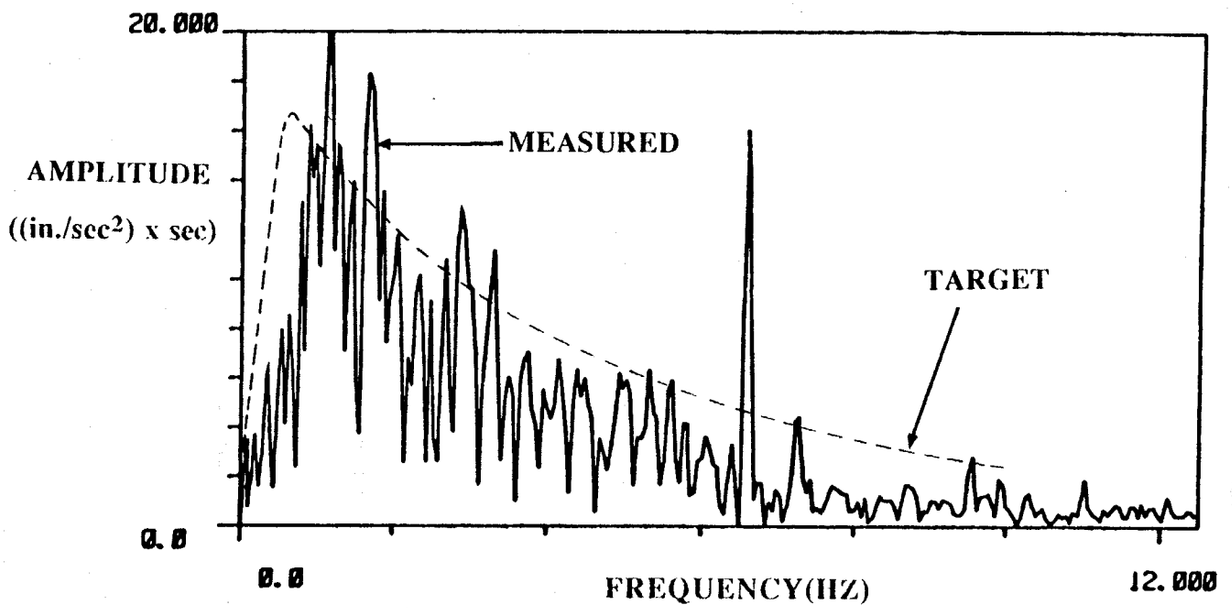

Fig. 6.4. Measured Spectrum versus Target Spectrum, Test H2.

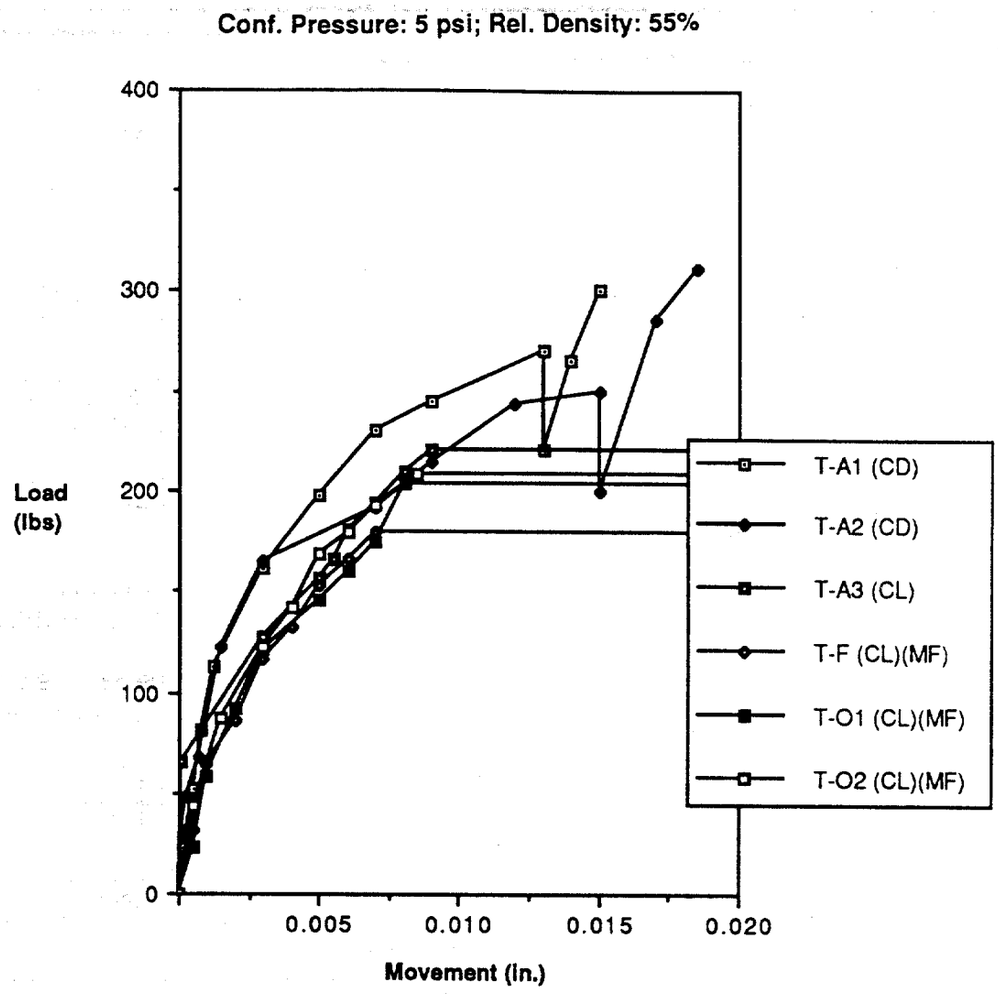

Fig. 6.5. Load-Movement Curves, Tests A1, A2, A3, F, O1 and O2.

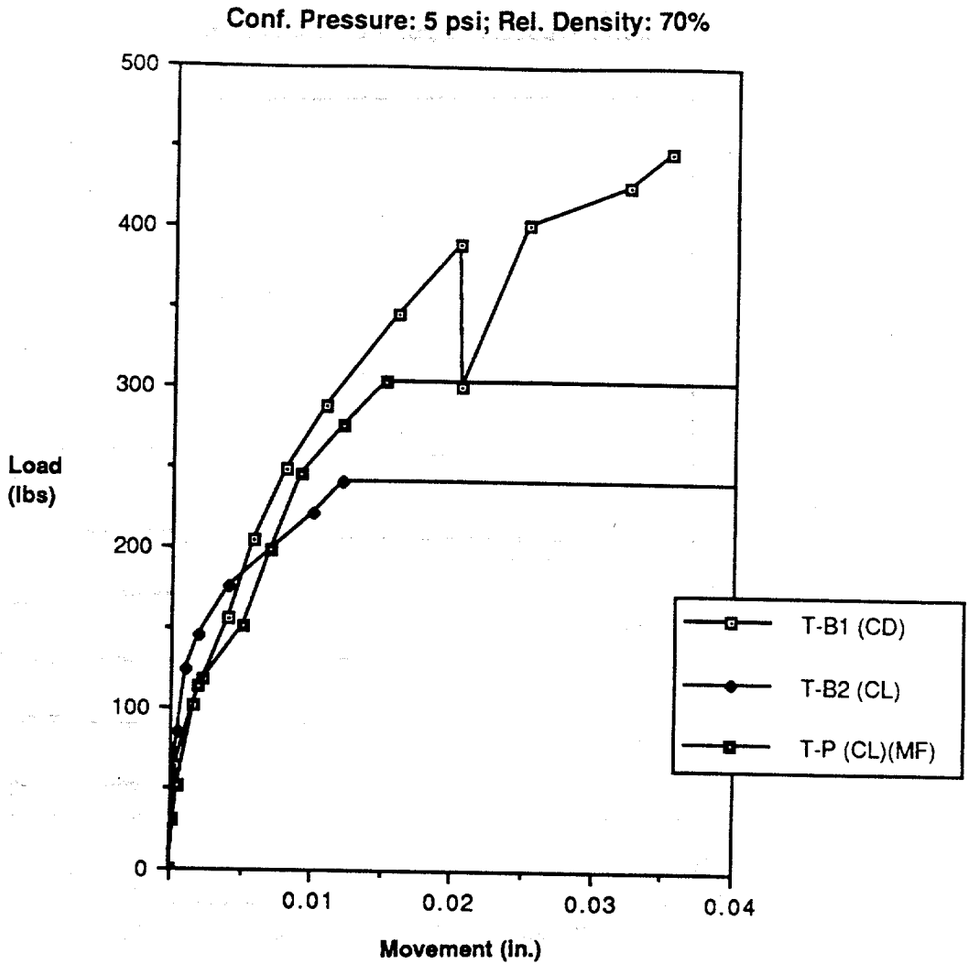

Fig. 6.6. Load-Movement Curves, Tests B1, B2 and P.

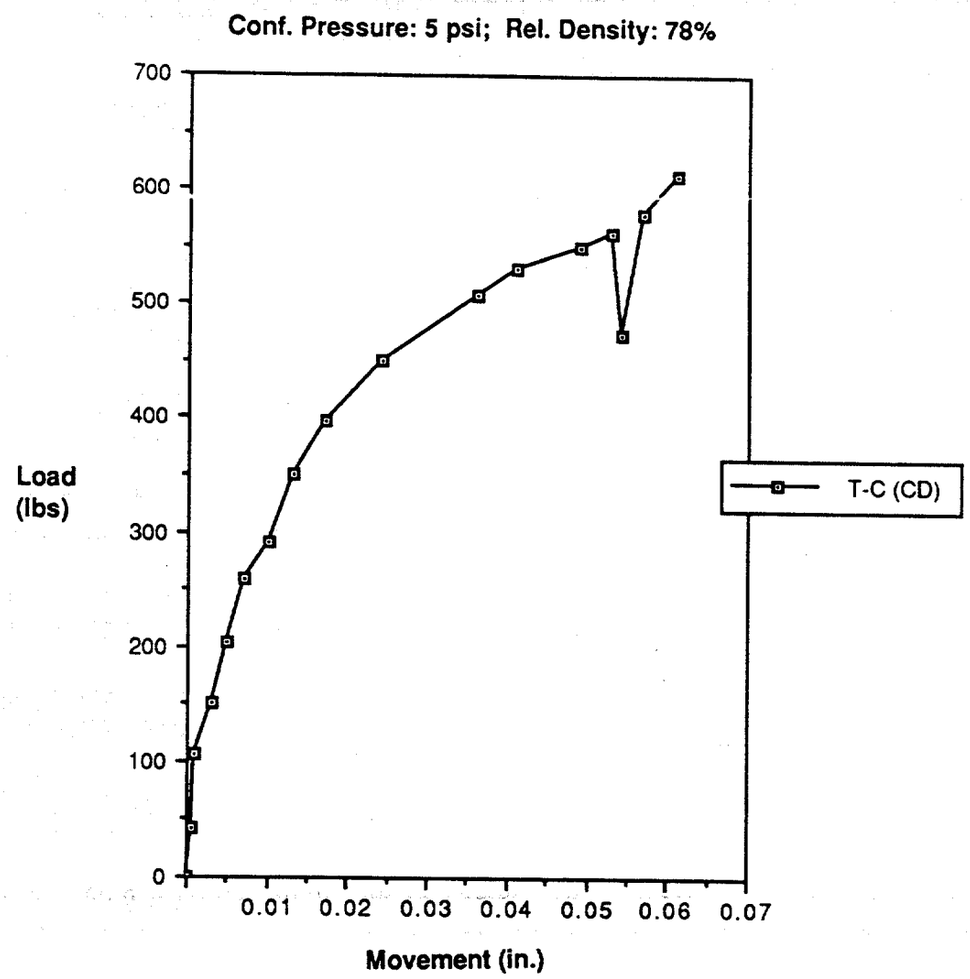

Fig. 6.7. Load-Movement Curve, Test C.

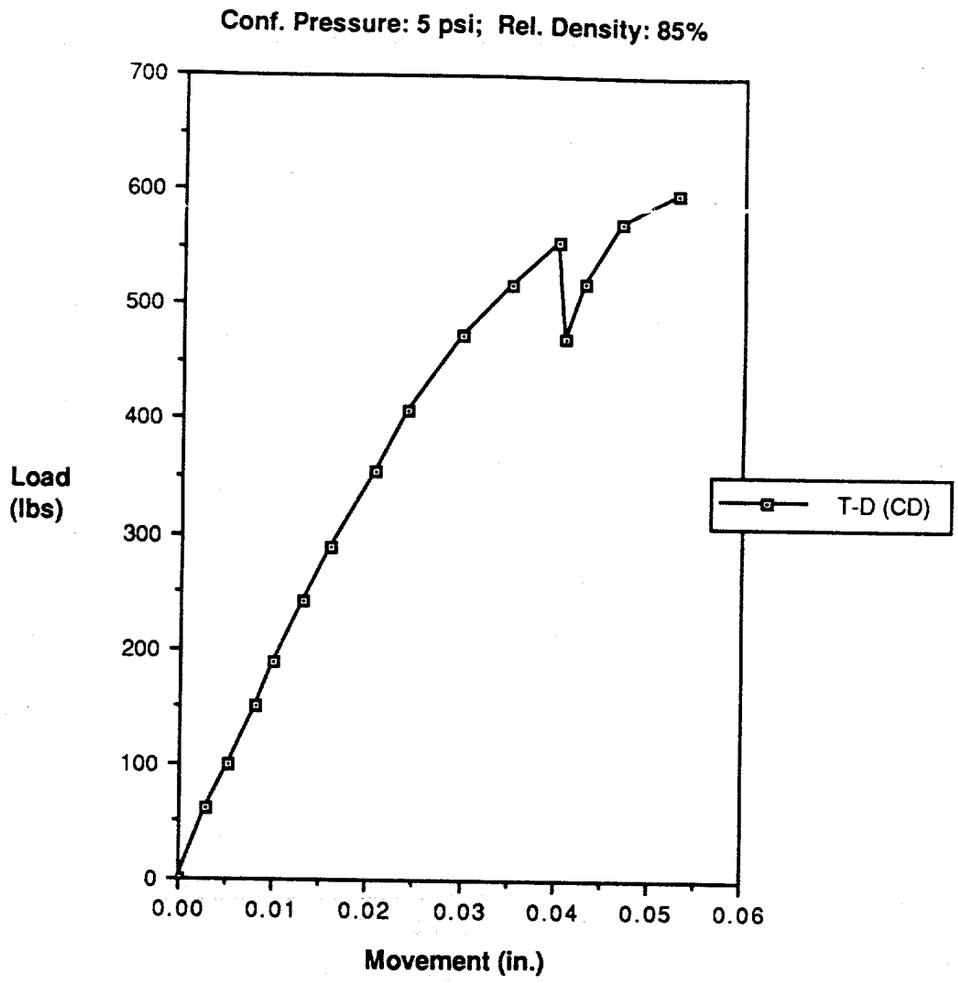

Fig. 6.8. Load-Movement Curve, Test D.

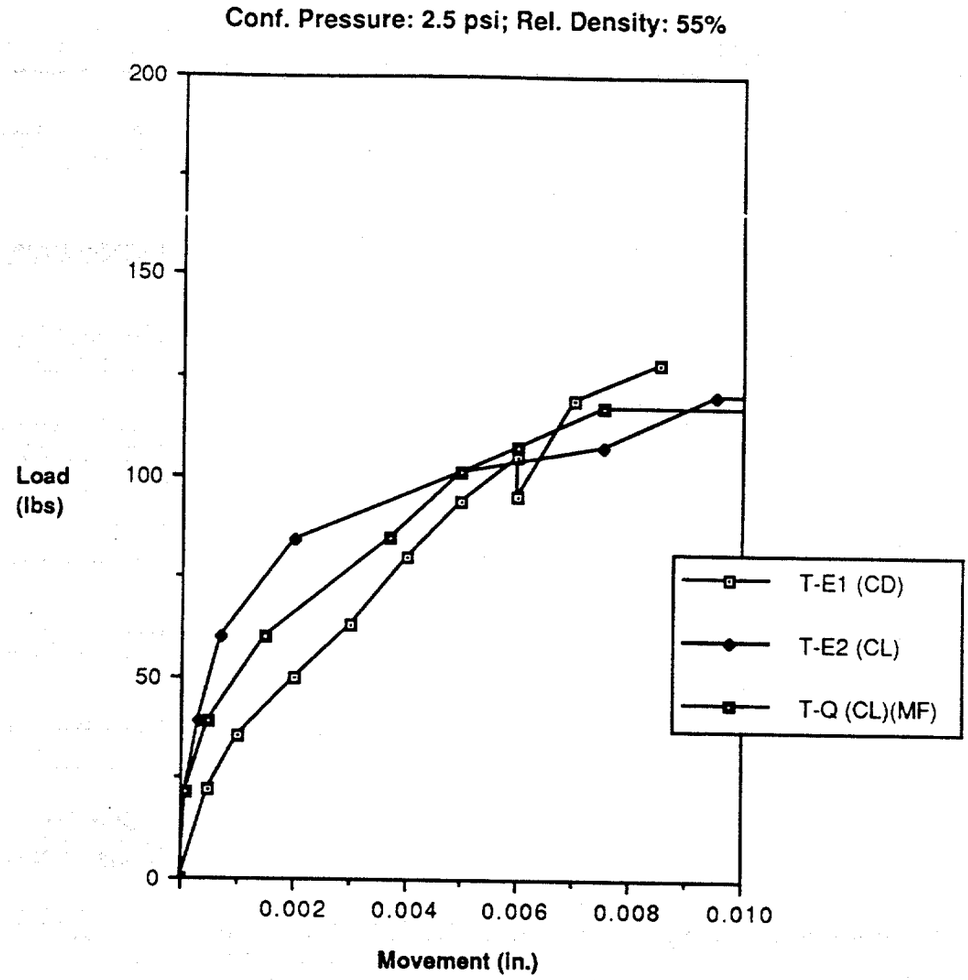

Fig. 6.9. Load-Movement Curve, Tests E1, E2 and Q.

(e) Higher relative densities produced higher static capacities.

Static Unit Load Transfer Characteristics

Experimentally derived relationships of static unit shaft shearing resistance (f) to local pile movement (w) for all static tests (A1-F, O1-Q) are presented graphically in this section. Such information is useful in visually interpreting the development of load transfer at the pile-soil interface, particularly in terms of the relative effects of the test parameters. Unit load transfer relationships can be used to synthesize the static axial behavior of piles of dimensions different from those employed in this study, provided the effective stresses in the system are equivalent to those in the chamber.

In order to develop the relationships of f to w, it was necessary first to determine the load distribution along the pile. This was accomplished for every static test by using the calibrated output of the three strain gages placed at the pile-head, mid-section and near-toe locations, respectively. Figs. E1 - E14 in Appendix E show the load distribution for static tests A1-F and O1-Q. In all tests except for Test C the inferred load at the toe was zero or very small at failure. In Test C, a controlled displacement (CD) test in dense sand (D_r = 78%), either some suction developed against the toe or extremely high side load transfer developed between the toe and lower level of strain gages. Considering the slow rate of movement in the CD tests (0.0033 in./sec), the latter explanation appears more plausible. In such plots negative values of load indicate tension, while positive values indicate compression. The weight of the pile is not explicitly included in the results since its effect was zeroed during the initial readings. Therefore, the strain gage readings represent the effect of external forces acting on the pile during the static load tests. It is emphasized that the measured loads are based on zero readings taken before the pile was driven, and the unit load transfer curves that were developed from these load distributions contain the effects of any residual stresses that were developed during the pile installation.

The f-w relations were developed for two sections (between gage points): top section (0 - 7 in. sand penetration) and bottom section (7 - 14 in.). Unit shaft load transfer, f, was computed from the following expression,

$$f = \frac{\Delta Q}{\pi dz} \quad , \qquad (6.1)$$

where

ΔQ = load difference in the pile between gage points,
d = pile diameter, and
z = length difference between gage points.

The value of w is the pile-head displacement for the corresponding applied load, measured by means of the LVDT mounted to the pile head. Pile elongation was negligible. This process was repeated for each load to develop sets of points defining the f-w relations. The unit shear transfer and the movements from these relations were then normalized by the effective horizontal chamber pressure, σ'_h, and the pile diameter, d, respectively. Figures 6.10 - 6.14 show the normalized f-w relationships for each of the static tests grouped according to the confining pressure and relative density, for both top and bottom sections.

Several observations from Figs. 6.10 - 6.14 can be made:

(a) Greater maximum values of unit shaft resistance occurred in the lower half of the pile (depths greater than seven diameters).

(b) Average ultimate f values divided by the mean effective chamber pressure for all load tests from Figs. 6.10 - 6.14 were as follows:

Top Half of the Pile	0.59
Bottom Half of the Pile	1.74

These data suggest that a surface effect existed during uplift loading, whereby the flexible, pressurized surface of the sand within the chamber permitted development of shear planes at an angle to the interface, which possessed a lower shear strength than the interface plane, and which, therefore, permitted failure to occur at a lower interface shearing stress.

(c) The ultimate value of f was, on the average, for all tests on SJR sand, 102% of the lateral effective chamber pressure for D_r = 55%. Since the angle of the interface shear was, approximately, 27° (Fig. 4.5), it can be demonstrated that the insertion of the pile into the chamber produced an increase in the horizontal effective stress in the chamber at the pile-soil interface. Assuming that $f_{max} = \sigma'_h \tan \delta$, where σ'_h = horizontal effective stress at the pile-soil interface, and δ = angle of interface shear (27°), the average horizontal effective stress at the pile-soil interface can be computed to be 1.02 / tan 27° = 2.0 times the simulated horizontal in-situ (lateral effective chamber) pressure for D_r = 55%. The inertia of the pile, therefore, must have increased the effective stress in the soil immediately

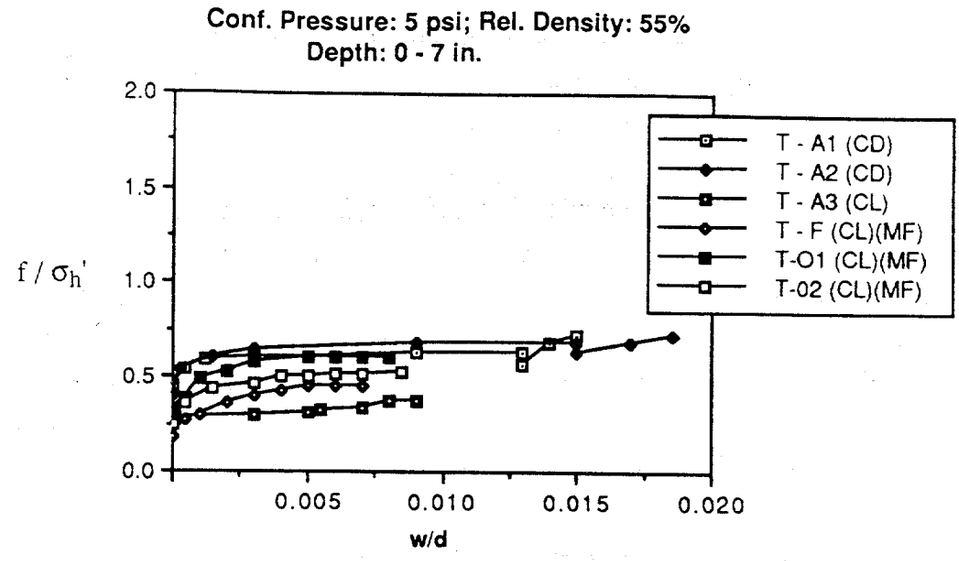

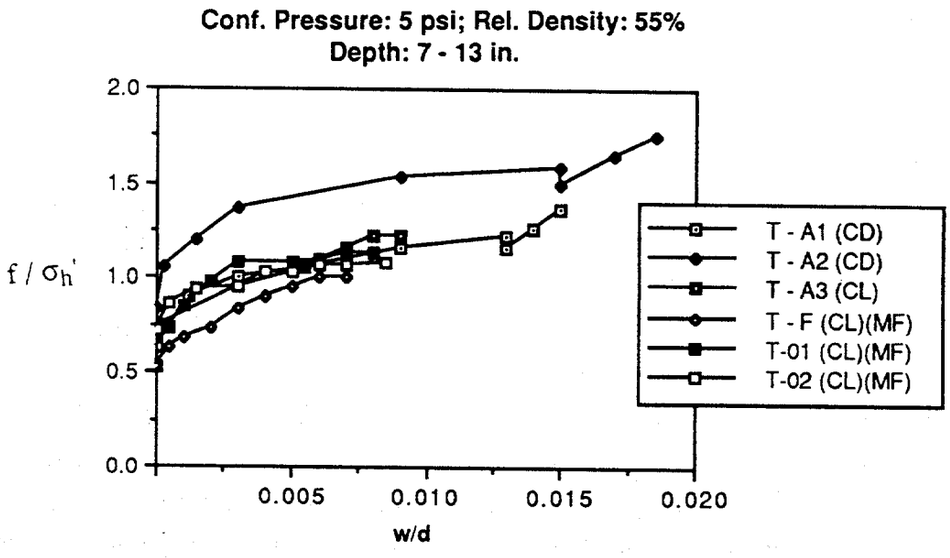

Fig. 6.10. Relationships of f versus w, Tests A1, A2, A3, F, O1, O2.

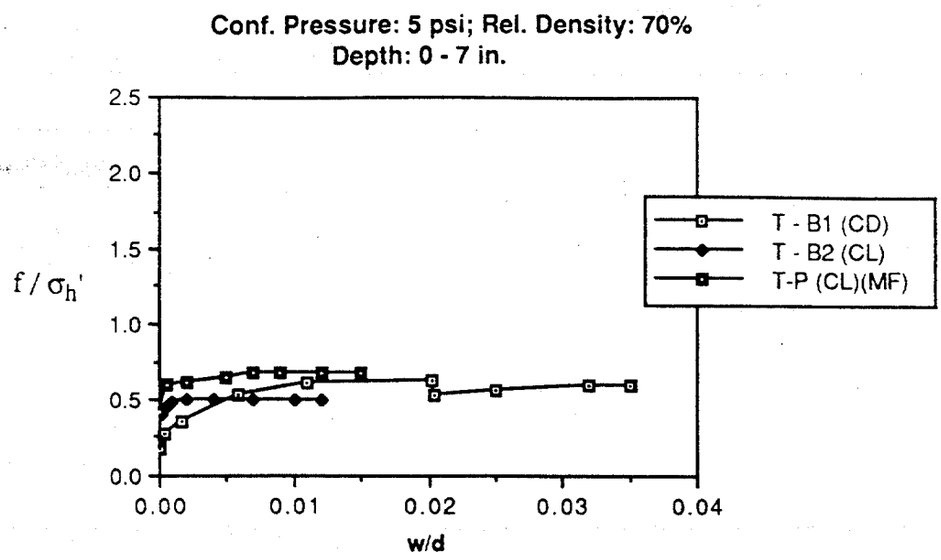

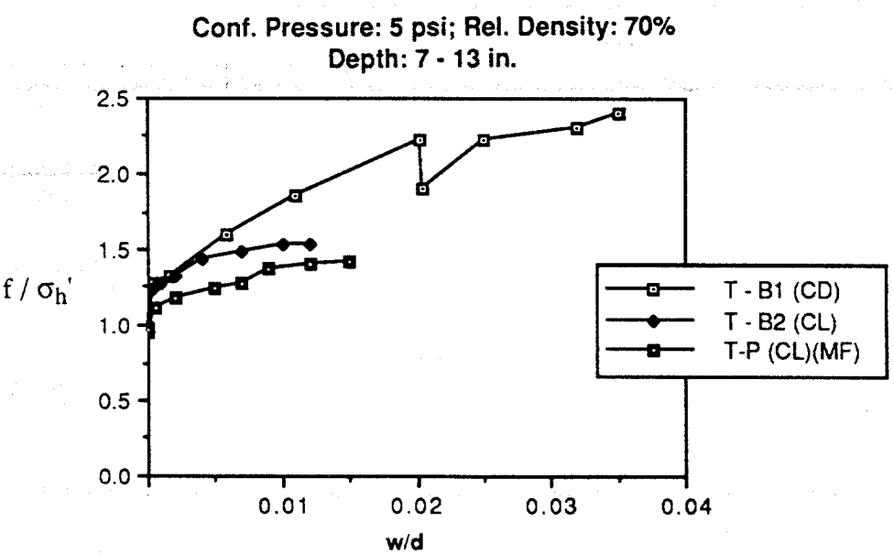

Fig. 6.11. Relationships of f versus w, Tests B1, B2, P.

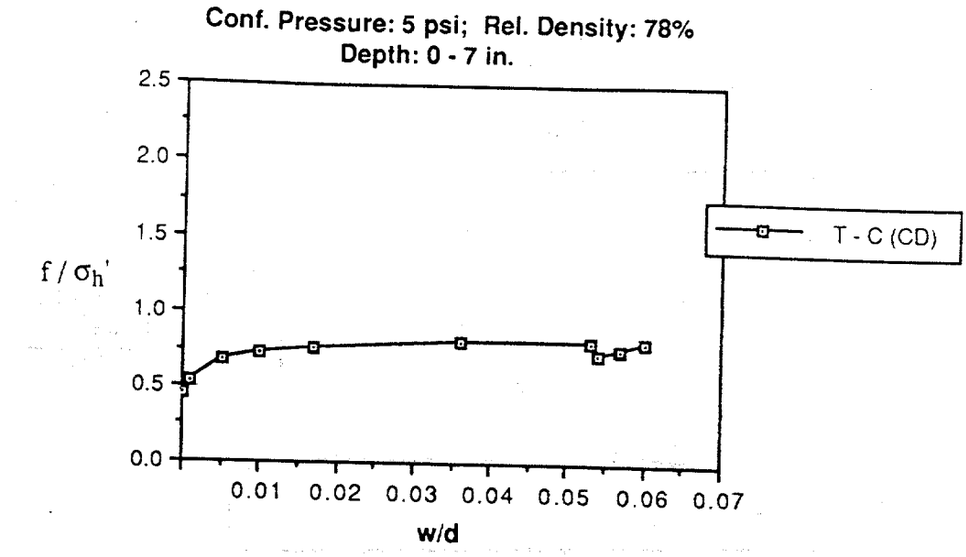

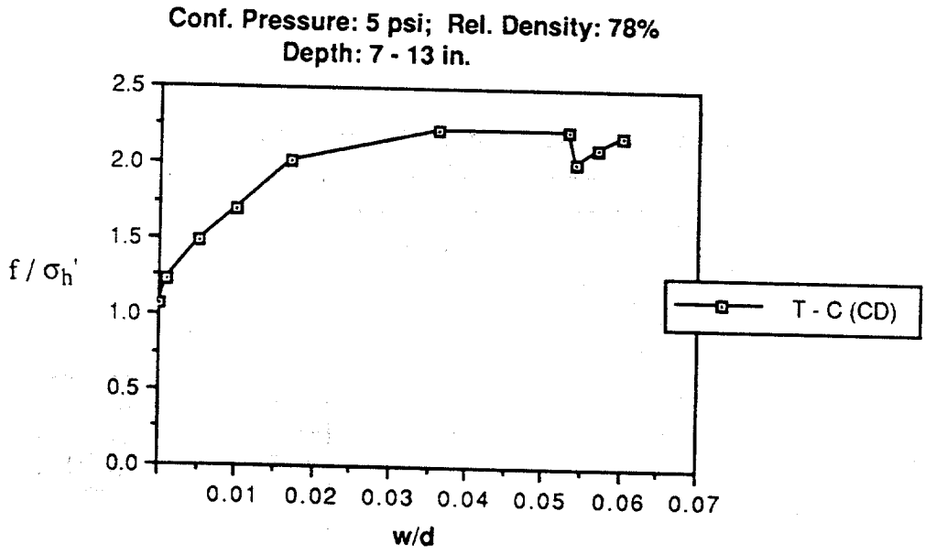

Fig. 6.12. Relationships of f versus w, Test C.

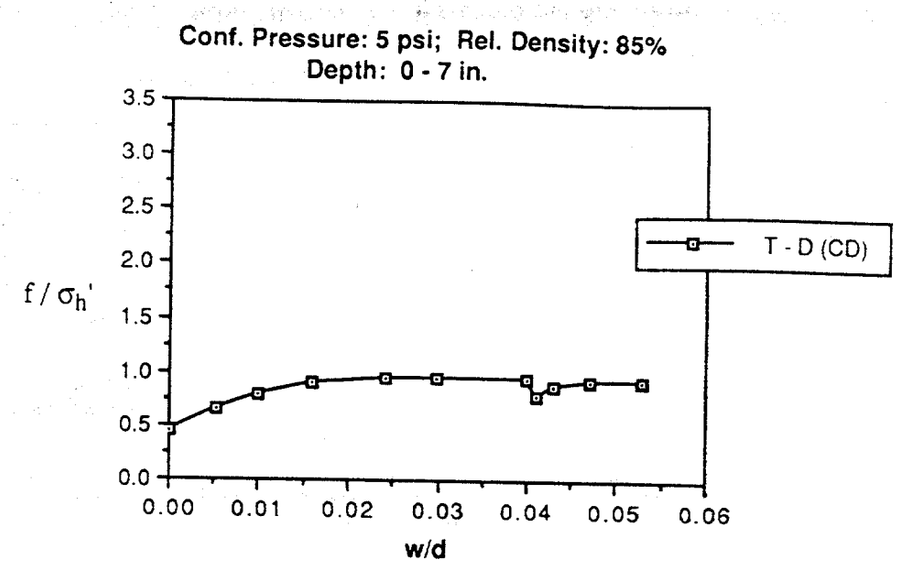

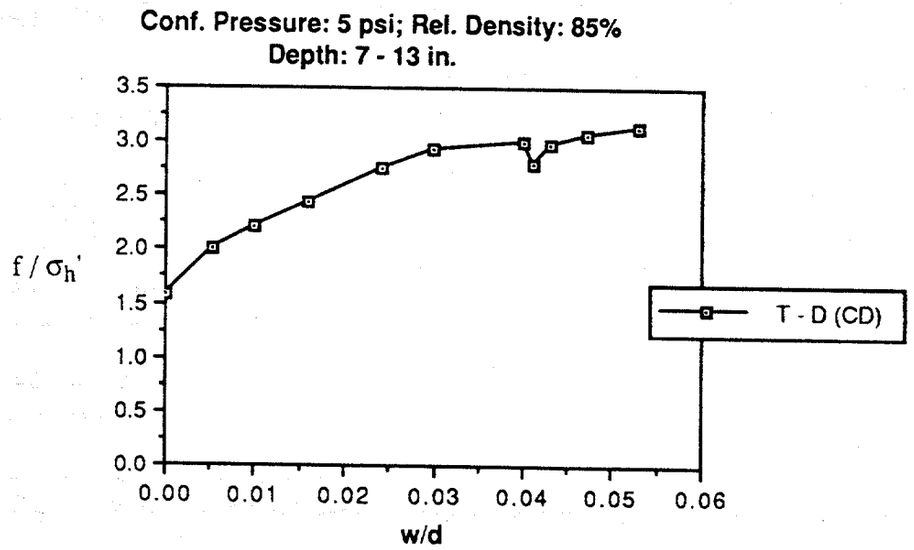

Fig. 6.13. Relationships of f versus w, Test D.

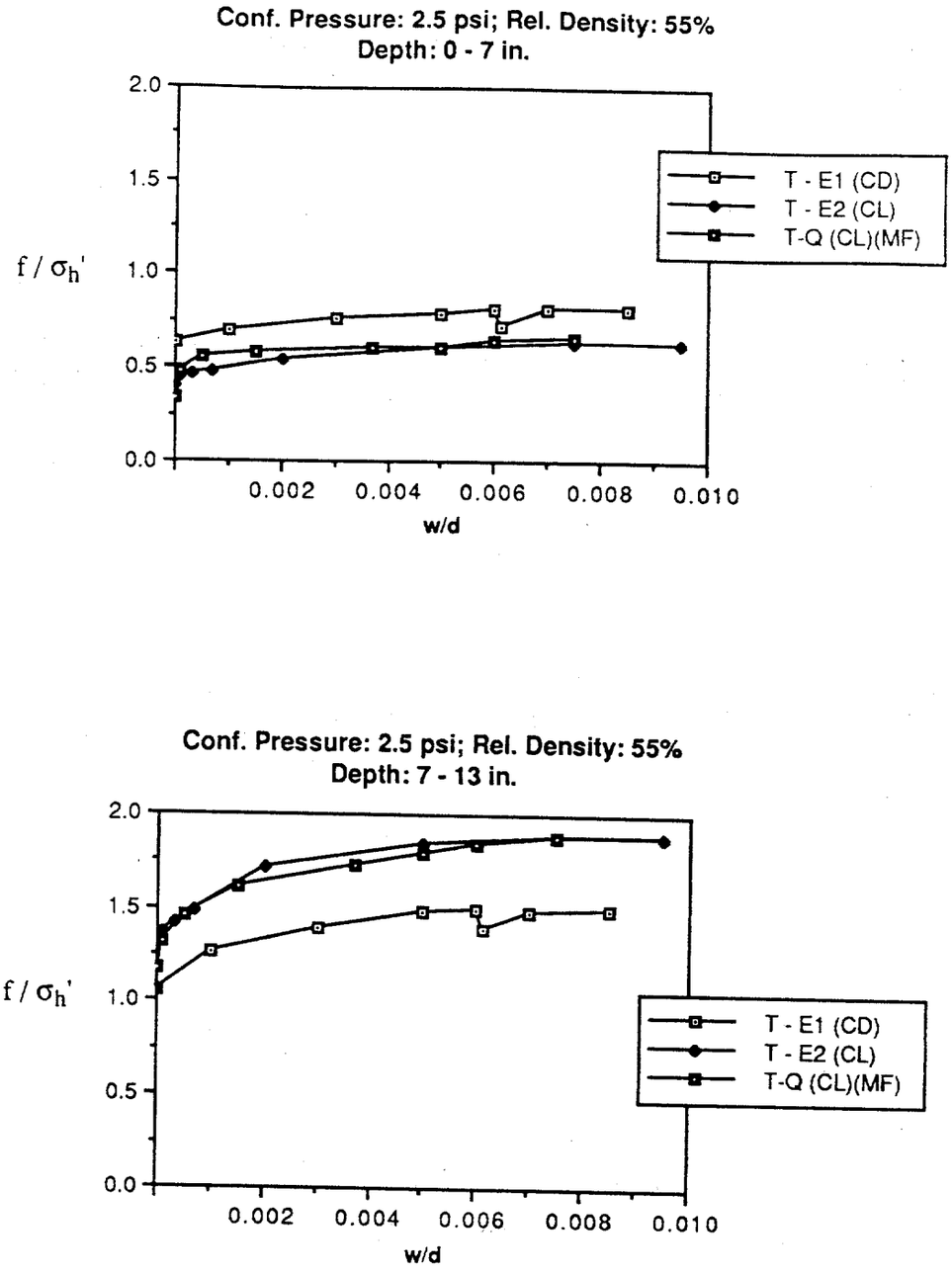

Fig. 6.14. Relationships of f versus w, Tests E1, E2, Q.

surrounding the pile, as is predicted by expanding cavity models [e.g., Vesic (1972)], which may have served to resist liquefaction. The potential effect of the insertion of the pile in the sand to resist liquefaction may be similar to the influence of the superstructure mat on reducing liquefaction potential [Yoshimi and Tokimatzu (1977); Rollins and Seed (1990)].

(d) On average, the ultimate values of f were developed at local displacements of 1% of the pile diameter.

(e) Much of the unit side load transfer (typically 40 - 60%) was already developed in the form of residual stresses before the pile was subjected to uplift loading.

(f) Minor increases in values of ultimate shearing resistance (f) in tests in which the pile was driven off center (Tests O1 - Q) indicated negligible boundary effects (due to chamber wall and inner cylinder) on the pile response.

PILE AND SOIL RESPONSE DURING THE SIMULATED SEISMIC EVENT

Time history measurements of (1) load on the pile at the strain gage locations, (2) generation of pore water pressures (near field and far field), and (3) pile head movement during the simulated seismic event were taken for all dynamic tests (G-N2). Data for representative tests, H1, I2 and K, are shown in Figs. 6.15 - 6.25. Data from other dynamic tests (vertical motion) are presented in Appendix F (F.1 - F.32). Test H1 represents the condition in which the pile capacity was not influenced by the vertical excitation of the seismic event (sustained load on the pile with minimum or no pile movement, or stability condition). Test I2 represents the case where the pile was failed (pulled out) during the seismic event (dropping of load with excessive pile movement), mainly due to the bias load-spring-pile dynamic interaction. Test K can be considered as mobility condition, characterized by sustained pile capacity during the seismic event but with associated substantial pile movement. Particular descriptions of Tests H1, I2 and K follows.

(a) **Test H1**:

(1) Time history of load measurements in the pile during the seismic event at three locations, the pile head, at a depth of 7 in., and 1.0 in. above the pile toe, are shown in Fig. 6.15.

(2) Time history of pore water pressure measurements during the seismic event in two locations, 1.0 in. from the pile wall (near field) and 5.0 in. from pile wall (far field), are shown in Fig. 6.16. It can be seen that no buildup of pore water pressure took place during the seismic that might have produced loss of pile capacity for the applied bias load.

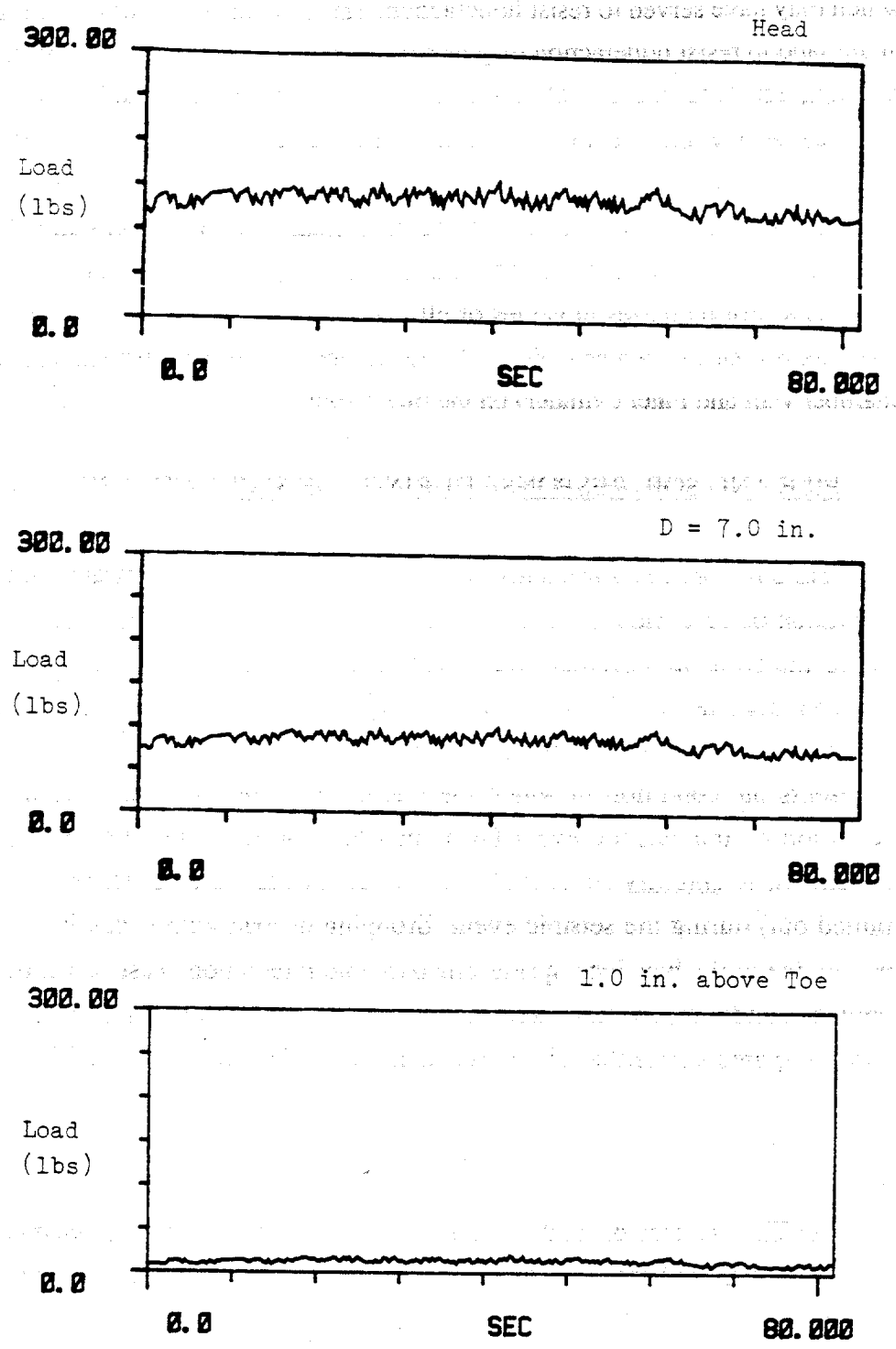

Fig. 6.15. Time History Measurements of Dynamic Load on Pile, Test H1.

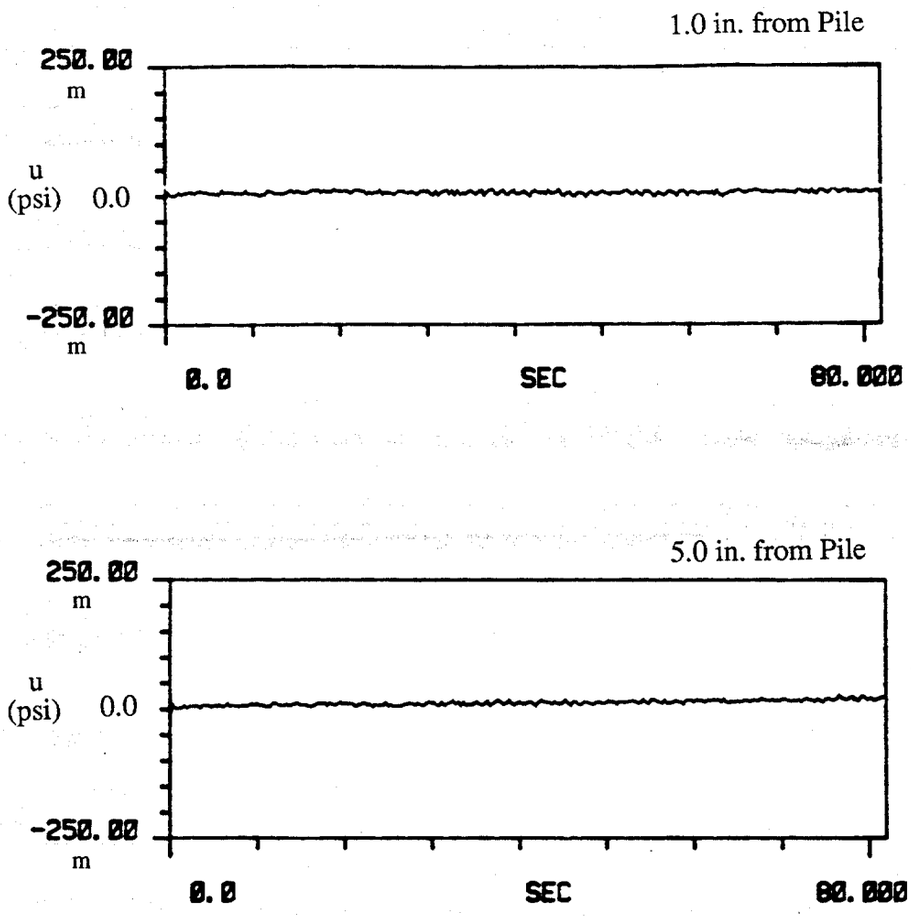

Fig. 6.16. Time History Measurements of Near and Far Field Pore Water Pressures, Test H1, [m = milli].

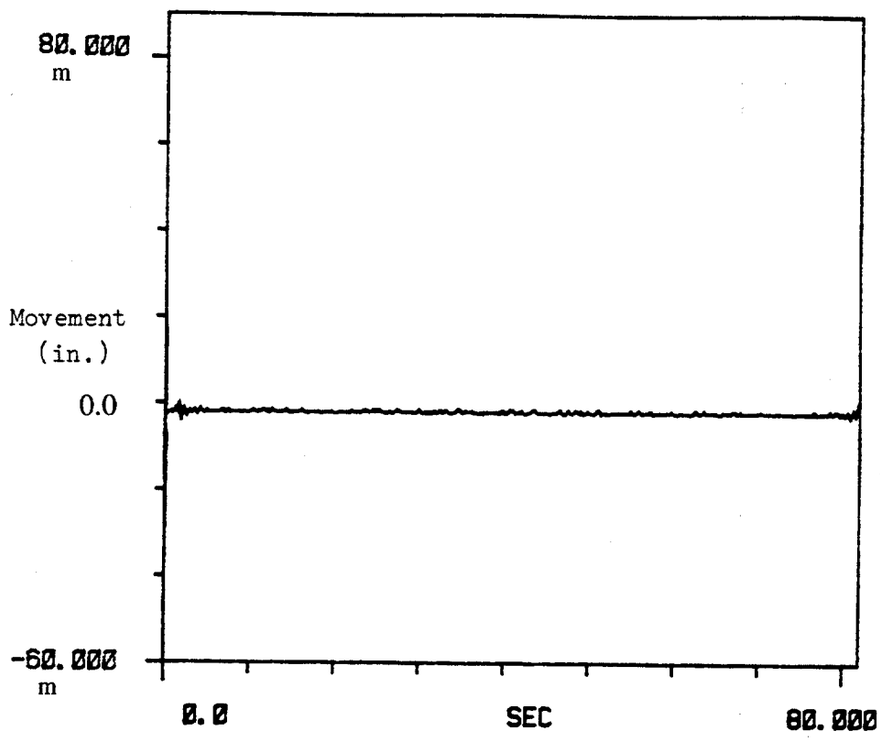

Fig. 6.17. Time History Measurements of Pile Head Movement, Test H1, [m = milli].

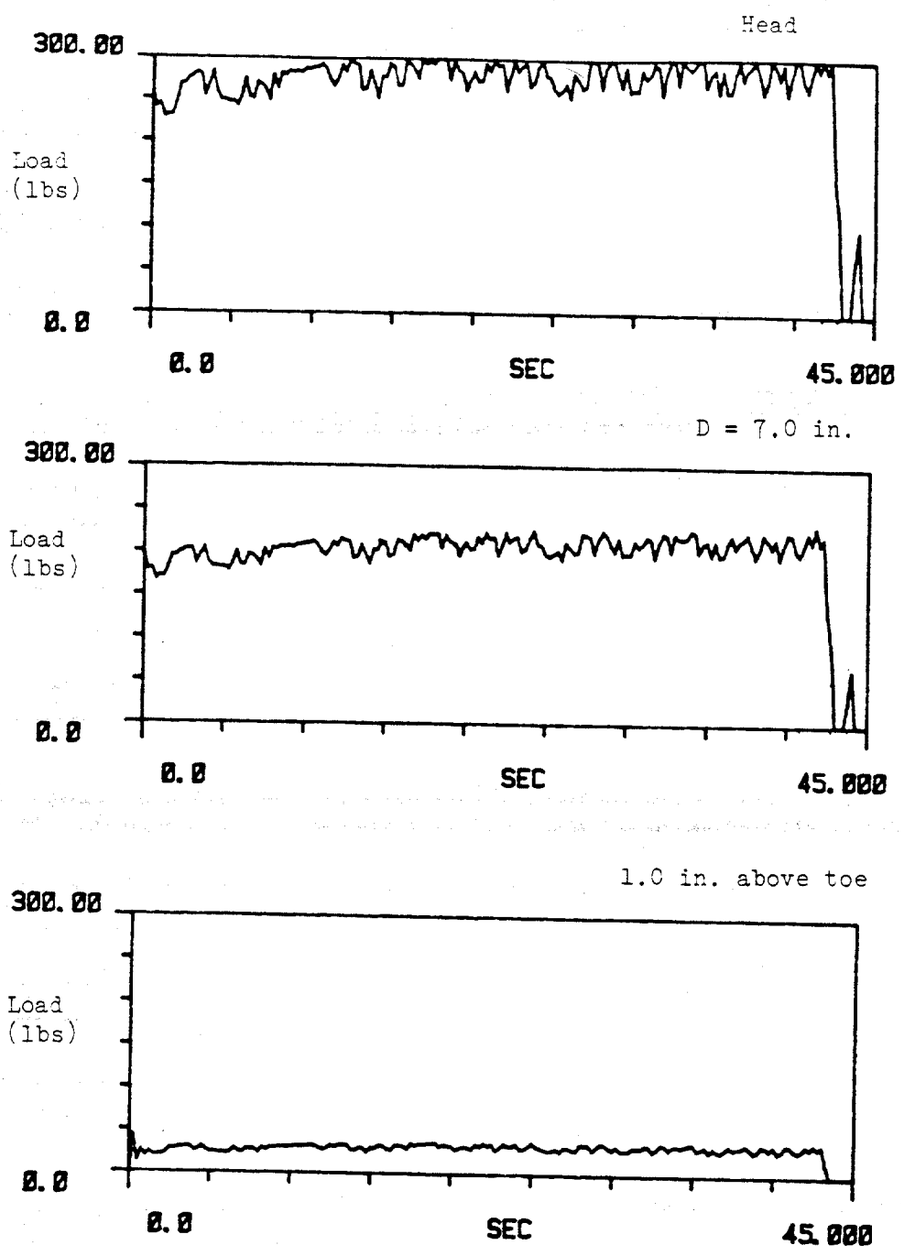

Fig. 6.18. Time History Measurements of Dynamic Load on Pile, Test I2.

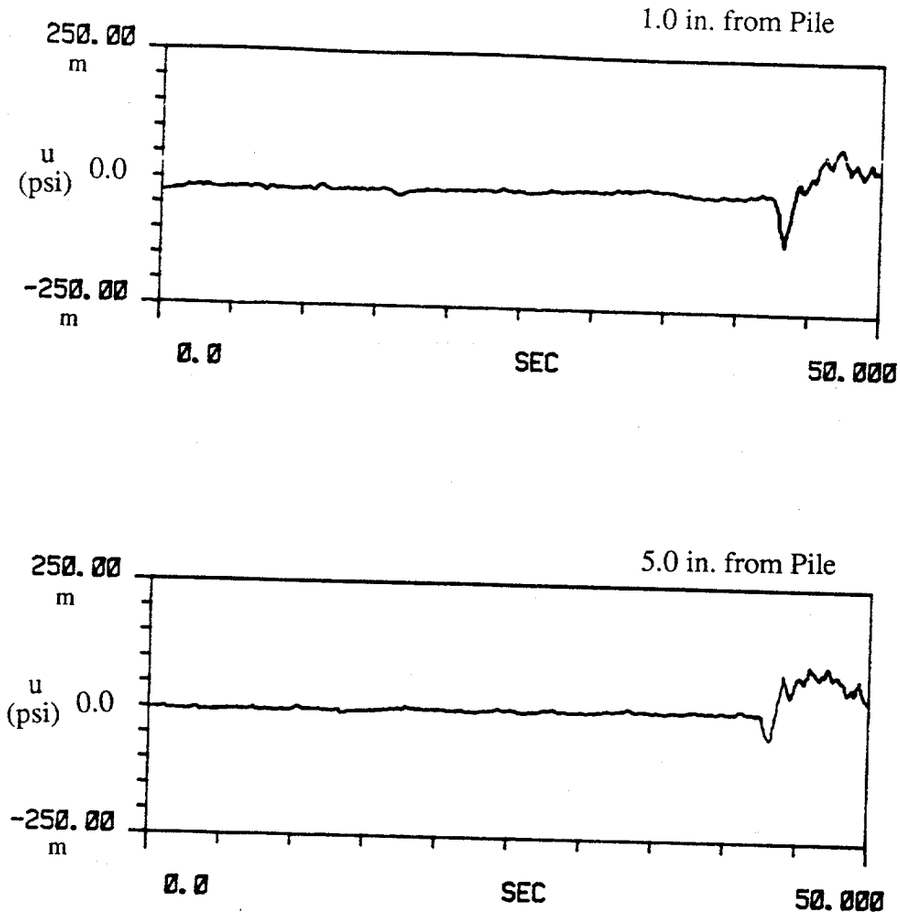

Fig. 6.19. Time History Measurements of Near and Far Field Pore Water Pressures, Test I2, [m = milli].

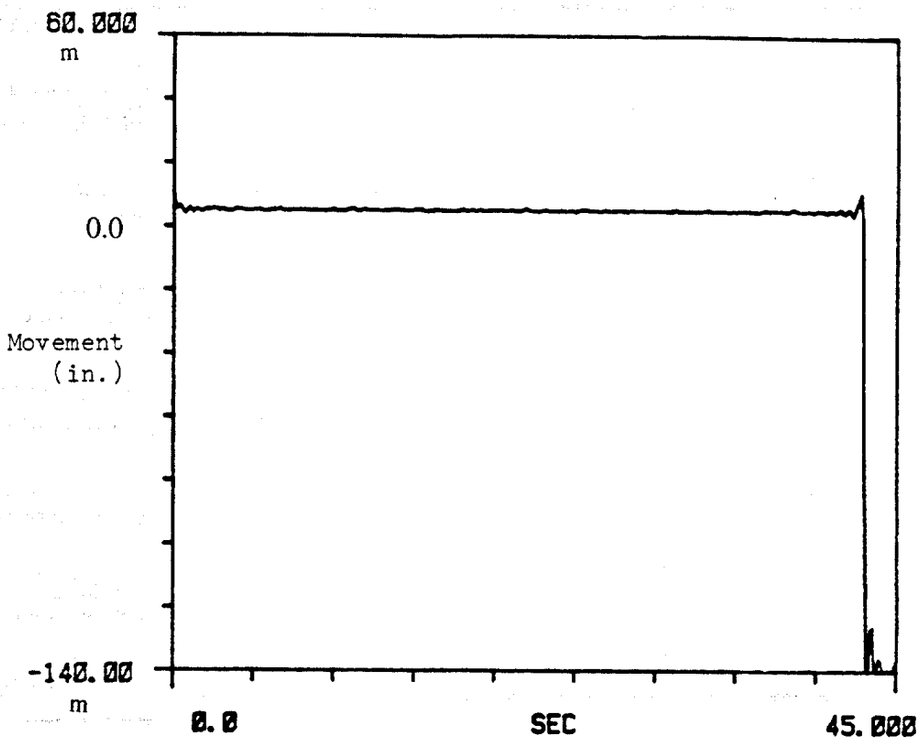

Fig. 6.20. Time History Measurements of Pile Head Movement, Test I2, [m = milli].

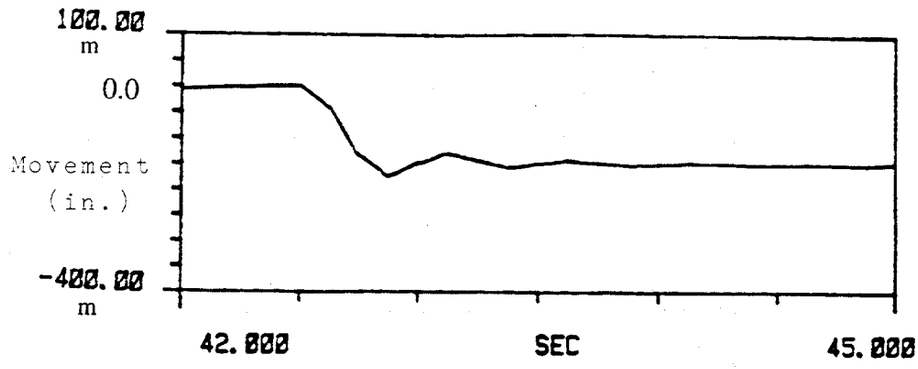

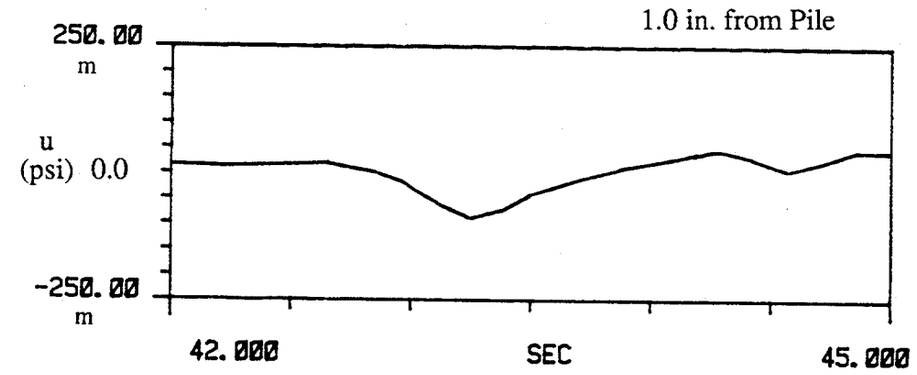

Fig. 6.21. Time History Measurements of Pile Head Movement and Near Field Pore Water Pressure, Test I2, [m = milli].

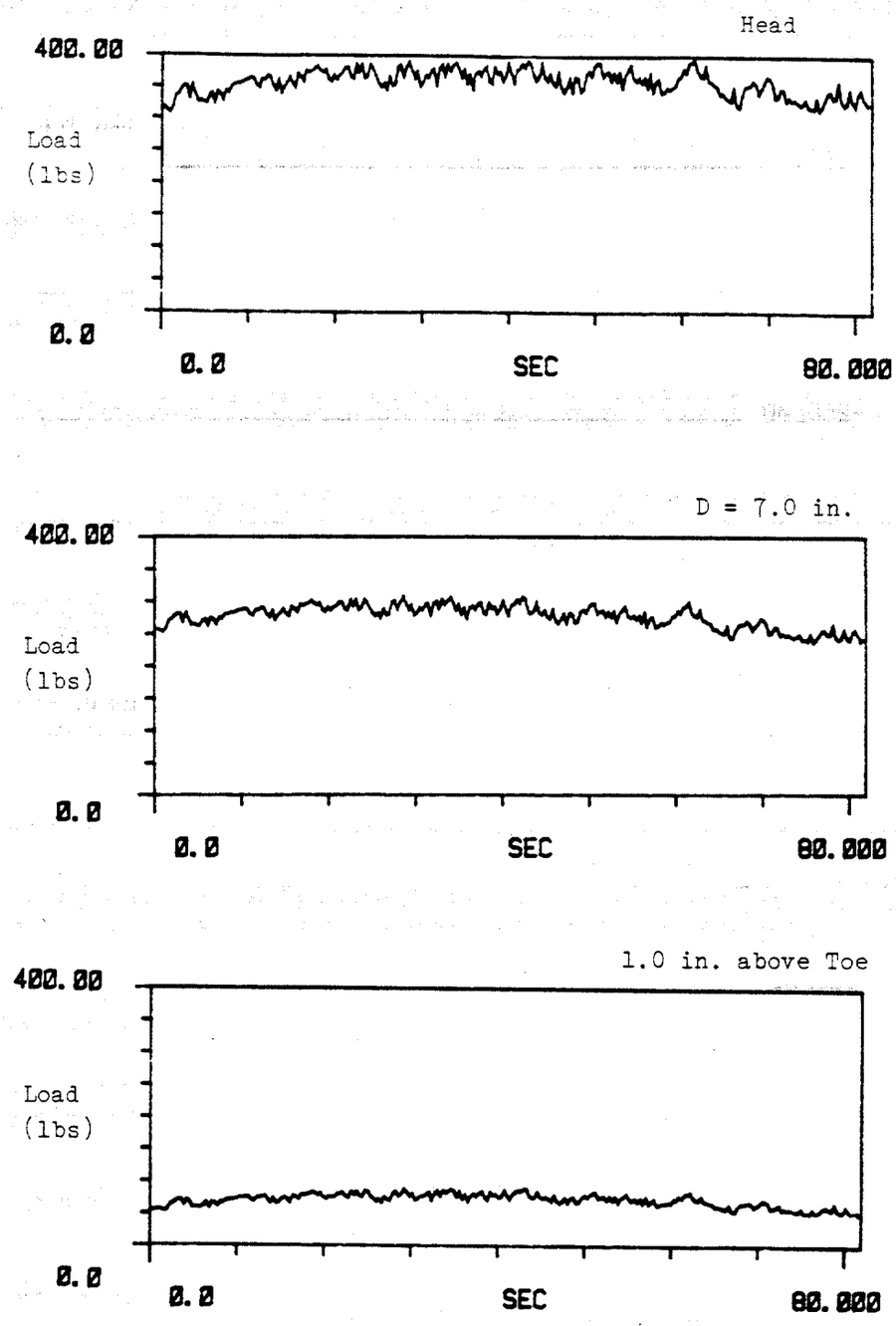

Fig. 6.22. Time History Measurements of Dynamic Load on Pile, Test K.

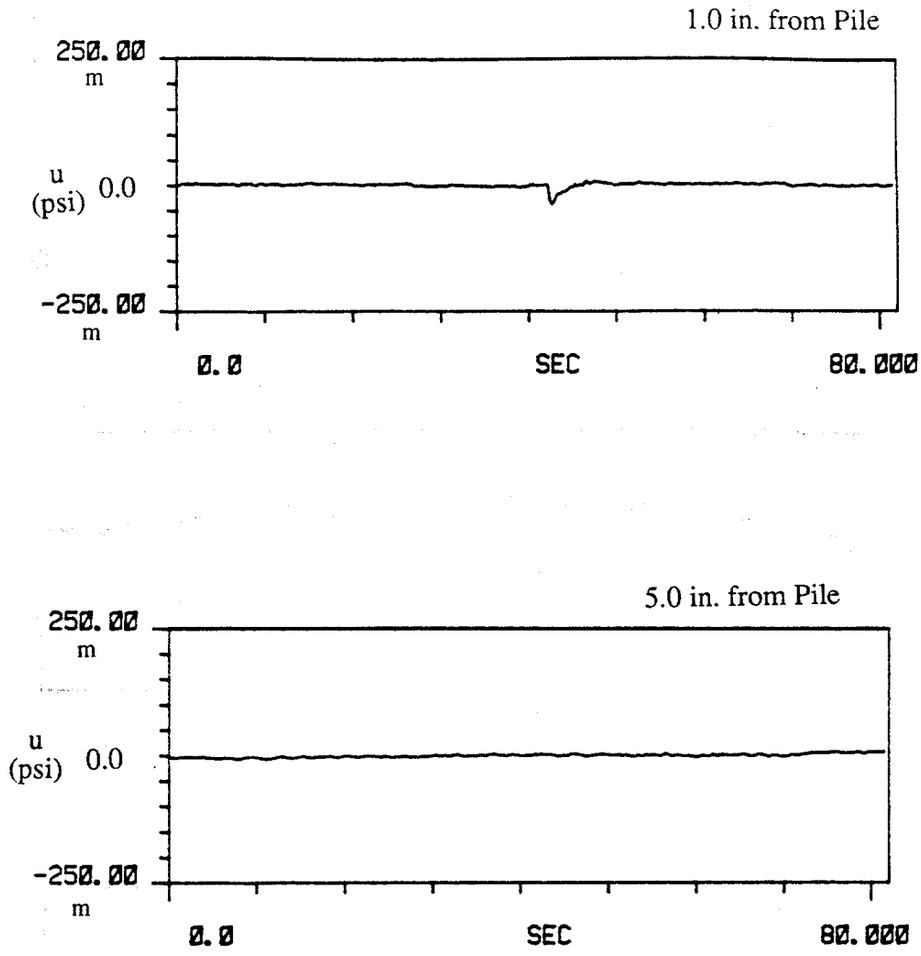

Fig. 6.23. Time History Measurements of Near and Far Field Pore Water Pressures, Test K, [m = milli].

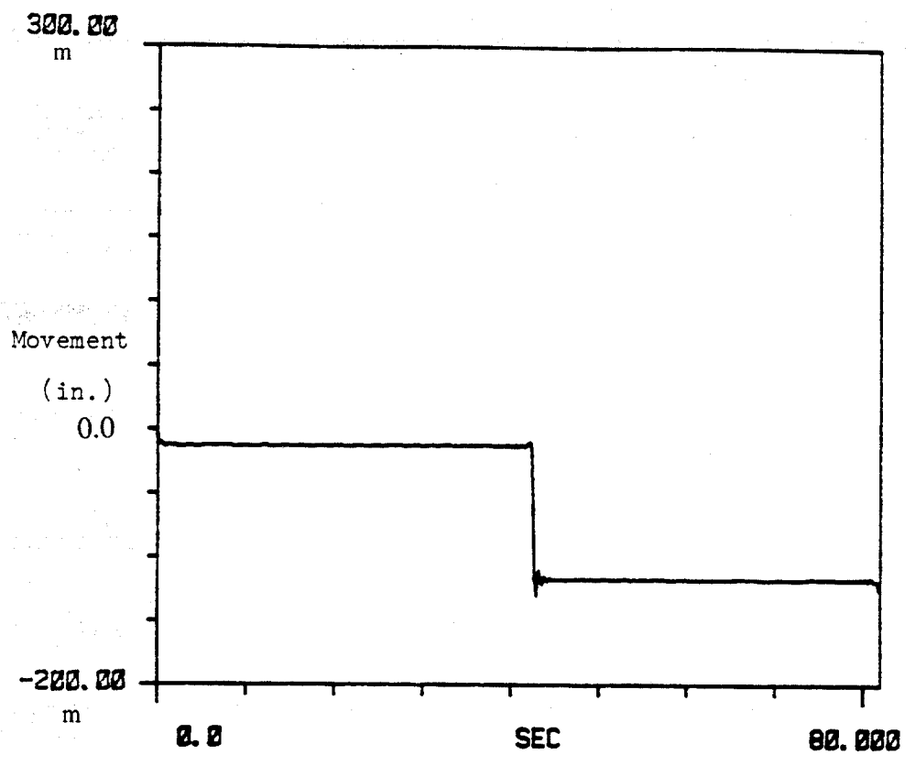

Fig. 6.24. Time History Measurements of Pile Head Movement, Test K, [m = milli].

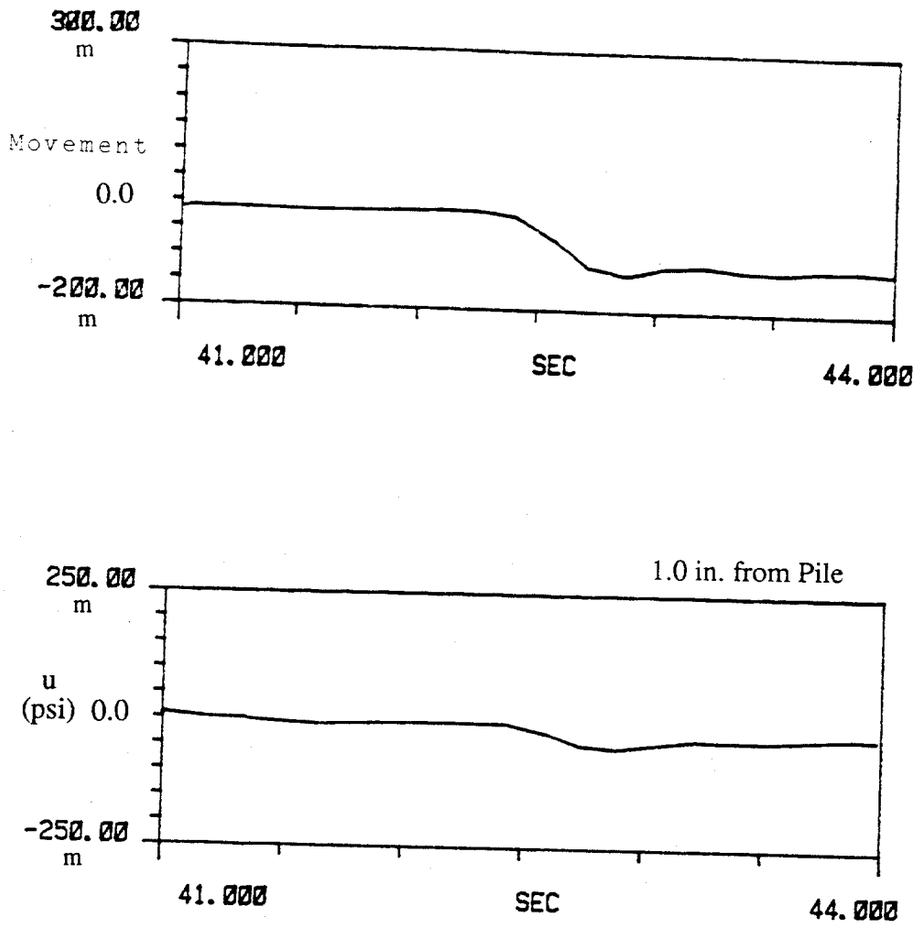

Fig. 6.25. Time History Measurements of Pile Head Movement and Near Field Pore Water Pressure, Test K, [m = milli].

(3) Time history of measurement of pile head movement is shown in Fig. 6.17. No appreciable movement is observed.

(b) **Test I2:**

(1) Time history measurements of load at the pile head, pile mid-section and near-toe location during the vertical seismic motion are depicted in Fig. 6.18.

(2) Time history of pore water pressure generation for near and far fields are shown in Fig. 6.19.

(3) The pile head movement - time record is shown in Fig. 6.20.

(4) The time window records (between 42 and 45 sec. of simulated event) of near-field pore water pressure and pile head movement are shown in Fig. 6.21, for comparison purposes.

Some comments can be made regarding Test I2. First, failure took place 42.5 sec. after the start of the simulated seismic event, corresponding to the first severe ground displacement peak (Fig. 5.13) and the one in a train of points of peak force at the pile head (Fig. 6.18). Second, failure occurred without the prior buildup of excess pore water pressure or generation of major side shear redistribution. Third, negative pore water pressure (suction) was triggered by the pile while being pulled out, with a small time lag between the initial pile movement and the rise point of negative pore water pressure (Fig. 6.21). This behavior is consistent with an earlier study in the centrifuge [Lambson (1988)] of small scale piles embedded in clay and subjected to tensile cyclic loading that also exhibited similar trends in pile displacement and generation of negative pore water pressure. Generation of pore water pressures and/or soil liquefaction due to the vertical seismic motion did not occur, which confirms that the estimated maximum shearing strains developed in the soil induced by the vertical seismic excitation were well below the threshold required to produce liquefaction (Chapter III). Fourth, failure appears to have occurred when the bias load (90% of inferred static capacity) plus the dynamic head load produced by the interaction of the vibrating pile and the sprig-mass system became approximately equal to the static capacity of the pile. This behavior was typical in purely vertical shaking tests in which failure occurred.

(c) **Test K:**

Time history measurements of (1) load on the pile at three different levels, (2) pore water pressures in the soil mass, and (3) pile head movement are given in Figs. 6.22 - 6.24. Time window records of pile-head movement and near-field induced pore water

pressure are shown in Fig. 6.25. Similar trends to those in Test I2 were obtained, except that the pile did not lose its capacity during the seismic motion. Slight battering of the pile and, therefore, additional passive pressures acting on the pile, may have prevented the pile from being pulled out, even though some initial movement associated and negative pore water pressure were monitored.

POST-SHAKING STATIC CAPACITIES AFTER SIMULATED SEISMIC EVENT

Load-movement curves plotted in the same sequence as occurred during testing (i.e., first, application of bias load, then shaking test, and last, application of post-shaking load to failure, if applicable) are shown for representative tests in Figs. 6.26 - 6.29. These curves have been grouped based upon the blow count, a parameter that indirectly relates the soil grain characteristics, confining pressure and relative density to the pile's static capacity, for tests in which the pile was driven centered in the test chamber. The load-movement curves are shown in the following groupings:

(a) Tests on SJR sand averaging 6.5 b/in. (Fig. 6.26),
(b) Tests on micro-fine sand averaging 5.6 b/in. (Fig. 6.27),
(c) Tests on SJR sand averaging 4.5 b/in. (Fig. 6.28), and
(d) Tests on both sands averaging 6.0 b/in. (Fig. 6.29).

Several observations can be made from the load-movement curves (Figs. 6.26 - 6.29) and post-shaking static capacities listed in Table 6.2:

(a) Post-shaking static capacities (from dynamic tests) were, in general, near the ultimate static capacities (static tests), indicating no significant loss of soil capacity during the simulated seismic event.

(b) A greater interaction in the bias load-spring-pile system can be observed on Fig. 6.26 for test using the original time record (predominant frequencies: 1.0 - 2.0 Hz) than the test using scaled time record (predominant frequencies: 6 - 10 Hz).

(c) For similar conditions (confining pressure, relative density, and blow count), post-shaking static capacities in micro-fine sand were slightly lower than those in SJR sand.

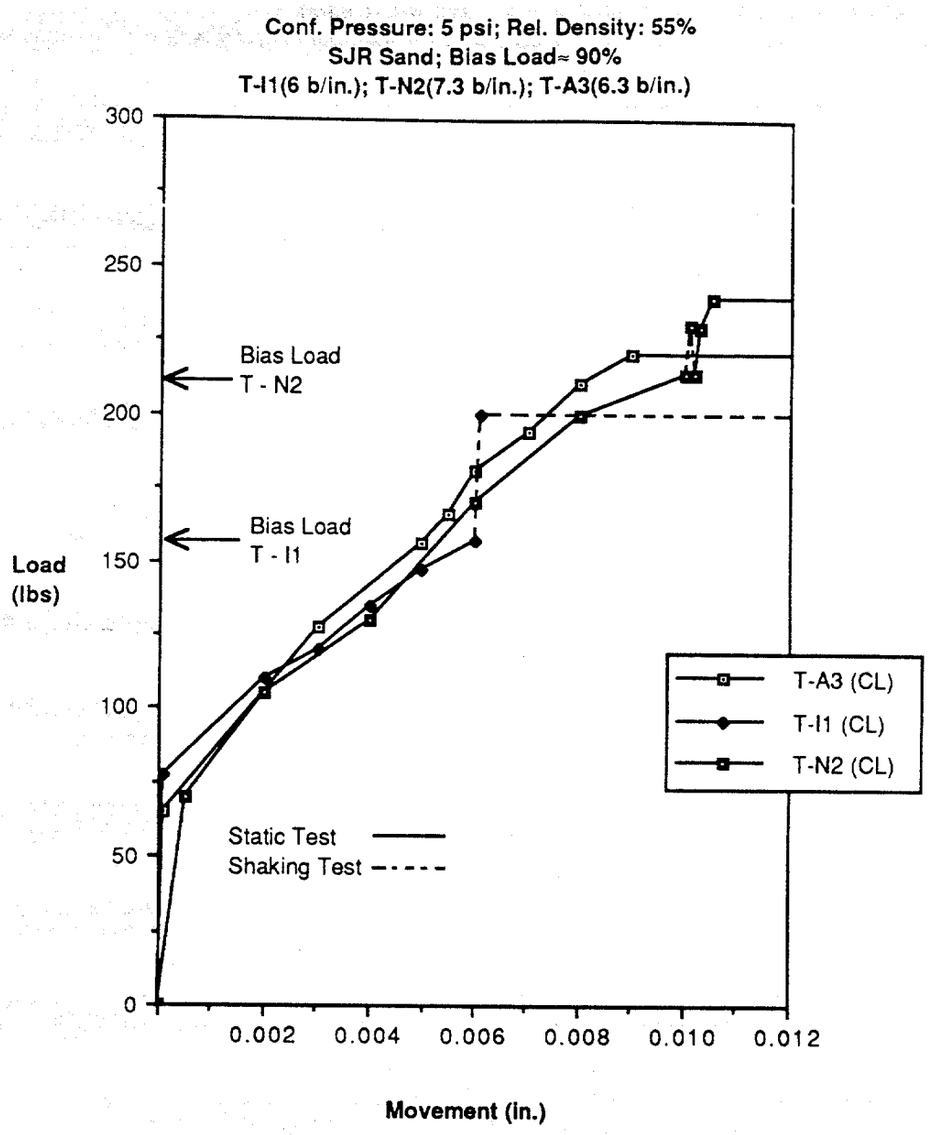

Fig. 6.26. Load-Movement Curves, Tests A3, I1, N2.

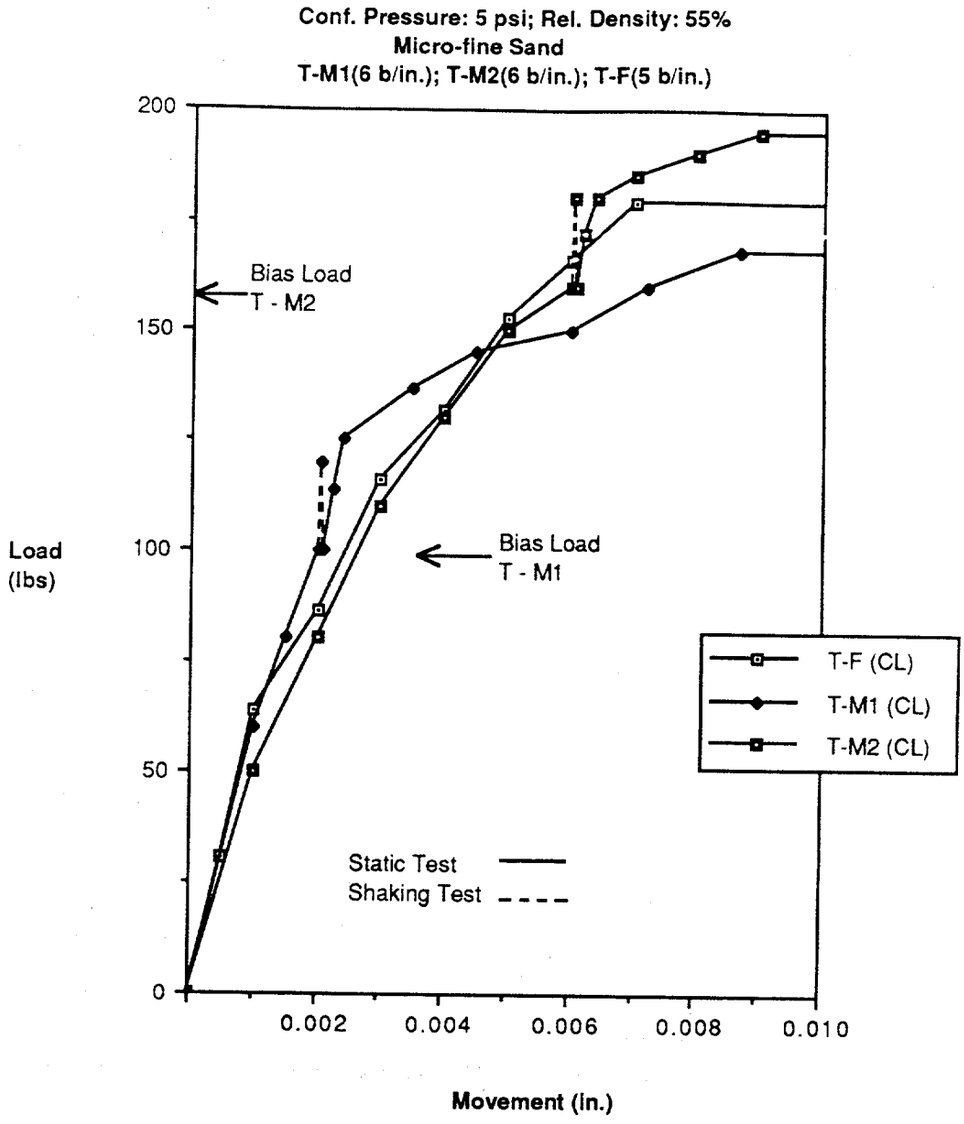

Fig. 6.27. Load-Movement Curves, Tests F, M1, M2.

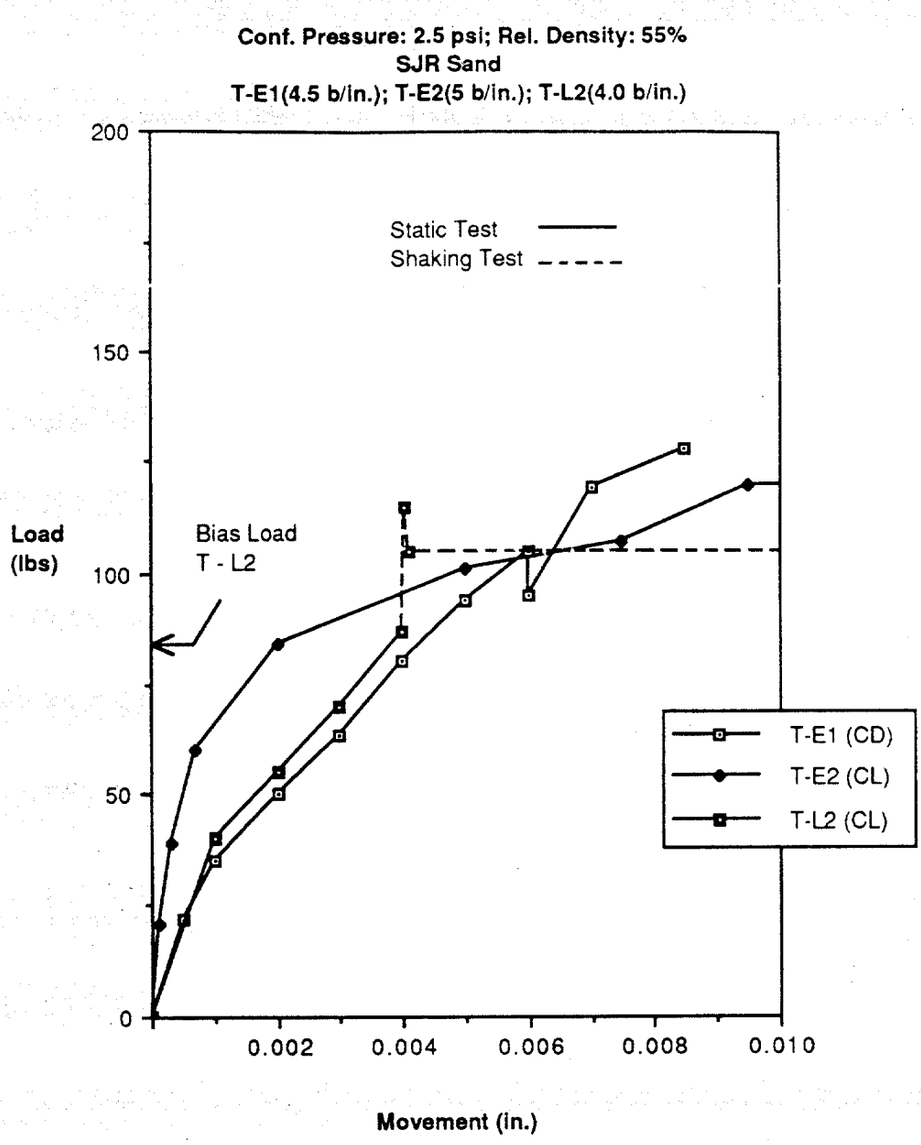

Fig. 6.28. Load-Movement Curves, Tests E1, E2, L2.

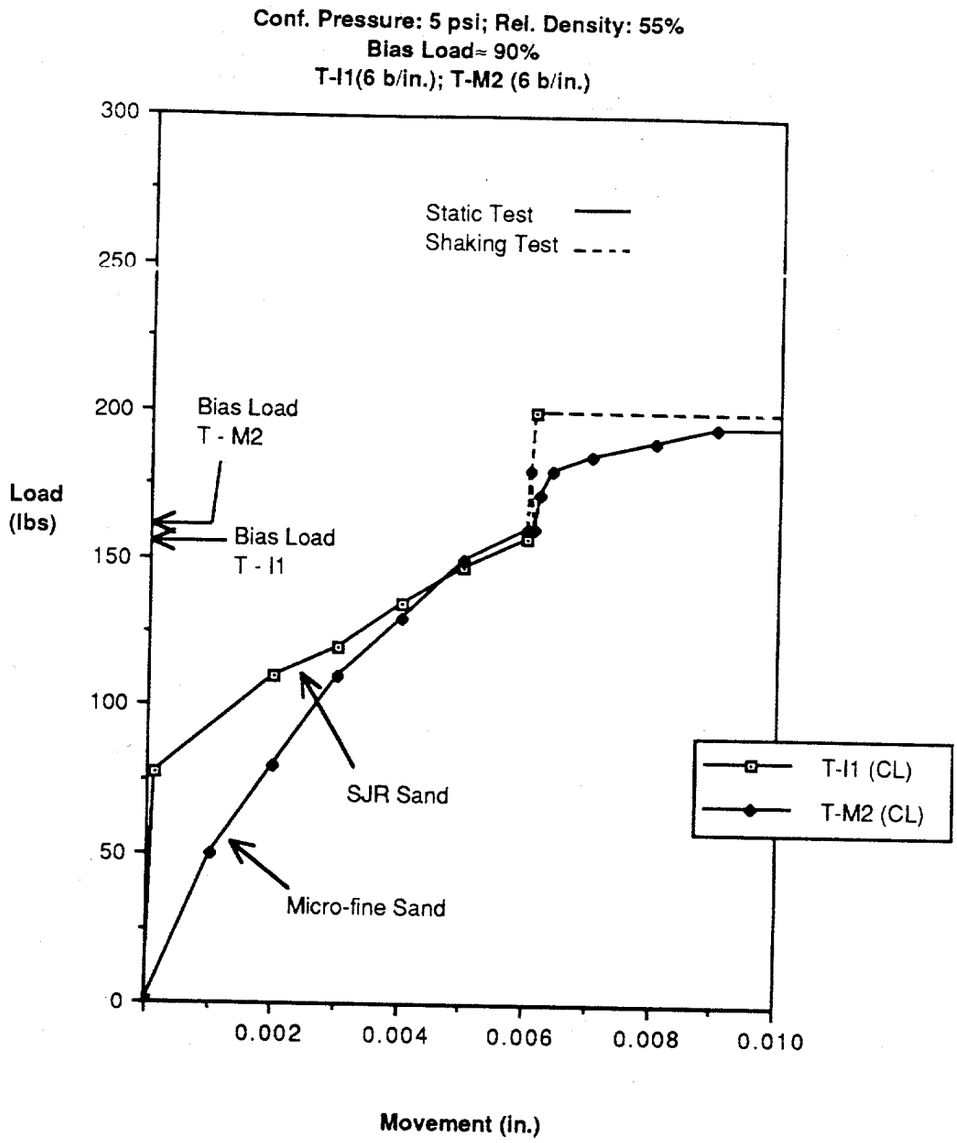

Fig. 6.29. Load-Movement Curves, Tests I1, M2.

DYNAMIC LOAD TRANSFER CHARACTERISTICS

Time histories of dynamic unit load transfer (normalized by the effective horizontal chamber pressure, σ_h') for Test H1 (stability condition) and Test I2 (failure condition) are shown in Fig. 6.30 for the upper ("top") and lower ("bottom") halves of the pile. Few definitive time-dependent trends can be observed, mainly due to the random nature of the excitation source (seismic event). In Test I2, a drastic reduction in the load transfer is observed while the pile is being pulled out by the dynamic interaction of the bias load-spring-pile system excited by the seismic event.

In both tests the normalized load transfer values are similar in the top portion of the pile. In Test H1, in which the bias load corresponds to a possible design condition (factor of safety = 2), the unit load transfer is nearly constant along the pile and with time. In Test I2, in which the bias load is very near the static capacity, the additional load transfer is concentrated in the bottom half of the pile. Failure appeared to be preceded by a slight increase in unit load transfer in the bottom section with no corresponding increase near the surface.

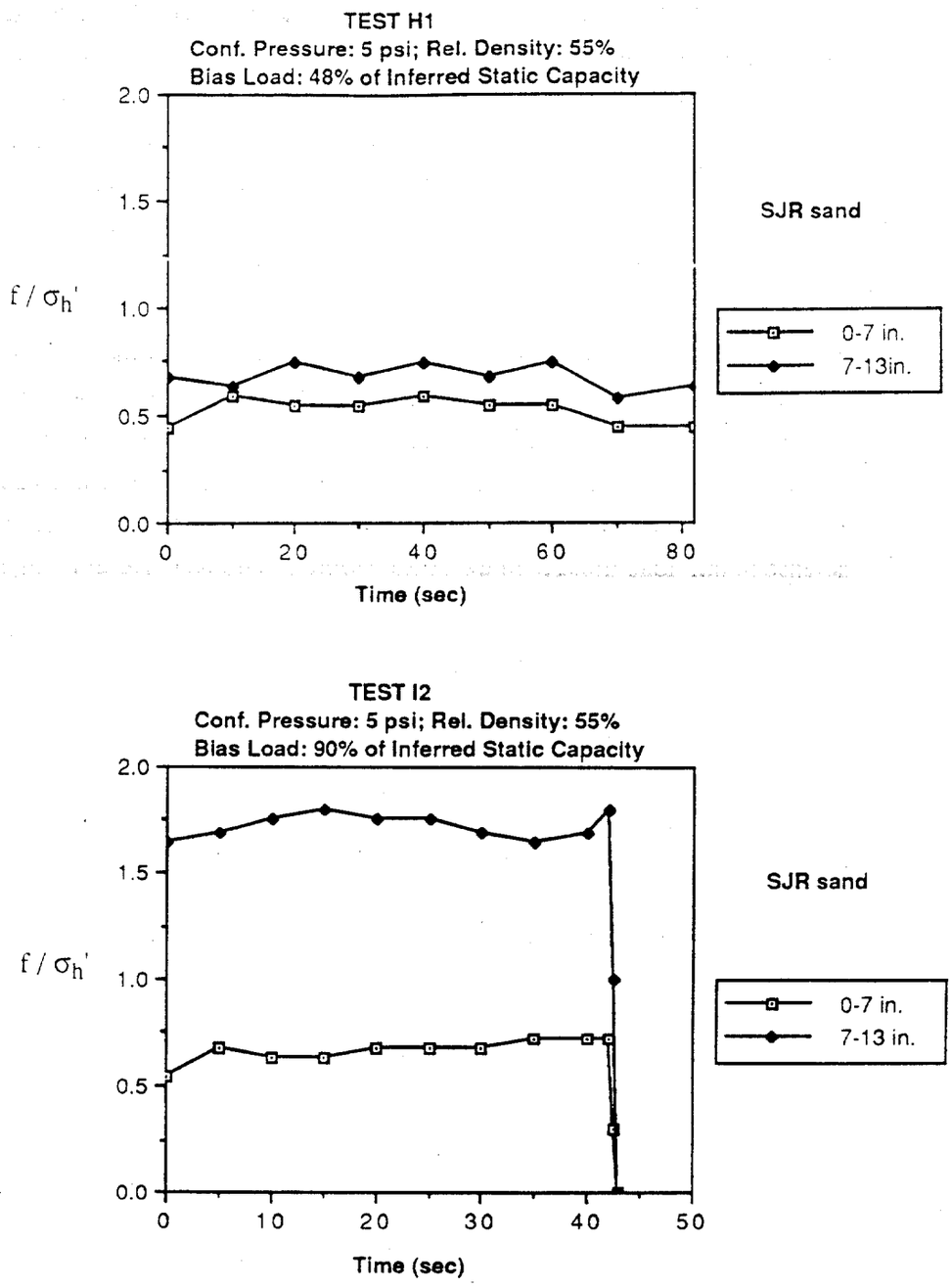

Fig. 6.30. Top and Bottom Time Histories of Normalized Unit Load Transfer, Tests H1 and H2.

CHAPTER VII

Analysis of Results, Horizontal and Combined Horizontal and Vertical Motions

This chapter describes the analysis of relevant test data in order to develop a better understanding of the dynamic response of axially loaded piles with tension bias under the horizontal and combined horizontal and vertical components of earthquake loading. The following aspects were investigated: (a) Comparison between the horizontal measured and target spectra, (b) Pile and soil response during the horizontal component of the simulated seismic event, (c) Pile and soil response during combined horizontal and vertical components of the simulated seismic event, (d) Post-shaking static capacities after the seismic event , and (e) Dynamic load transfer characteristics.

Summary of the dynamic (horizontal and combined horizontal and vertical motions) test program results is given in Table 7.1. The static tests (A1 - F, O1 - Q), described in Chapter VI, were also used as the baseline in determining values of biased load for the dynamic tests in this phase.

COMPARISON OF MEASURED AND TARGET SPECTRA

The actual horizontal acceleration spectrum measured by means of a low-g accelerometer (one of the two accelerometers used for measuring strains in dry sand, as described in Chapter III) is shown in Fig. 7.1. The target spectrum (also shown in Fig. 7.1) corresponds to the spectrum of the scaled horizontal acceleration time history for the Magnitude 8.0 Oceanside event (signal that was integrated numerically and input into the Instron's controller for testing). The measured spectrum indicated a reasonable match with the target spectrum for applied motions below 15 Hz, but some loss of of energy above 15 Hz, possibly due to the filtering caused by the limitation of the servo-hydraulic system of the Instron testing machine.

CHAPTER VII

Analysis of Results, Horizontal Horizontal and Vertical

This chapter describes the analysis of relevant te understanding of the dynamic response of axially loade horizontal and combined horizontal and vertical comp following aspects were investigated: (a) Comparison be target spectra, (b) Pile and soil response during the hori seismic event, (c) Pile and soil response during c components of the simulated seismic event, (d) Post- seismic event , and (e) Dynamic load transfer characteris

Summary of the dynamic (horizontal and combin test program results is given in Table 7.1. The static te Chapter VI, were also used as the baseline in determi dynamic tests in this phase.

COMPARISON OF MEASURED AND T

The actual horizontal acceleration spectrum me accelerometer (one of the two accelerometers used for m described in Chapter III) is shown in Fig. 7.1. The tar 7.1) corresponds to the spectrum of the scaled horizont Magnitude 8.0 Oceanside event (signal that was integra Instron's controller for testing). The measured spectrum the target spectrum for applied motions below 15 Hz, bu Hz, possibly due to the filtering caused by the limitatio the Instron testing machine.

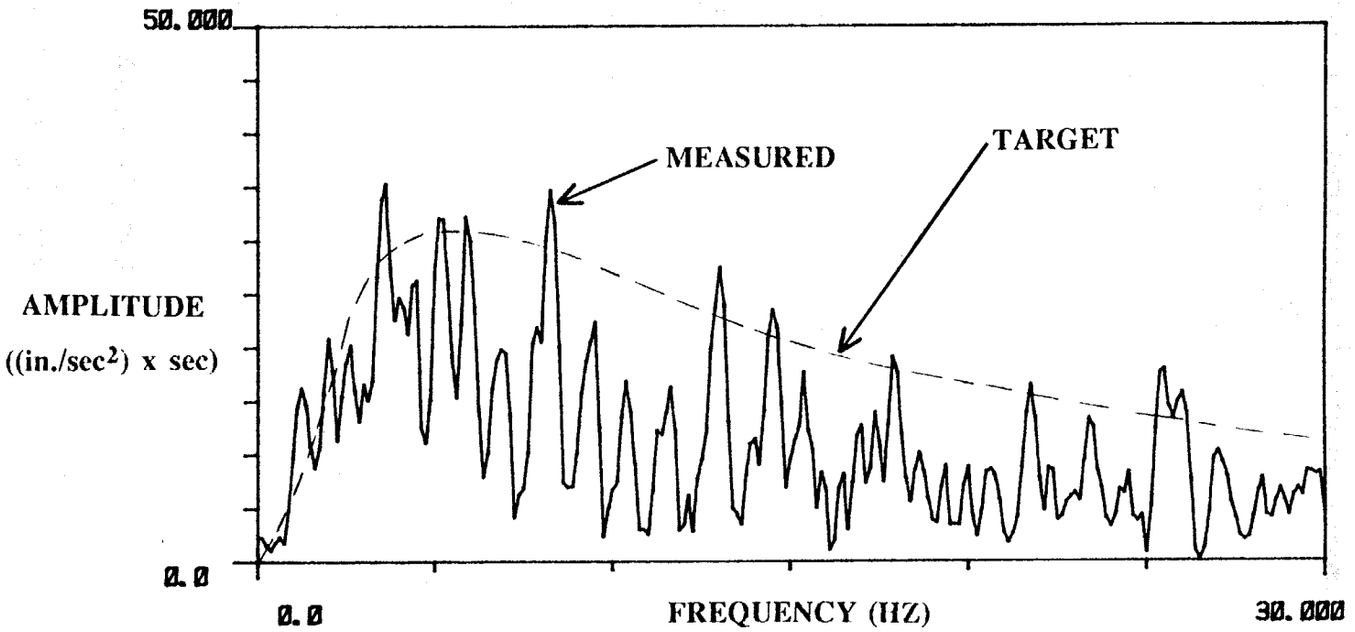

Fig. 7.1. Measured Spectrum versus Target Spectrum, Horizontal Motion.

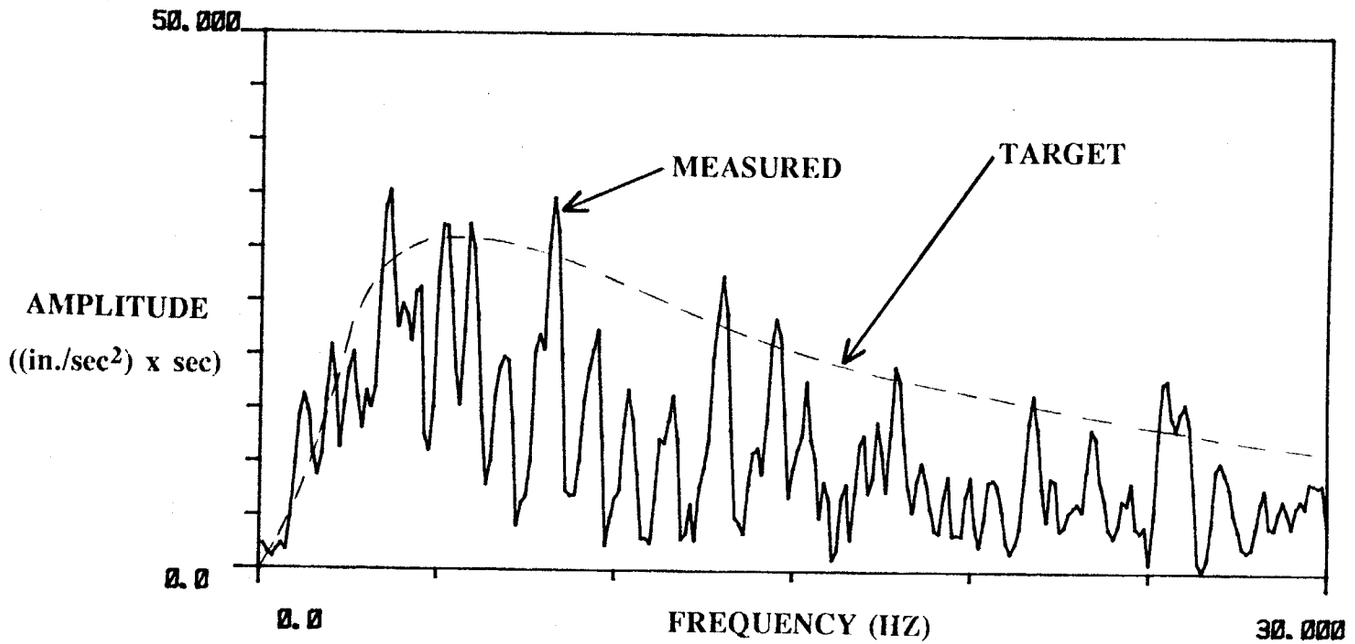

Fig. 7.1. Measured Spectrum versus Target Spectrum, Horizontal Motion.

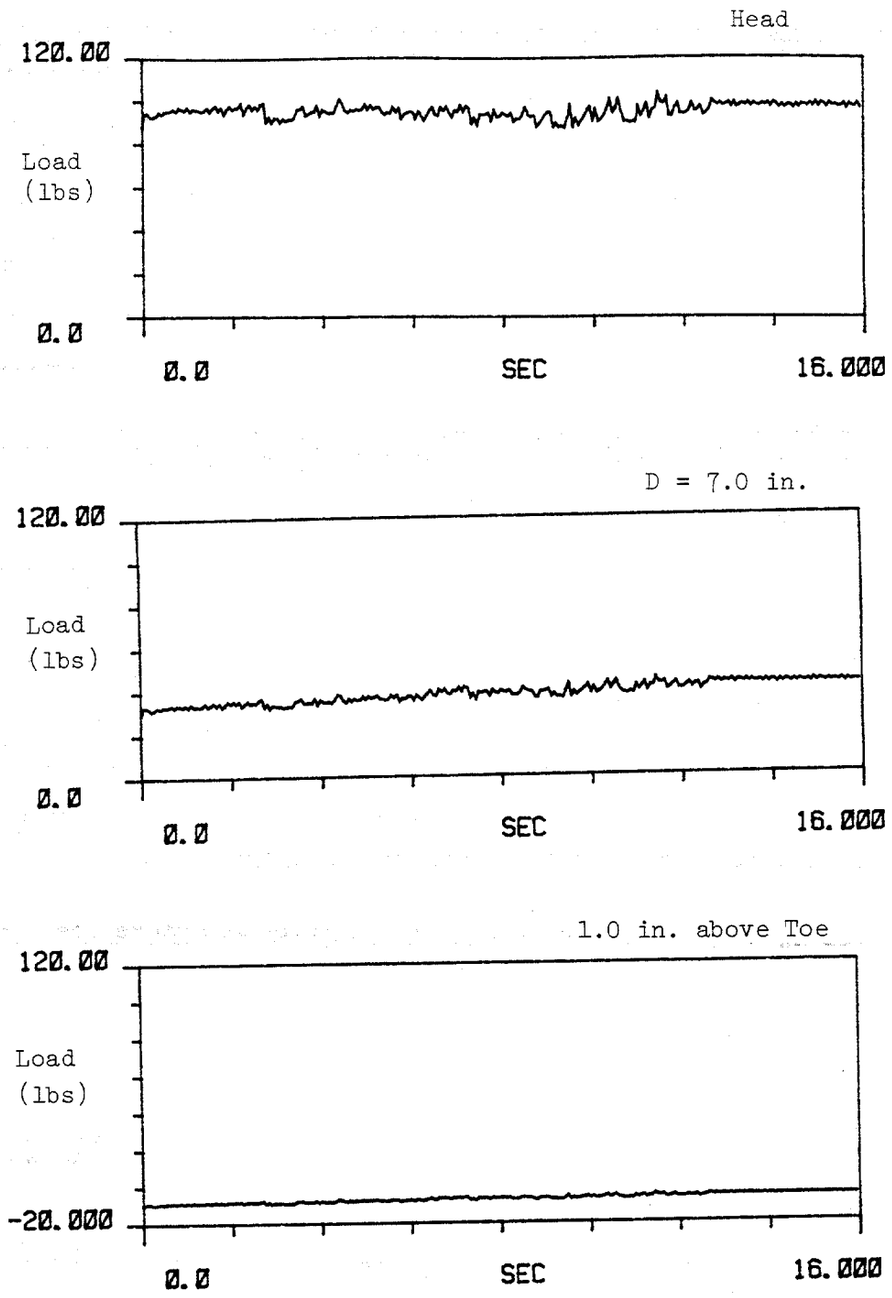

Fig. 7.2. Time History Measurements of Dynamic Load on Pile, Test R2.

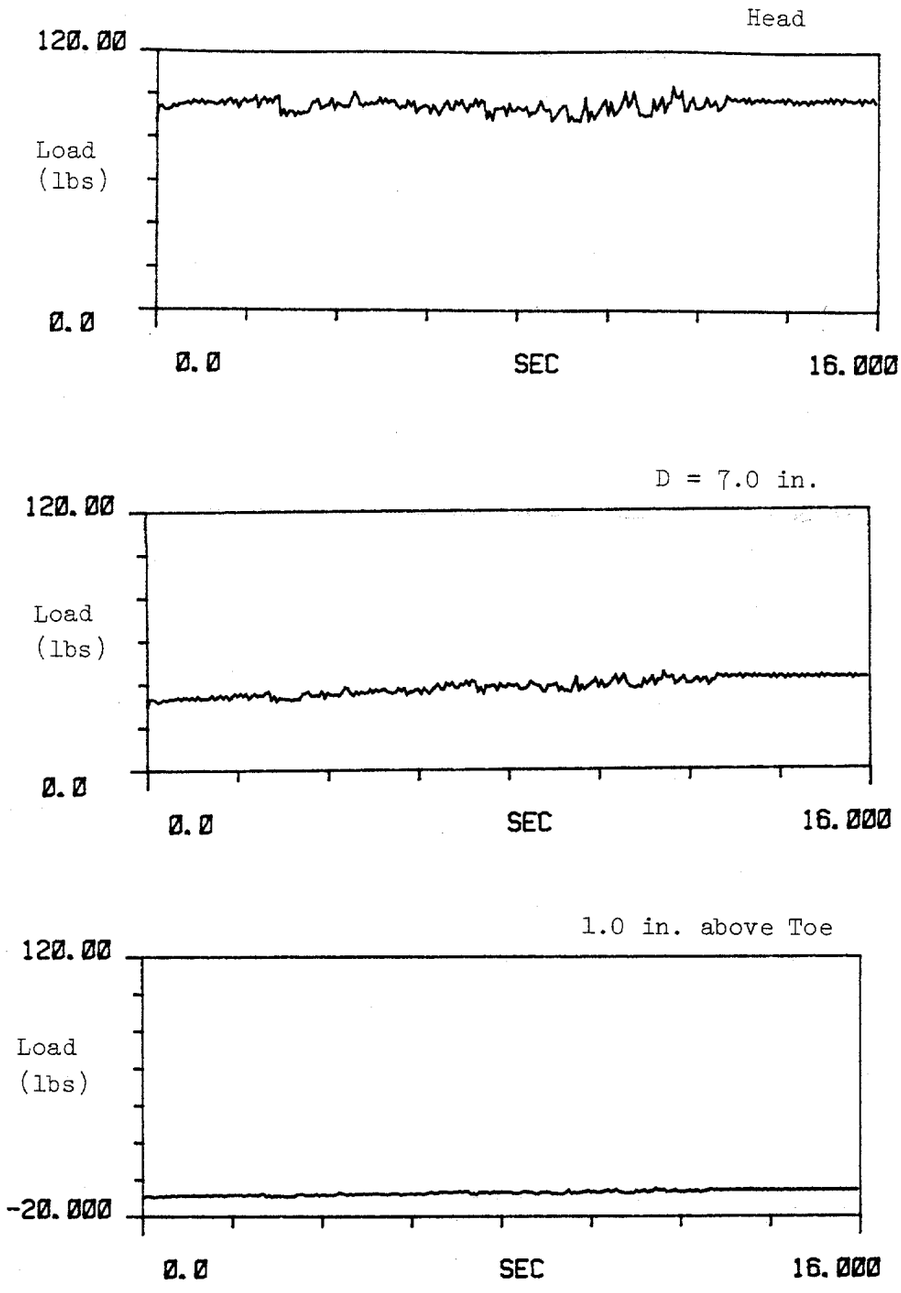

Fig. 7.2. Time History Measurements of Dynamic Load on Pile, Test R2.

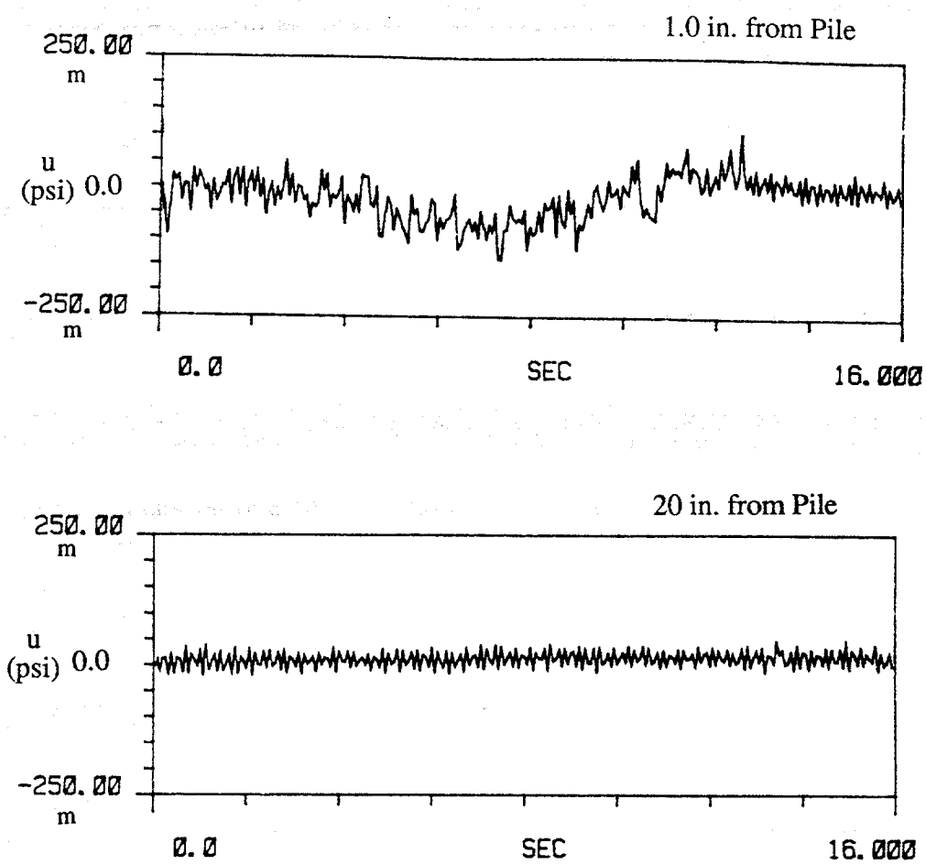

Fig. 7.3. Time History Measurements of Near and Far Field Pore Water Pressures, Test R2, [m = milli].

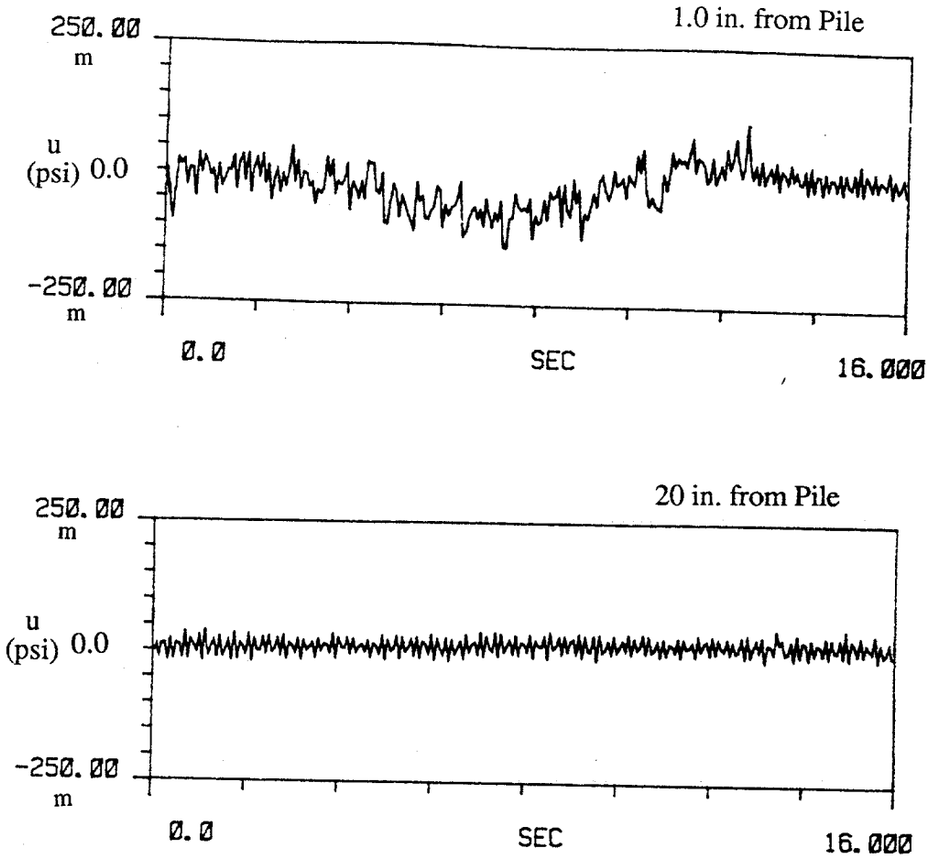

Fig. 7.3. Time History Measurements of Near and Far Field Pore Water Pressures, Test R2, [m = milli].

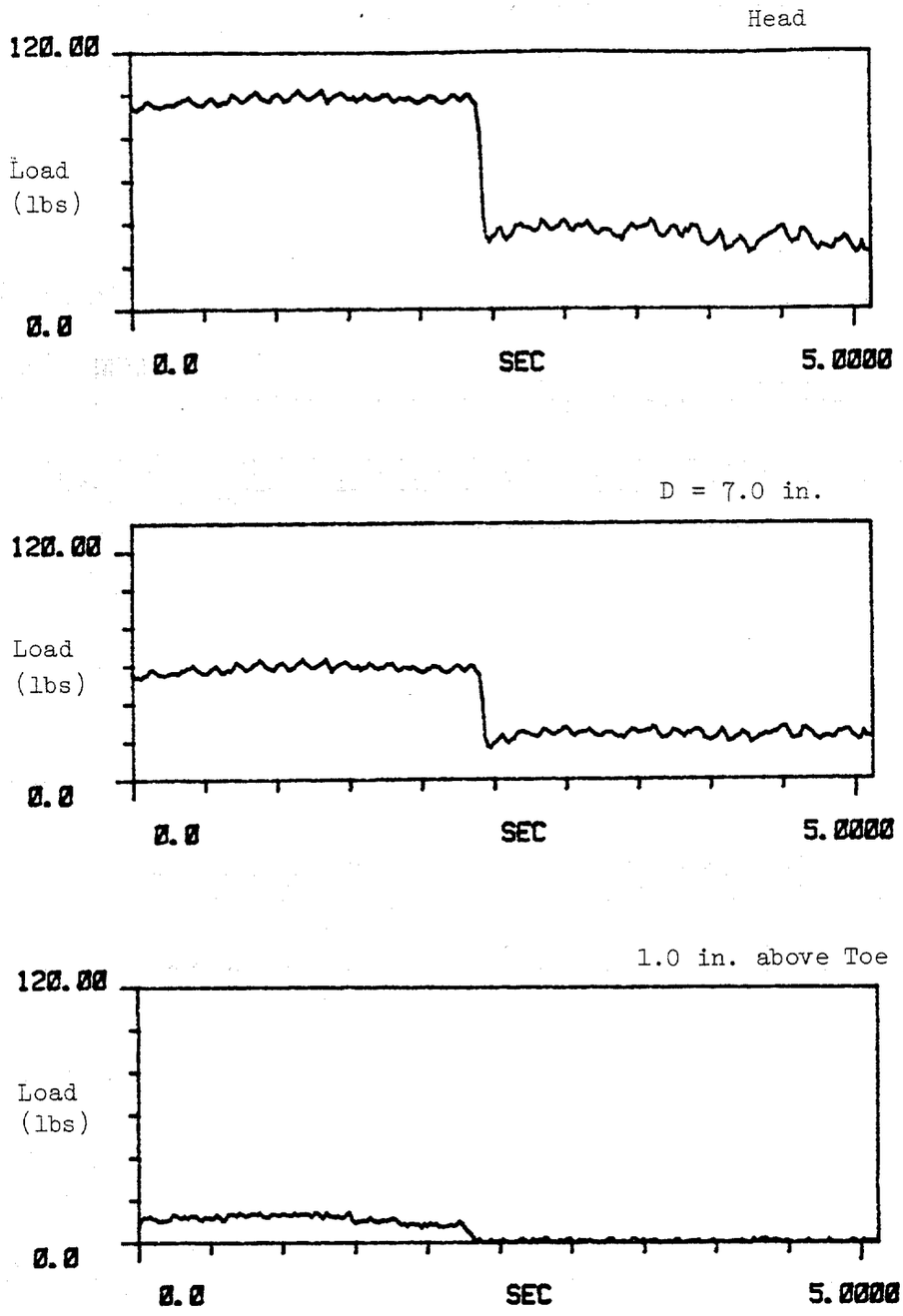

Fig. 7.5. Time History Measurements of Dynamic Load on Pile, Test S4.

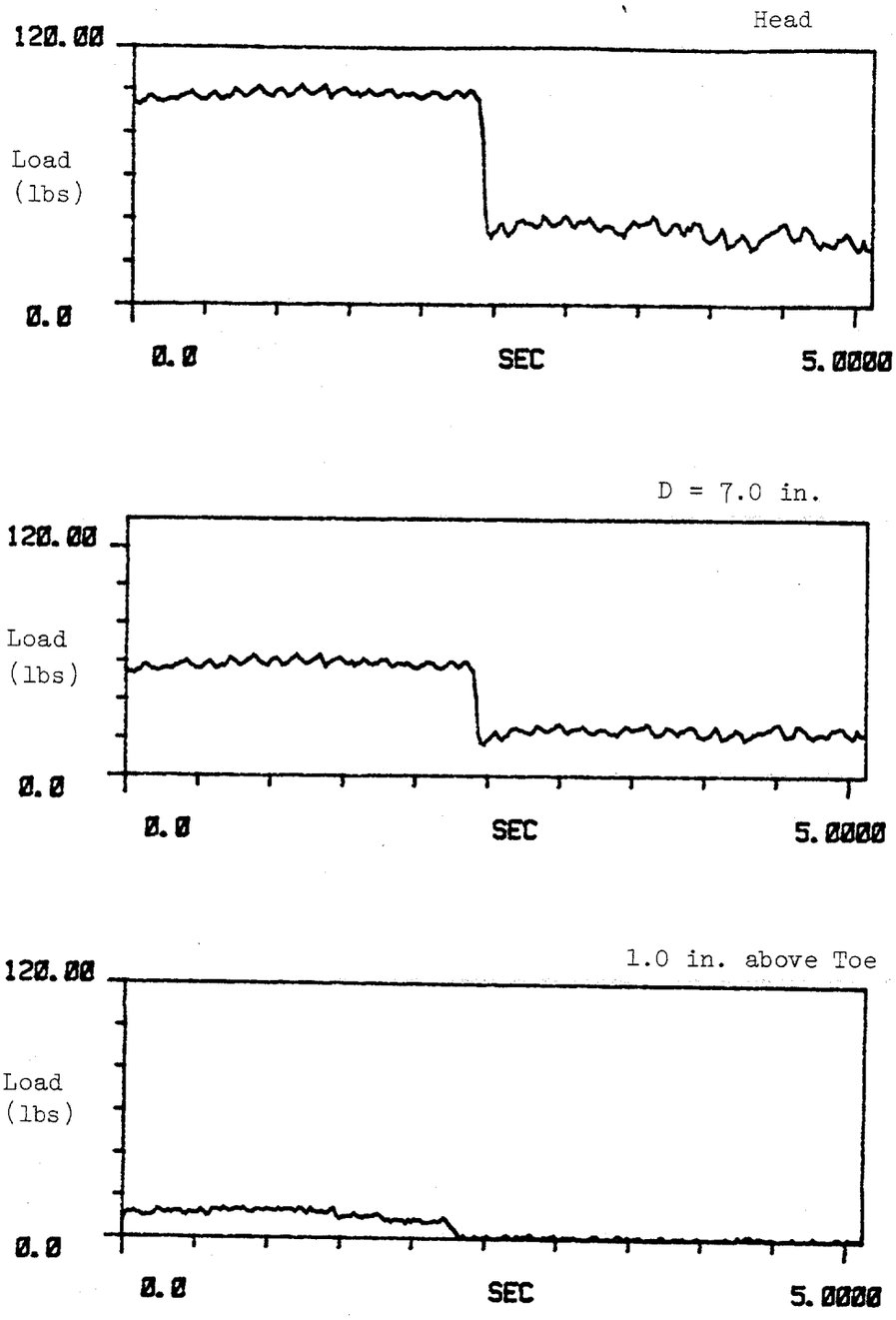

Fig. 7.5. Time History Measurements of Dynamic Load on Pile, Test S4.

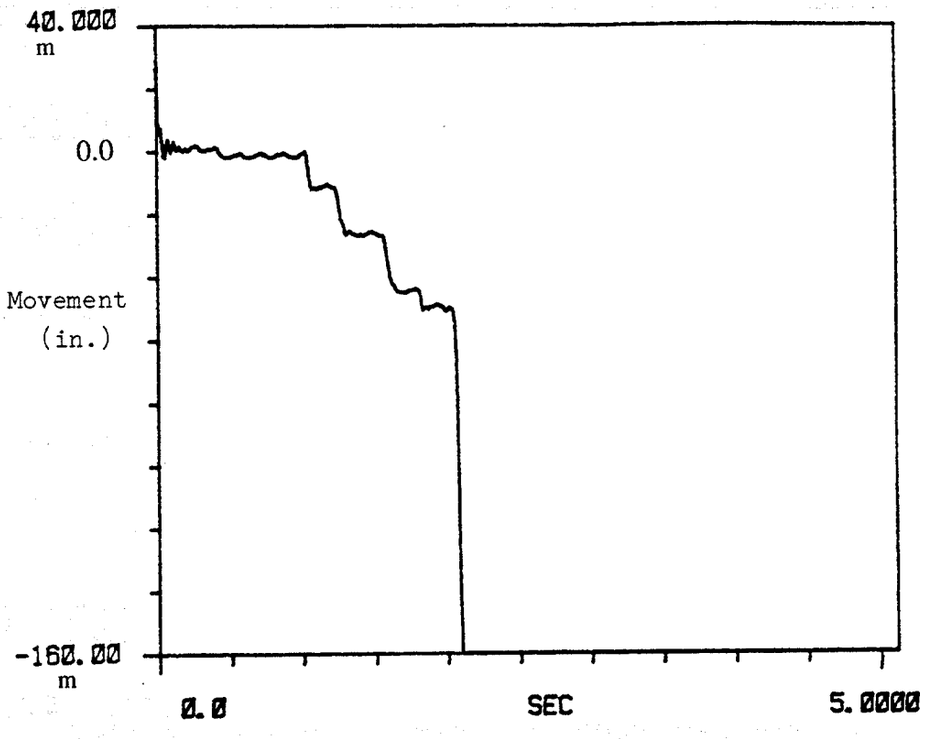

Fig. 7.7. Time History Measurements of Pile Head Movement, Test S4, [m = milli].

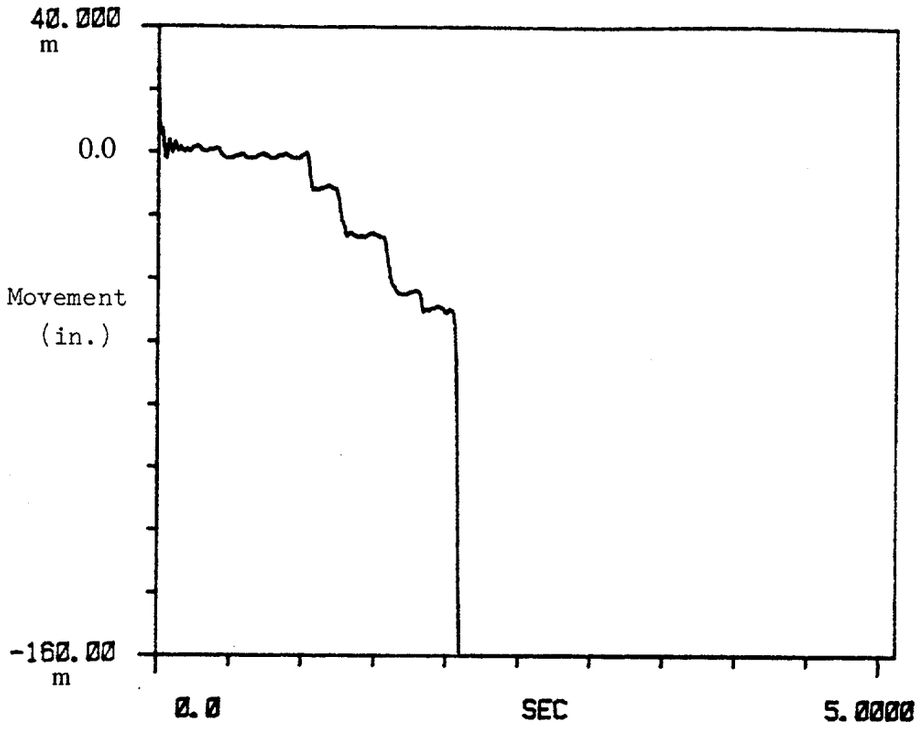

Fig. 7.7. Time History Measurements of Pile Head Movement, Test S4, [m = milli].

phenomenon of failure under these conditions therefore appears to be identical to that associated with pile failure in the purely vertical tests (Chapter VI). That is, no degradation of unit shaft resistance occurred during the event, but the soil-pile-structure interaction produced enough additional instantaneous load at the pile head to exceed the pile's static capacity, following which failure occurred. Third, small negative pressure (suction) was triggered by the pile while it was pulling out. The magnitude of this negative pore water pressure was insufficient to arrest the pile movement.

(c) Test U1

Test U1 was performed under the following conditions: (a) Mean effective confining pressure: 2.5 psi; (b) Relative density: 55%; (c) Earthquake Magnitude: 8.0; (d) Applied bias load: 45% of the inferred static capacity. Time history measurements of (1) load on the pile at three different levels, (2) pore water pressures in the soil mass, and (3) pile head movement are given in Figs. 7.9 - 7.11. Similar trends to those in Test R2 were observed, except that the dynamic load excursions on the pile head were larger (due to increased movement of the chamber associated with the larger earthquake and increased lag between the pile head and loading pulley (Fig. J.28)). Pile movement was substantially smaller than in Test R2 (0.020 in., which deconvolves to 0.14 in. in the prototype). Such movement is interpreted as representing a "stable" condition. Buildup of pore water pressures in both the near and far fields was observed, especially just prior to and after the completion of the simulated seismic event (Magnitude 8.0). Positive pore pressures reached 20% of the initial ambient effective stress, which implies a maximum reduction in the pile capacity of 20%. Since the combined static bias and dynamic axial head load did not exceed about 60 per cent of the pile's static capacity, failure did not occur.

(d) Test U3

The conditions under which Test U3 were performed were as follows: (a) Mean effective confining pressure: 2.5 psi; (2) Relative density: 55%; (c) Earthquake magnitude: 8.0; (d) Applied bias load: 75% of the inferred static capacity. Time history of (1) load on the pile at pile head, mid section and 1.0 in. above pile toe, (2) pore water pressures at the near and far fields, and (3) pile-head movement are given in Figs. 7.12 - 7.14. Time window records (between scaled time of 12 and 15 sec. of the simulated Magnitude 8.0 seismic event) of near- and far-field pore water pressures and pile head movement are shown in Fig. 7.15.

phenomenon of failure under these conditions therefore appears to be identical to that associated with pile failure in the purely vertical tests (Chapter VI). That is, no degradation of unit shaft resistance occurred during the event, but the soil-pile-structure interaction produced enough additional instantaneous load at the pile head to exceed the pile's static capacity, following which failure occurred. Third, small negative pressure (suction) was triggered by the pile while it was pulling out. The magnitude of this negative pore water pressure was insufficient to arrest the pile movement.

(c) Test U1

Test U1 was performed under the following conditions: (a) Mean effective confining pressure: 2.5 psi; (b) Relative density: 55%; (c) Earthquake Magnitude: 8.0; (d) Applied bias load: 45% of the inferred static capacity. Time history measurements of (1) load on the pile at three different levels, (2) pore water pressures in the soil mass, and (3) pile head movement are given in Figs. 7.9 - 7.11. Similar trends to those in Test R2 were observed, except that the dynamic load excursions on the pile head were larger (due to increased movement of the chamber associated with the larger earthquake and increased lag between the pile head and loading pulley (Fig. J.28)). Pile movement was substantially smaller than in Test R2 (0.020 in., which deconvolves to 0.14 in. in the prototype). Such movement is interpreted as representing a "stable" condition. Buildup of pore water pressures in both the near and far fields was observed, especially just prior to and after the completion of the simulated seismic event (Magnitude 8.0). Positive pore pressures reached 20% of the initial ambient effective stress, which implies a maximum reduction in the pile capacity of 20%. Since the combined static bias and dynamic axial head load did not exceed about 60 per cent of the pile's static capacity, failure did not occur.

(d) Test U3

The conditions under which Test U3 were performed were as follows: (a) Mean effective confining pressure: 2.5 psi; (2) Relative density: 55%; (c) Earthquake magnitude: 8.0; (d) Applied bias load: 75% of the inferred static capacity. Time history of (1) load on the pile at pile head, mid section and 1.0 in. above pile toe, (2) pore water pressures at the near and far fields, and (3) pile-head movement are given in Figs. 7.12 - 7.14. Time window records (between scaled time of 12 and 15 sec. of the simulated Magnitude 8.0 seismic event) of near- and far-field pore water pressures and pile head movement are shown in Fig. 7.15.

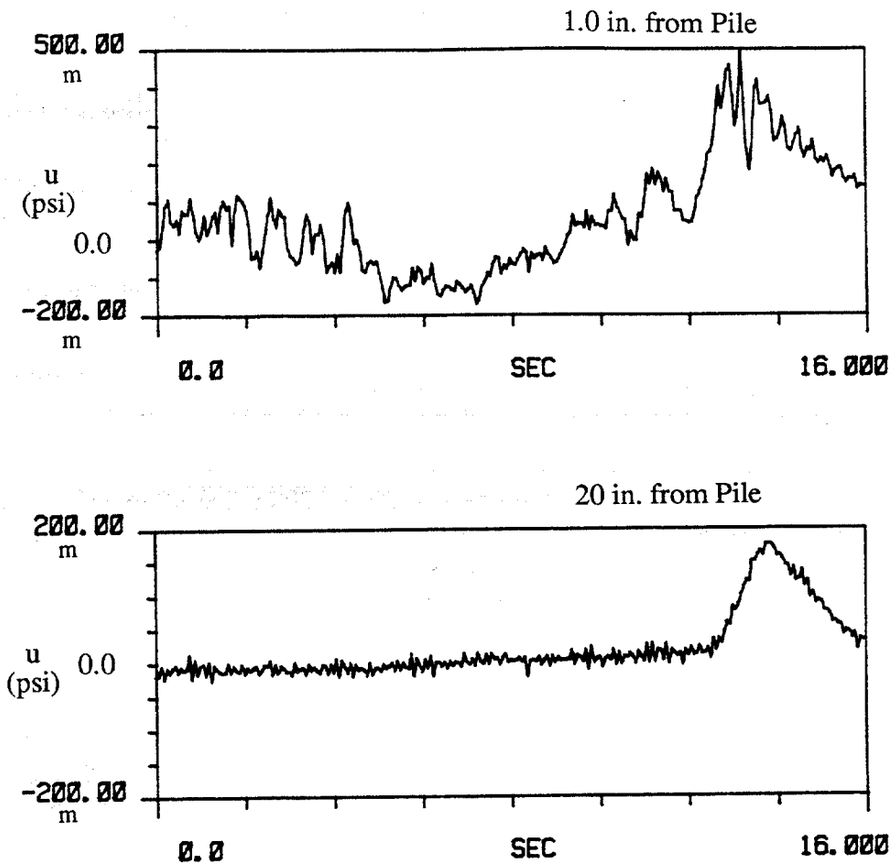

Fig. 7.10. Time History Measurements of Near and Far Field Pore Water Pressures, Test U1, [m = milli].

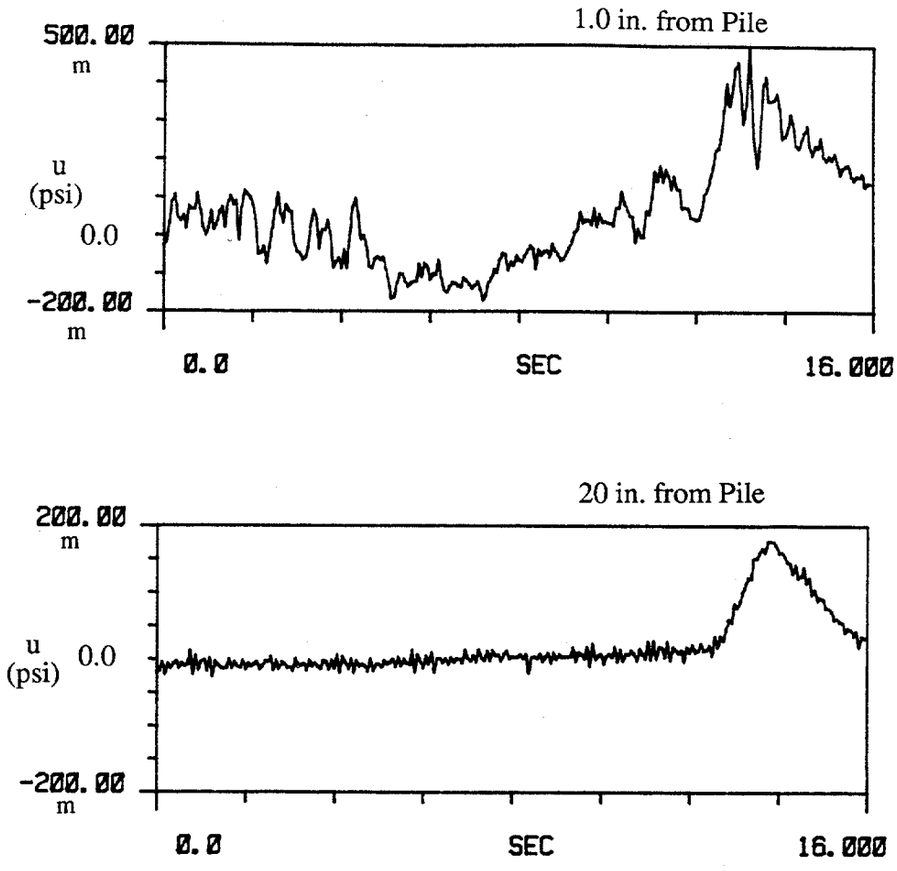

Fig. 7.10. Time History Measurements of Near and Far Field Pore Water Pressures, Test U1, [m = milli].

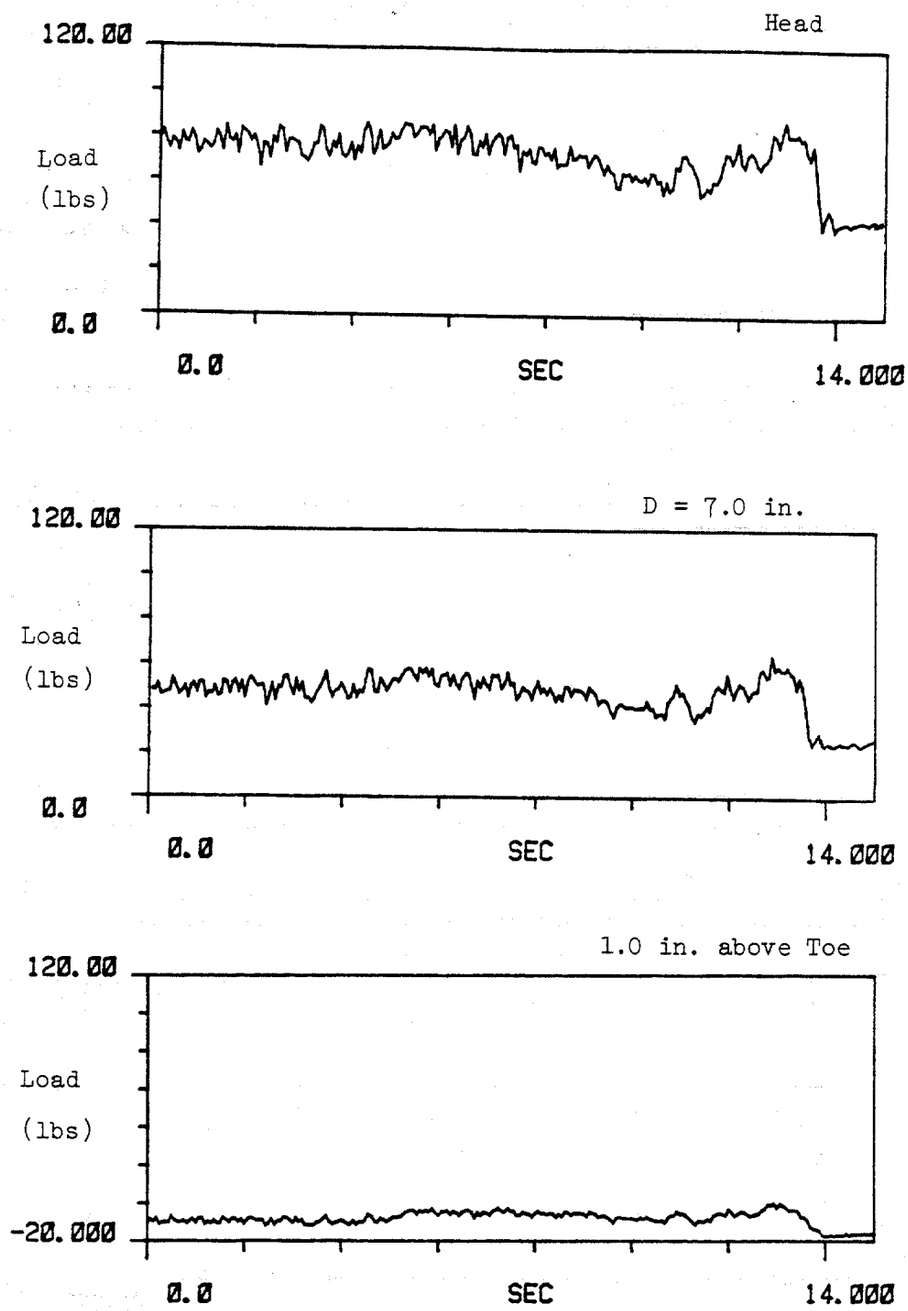

Fig. 7.12. Time History Measurements of Dynamic Load on Pile, Test U3.

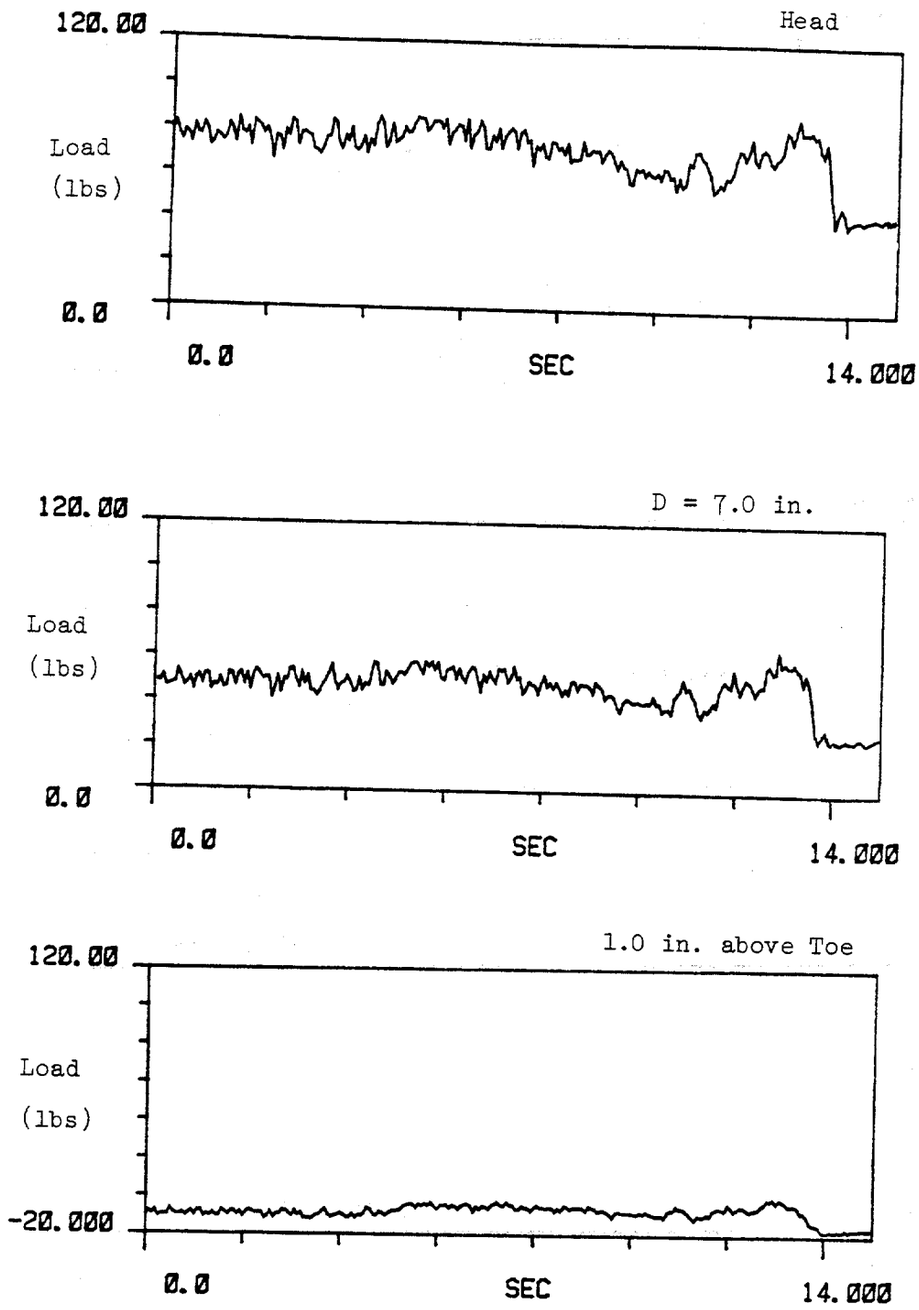

Fig. 7.12. Time History Measurements of Dynamic Load on Pile, Test U3.

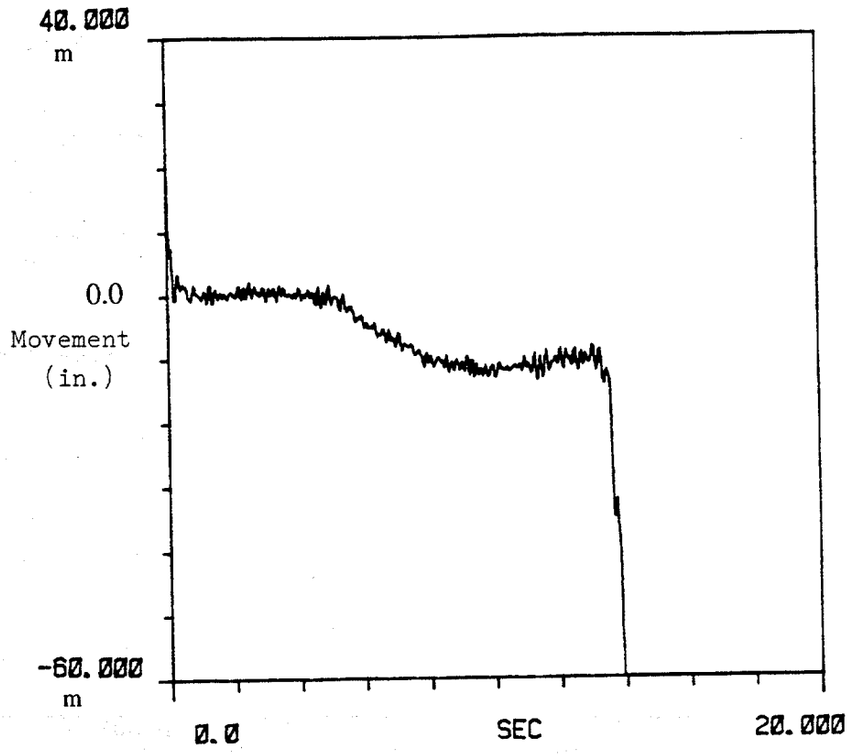

Fig. 7.14. Time History Measurements of Pile Head Movement, Test U3, [m = milli].

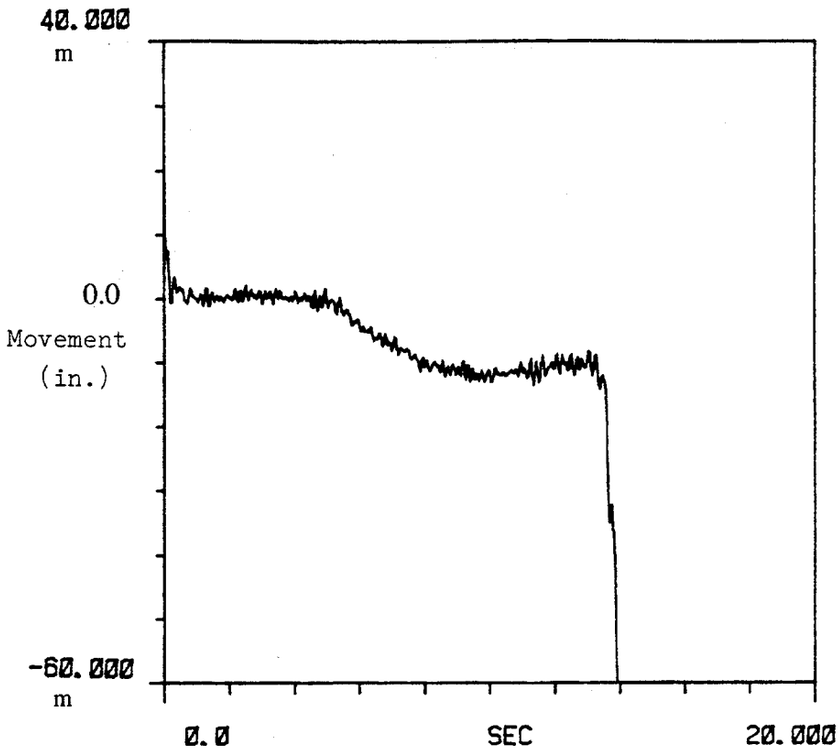

Fig. 7.14. Time History Measurements of Pile Head Movement, Test U3, [m = milli].

Some comments can be made regarding Test U3. First, excess pore water pressures were measured in both near and far fields. The magnitude of these pressures were essentially equal to the those measured in Test U1 (smaller biased load) although they increased somewhat more rapidly in Test U3 than in Test U1, possibly due to the effect of the initial shear strain in the sand due to the presence of higher bias load. The peak pore water pressure of 0.575 psi was 23% of the initial effective stress in the soil. It is likely that the induced pore water pressure at the interface was even higher. The loss of capacity produced by generation of excess pore water pressure coupled with the dynamic load excursion on the pile head of about 10% of the static bias (Fig. 7.12) combined to produce complete and catastrophic failure just at the completion of shaking (13 sec. in the model; 81 sec. in the prototype). It is of interest to note that the measured peak near-field excess pore water pressure (23% of chamber pressure) was about equal to the excess pore water pressure produced by driving (Fig. 6.1). Second, liquefaction (a phenomenon manifested physically by sand boiling, as displayed in Fig. 7.16) took place visually about two sec. after the completion of the shaking test. Third, for liquefaction to have developed, the magnitude of excess pore water pressure must be equal to the applied confining pressure at some point in the chamber. Since the magnitude of pore water pressures at locations of the pore pressure transducers (mid-depth of the chamber) was about 1/5 of the applied confining pressure, it is believed that liquefaction may have started in another location of the chamber. The sudden pullout of the pile may have induced flow of loose soil and water into the cavity left by the pile at the toe. It is believed that this action may have triggered liquefaction at or near the toe of the pile. The situation modelled in this test may be more severe for the case of piles driven as a group, in which the interaction of the nearby piles may significantly speed up the buildup of pore water pressures in the surrounding soil to a level enough to promote grater degradation of skin friction than occurs with a single pile.

Finally, the dissipation of excess pore water pressure was observed about 18 sec. (approximately 2 min. of time in the prototype). See Fig. 7.13. Immediately after pile pullout, negative pore water pressure developed in the near-field transducer, due either to dilation of the sand near the pile-soil interface or to lifting of the sand along with the pile. At this location, however, positive pore pressures were re-established within about four sec., after which slow dissipation occurred. An opposite effect appeared in the far-field transducer. As the pile pulled out a significant jump in pore pressure occurred, possibly in response to local liquefaction at the pile toe, coupled with minimal influence of the near-field condition described above that produced locally negative pore water pressures near the

Some comments can be made regarding Test U3. First, excess pore water pressures were measured in both near and far fields. The magnitude of these pressures were essentially equal to the those measured in Test U1 (smaller biased load) although they increased somewhat more rapidly in Test U3 than in Test U1, possibly due to the effect of the initial shear strain in the sand due to the presence of higher bias load. The peak pore water pressure of 0.575 psi was 23% of the initial effective stress in the soil. It is likely that the induced pore water pressure at the interface was even higher. The loss of capacity produced by generation of excess pore water pressure coupled with the dynamic load excursion on the pile head of about 10% of the static bias (Fig. 7.12) combined to produce complete and catastrophic failure just at the completion of shaking (13 sec. in the model; 81 sec. in the prototype). It is of interest to note that the measured peak near-field excess pore water pressure (23% of chamber pressure) was about equal to the excess pore water pressure produced by driving (Fig. 6.1). Second, liquefaction (a phenomenon manifested physically by sand boiling, as displayed in Fig. 7.16) took place visually about two sec. after the completion of the shaking test. Third, for liquefaction to have developed, the magnitude of excess pore water pressure must be equal to the applied confining pressure at some point in the chamber. Since the magnitude of pore water pressures at locations of the pore pressure transducers (mid-depth of the chamber) was about 1/5 of the applied confining pressure, it is believed that liquefaction may have started in another location of the chamber. The sudden pullout of the pile may have induced flow of loose soil and water into the cavity left by the pile at the toe. It is believed that this action may have triggered liquefaction at or near the toe of the pile. The situation modelled in this test may be more severe for the case of piles driven as a group, in which the interaction of the nearby piles may significantly speed up the buildup of pore water pressures in the surrounding soil to a level enough to promote grater degradation of skin friction than occurs with a single pile.

Finally, the dissipation of excess pore water pressure was observed about 18 sec. (approximately 2 min. of time in the prototype). See Fig. 7.13. Immediately after pile pullout, negative pore water pressure developed in the near-field transducer, due either to dilation of the sand near the pile-soil interface or to lifting of the sand along with the pile. At this location, however, positive pore pressures were re-established within about four sec., after which slow dissipation occurred. An opposite effect appeared in the far-field transducer. As the pile pulled out a significant jump in pore pressure occurred, possibly in response to local liquefaction at the pile toe, coupled with minimal influence of the near-field condition described above that produced locally negative pore water pressures near the

pile wall. At both near and far-field locations, however, only about one half of the excess pore pressure generated at the time of pile failure had dissipated two prototype minutes later.

EFFECT OF COMBINED HORIZONTAL AND VERTICAL MOTIONS ON PILE RESPONSE

Effect of superimposing vertical and horizontal components of motion of the scaled Magnitude 7.5 Oceanside event was also investigated in Test T1. The objective of Test T1 was to investigate whether superposition of a vertical soil loading component would change the performance of the pile from one of "stability" with a static bias of 62% of static capacity (factor of safety of 1.6) to one of "mobility". This test was identical to Tests S1 and S2 except for the imposed vertical motion. The superimposed vertical motion applied to the chamber consisted of the equivalent low-frequency high-amplitude sinusoidal displacement-time signal that was implemented for the analysis of induced water pressure due to vertical water mass excitation (Appendix D). This motion produces more load excursions on the pile than the wide-band vertical component of earthquake motion from the Oceanside event of 1986 (Chapter VI). Such a signal (predominant frequency = 0.12 Hz, amplitude of displacement = 0.73 in.) was then scaled to account for scaling effects between model and prototype (Chapter V). The scaled signal, with vertical displacement amplitude of 0.10 in. and frequency of 0.85 Hz, was then programmed into the Instron controller for testing. The horizontal motion, applied simultaneously with the vertical motion, was as applied in Tests S1 - S4.

Time history measurements of load on the pile (at three different levels), pore water pressures in near and far fields, and pile-head movement are shown in Figs. 7.17 - 7.19. Pore water pressures and pile-head movement measurements showed similar trends to those tests performed in similar conditions but subjected to horizontal motions of the simulated Magnitude 7.5 Oceanside event (i.e., Tests S1 and S2). Regarding load measurements on the pile (Fig. 7. 17), Test T1 showed rather a predominant harmonic trend (as a result of the imposed vertical excitation component) than a random variation of load, as seen for Tests S1 and S2. As can be seen in Fig. 7.19, no appreciable pile movement ocurred. The effect of superposition of soil motion components was reflected by an additional 5% reduction in post-shaking static capacity. That is, the post-shaking static capacity for the test performed with combined soil loading was 88% of inferred static capacity , whereas, tests performed with purely horizontal soil motion averaged 93% of

pile wall. At both near and far-field locations, however, only about one half of the excess pore pressure generated at the time of pile failure had dissipated two prototype minutes later.

EFFECT OF COMBINED HORIZONTAL AND VERTICAL MOTIONS ON PILE RESPONSE

Effect of superimposing vertical and horizontal components of motion of the scaled Magnitude 7.5 Oceanside event was also investigated in Test T1. The objective of Test T1 was to investigate whether superposition of a vertical soil loading component would change the performance of the pile from one of "stability" with a static bias of 62% of static capacity (factor of safety of 1.6) to one of "mobility". This test was identical to Tests S1 and S2 except for the imposed vertical motion. The superimposed vertical motion applied to the chamber consisted of the equivalent low-frequency high-amplitude sinusoidal displacement-time signal that was implemented for the analysis of induced water pressure due to vertical water mass excitation (Appendix D). This motion produces more load excursions on the pile than the wide-band vertical component of earthquake motion from the Oceanside event of 1986 (Chapter VI). Such a signal (predominant frequency = 0.12 Hz, amplitude of displacement = 0.73 in.) was then scaled to account for scaling effects between model and prototype (Chapter V). The scaled signal, with vertical displacement amplitude of 0.10 in. and frequency of 0.85 Hz, was then programmed into the Instron controller for testing. The horizontal motion, applied simultaneously with the vertical motion, was as applied in Tests S1 - S4.

Time history measurements of load on the pile (at three different levels), pore water pressures in near and far fields, and pile-head movement are shown in Figs. 7.17 - 7.19. Pore water pressures and pile-head movement measurements showed similar trends to those tests performed in similar conditions but subjected to horizontal motions of the simulated Magnitude 7.5 Oceanside event (i.e., Tests S1 and S2). Regarding load measurements on the pile (Fig. 7. 17), Test T1 showed rather a predominant harmonic trend (as a result of the imposed vertical excitation component) than a random variation of load, as seen for Tests S1 and S2. As can be seen in Fig. 7.19, no appreciable pile movement ocurred. The effect of superposition of soil motion components was reflected by an additional 5% reduction in post-shaking static capacity. That is, the post-shaking static capacity for the test performed with combined soil loading was 88% of inferred static capacity , whereas, tests performed with purely horizontal soil motion averaged 93% of

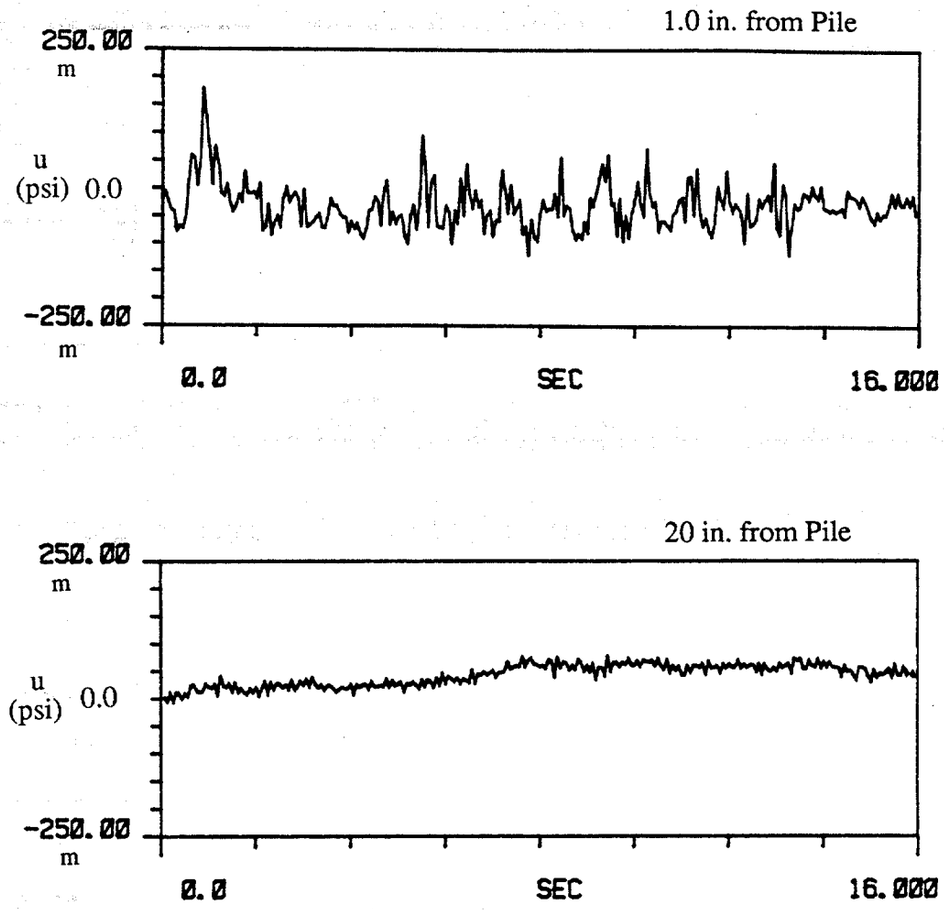

Fig. 7.18. Time History Measurements of Near and Far Field Pore Water Pressures, Test T1, [m = milli].

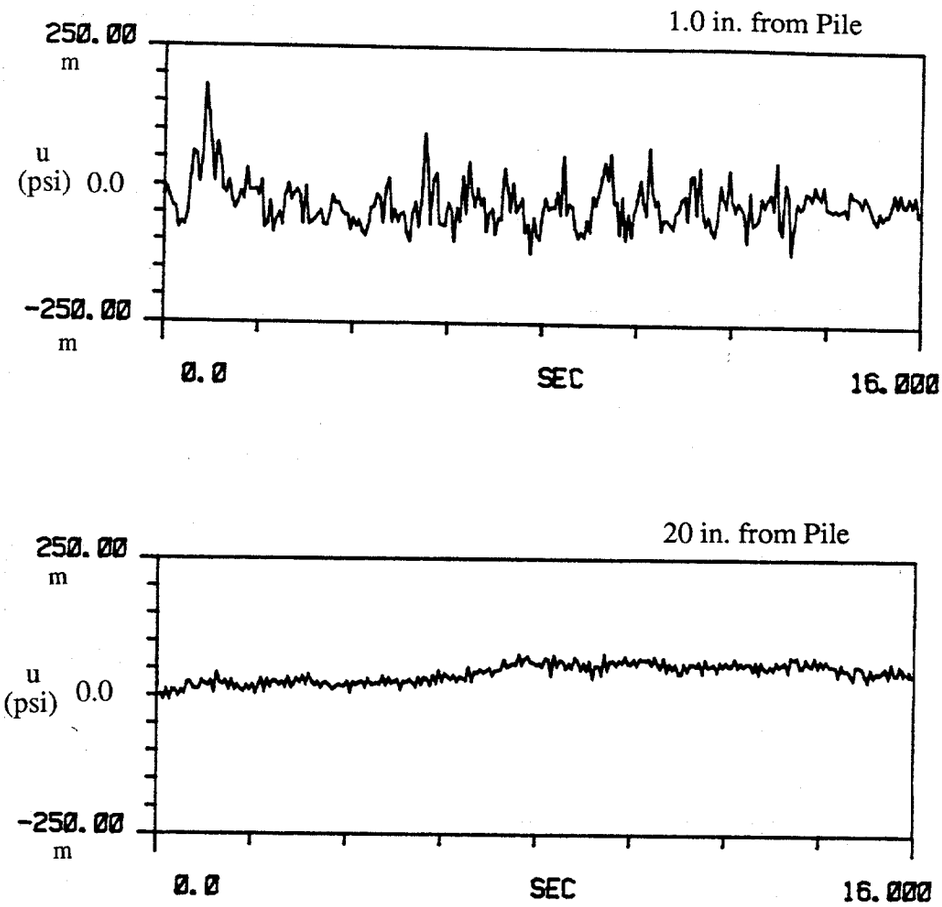

Fig. 7.18. Time History Measurements of Near and Far Field Pore Water Pressures, Test T1, [m = milli].

inferred static capacity. As can be seen in Fig. 7.19, no appreciable pile movement occurred.

EFFECT OF FUNDAMENTAL PERIOD OF MODEL SUPERSTRUCTURE

The scaling of the fundamental period of the superstructure (modelled by means of a one-degree-of-freedom spring-mass system) was investigated in Test T2. A stiff spring (as displayed in Fig. 3.9) provided a fundamental period of the spring-mass system of about 0.16 sec. (6.25 Hz), a period 6 times smaller than the unscaled period of the modelled superstructure used in all other tests. The conditions in which Test T2 was performed were identical to those in Test T1, except that the stiffer spring was used. Time history measurements of (1) load on the pile at three different levels, (2) pore water pressures in near and far fields of the soil mass, and (3) pile-head movement are shown in Fig. 7. 20 - 7.22. Similar trends of the time history measurements in Tests T1 and T2 indicated no important scaling scaling effects regarding the natural period of the modelled superstructure on the pile-soil behavior during the simulated seismic event. As expected, the dynamic excursions were lower in this test than in Test T1 because of the larger differences in forcing frequency of the soil and natural frequency of the model superstructure.

POST-SHAKING STATIC CAPACITIES AFTER SIMULATED SEISMIC EVENT

Load-movement curves plotted in the same sequence as occurred during testing (i.e., first, application of bias load, then shaking test, and last, application of post-shaking static load to failure, if the pile did not fail during shaking) are shown in for representative tests in Figs. 7.23 - 7.27. In these figures, the dashed line represents the total pile movement developed during the simulated seismic event (shaking test). Exact load and displacement versus time histories during shaking have been presented earlier in this chapter.

The load-movement curves are shown in the following groupings:

(a) Tests on piles averaging 4.1 blows/in. driving resistance and 75% bias load, for event Magnitudes of 7.0, 7.5 and 8.0 (Fig. 7.23),

(b) Tests on piles averaging 4.2 blows/in. driving resistance and 90% bias load, for event Magnitudes of 7.0 and 7.5 (Fig. 7.24),

inferred static capacity. As can be seen in Fig. 7.19, no appreciable pile movement occurred.

EFFECT OF FUNDAMENTAL PERIOD OF MODEL SUPERSTRUCTURE

The scaling of the fundamental period of the superstructure (modelled by means of a one-degree-of-freedom spring-mass system) was investigated in Test T2. A stiff spring (as displayed in Fig. 3.9) provided a fundamental period of the spring-mass system of about 0.16 sec. (6.25 Hz), a period 6 times smaller than the unscaled period of the modelled superstructure used in all other tests. The conditions in which Test T2 was performed were identical to those in Test T1, except that the stiffer spring was used. Time history measurements of (1) load on the pile at three different levels, (2) pore water pressures in near and far fields of the soil mass, and (3) pile-head movement are shown in Fig. 7. 20 - 7.22. Similar trends of the time history measurements in Tests T1 and T2 indicated no important scaling scaling effects regarding the natural period of the modelled superstructure on the pile-soil behavior during the simulated seismic event. As expected, the dynamic excursions were lower in this test than in Test T1 because of the larger differences in forcing frequency of the soil and natural frequency of the model superstructure.

POST-SHAKING STATIC CAPACITIES AFTER SIMULATED SEISMIC EVENT

Load-movement curves plotted in the same sequence as occurred during testing (i.e., first, application of bias load, then shaking test, and last, application of post-shaking static load to failure, if the pile did not fail during shaking) are shown in for representative tests in Figs. 7.23 - 7.27. In these figures, the dashed line represents the total pile movement developed during the simulated seismic event (shaking test). Exact load and displacement versus time histories during shaking have been presented earlier in this chapter.

The load-movement curves are shown in the following groupings:

(a) Tests on piles averaging 4.1 blows/in. driving resistance and 75% bias load, for event Magnitudes of 7.0, 7.5 and 8.0 (Fig. 7.23),

(b) Tests on piles averaging 4.2 blows/in. driving resistance and 90% bias load, for event Magnitudes of 7.0 and 7.5 (Fig. 7.24),

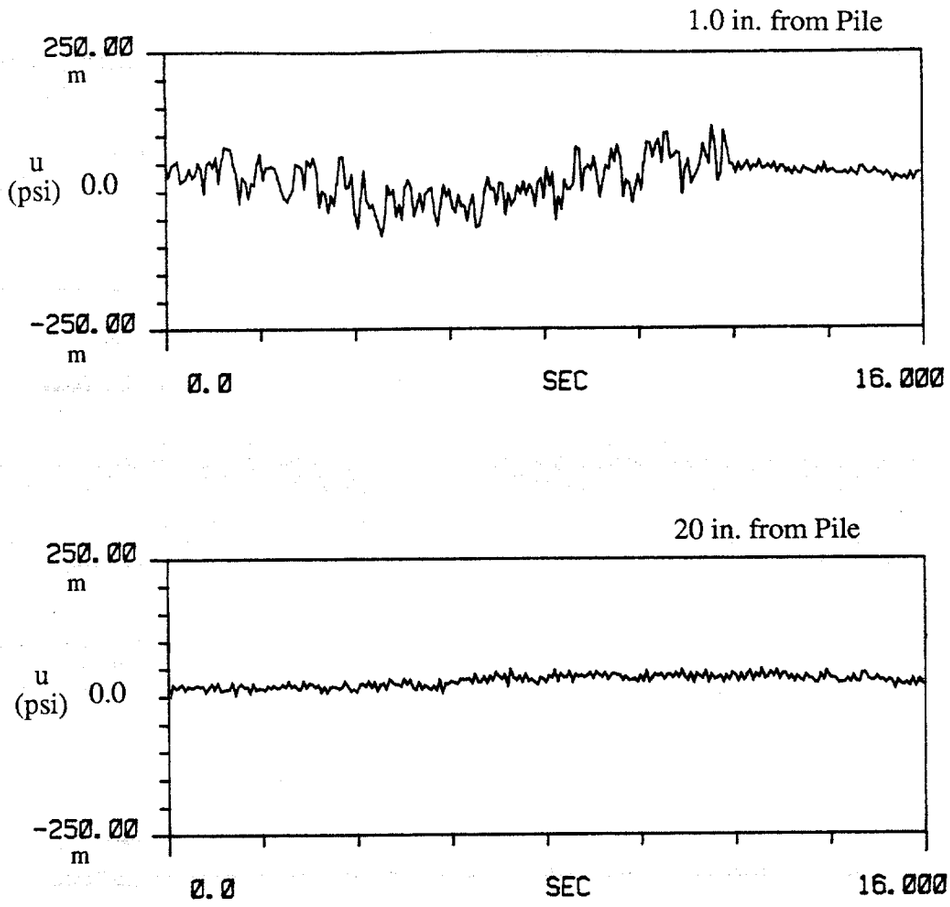

Fig. 7.21. Time History Measurements of Near and Far Field Pore Water Pressures, Test T2, [m = milli].

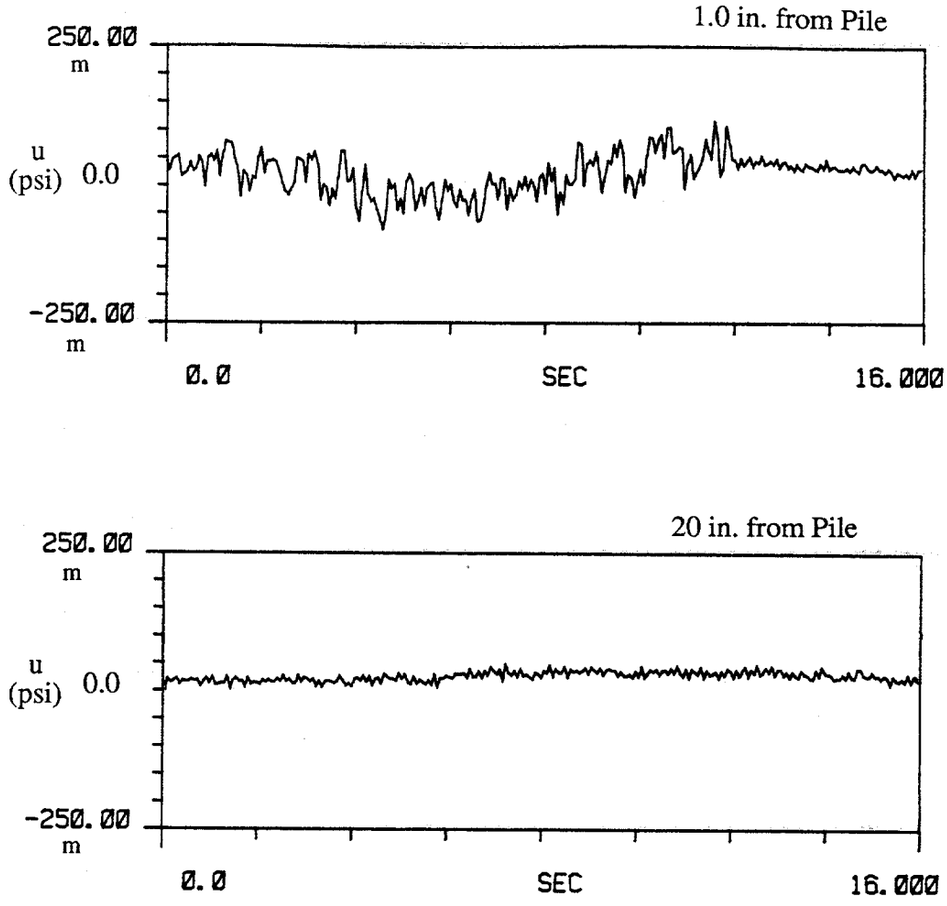

Fig. 7.21. Time History Measurements of Near and Far Field Pore Water Pressures, Test T2, [m = milli].

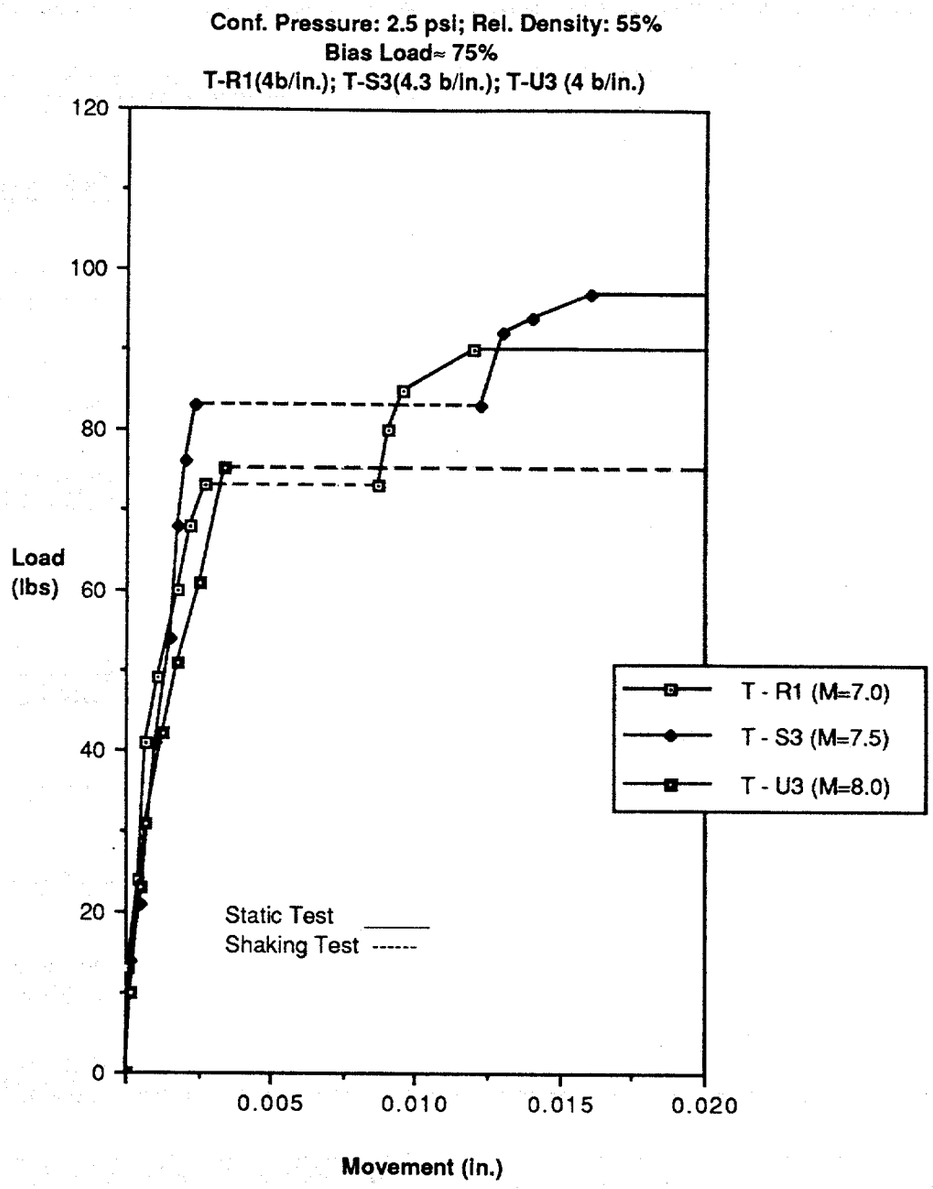

Fig. 7.23. Load-Movement Curves, Tests R1, S3, U3.

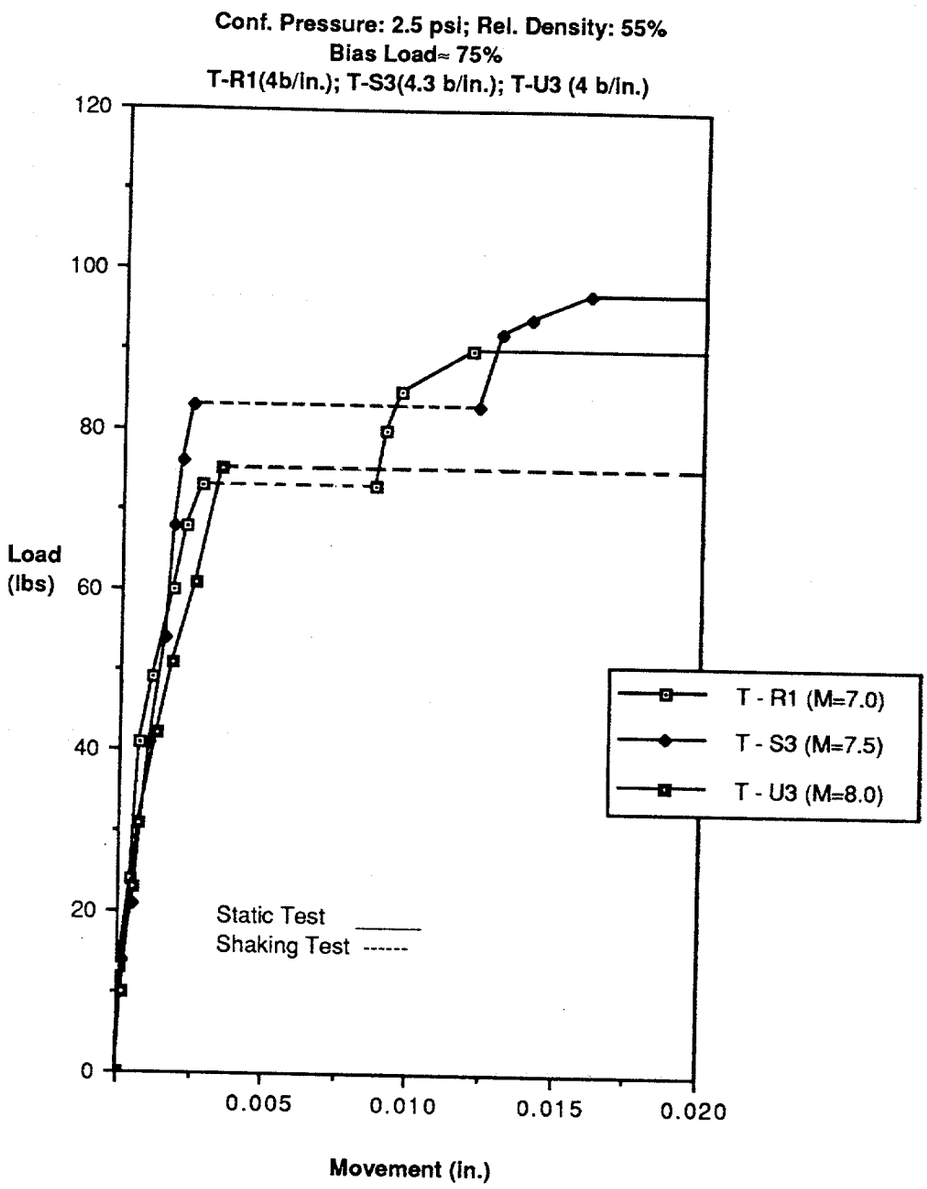

Fig. 7.23. Load-Movement Curves, Tests R1, S3, U3.

(c) Tests performed under horizontal motion, combined horizontal and vertical motion, and combined horizontal and vertical motion with stiff superstructure spring, event Magnitude of 7.5 and applied bias load of 60% of inferred static capacities (Fig. 7.25),

(d) Tests on piles averaging 4 blows/in. driving resistance under different applied bias loads (45%, 64% and 78%) for an event Magnitude of 8.0 (Fig. 7.26), and

(e) Tests on piles with applied bias load of 78% and event Magnitude of 8.0, for two mean confining pressures (2.5 psi and 5.0 psi) and two relative densities (55% and 70%) (Fig. 7.27).

Several observations can be made from the load-movement curves (Fig. 7.23 - 7.27) and post-shaking static capacities listed in Table 7.1:

(a) It is evident from Fig. 7.27 that failure conditions are more likely to happen for conditions of low confining pressures (shallow depths) and low relative densities. Larger pile movements during shaking tests were associated with large magnitude events and large applied bias loads,

(b) Post-test loss of static uplift capacity for tests performed with confining pressure of 2.5 psi and relative density of 55 are given in Table 7.2. The losses were determined by comparing measured capacity with capacity inferred from Fig. 6.3. The pile behavior from Magnitude 7.0 events (no loss of capacity after shaking) was similar to the behavior of piles subjected to purely vertical motion at Magnitude 8.0 (Chapter VI),

(c) Similar load-deformation trends and post-shaking static capacities for tests conducted with soft and stiff springs were observed, which indicates no significant effect of superstructure period on post-shaking static capacity, and

(d) Similar behavior was observed among dynamic tests conducted at a mean confining pressure of 5 psi and relative density of 55%, and at 2.5 psi and 70%, for an event Magnitude of 8.0 and equivalent bias load, which suggests an approximate cross-correlation between effective stress, relative density and ratio of bias load to static capacity.

DYNAMIC LOAD TRANSFER CHARACTERISTICS

Time histories of dynamic unit load transfer (normalized by the effective horizontal chamber pressure, σ'_h) for Test R1 ("stability" condition) and Test U3 ("failure" condition) are shown in Fig. 7.28 for the upper ("top") and lower ("bottom") halves of the pile, for bias loads of 75% of the inferred static capacities and event Magnitudes of 7.0 and 8.0. Few definitive time-dependent trends can be observed, mainly due to the random nature of the excitation source (seismic event). In both tests, most of the shear load is

(c) Tests performed under horizontal motion, combined horizontal and vertical motion, and combined horizontal and vertical motion with stiff superstructure spring, event Magnitude of 7.5 and applied bias load of 60% of inferred static capacities (Fig. 7.25),

(d) Tests on piles averaging 4 blows/in. driving resistance under different applied bias loads (45%, 64% and 78%) for an event Magnitude of 8.0 (Fig. 7.26), and

(e) Tests on piles with applied bias load of 78% and event Magnitude of 8.0, for two mean confining pressures (2.5 psi and 5.0 psi) and two relative densities (55% and 70%) (Fig. 7.27).

Several observations can be made from the load-movement curves (Fig. 7.23 - 7.27) and post-shaking static capacities listed in Table 7.1:

(a) It is evident from Fig. 7.27 that failure conditions are more likely to happen for conditions of low confining pressures (shallow depths) and low relative densities. Larger pile movements during shaking tests were associated with large magnitude events and large applied bias loads,

(b) Post-test loss of static uplift capacity for tests performed with confining pressure of 2.5 psi and relative density of 55 are given in Table 7.2. The losses were determined by comparing measured capacity with capacity inferred from Fig. 6.3. The pile behavior from Magnitude 7.0 events (no loss of capacity after shaking) was similar to the behavior of piles subjected to purely vertical motion at Magnitude 8.0 (Chapter VI),

(c) Similar load-deformation trends and post-shaking static capacities for tests conducted with soft and stiff springs were observed, which indicates no significant effect of superstructure period on post-shaking static capacity, and

(d) Similar behavior was observed among dynamic tests conducted at a mean confining pressure of 5 psi and relative density of 55%, and at 2.5 psi and 70%, for an event Magnitude of 8.0 and equivalent bias load, which suggests an approximate cross-correlation between effective stress, relative density and ratio of bias load to static capacity.

DYNAMIC LOAD TRANSFER CHARACTERISTICS

Time histories of dynamic unit load transfer (normalized by the effective horizontal chamber pressure, σ'_h) for Test R1 ("stability" condition) and Test U3 ("failure" condition) are shown in Fig. 7.28 for the upper ("top") and lower ("bottom") halves of the pile, for bias loads of 75% of the inferred static capacities and event Magnitudes of 7.0 and 8.0. Few definitive time-dependent trends can be observed, mainly due to the random nature of the excitation source (seismic event). In both tests, most of the shear load is

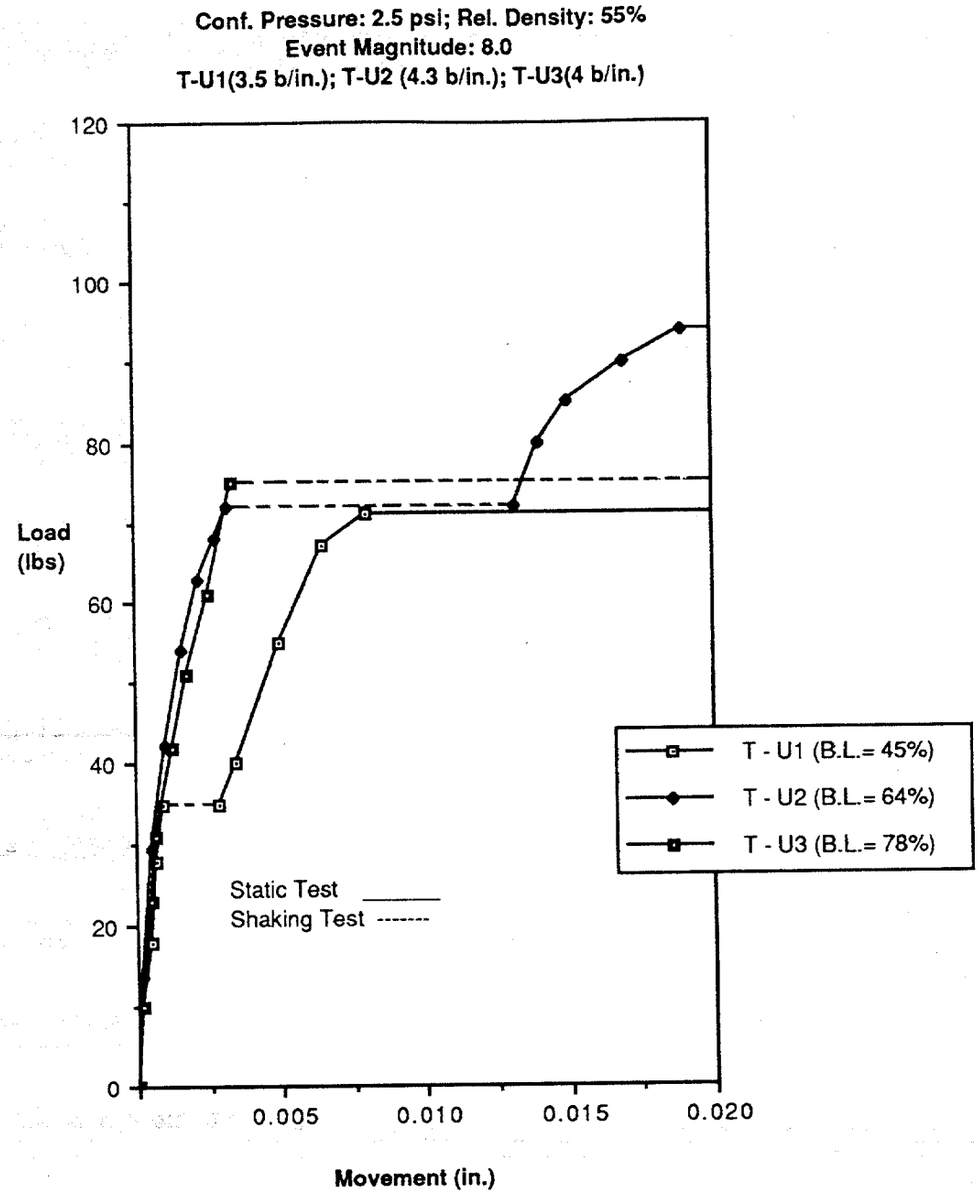

Fig. 7.26. Load-Movement Curves, Tests U1, U2, U3.

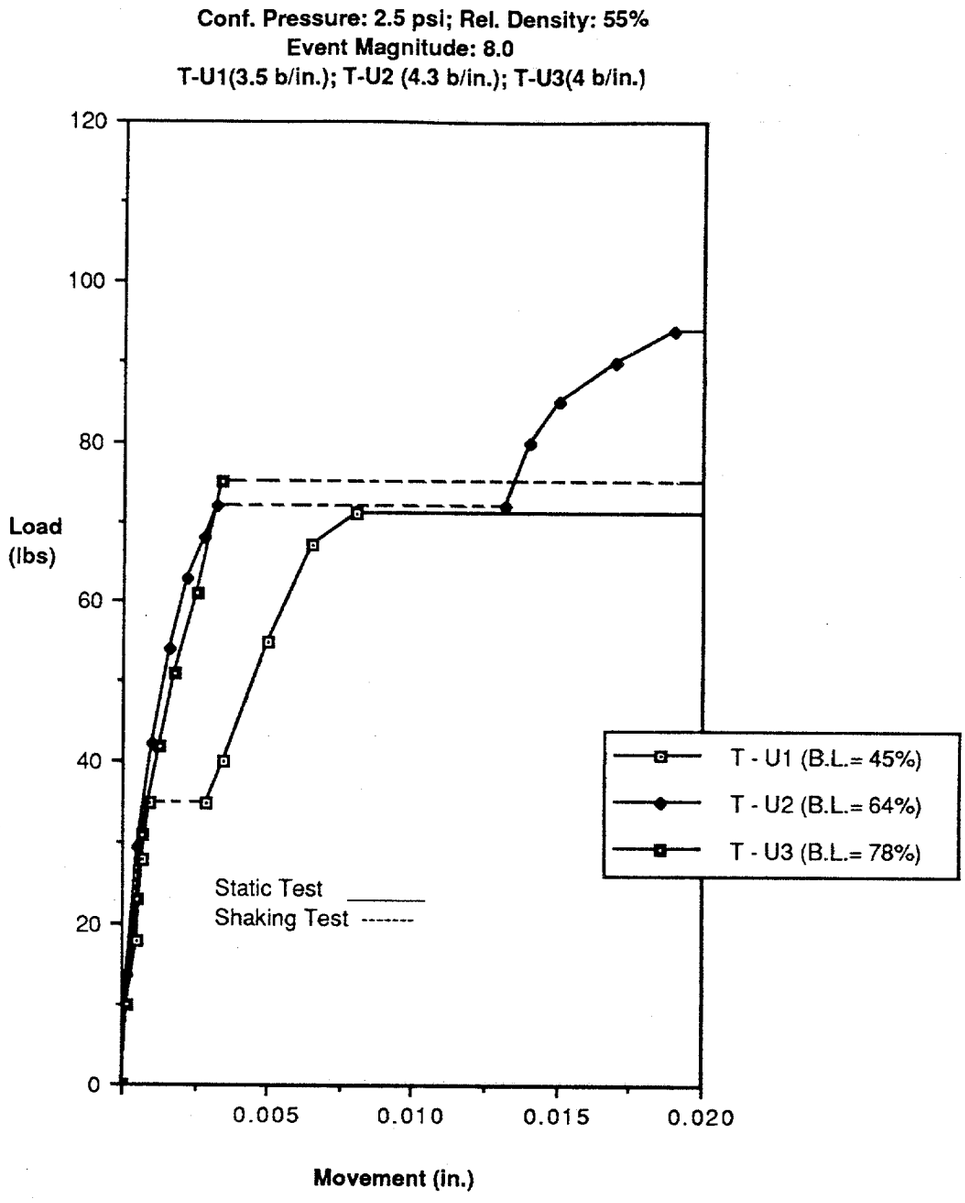

Fig. 7.26. Load-Movement Curves, Tests U1, U2, U3.

Table 7.2. Post-Test Loss of Static Uplift Capacity (Conf. Pressure = 2.5 psi, Rel. Density = 55%).

Magnitude	Static Bias (% of Static Capacity)	Per Cent Loss of Static Capacity
7.0	≤ 90	4
7.5	≥ 60 < 90	8
7.5[a]	62	12
7.5	≥ 90	Total Failure During Event
8.0	45	10
8.0	64	15
8.0	≥ 75	Total Failure During Event

a. Combined horizontal and vertical soil motions

Table 7.2. Post-Test Loss of Static Uplift Capacity (Conf. Pressure = 2.5 psi, Rel. Density = 55%).

Magnitude	Static Bias (% of Static Capacity)	Per Cent Loss of Static Capacity
7.0	≤ 90	4
7.5	≥ 60 < 90	8
7.5[a]	62	12
7.5	≥ 90	Total Failure During Event
8.0	45	10
8.0	64	15
8.0	≥ 75	Total Failure During Event

a. Combined horizontal and vertical soil motions

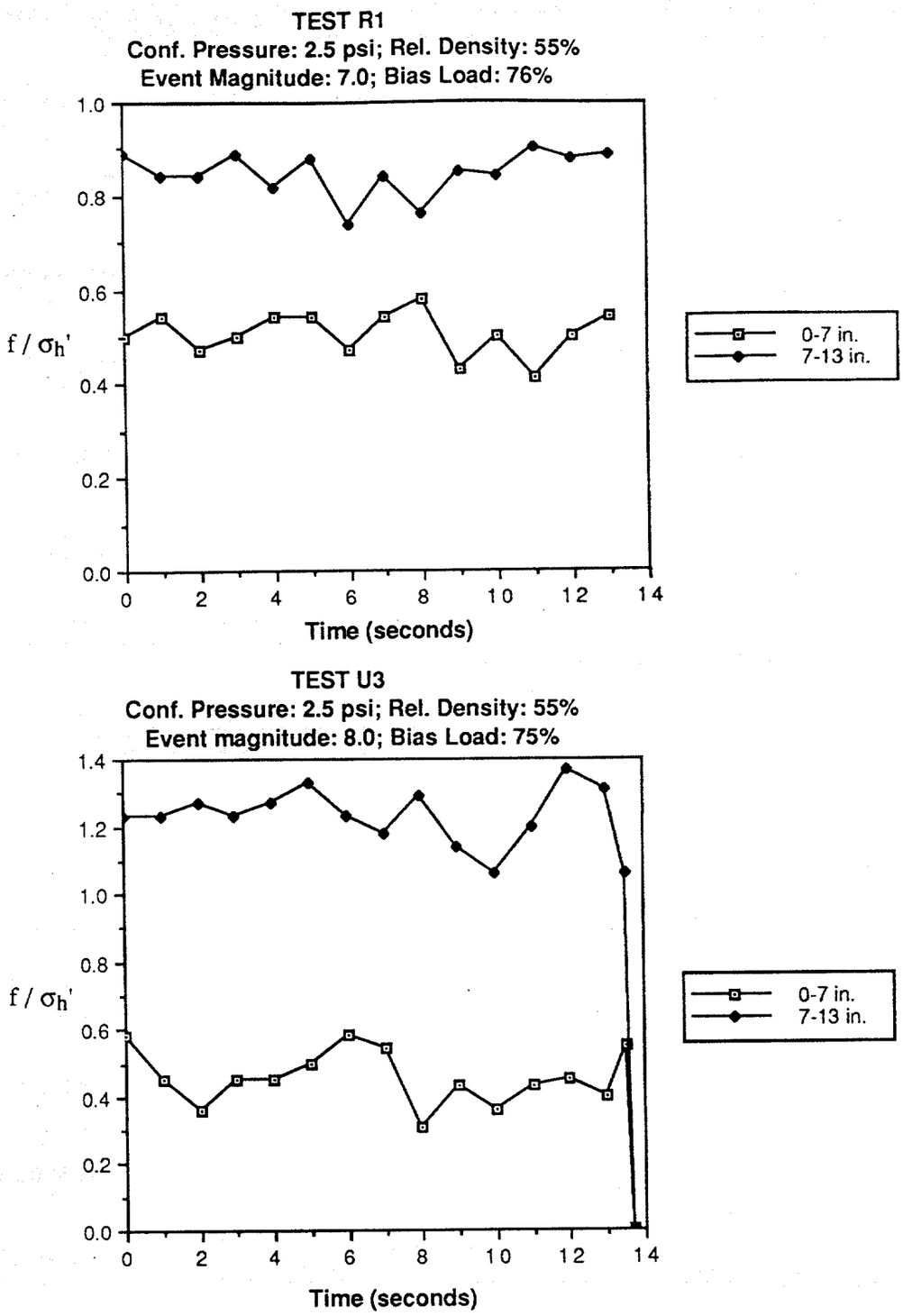

Fig. 7.28. Top and Bottom Time Histories of Normalized Unit Load Transfer, Tests R1 and U3.

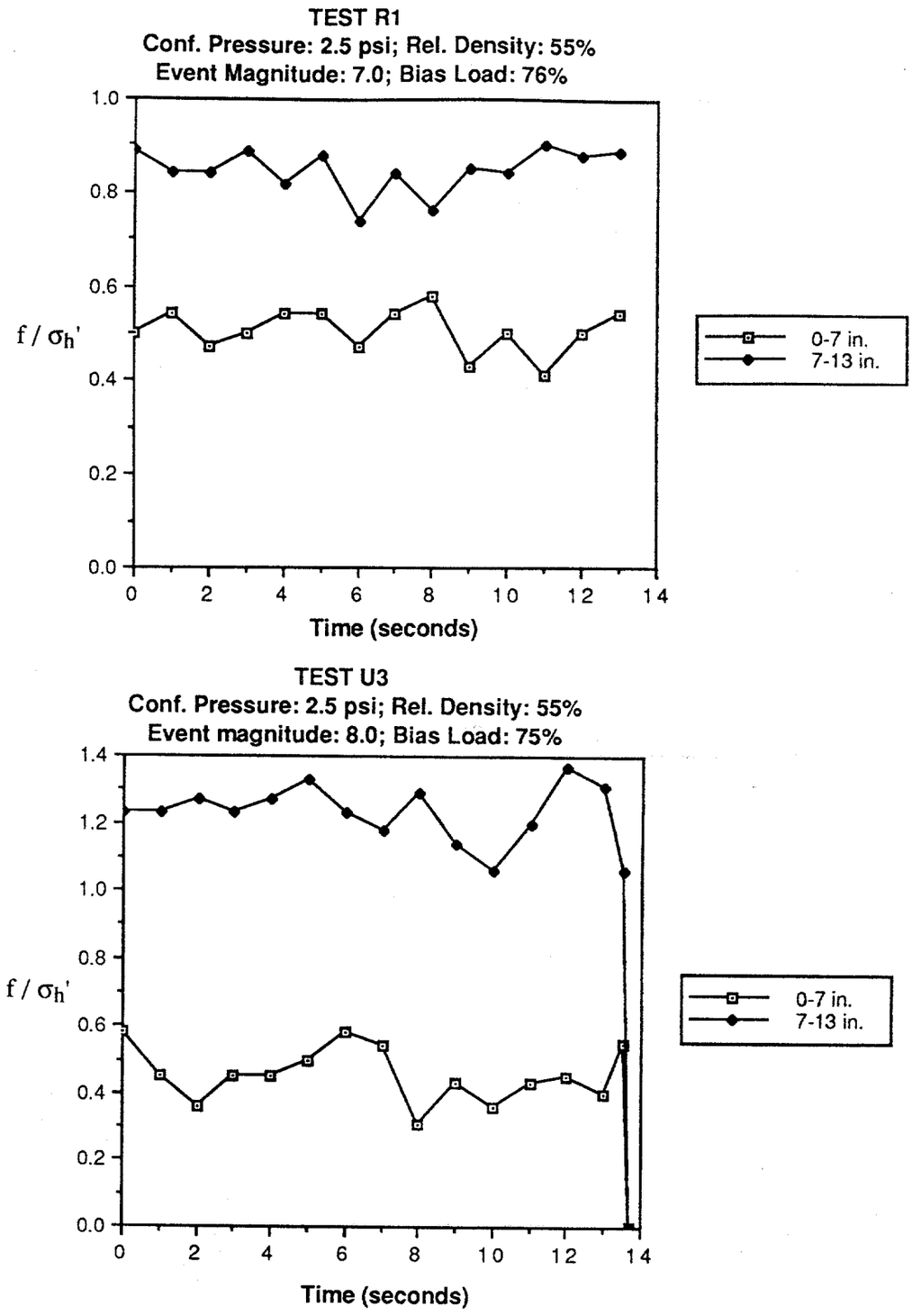

Fig. 7.28. Top and Bottom Time Histories of Normalized Unit Load Transfer, Tests R1 and U3.

were used to control the motion of a pressurized test chamber into which the model pile was driven.

An Instron testing machine was used to apply the programmed seismic motion to the soil contained in the test chamber, which was 21 in. in height and 20 in. in diameter. The model test pile, which was driven by impact into pressurized, submerged, very fine sand in the chamber, was a steel closed-ended cylinder, 1 in. in diameter and 16 in. long. The pile was instrumented internally with three levels of strain gages to sense axial load distribution. Two applied chamber pressures, 2.5 and 5.0 psi, simulated a range of depth-average, isotropic ambient effective soil stress conditions corresponding to pile penetrations of 20 and 40 ft, respectively. Movement at the pile head was monitored by a single LVDT. A flexible cable was attached to the head of the pile through which biased tension load was applied by mean of a dead-weight-and-spring-system to simulate the presence of a simple superstructure. The simulated seismic records were applied through the base of the chamber, while the biased tension load was applied simultaneously and continuously by the flexible cable to the head of the pile that protruded from the top of the test chamber. Two miniature pore water pressure transducers were also buried within the chamber to sense the build up of pore water pressure near the wall of the pile and several inches from the pile wall.

In order to scale the effect of drainage distance and its effects on pore pressure generation and dissipation, both the simulated seismic record (acceleration and/or time axes) and soil permeability were scaled in some tests with vertical motion and for all tests with horizontal motion. A mixture of a very fine sand and finely ground glass beads, termed micro-fine sand, was used as the model sand for the latter purpose. Sand was placed in the test chamber by raining through air.

A number of static controlled load (CL) tests and controlled deformation (CD) tests were conducted to confirm repeatability of uplift capacity, sensitivity of uplift capacity to relative density, confining pressure and failure criteria. A relation between penetration resistance and uplift static capacity was derived to infer the percentile of the static capacity corresponding to the applied bias load in dynamic (simulated seismic loading) tests. Dynamic tests were performed under conditions similar to those that existed in the static tests by applying the magnitude-scaled or magnitude-and-frequency-scaled displacement time histories for the selected seismic event to the soil while the pile was held under biased

were used to control the motion of a pressurized test chamber into which the model pile was driven.

An Instron testing machine was used to apply the programmed seismic motion to the soil contained in the test chamber, which was 21 in. in height and 20 in. in diameter. The model test pile, which was driven by impact into pressurized, submerged, very fine sand in the chamber, was a steel closed-ended cylinder, 1 in. in diameter and 16 in. long. The pile was instrumented internally with three levels of strain gages to sense axial load distribution. Two applied chamber pressures, 2.5 and 5.0 psi, simulated a range of depth-average, isotropic ambient effective soil stress conditions corresponding to pile penetrations of 20 and 40 ft, respectively. Movement at the pile head was monitored by a single LVDT. A flexible cable was attached to the head of the pile through which biased tension load was applied by mean of a dead-weight-and-spring-system to simulate the presence of a simple superstructure. The simulated seismic records were applied through the base of the chamber, while the biased tension load was applied simultaneously and continuously by the flexible cable to the head of the pile that protruded from the top of the test chamber. Two miniature pore water pressure transducers were also buried within the chamber to sense the build up of pore water pressure near the wall of the pile and several inches from the pile wall.

In order to scale the effect of drainage distance and its effects on pore pressure generation and dissipation, both the simulated seismic record (acceleration and/or time axes) and soil permeability were scaled in some tests with vertical motion and for all tests with horizontal motion. A mixture of a very fine sand and finely ground glass beads, termed micro-fine sand, was used as the model sand for the latter purpose. Sand was placed in the test chamber by raining through air.

A number of static controlled load (CL) tests and controlled deformation (CD) tests were conducted to confirm repeatability of uplift capacity, sensitivity of uplift capacity to relative density, confining pressure and failure criteria. A relation between penetration resistance and uplift static capacity was derived to infer the percentile of the static capacity corresponding to the applied bias load in dynamic (simulated seismic loading) tests. Dynamic tests were performed under conditions similar to those that existed in the static tests by applying the magnitude-scaled or magnitude-and-frequency-scaled displacement time histories for the selected seismic event to the soil while the pile was held under biased

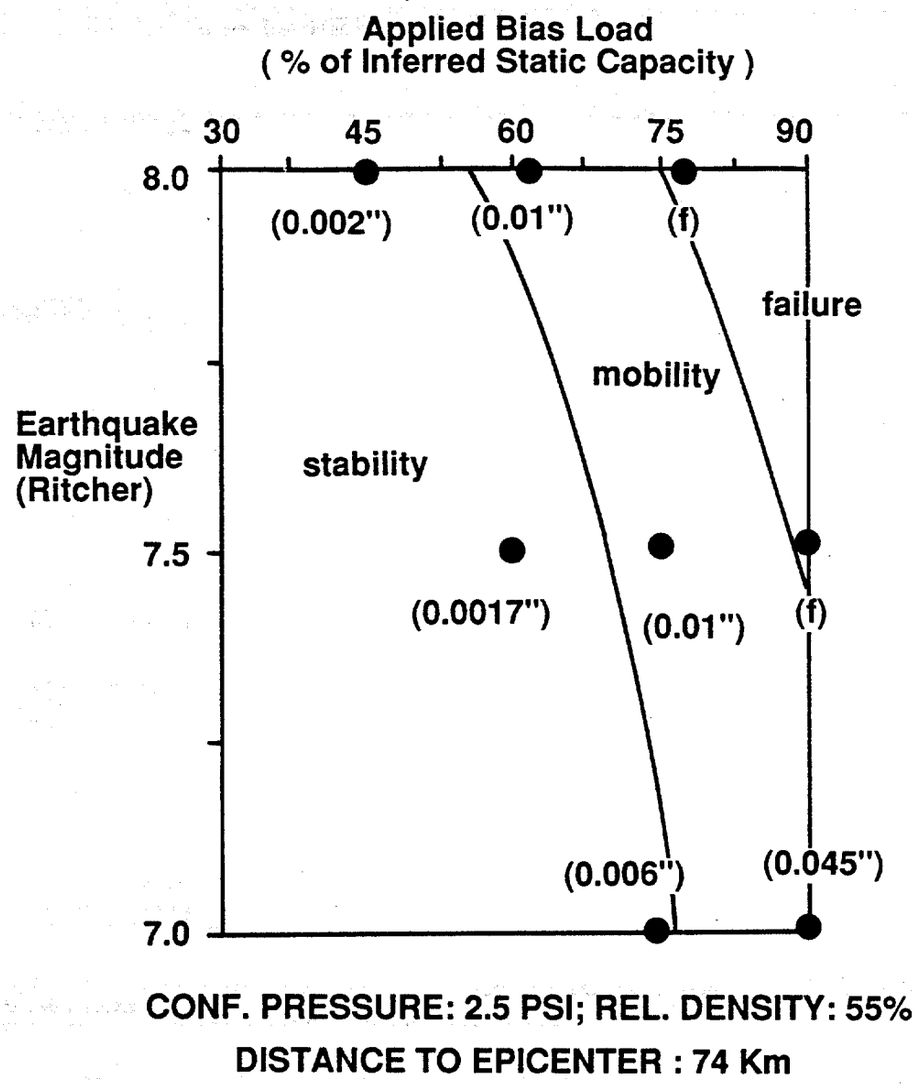

Fig. 8.1. Contour Plot of Stability, Mobility and Failure Conditions Under Horizontal Earthquake Loading (Confining Pressure = 2.5 psi and Relative Density = 55%).

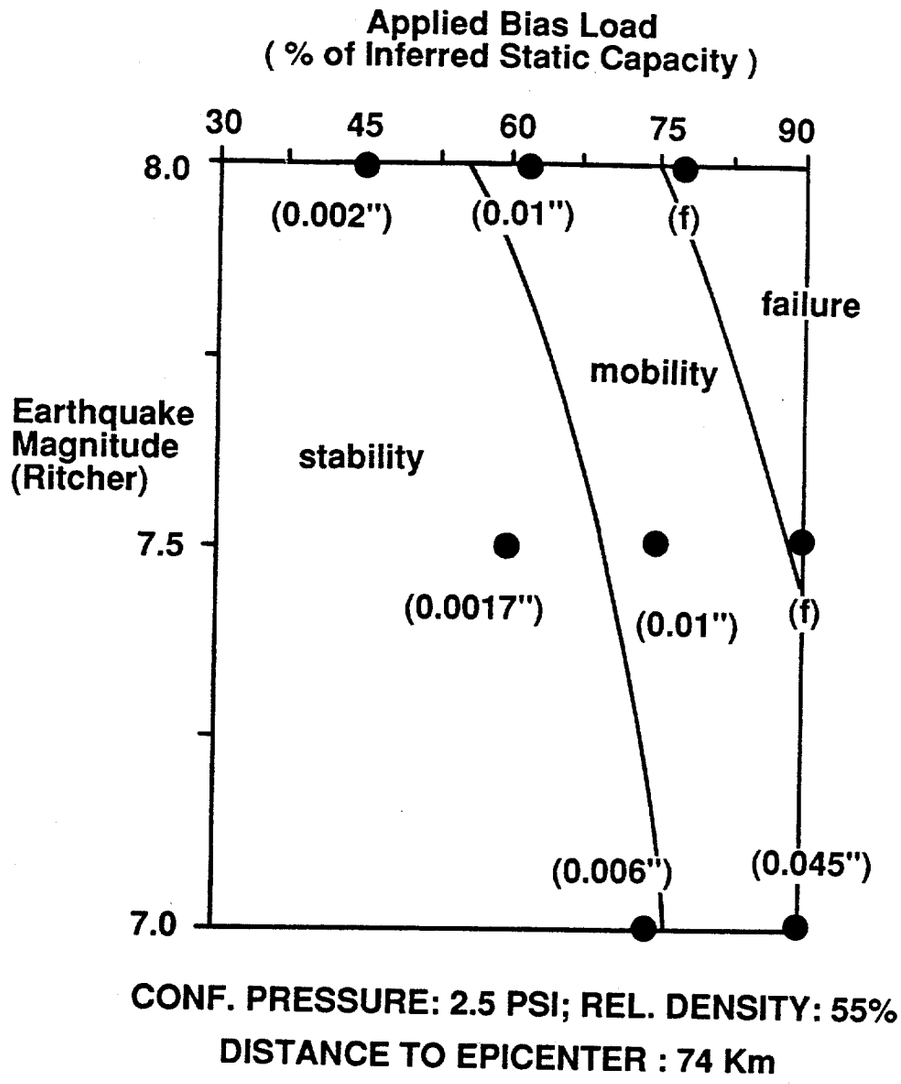

Fig. 8.1. Contour Plot of Stability, Mobility and Failure Conditions Under Horizontal Earthquake Loading (Confining Pressure = 2.5 psi and Relative Density = 55%).

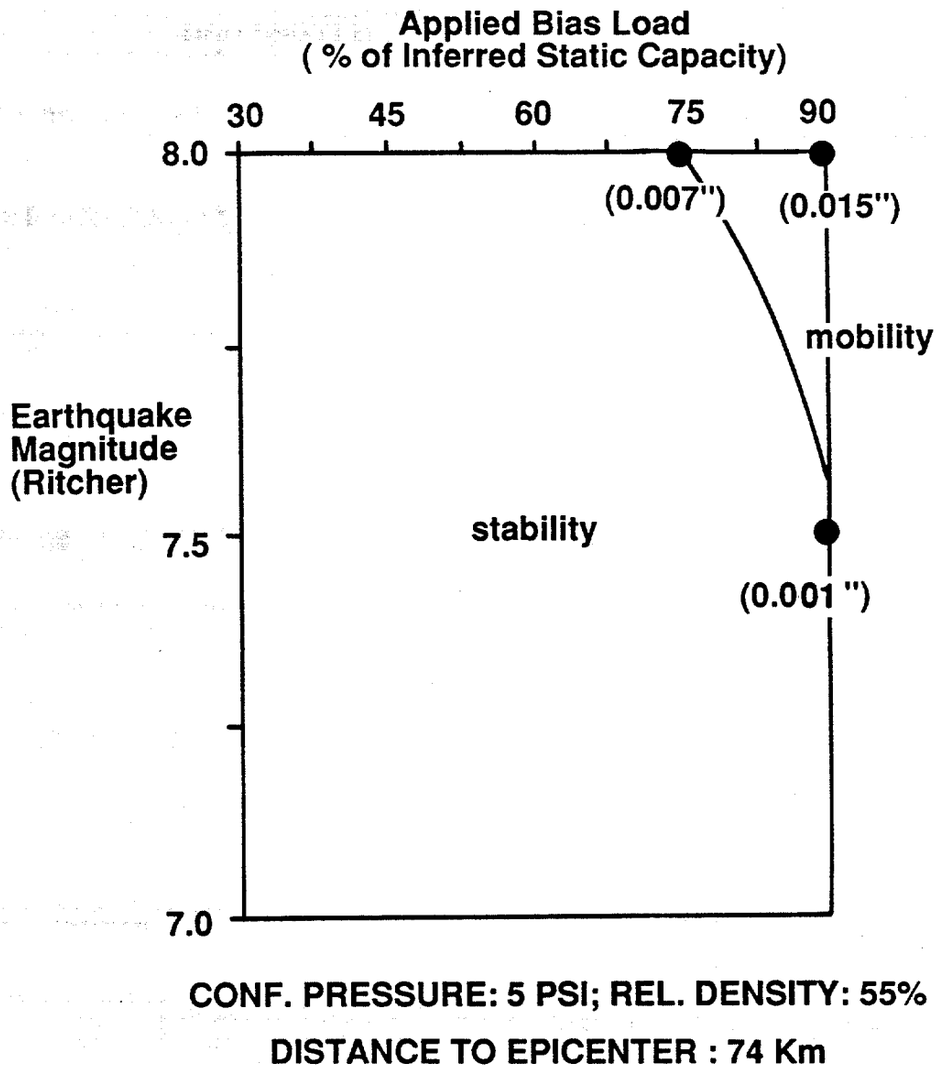

Fig. 8.3. Contour Plot of Stability and Mobility Conditions Under Horizontal Earthquake Loading (Confining Pressure = 5.0 psi and Relative Density = 55%).

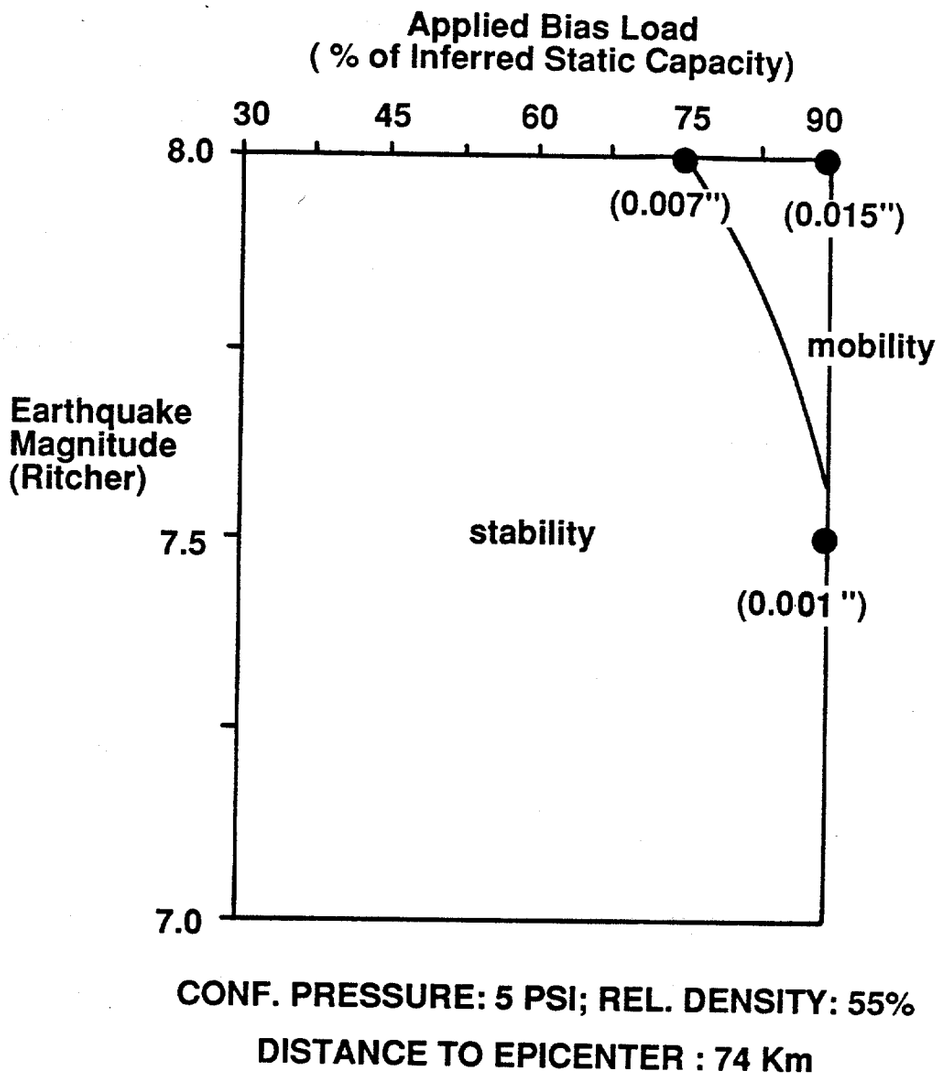

Fig. 8.3. Contour Plot of Stability and Mobility Conditions Under Horizontal Earthquake Loading (Confining Pressure = 5.0 psi and Relative Density = 55%).

Stated in other terms, the pile should be designed for a factor of safety against pullout of 1/0.60 = 1.67, provided other factors, such as wave loading simultaneous with seismic loading, are not included in the design condition. For design analyses that consider the structure to be ductile, one might design at the "mobility "-"failure" interface.

For piles 40 ft long (or the upper 40 ft of longer piles) and for medium dense sites it was not possible to develop contours of stability-mobility for varying epicentral distances, since not enough tests were conducted at high biased loads in the chamber when a 5 psi confining pressure or a relative density of 70% was employed. However, one can use Figs. 8.2 and 8.3 to ascertain the permissible static biased load for a 74 km epicentral distance (or greater). These figures indicate stability for all Richter Magnitudes up to 8 provided that the factor of safety against static uplift capacity is 1.33 or higher. Because this value is less than the minimum factor of safety of 1.5 normally assumed for static or quasi-static conditions, at this epicentral distance earthquake conditions would not control the design. Further research would be critical at smaller epicentral distances in medium dense sands and for long piles.

Phenomenologically, it is clear from a comparison of Figs. 8.1 and 8.3 that the pile foundation of a TLP or a biased-loaded hydraulic structure should consist of fewer, longer piles, rather than more, shorter piles to develop the maximum resistance to pullout failure during earthquakes.

This design hypothesis is based on the assumption that the magnitude of the structural feedback forces have been modelled correctly in this study for a particular case. This will have been correct only if the superstructure behaves as a simple mass-spring system that responds only to the vertical motion of the pile, which is approximately correct for a TLP in a essentially calm sea state. Other resources of dynamic superstructure loading, such as wave and inertial loadings, may cause the magnitude of pile loading to be different from the simple feedback loading reproduced in these experiments. In the absence of information on this effect, it is suggested that the factor of safety be applied not to the static biased load but rather to the sum of the static biased load and the peak dynamic load applied to the pile by the superstructure during the seismic event.

CONCLUSIONS

The following conclusions have been drawn from this study:

Stated in other terms, the pile should be designed for a factor of safety against pullout of 1/0.60 = 1.67, provided other factors, such as wave loading simultaneous with seismic loading, are not included in the design condition. For design analyses that consider the structure to be ductile, one might design at the "mobility "-"failure" interface.

For piles 40 ft long (or the upper 40 ft of longer piles) and for medium dense sites it was not possible to develop contours of stability-mobility for varying epicentral distances, since not enough tests were conducted at high biased loads in the chamber when a 5 psi confining pressure or a relative density of 70% was employed. However, one can use Figs. 8.2 and 8.3 to ascertain the permissible static biased load for a 74 km epicentral distance (or greater). These figures indicate stability for all Richter Magnitudes up to 8 provided that the factor of safety against static uplift capacity is 1.33 or higher. Because this value is less than the minimum factor of safety of 1.5 normally assumed for static or quasi-static conditions, at this epicentral distance earthquake conditions would not control the design. Further research would be critical at smaller epicentral distances in medium dense sands and for long piles.

Phenomenologically, it is clear from a comparison of Figs. 8.1 and 8.3 that the pile foundation of a TLP or a biased-loaded hydraulic structure should consist of fewer, longer piles, rather than more, shorter piles to develop the maximum resistance to pullout failure during earthquakes.

This design hypothesis is based on the assumption that the magnitude of the structural feedback forces have been modelled correctly in this study for a particular case. This will have been correct only if the superstructure behaves as a simple mass-spring system that responds only to the vertical motion of the pile, which is approximately correct for a TLP in a essentially calm sea state. Other resources of dynamic superstructure loading, such as wave and inertial loadings, may cause the magnitude of pile loading to be different from the simple feedback loading reproduced in these experiments. In the absence of information on this effect, it is suggested that the factor of safety be applied not to the static biased load but rather to the sum of the static biased load and the peak dynamic load applied to the pile by the superstructure during the seismic event.

CONCLUSIONS

The following conclusions have been drawn from this study:

viscoelastic effects and loss in capacity, mainly in skin friction) were slightly lower than those capacities found by others [i.e., Poulos (1982)] in tests with direct loading of the pile under a slow rate of cyclic loading.

(6) The effect of superposition of soil motion components was reflected by an additional 5% reduction in post-shaking static capacity compared to those post-shaking capacities in tests performed under purely horizontal soil motion. As far as liquefaction potential is concerned, the effect of superposition of soil motion was not conclusive, since liquefaction did not occurred in either of the tests with combined motion.

(7) The failure mechanism of the pile during an event of Magnitude 8.0 can be explained as follows. Shearing strains in the soil generated primarily by the sudden repetitive pullouts of the pile (in response of the superstructure feedback), and additional shearing strains in soil generated by the horizontal component of the seismic event induced buildup of pore water pressures in the soil to a level high enough to promote significant degradation of skin friction to produce complete failure. This event seems to have taken place before liquefaction in the free field. Evidence exists that failure started at or near the toe of the pile. Once the pile move significantly upward, the effective stress in the soil beneath the toe was reduced to the point when the soil liquefied. This occurrence has important implications relative to potential rapid progressive failure in pile groups.

(8) By inference from load transfer data during static tests, the radial effective stress at the soil-pile interface at pile failure were approximately twice the ambient values applied to the chamber, mainly due to the insertion of the pile in the soil mass and pile driving effects. This effect may have made it necessary for higher pore water pressures to develop at the pile-soil interface than were measured in the soil mass near the wall of the pile before failure occurred.

(9) Excess water pressure produced at the soil surface by the induced vertical motion of a great depth of water overlying the seafloor was shown to be potentially important in producing shallow liquefaction in the soil deposit, as computed instantaneous water pressures for a typical site with 1000 ft of water produced by the vertical component of the scaled earthquake exceeded the effective stresses in the chamber. The interaction of the seafloor and overlying water was not investigated experimentally in this study. However, since the simulated vertical seismic motion did not degrade the soil in the absence of a deep

viscoelastic effects and loss in capacity, mainly in skin friction) were slightly lower than those capacities found by others [i.e., Poulos (1982)] in tests with direct loading of the pile under a slow rate of cyclic loading.

(6) The effect of superposition of soil motion components was reflected by an additional 5% reduction in post-shaking static capacity compared to those post-shaking capacities in tests performed under purely horizontal soil motion. As far as liquefaction potential is concerned, the effect of superposition of soil motion was not conclusive, since liquefaction did not occurred in either of the tests with combined motion.

(7) The failure mechanism of the pile during an event of Magnitude 8.0 can be explained as follows. Shearing strains in the soil generated primarily by the sudden repetitive pullouts of the pile (in response of the superstructure feedback), and additional shearing strains in soil generated by the horizontal component of the seismic event induced buildup of pore water pressures in the soil to a level high enough to promote significant degradation of skin friction to produce complete failure. This event seems to have taken place before liquefaction in the free field. Evidence exists that failure started at or near the toe of the pile. Once the pile move significantly upward, the effective stress in the soil beneath the toe was reduced to the point when the soil liquefied. This occurrence has important implications relative to potential rapid progressive failure in pile groups.

(8) By inference from load transfer data during static tests, the radial effective stress at the soil-pile interface at pile failure were approximately twice the ambient values applied to the chamber, mainly due to the insertion of the pile in the soil mass and pile driving effects. This effect may have made it necessary for higher pore water pressures to develop at the pile-soil interface than were measured in the soil mass near the wall of the pile before failure occurred.

(9) Excess water pressure produced at the soil surface by the induced vertical motion of a great depth of water overlying the seafloor was shown to be potentially important in producing shallow liquefaction in the soil deposit, as computed instantaneous water pressures for a typical site with 1000 ft of water produced by the vertical component of the scaled earthquake exceeded the effective stresses in the chamber. The interaction of the seafloor and overlying water was not investigated experimentally in this study. However, since the simulated vertical seismic motion did not degrade the soil in the absence of a deep

REFERENCES

Annual Book of ASTM Standards, American Society for Testing and Materials, Soil and Rock/Building Stones, Vol. 04.08, 1988, pp. 554-572.

Bea, R. G., "Dynamic Response of Piles in Offshore Platforms," Dynamic Response of Pile Foundations: Analytical Aspects, Ed. by M. W. O'Neill and R. Dobry, ASCE, October, 1980, pp. 80-103.

Blaney, G.W., Muster, G.L.,II, and O'Neill, M.W., "Vertical Vibration Test of a Full-Scale Pile Group," Geotechnical Special Publication No. 11, Ed. by T. Nogami, ASCE, April, 1987, pp. 149-165.

Bradshaw, H., Barton, R.R., and McKenzie, R.H., "The Hutton TLP Foundation Design," Proceedings, Sixteen Offshore Technology Conference, Vol. 3, Houston, Texas, 1984, pp. 263-273.

Briaud, J.L., and Terry, T. A., "Rate Effect for Vertical and Lateral Pile Response," Proceedings, Third International Conference on Numerical Methods in Offshore Piling, Institut Francais du Petrole and Laboratorie Central des Ponts et Chausses, Nantes, France, May, 1986, pp. 387-405.

Casagrande, A., "Liquefaction and Cyclic Deformation of Sands, A critical Review," Proceedings, Fifth Panamerican Conference on Soil Mechanics and Foundation Engineering, Buenos Aires, Argentina, Nov., 1975, Harvard Soil Mechanics Series No. 88.

Castro, G., and Poulos, J., "Factors Affecting Liquefaction and Cyclic Mobility," Liquefaction Problems in Geotechnical Engineering, ASCE National Convention, September, 1976, pp. 105-138.

Castro, G., "Liquefaction of Sands," Harvard Soil Mechanics Series, No. 81, Harvard University, Cambridge, Mass., January, 1969.

Chakrabarti, S., Shaw, D., Stephenson, D.E., and Wijaya-Kumar, B.V.K, "Digital Signal Processing of Geotechnical Data," Journal of Engineering Mechanics Division, ASCE, Vol. 112, January, 1986, pp. 70-84.

Chang, S.F., and Hanna, T. H.,"Repeated Loading on Single Piles in Sand," Journal of the Geotechnical Engineering Division, ASCE, 1980, Vol 106, No. GT2, pp. 171-188.

Cooley, J.W., and Tukey, J.W., "An Algorithm for Machine Calculation of Complex Fourier Series," Mathematical Computation, Vol. 19, 1965, pp. 297-301.

De Alba, P., "Group Effects on Piles in a Liquefying Sand Deposit," Geotechnical Practice in Offshore Engineering, ASCE, Ed. by S.G. Wright, April, 1983, pp. 300-314.

DeGregorio, V.B., "Loading Systems, Sample Preparation and Liquefaction," Journal of the Geotechnical Engineering Division, ASCE, Vol. 116, No. 5, May, 1990, pp. 805-821.

Dobry, R., and Gazetas, G., "Dynamic Stiffness and Damping of Foundations by Simple methods," Ed. by G. Gazetas and E. Selig, ASCE, October, 1985, pp. 75-109.

REFERENCES

Annual Book of ASTM Standards, American Society for Testing and Materials, Soil and Rock/Building Stones, Vol. 04.08, 1988, pp. 554-572.

Bea, R. G., "Dynamic Response of Piles in Offshore Platforms," Dynamic Response of Pile Foundations: Analytical Aspects, Ed. by M. W. O'Neill and R. Dobry, ASCE, October, 1980, pp. 80-103.

Blaney, G.W., Muster, G.L.,II, and O'Neill, M.W., "Vertical Vibration Test of a Full-Scale Pile Group," Geotechnical Special Publication No. 11, Ed. by T. Nogami, ASCE, April, 1987, pp. 149-165.

Bradshaw, H., Barton, R.R., and McKenzie, R.H., "The Hutton TLP Foundation Design," Proceedings, Sixteen Offshore Technology Conference, Vol. 3, Houston, Texas, 1984, pp. 263-273.

Briaud, J.L., and Terry, T. A., "Rate Effect for Vertical and Lateral Pile Response," Proceedings, Third International Conference on Numerical Methods in Offshore Piling, Institut Francais du Petrole and Laboratorie Central des Ponts et Chausses, Nantes, France, May, 1986, pp. 387-405.

Casagrande, A., "Liquefaction and Cyclic Deformation of Sands, A critical Review," Proceedings, Fifth Panamerican Conference on Soil Mechanics and Foundation Engineering, Buenos Aires, Argentina, Nov., 1975, Harvard Soil Mechanics Series No. 88.

Castro, G., and Poulos, J., "Factors Affecting Liquefaction and Cyclic Mobility," Liquefaction Problems in Geotechnical Engineering, ASCE National Convention, September, 1976, pp. 105-138.

Castro, G., "Liquefaction of Sands," Harvard Soil Mechanics Series, No. 81, Harvard University, Cambridge, Mass., January, 1969.

Chakrabarti, S., Shaw, D., Stephenson, D.E., and Wijaya-Kumar, B.V.K, "Digital Signal Processing of Geotechnical Data," Journal of Engineering Mechanics Division, ASCE, Vol. 112, January, 1986, pp. 70-84.

Chang, S.F., and Hanna, T. H.,"Repeated Loading on Single Piles in Sand," Journal of the Geotechnical Engineering Division, ASCE, 1980, Vol 106, No. GT2, pp. 171-188.

Cooley, J.W., and Tukey, J.W., "An Algorithm for Machine Calculation of Complex Fourier Series," Mathematical Computation, Vol. 19, 1965, pp. 297-301.

De Alba, P., "Group Effects on Piles in a Liquefying Sand Deposit," Geotechnical Practice in Offshore Engineering, ASCE, Ed. by S.G. Wright, April, 1983, pp. 300-314.

DeGregorio, V.B., "Loading Systems, Sample Preparation and Liquefaction," Journal of the Geotechnical Engineering Division, ASCE, Vol. 116, No. 5, May, 1990, pp. 805-821.

Dobry, R., and Gazetas, G., "Dynamic Stiffness and Damping of Foundations by Simple methods," Ed. by G. Gazetas and E. Selig, ASCE, October, 1985, pp. 75-109.

Joyner, W.B., and Boore, D.M.," Measurement, Characteristics and Prediction of Strong Ground Motion," State-of-the-Art Report, Proceedings, Specialty Conference on Earthquake Engineering and Soil Dynamics II, ASCE, June, 1988, pp. 43-102.

Karlsrud, K., Nadim, F., and Haugen, T.,"Piles in Clay Under Cyclic Axial Loading: Field Tests and Computational Modelling," Proceedings, Third International Conference on Numerical Methods in Offshore Piling, Institut Francais du Petrole and Laboratorie Central des Ponts et Chausses, Nantes, France, May, 1986, pp. 165-190.

Lambson, M.D. and Craig, W,H., "Behavior of Piles under Axial Cyclic Loading," Proceedings, 20Th Offshore Technology Conference, Vol. 2, Houston, Texas, 1988, pp. 129-138.

Lee, K.L., and Seed, H.B.,"Cyclic Stress Conditions Causing Liquefaction of Sand," Journal of the Soil Mechanics and Foundation Division, ASCE, Vol. 93, SM1, Jan., 1967, pp. 47-70.

Martin, P.P., and Seed, H.B., "APOLLO, A Computer Program for the Analysis of Pore Pressure Generation and Dissipation in Horizontal Sand Layers During Cyclic or Earthquake Loading," Report No. EERC 78-21, Earthquake Engineering Research Center, 1978.

Mayne, P.W., and Kulhawy, F.H., "K_0-OCR Relationships in Soil," Journal of the Geotechnical Engineering Division, ASCE, Vol. 108, No. GT6, June, 1982, p. 863.

McAnoy, R.P.L., Cashman, A. C., and Purvis, D.,"Cyclic Tensile Testing of a Pile in Glacial Till," Proceedings, Second International Conference on Numerical Methods in Offshore Piling, ICE and The University of Texas, Austin, Texas, April, 1982, pp. 257-291.

Midorikawa, S., and Wakamatsu, K., "Intensity of Earthquake Ground Motion at Liquefied Sites," Soil and Foundations , Vol. 28, No. 2, June, 1988, pp. 73-84.

Mulilis, J.P., Chan, C.K., and Seed, H.B.,"The Effects of Method of Sample Preparation on the Cyclic Stress-Strain Behavior of Sand," Report No. EERC 75-18, Earthquake Engineering Research Center, 1975.

Muster, G. L., II, and O'Neill, M.W., "Dynamically Loaded Pile in Overconsolidated Clay," Geotechnical Testing Journal , ASTM, Vol. 9, No. 6, December, 1986, pp. 189-197.

Nogami, T. and Konagai, K., "Time Domain Axial Response of Dynamically Loaded Single Piles ," Journal of Engineering Mechanics, ASCE, Vol. 112, No. EM11, Nov. 1986, pp. 1241-1252.

Novak, M., and Aboul-Ella, F., "A Computer Program for Calculation of Stiffness and Damping in Layered Media," SACDA, University of Western Ontario, London, Ontario, June, 1979.

Page, R.A, Boore, D.M., Joyner, W,B., and Caulter, H.W., "Ground Motion Values for Use in the Seismic Design of the Trans-Alaska Pipeline System, USGS Circular 672, 1972.

Joyner, W.B., and Boore, D.M.," Measurement, Characteristics and Prediction of Strong Ground Motion," State-of-the-Art Report, Proceedings, Specialty Conference on Earthquake Engineering and Soil Dynamics II, ASCE, June, 1988, pp. 43-102.

Karlsrud, K., Nadim, F., and Haugen, T.,"Piles in Clay Under Cyclic Axial Loading: Field Tests and Computational Modelling," Proceedings, Third International Conference on Numerical Methods in Offshore Piling, Institut Francais du Petrole and Laboratorie Central des Ponts et Chausses, Nantes, France, May, 1986, pp. 165-190.

Lambson, M.D. and Craig, W,H., "Behavior of Piles under Axial Cyclic Loading," Proceedings, 20Th Offshore Technology Conference, Vol. 2, Houston, Texas, 1988, pp. 129-138.

Lee, K.L., and Seed, H.B.,"Cyclic Stress Conditions Causing Liquefaction of Sand," Journal of the Soil Mechanics and Foundation Division, ASCE, Vol. 93, SM1, Jan., 1967, pp. 47-70.

Martin, P.P., and Seed, H.B., "APOLLO, A Computer Program for the Analysis of Pore Pressure Generation and Dissipation in Horizontal Sand Layers During Cyclic or Earthquake Loading," Report No. EERC 78-21, Earthquake Engineering Research Center, 1978.

Mayne, P.W., and Kulhawy, F.H., "K_o-OCR Relationships in Soil," Journal of the Geotechnical Engineering Division, ASCE, Vol. 108, No. GT6, June, 1982, p. 863.

McAnoy, R.P.L., Cashman, A. C., and Purvis, D.,"Cyclic Tensile Testing of a Pile in Glacial Till," Proceedings, Second International Conference on Numerical Methods in Offshore Piling, ICE and The University of Texas, Austin, Texas, April, 1982, pp. 257-291.

Midorikawa, S., and Wakamatsu, K., "Intensity of Earthquake Ground Motion at Liquefied Sites," Soil and Foundations , Vol. 28, No. 2, June, 1988, pp. 73-84.

Mulilis, J.P., Chan, C.K., and Seed, H.B.,"The Effects of Method of Sample Preparation on the Cyclic Stress-Strain Behavior of Sand," Report No. EERC 75-18, Earthquake Engineering Research Center, 1975.

Muster, G. L., II, and O'Neill, M.W., "Dynamically Loaded Pile in Overconsolidated Clay," Geotechnical Testing Journal , ASTM, Vol. 9, No. 6, December, 1986, pp. 189-197.

Nogami, T. and Konagai, K., "Time Domain Axial Response of Dynamically Loaded Single Piles ," Journal of Engineering Mechanics, ASCE, Vol. 112, No. EM11, Nov. 1986, pp. 1241-1252.

Novak, M., and Aboul-Ella, F., "A Computer Program for Calculation of Stiffness and Damping in Layered Media," SACDA, University of Western Ontario, London, Ontario, June, 1979.

Page, R.A, Boore, D.M., Joyner, W,B., and Caulter, H.W., "Ground Motion Values for Use in the Seismic Design of the Trans-Alaska Pipeline System, USGS Circular 672, 1972.

Seed, H.B., and Wilson, S.D., "The Turnagain Heights Landslide in Anchorage, Alaska," Journal of the Soil Mechanics and Foundation Division, ASCE, Vol. 93 No.SM4, July, 1967, pp. 325-353.

Seed, H.B., "Evaluation of Soil Liquefaction Effects on Level Ground During Earthquakes," Liquefaction Problems in Geotechnical Engineering, ASCE National Convention, September, 1976, pp. 1-104.

Seed, H.B., Idriss, I.M., and Kiefer, F.W., "Characteristics of Rock Motions During Earthquakes," Journal of Soil Mechanics and Foundation Division, ASCE, Vol. 95, No. SM5, Sept., 1969, pp. 1199-1218.

Sleefe, G.E., and Engi, D., "Seafloor Response for Two Southern California Earthquakes," Proceedings, 1987 SEM Spring Conference on Experimental Mechanics, Houston, Texas, pp. 747-753.

Stokoe, K.H. II, and Nazarian , S., "Use of Rayleigh Waves in Liquefaction Studies," Measurements and Use of Shear Wave Velocity for Evaluating Dynamic Soil Properties, Ed. by R.D. Woods, ASCE, Denver, Colorado, 1985, pp. 1-17.

Tazoh, T., Shimizu, K., and Wakahara, T., " Seismic Observations and Analysis of Grouped Piles," Geotechnical Special Publication No. 11, Ed. By T. Nogami, ASCE, April, 1987, pp. 1-20.

Trifunac, M.D., "Preliminary Empirical Model for Scaling Fourier Amplitude Spectra of Strong Acceleration in Terms of Modified Mercalli Intensity and Recording Site Conditions," Earthquake Engineering and Structural Dynamics, Vol. 7, 1979, pp. 63-74.

Vaid, Y.P., and Negussey, D.," Relative Density of Pluviated Sand Samples," Soils and Foundations, Vol. 24, No. 2, June, 1984, pp. 101-105.

Vanzini, R., Rossetto, P., Ferro, G., and Manfredini, G.M., "Non-Linear Seismic Response Analysis of an Offshore Platform on Liquefiable Soil," Proceedings,Vol. 3, 20th Offshore Technology Conference, Houston, Texas, May, 1988, pp. 159-169.

Vesic, A.S., "Expansion of Cavities in Infinite Soil Mass," Journal of Soil Mechanics and Foundation Division, ASCE, Vol. 98, No. SM3, March, 1972, pp. 265-290.

Veyera, G.E., and Charlie, W.A.," Laboratory Study of Compressional Liquefaction," Journal of the Geotechnical Engineering Division, ASCE, Vol. 116, No.5, May, 1990, pp. 45-49.

Williams, A.N., and Mau, S.T., "Earthquake Response of Submerged Circular Arch," Journal of Waterways, Ports, Coastal, and Ocean Engineering, ASCE, Vol. 114, No. 4, July, 1988, p.410.

Yoshimi, Y., and Tokimatzu, K., "Settlement of Buildings on Saturated Sand During Earthquakes," Soils and Foundations, Vol. 17, No. 1, March, 1977, pp. 23-38.

Yoshimi, Y., Tamara, K., and Tokimatsu, K., "Liquefaction Resistance of Partially Saturated Sand," Soils and Foundations, Vol.. 29, No. 3, September, 1989, pp. 157-162.

Seed, H.B., and Wilson, S.D., "The Turnagain Heights Landslide in Anchorage, Alaska," Journal of the Soil Mechanics and Foundation Division, ASCE, Vol. 93 No.SM4, July, 1967, pp. 325-353.

Seed, H.B., "Evaluation of Soil Liquefaction Effects on Level Ground During Earthquakes," Liquefaction Problems in Geotechnical Engineering, ASCE National Convention, September, 1976, pp. 1-104.

Seed, H.B., Idriss, I.M., and Kiefer, F.W., "Characteristics of Rock Motions During Earthquakes," Journal of Soil Mechanics and Foundation Division, ASCE, Vol. 95, No. SM5, Sept., 1969, pp. 1199-1218.

Sleefe, G.E., and Engi, D., "Seafloor Response for Two Southern California Earthquakes," Proceedings, 1987 SEM Spring Conference on Experimental Mechanics, Houston, Texas, pp. 747-753.

Stokoe, K.H. II, and Nazarian , S., "Use of Rayleigh Waves in Liquefaction Studies," Measurements and Use of Shear Wave Velocity for Evaluating Dynamic Soil Properties, Ed. by R.D. Woods, ASCE, Denver, Colorado, 1985, pp. 1-17.

Tazoh, T., Shimizu, K., and Wakahara, T., " Seismic Observations and Analysis of Grouped Piles," Geotechnical Special Publication No. 11, Ed. By T. Nogami, ASCE, April, 1987, pp. 1-20.

Trifunac, M.D., "Preliminary Empirical Model for Scaling Fourier Amplitude Spectra of Strong Acceleration in Terms of Modified Mercalli Intensity and Recording Site Conditions," Earthquake Engineering and Structural Dynamics, Vol. 7, 1979, pp. 63-74.

Vaid, Y.P., and Negussey, D.," Relative Density of Pluviated Sand Samples," Soils and Foundations, Vol. 24, No. 2, June, 1984, pp. 101-105.

Vanzini, R., Rossetto, P., Ferro, G., and Manfredini, G.M., "Non-Linear Seismic Response Analysis of an Offshore Platform on Liquefiable Soil," Proceedings,Vol. 3, 20th Offshore Technology Conference, Houston, Texas, May, 1988, pp. 159-169.

Vesic, A.S., "Expansion of Cavities in Infinite Soil Mass," Journal of Soil Mechanics and Foundation Division, ASCE, Vol. 98, No. SM3, March, 1972, pp. 265-290.

Veyera, G.E., and Charlie, W.A.," Laboratory Study of Compressional Liquefaction," Journal of the Geotechnical Engineering Division, ASCE, Vol. 116, No.5, May, 1990, pp. 45-49.

Williams, A.N., and Mau, S.T., "Earthquake Response of Submerged Circular Arch," Journal of Waterways, Ports, Coastal, and Ocean Engineering, ASCE, Vol. 114, No. 4, July, 1988, p.410.

Yoshimi, Y., and Tokimatzu, K., "Settlement of Buildings on Saturated Sand During Earthquakes," Soils and Foundations, Vol. 17, No. 1, March, 1977, pp. 23-38.

Yoshimi, Y., Tamara, K., and Tokimatsu, K., "Liquefaction Resistance of Partially Saturated Sand," Soils and Foundations, Vol.. 29, No. 3, September, 1989, pp. 157-162.

Appendix B

Calibration Equations

Appendix B

Calibration Equations

Table B.1. Pore Water Pressure Transducer (PDCR 81) Calibration Equation

Transducer Serial No.	Calibration Equation
4254	p (psi) = 0.1484 x (mv/10v)
3336	p (psi) = 0.131 x (mv/10v)

Table B.2. Test Chamber Calibration

Applied Pressure at Contol Panel (psi)	Measured Pressure at Pressure Cell (psi)	
	Sensotec 124296	Sensotec 124297
0	0.1	0.05
6	5.0	6.0
10	9.0	10.0
15	13.8	14.8
20	18.5	19.5
25	22.5	24.0
30	28.0	29.0

Table B.1. Pore Water Pressure Transducer (PDCR 81) Calibration Equation

Transducer Serial No.	Calibration Equation
4254	p (psi) = 0.1484 x (mv/10v)
3336	p (psi) = 0.131 x (mv/10v)

Table B.2. Test Chamber Calibration

Applied Pressure at Contol Panel (psi)	Measured Pressure at Pressure Cell (psi)	
	Sensotec 124296	Sensotec 124297
0	0.1	0.05
6	5.0	6.0
10	9.0	10.0
15	13.8	14.8
20	18.5	19.5
25	22.5	24.0
30	28.0	29.0

Considering SJR sand as the prototype sand, $\phi' = 39^o$ at Dr = 55% (letting $Dr_m = Dr_p$), then

$$K_{op} = (0.371)(1.290) = 0.48, \quad \text{and}$$

$$(\sigma_o'_{av})_p = 20(\gamma)((1+ 2K_{op})/ 3) = 719 \text{ psf} \cong 5.0 \text{ psi}.$$

Now, if

$$(\sigma_o'_{av})_m = (\sigma_o'_{av})_p \quad \text{(effective stress similitude), and}$$
$$\gamma_m \cong \gamma_p,$$

then for Eq. C.1. to hold,

$$(L_{50\%})_m \times n = (L_{67\%})_p , \qquad (C.3)$$

where

n = Length scaling factor,

or,

$$n = (L_{67\%})_p / (L_{50\%})_m = 20 / 0.67 \cong 30 .$$

B. 'Dynamic" Model to Prototype Similitude:

Scaling factors for basic soil parameters given in Table C.1 have been derived (dimensional analysis) assuming that acceleration is scaled by n (velocity is being preserved), model length is scaled by 1/n, and that prototype's material/pore fluid are used in the model. This means that density, viscocity and particle size are scaled by a factor of 1.

Considering SJR sand as the prototype sand, $\phi' = 39^o$ at Dr = 55% (letting $Dr_m = Dr_p$), then

$$K_{op} = (0.371)(1.290) = 0.48, \quad \text{and}$$

$$(\sigma_o'_{av})_p = 20(\gamma')((1+ 2K_{op})/ 3) = 719 \text{ psf} \cong 5.0 \text{ psi}.$$

Now, if

$$(\sigma_o'_{av})_m = (\sigma_o'_{av})_p \quad \text{(effective stress similitude), and}$$

$$\gamma_m \cong \gamma_p,$$

then for Eq. C.1. to hold,

$$(L_{50\%})_m \times n = (L_{67\%})_p , \qquad (C.3)$$

where

n = Length scaling factor,

or,

$$n = (L_{67\%})_p / (L_{50\%})_m = 20 / 0.67 \cong 30 .$$

B. 'Dynamic" Model to Prototype Similitude:

Scaling factors for basic soil parameters given in Table C.1 have been derived (dimensional analysis) assuming that acceleration is scaled by n (velocity is being preserved), model length is scaled by 1/n, and that prototype's material/pore fluid are used in the model. This means that density, viscocity and particle size are scaled by a factor of 1.

APPENDIX D

Induced Pressure due to Vertical Water Mass Excitation

The total pressure at any particular point in the water mass for the system depicted in Fig. 5.22, and subjected to a vertical seafloor excitation, can be evaluated by adding the effects of the hydrodynamic pressure field (induced water pressure) generated by the water mass vertical motion, to the existing hydrostatic pressure field. Therefore, the total pressure can be expressed as follows:

$$p = \rho\frac{\partial\phi}{\partial t} + \rho g z \ , \tag{D.1}$$

where

p = Total fluid pressure at distance z from seafloor,
ρ = Fluid density,
ϕ = Fluid velocity potential,
z = Distance above seafloor, and
g = Acceleration due to gravity.

The fluid velocity potential function is given by:

$$\phi(z,t) = \Phi(z)\, e^{i\Omega t} \ , \tag{D.2}$$

in which

Φ = Fluid velocity potential amplitude,
Ω = Displacement excitation frequency,
t = time,
e = exponential, and
$i = \sqrt{-1}$.

Thus

$$\frac{\partial\phi}{\partial t} = i\Omega\Phi e^{i\Omega t} \ . \tag{D.3}$$

APPENDIX D

Induced Pressure due to Vertical Water Mass Excitation

The total pressure at any particular point in the water mass for the system depicted in Fig. 5.22, and subjected to a vertical seafloor excitation, can be evaluated by adding the effects of the hydrodynamic pressure field (induced water pressure) generated by the water mass vertical motion, to the existing hydrostatic pressure field. Therefore, the total pressure can be expressed as follows:

$$p = \rho\frac{\partial\phi}{\partial t} + \rho g z \ , \qquad \text{(D.1)}$$

where

p = Total fluid pressure at distance z from seafloor,
ρ = Fluid density,
ϕ = Fluid velocity potential,
z = Distance above seafloor, and
g = Acceleration due to gravity.

The fluid velocity potential function is given by:

$$\phi(z,t) = \Phi(z)\, e^{i\Omega t} \ , \qquad \text{(D.2)}$$

in which

Φ = Fluid velocity potential amplitude,
Ω = Displacement excitation frequency,
t = time,
e = exponential, and
$i = \sqrt{-1}$.

Thus

$$\frac{\partial\phi}{\partial t} = i\Omega\Phi e^{i\Omega t} \ . \qquad \text{(D.3)}$$

Thus, Eq. D.3 becomes

$$\frac{\partial \phi}{\partial t} = \frac{\Omega^2 W}{k} \frac{\sin k(z-h)}{\cos kh} e^{i\Omega t} \quad . \tag{D.11}$$

For z = 0,

$$\frac{\partial \phi}{\partial t} = \frac{\Omega^2 W}{k} \tan (kh)\, e^{i\Omega t} \quad . \tag{D.12}$$

Let

$c = 1430$ m/sec $= 4691.8$ ft/sec,
$h = 1000$ feet,
$\rho = \gamma / g = 1.93$ lb-sec^2 / ft^4 .

For

(a) Low-frequency high-amplitude signal (Fig. 5.23):

$\Omega = 0.12$ Hz $= 0.766$ rad/sec,
$k = 0.766 / 4691.8 = 0.000163$ rad/ft,
$W = 0.73$ in. $= 0.0608$ ft,

thus, $\rho\, (\partial\phi/\partial t)_{max}$ is computed as 69.49 psf (0.48 psi).

(b) High-frequency low-amplitude signal (Fig. 5.23):

$\Omega = 1$ Hz $= 6.28$ rad/sec,
$k = 6.28 / 4691.8 = 0.00133$ rad/ft,
$W = 0.05$ in. $= 0.0041$ ft,

thus, $\rho\, (\partial\phi/\partial t)_{max}$ is computed as 955 psf (6.63 psi).

The total excess soil surface pressure generated by the two signals of the vertical component of motion is, therefore, 7. 11 psi.

Thus, Eq. D.3 becomes

$$\frac{\partial \phi}{\partial t} = \frac{\Omega^2 W}{k} \frac{\sin k(z-h)}{\cos kh} e^{i\Omega t} \quad . \tag{D.11}$$

For z = 0,

$$\frac{\partial \phi}{\partial t} = \frac{\Omega^2 W}{k} \tan (kh)\, e^{i\Omega t} \quad . \tag{D.12}$$

Let

$c = 1430$ m/sec $= 4691.8$ ft/sec,
$h = 1000$ feet,
$\rho = \gamma / g = 1.93$ lb-sec^2 / ft^4 .

For

(a) Low-frequency high-amplitude signal (Fig. 5.23):

$\Omega = 0.12$ Hz $= 0.766$ rad/sec,
$k = 0.766 / 4691.8 = 0.000163$ rad/ft,
$W = 0.73$ in. $= 0.0608$ ft,

thus, $\rho\, (\partial\phi/\partial t)_{max}$ is computed as 69.49 psf (0.48 psi).

(b) High-frequency low-amplitude signal (Fig. 5.23):

$\Omega = 1$ Hz $= 6.28$ rad/sec,
$k = 6.28 / 4691.8 = 0.00133$ rad/ft,
$W = 0.05$ in. $= 0.0041$ ft,

thus, $\rho\, (\partial\phi/\partial t)_{max}$ is computed as 955 psf (6.63 psi).

The total excess soil surface pressure generated by the two signals of the vertical component of motion is, therefore, 7. 11 psi.

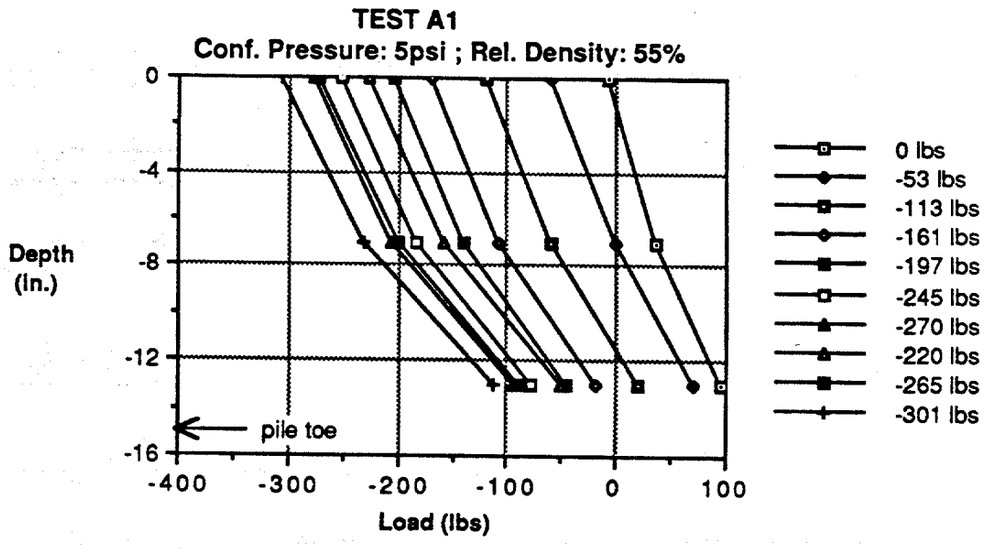

Fig. E.1. Load-Depth Relationships, Test A1.

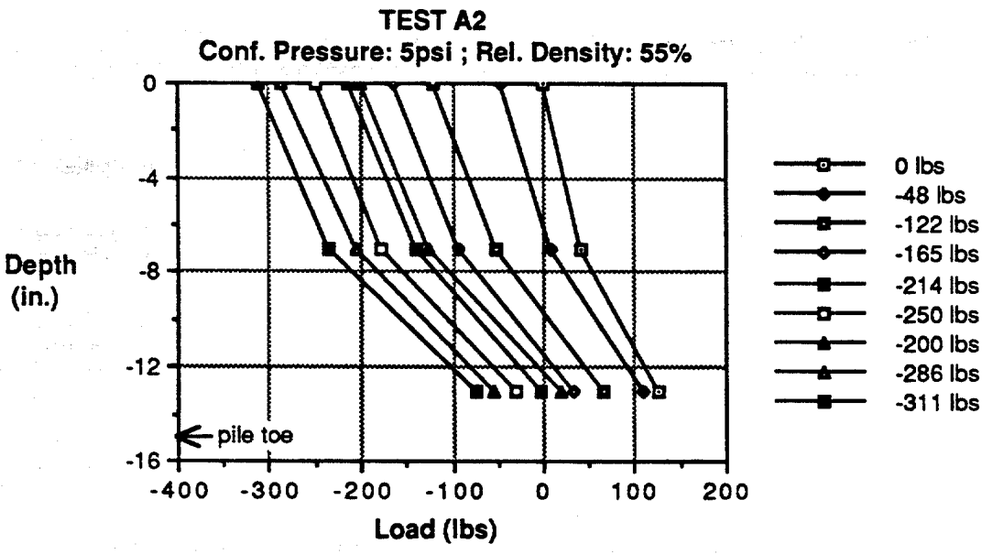

Fig. E.2. Load-Depth Relationships, Test A2.

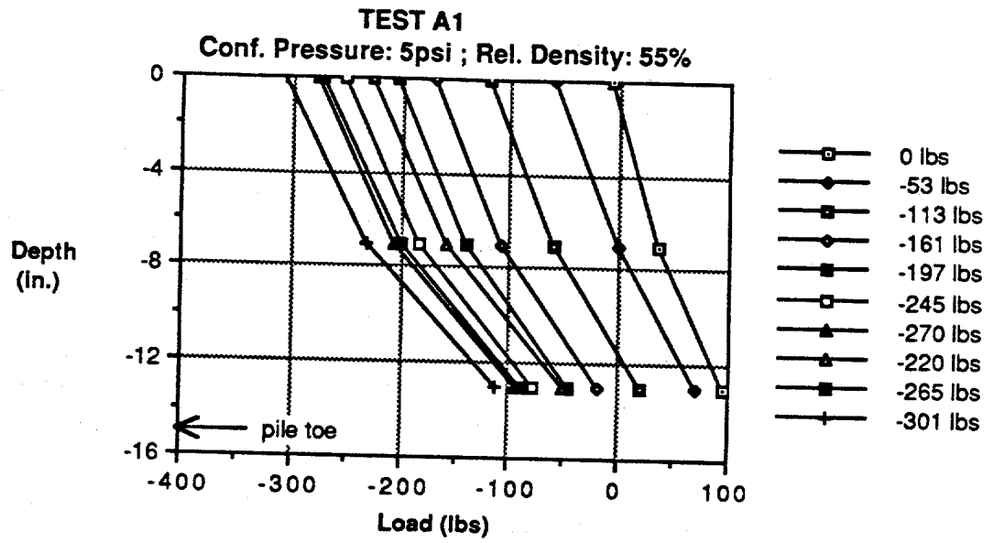

Fig. E.1. Load-Depth Relationships, Test A1.

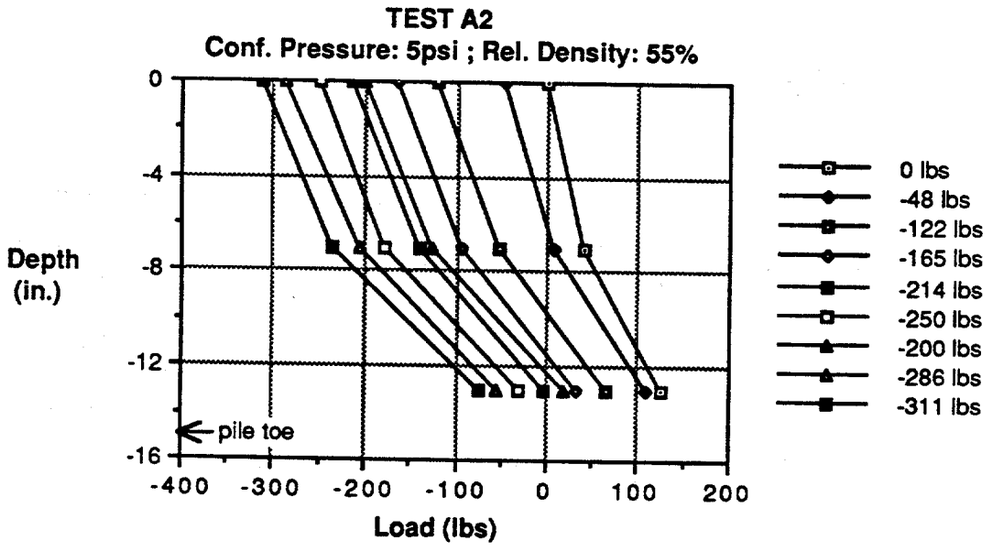

Fig. E.2. Load-Depth Relationships, Test A2.

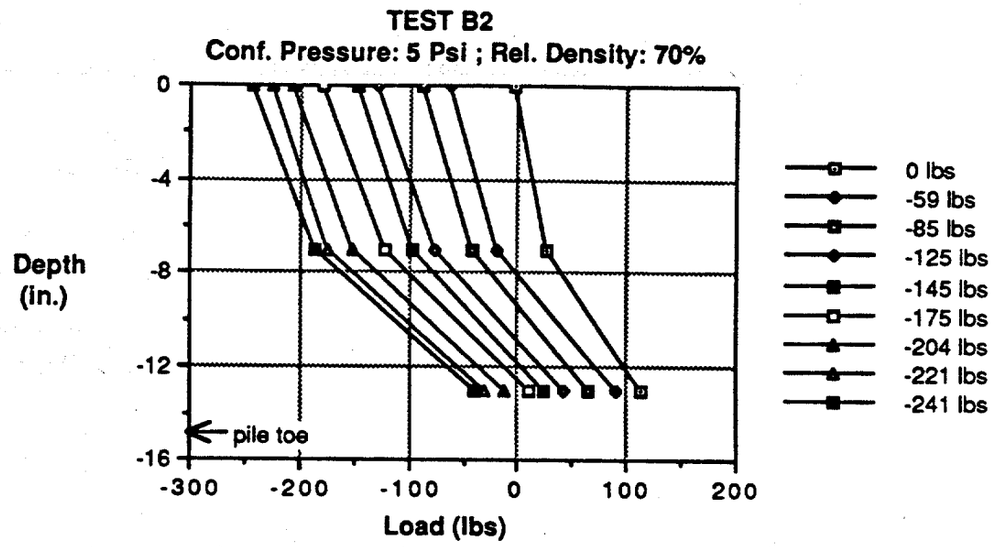

Fig. E.5. Load-Depth Relationships, Test B2.

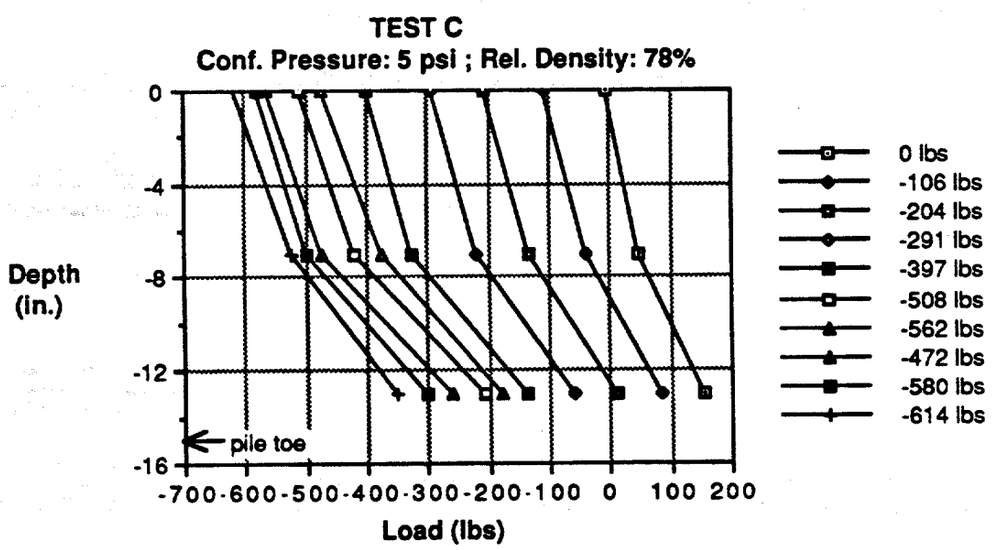

Fig. E.6. Load-Depth Relationships, Test C.

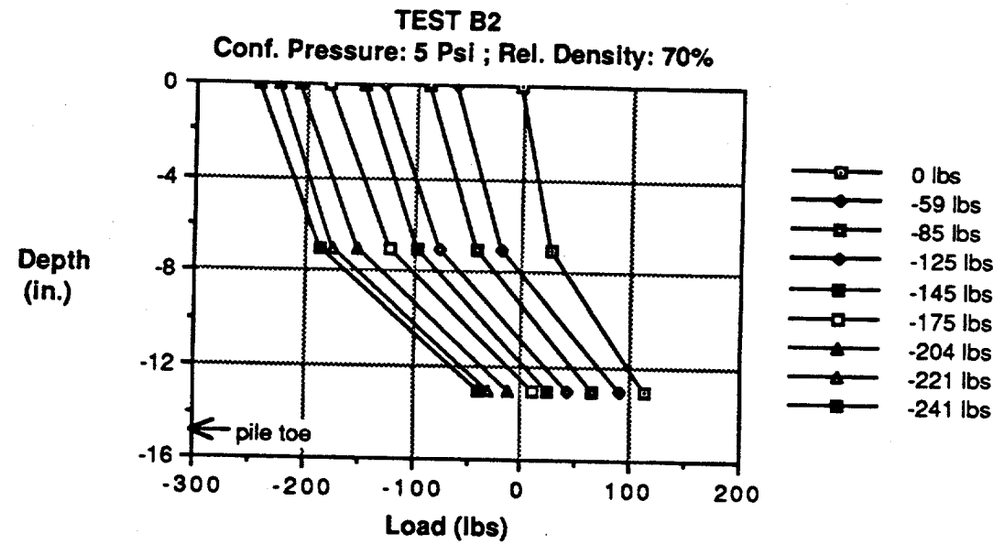

Fig. E.5. Load-Depth Relationships, Test B2.

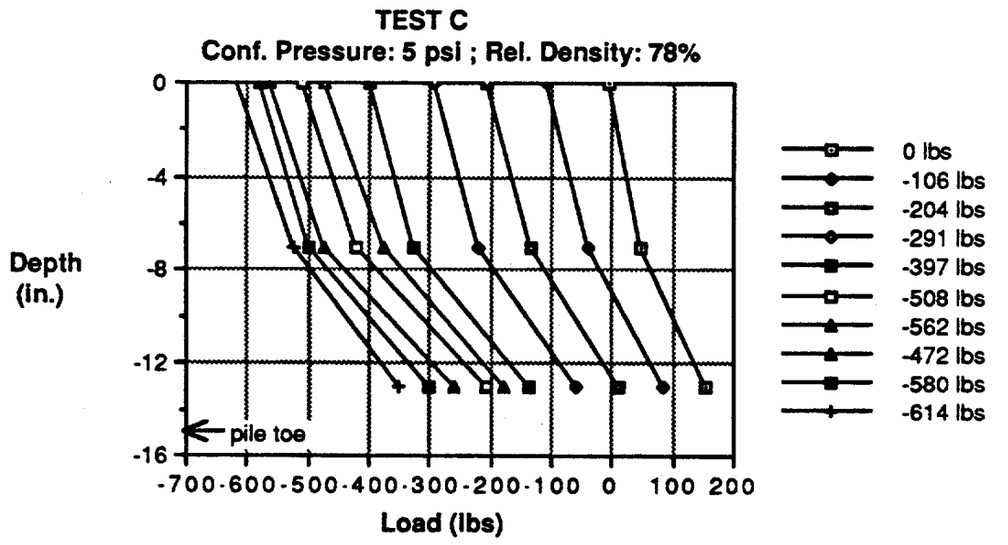

Fig. E.6. Load-Depth Relationships, Test C.

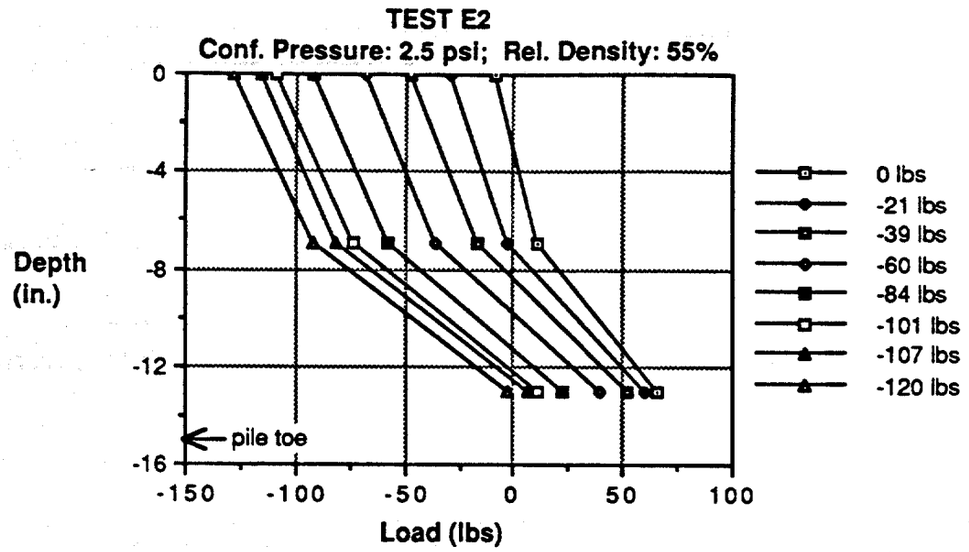

Fig. E.9. Load-Depth Relationships, Test E2.

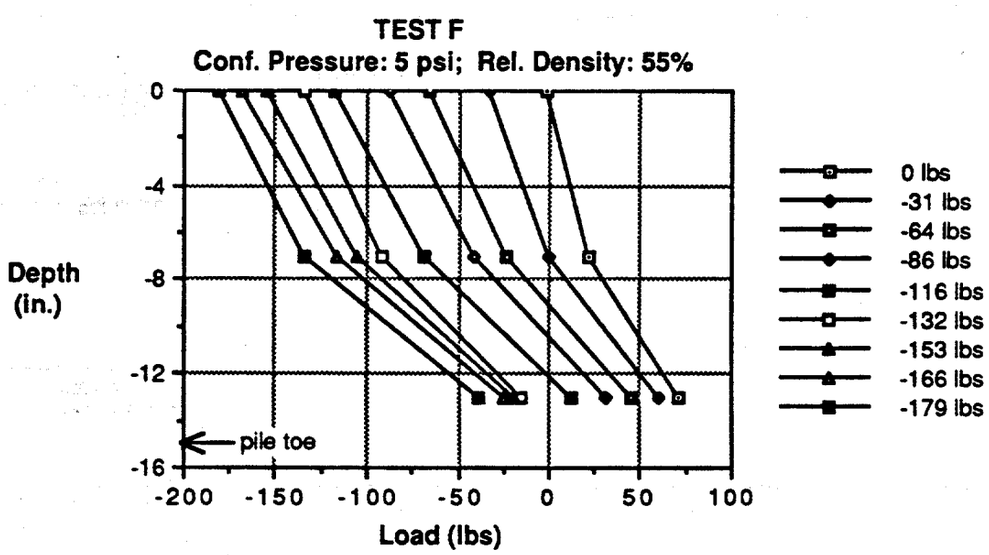

Fig. E.10. Load-Depth Relationships, Test F.

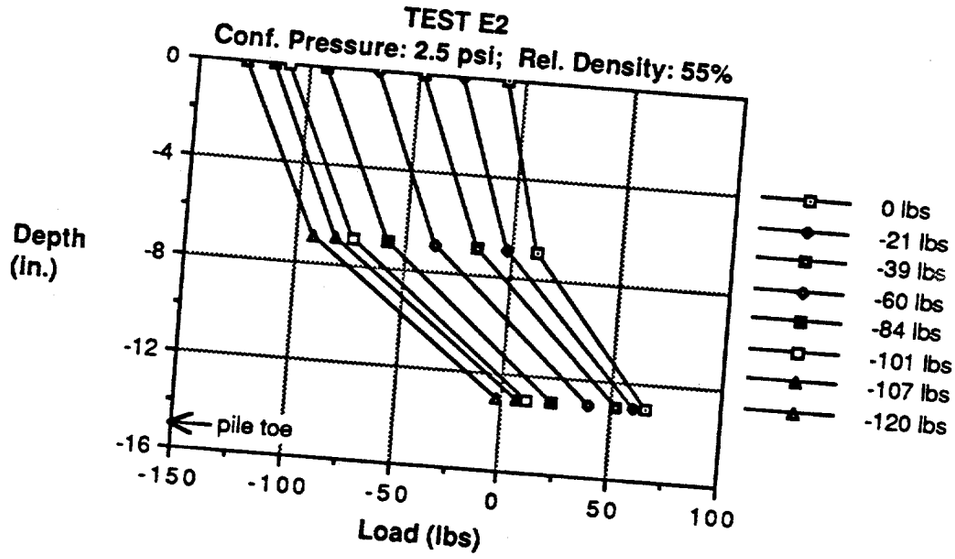

Fig. E.9. Load-Depth Relationships, Test E2.

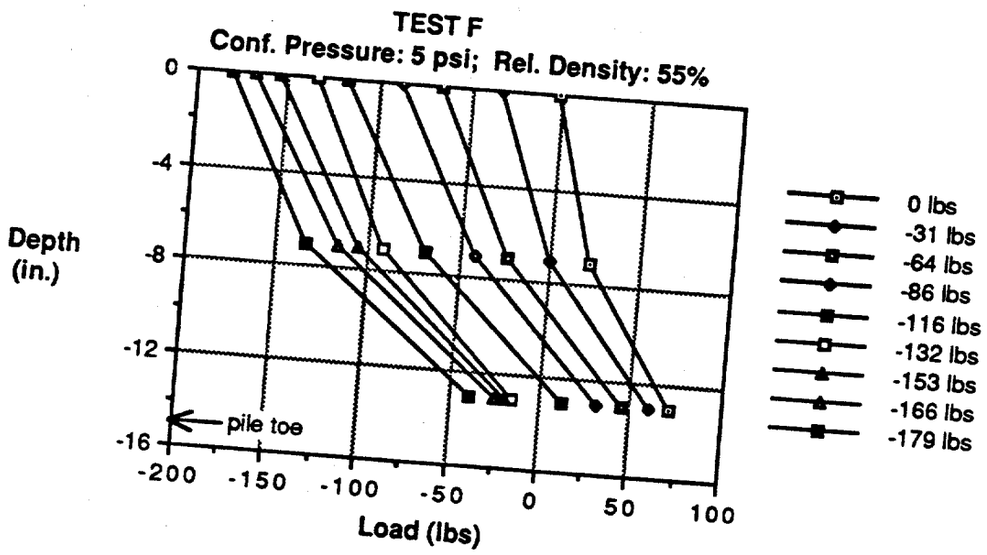

Fig. E.10. Load-Depth Relationships, Test F.

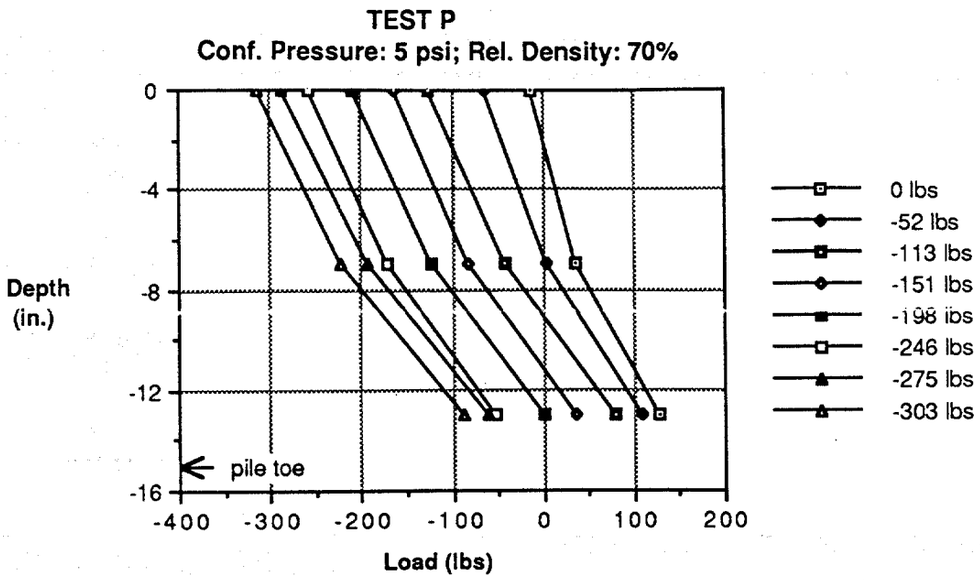

Fig. E.13. Load-Depth Relationships, Test P.

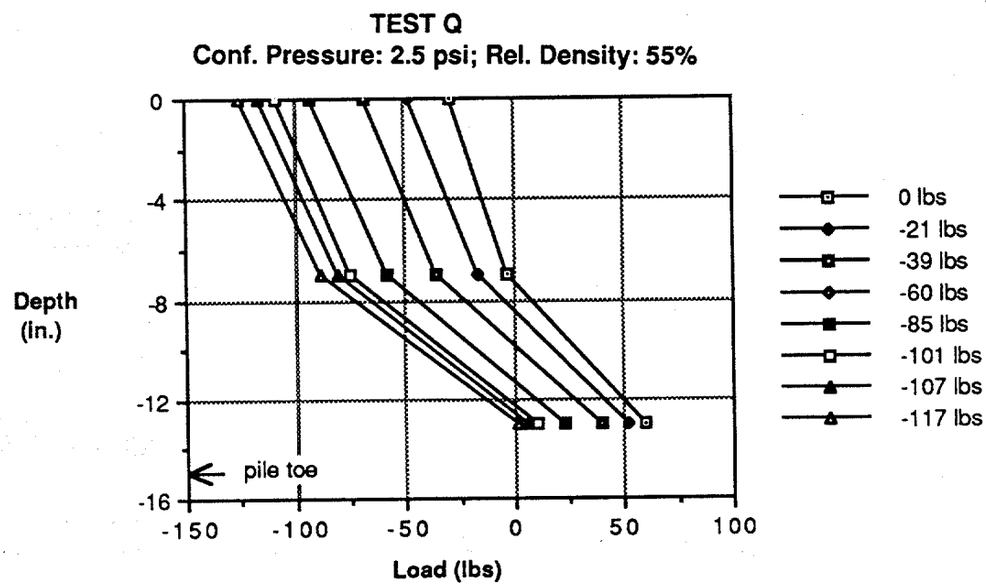

Fig. E.14. Load-Depth Relationships, Test Q.

Appendix F

Time History Measurements During Dynamic Tests, Vertical Motion (Raw Data).

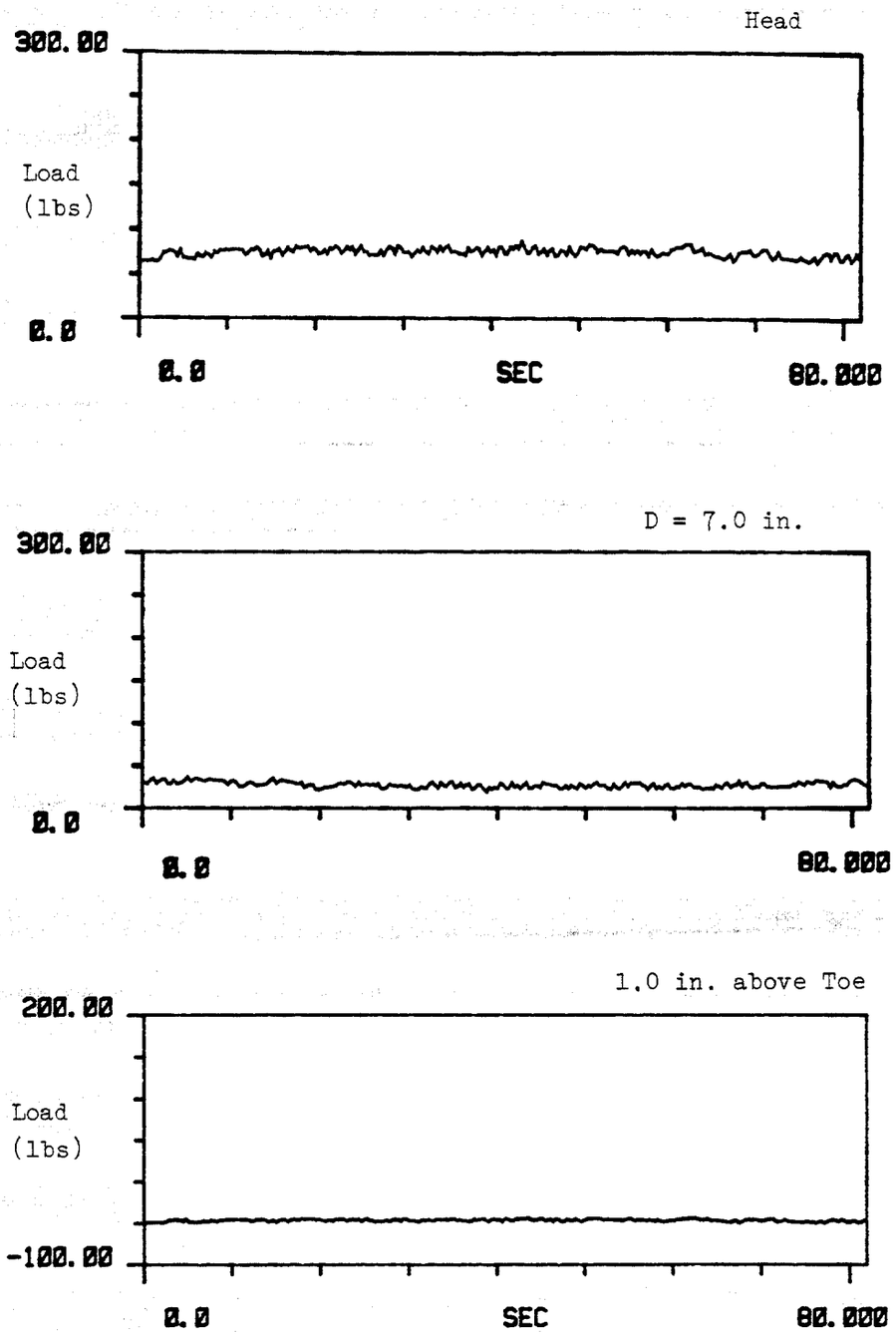

Fig. F.1. Time History Measurements of Dynamic Load on Pile, Test G.

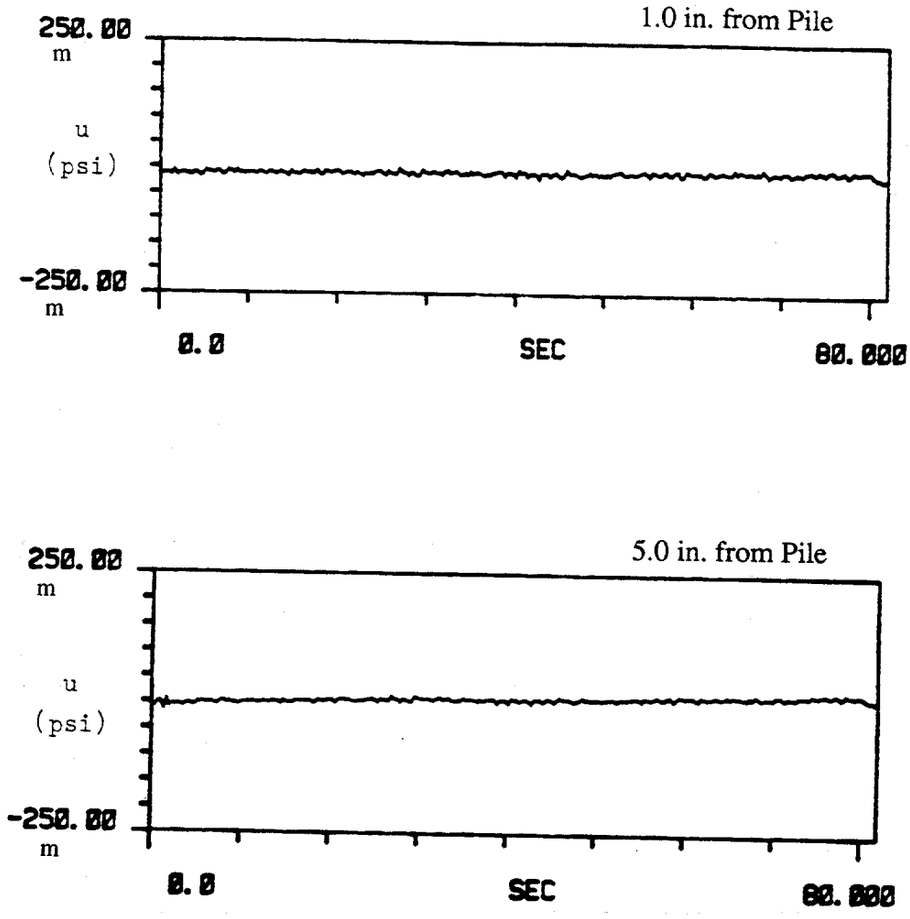

Fig. F.2. Time History Measurements of Near and Far Field Pore Water Pressures, Test G, [m = milli].

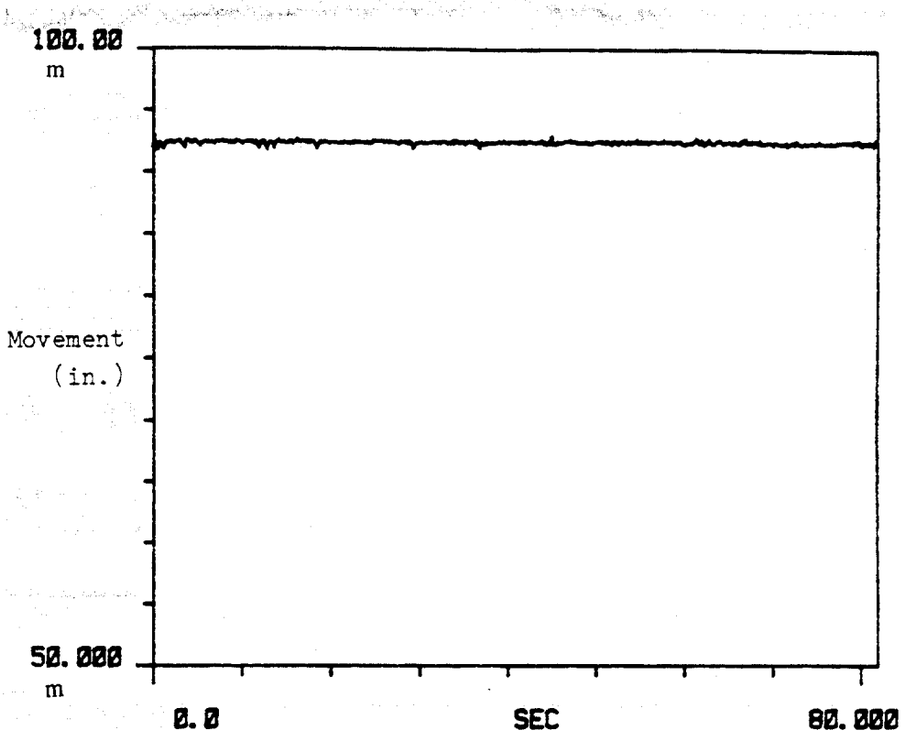

Fig. F.3. Time History Measurements of Pile Head Movement, Test G, [m = milli].

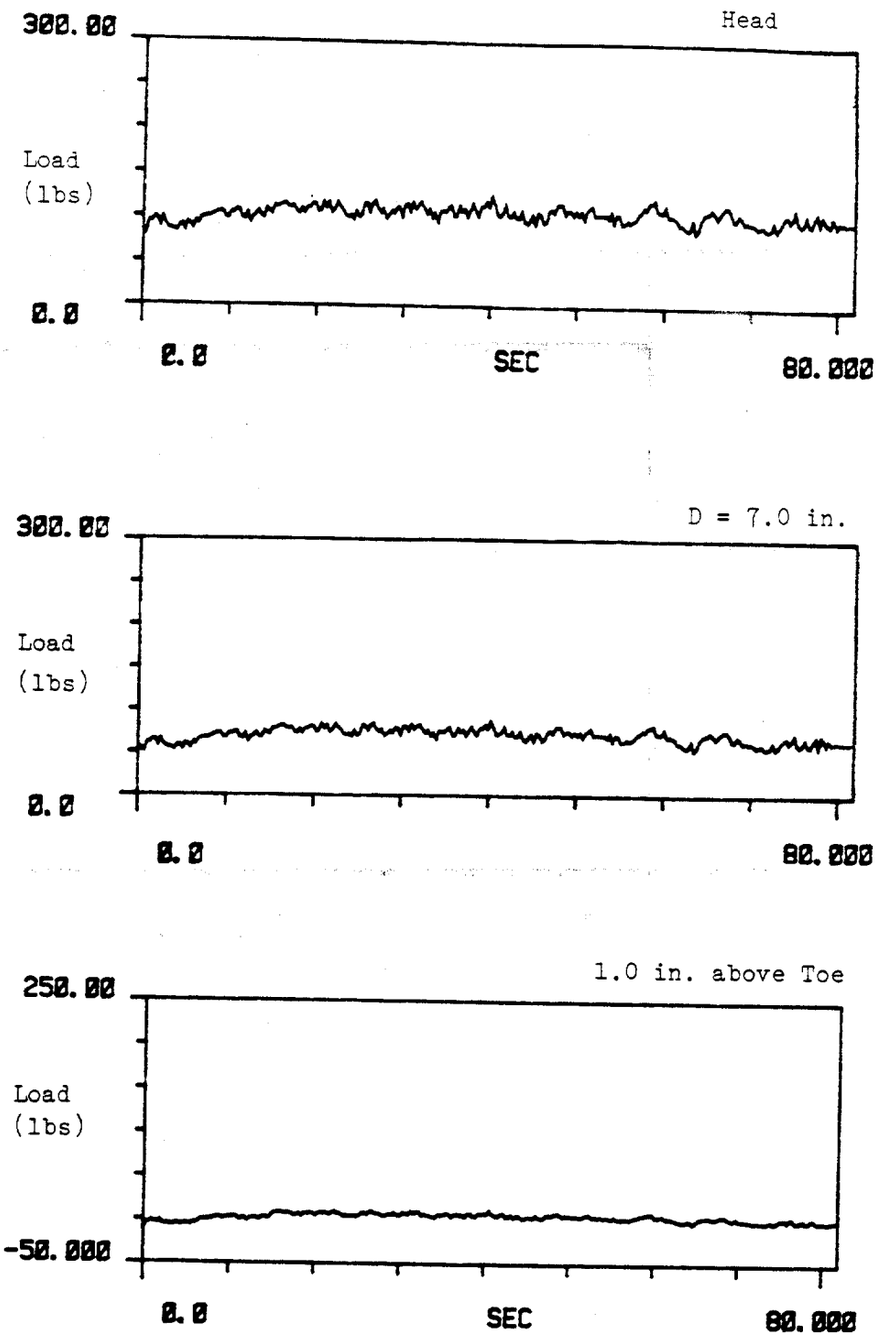

Fig. F.4. Time History Measurements of Dynamic Load on Pile, Test H2.

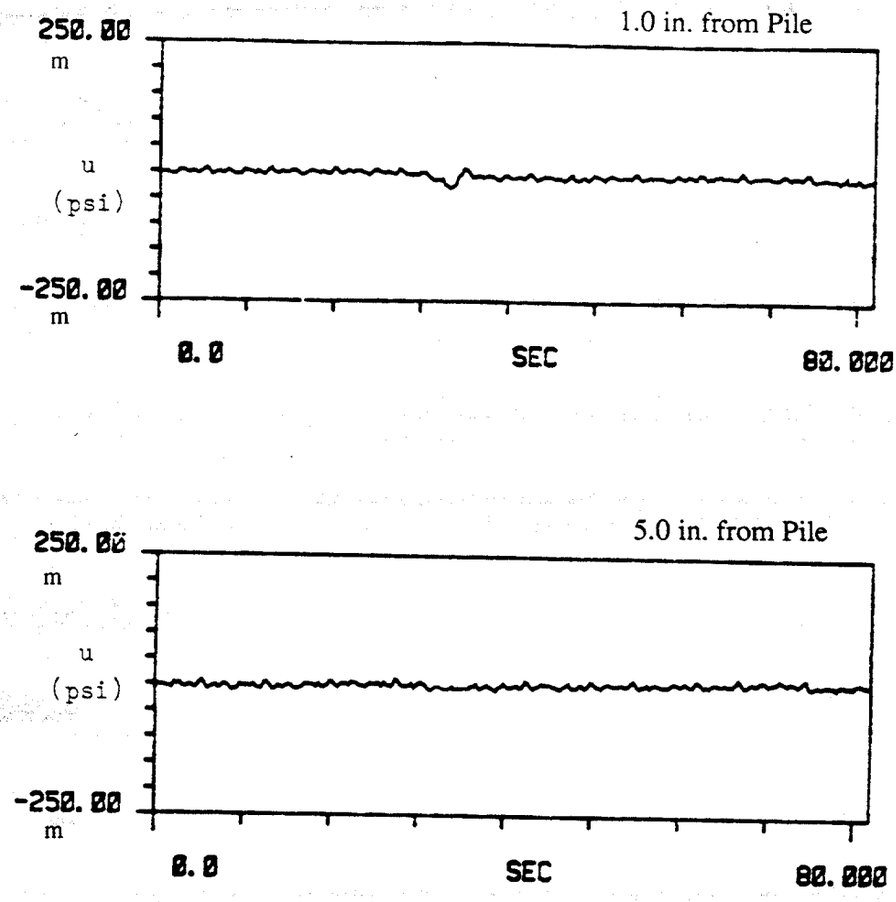

Fig. F.5. Time History Measurements of Near and Far Field Pore Water Pressures, Test H2, [m = milli].

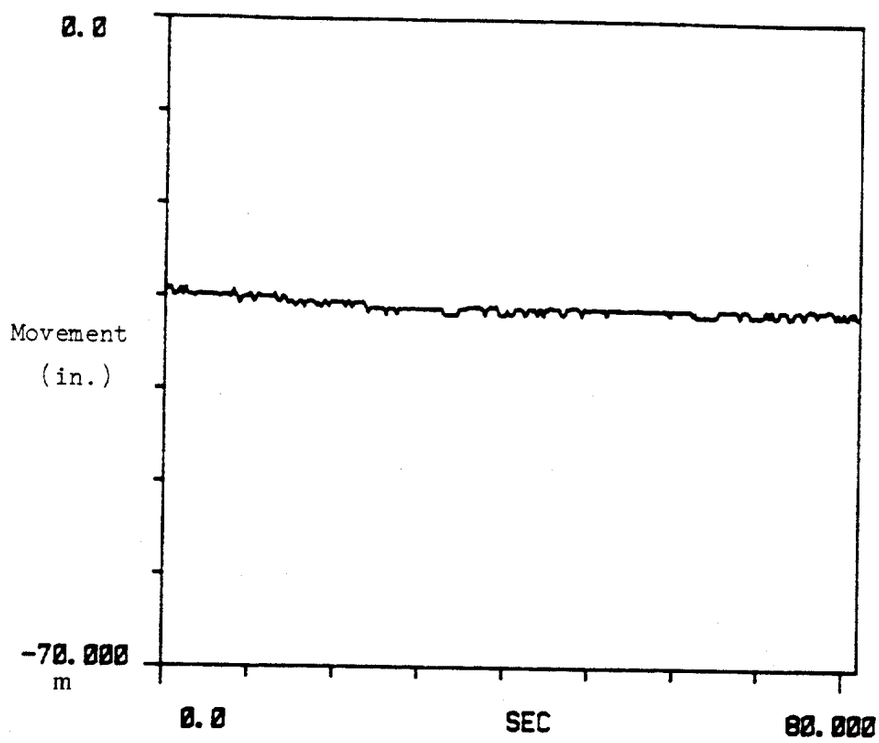

Fig. F.6. Time History Measurements of Pile Head Movement, Test H2, [m = milli].

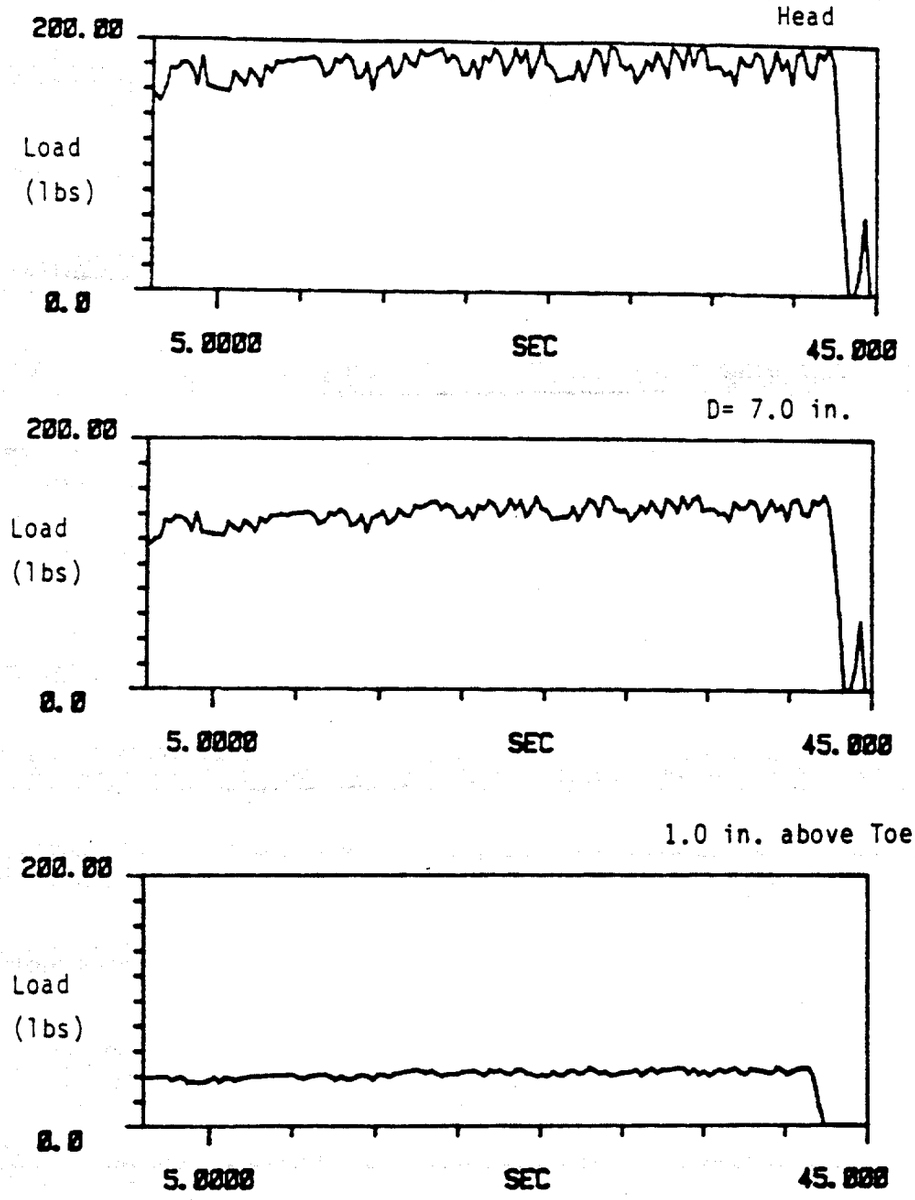

Fig. F.7. Time History Measurements of Dynamic Load on Pile, Test I1.

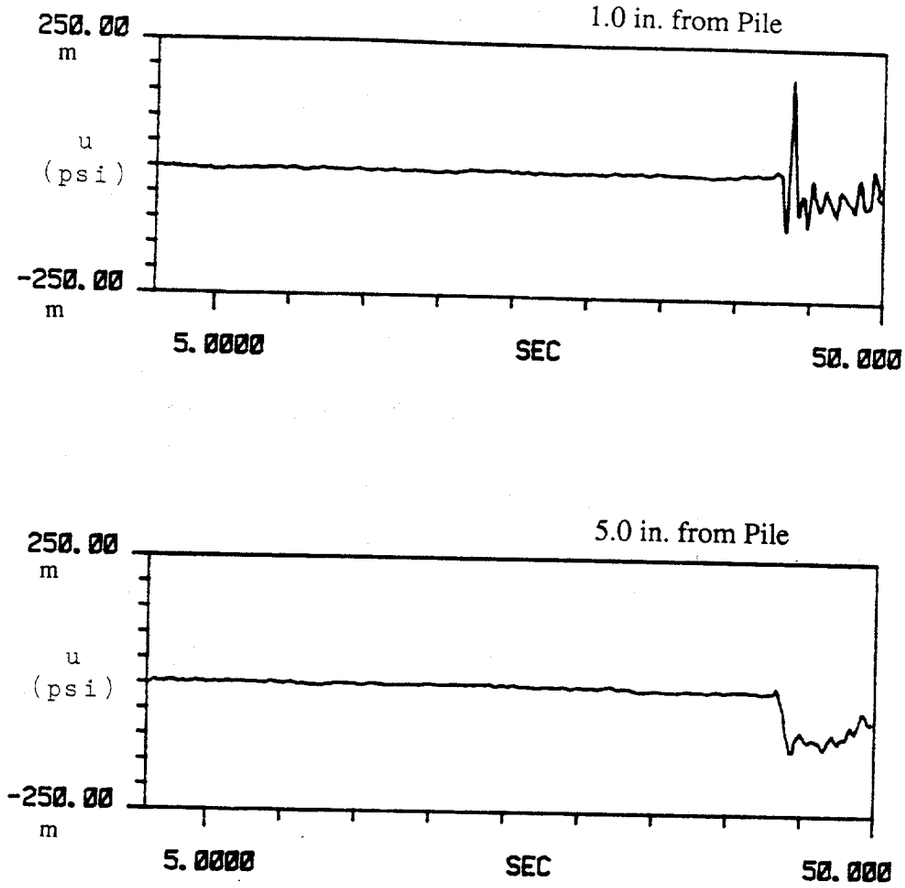

Fig. F.8. Time History Measurements of Near and Far Field Pore Water Pressures, Test I1, [m = milli].

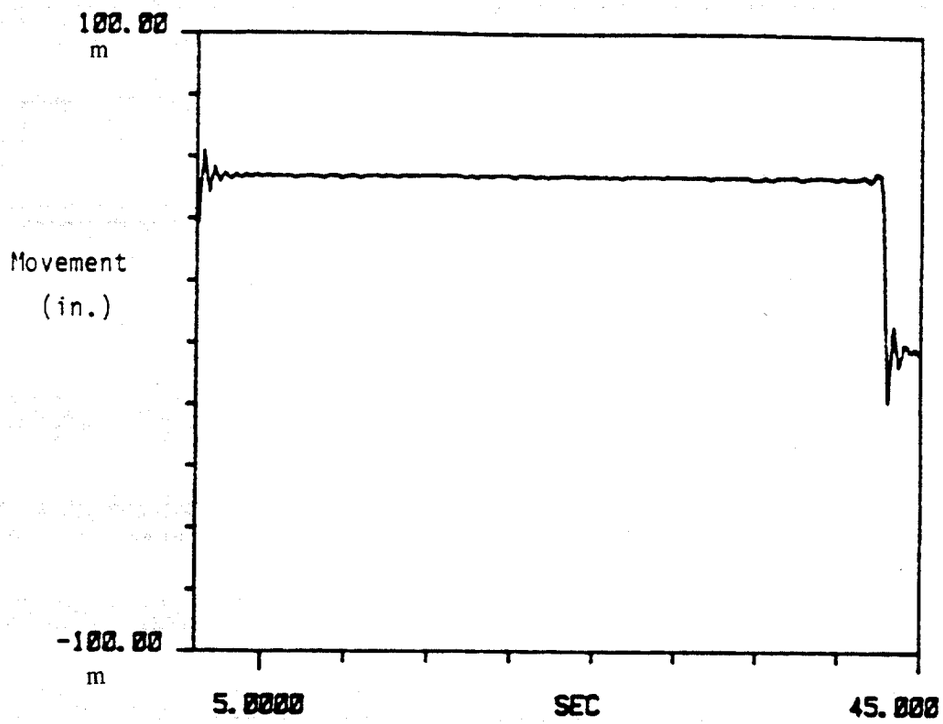

Fig. F.9. Time History Measurements of Pile Head Movement, Test I1, [m = milli].

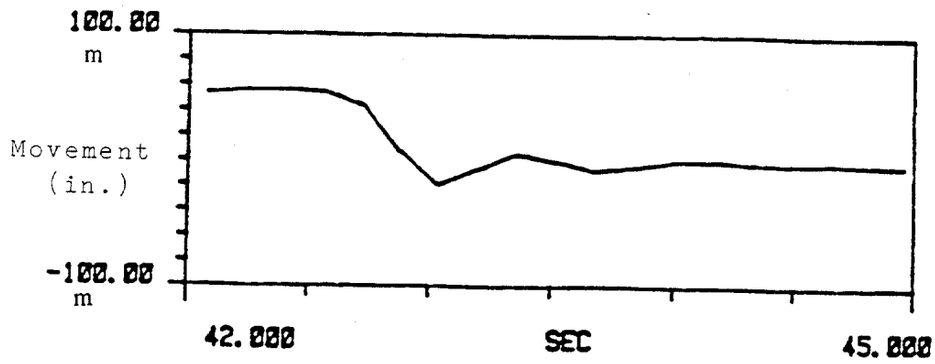

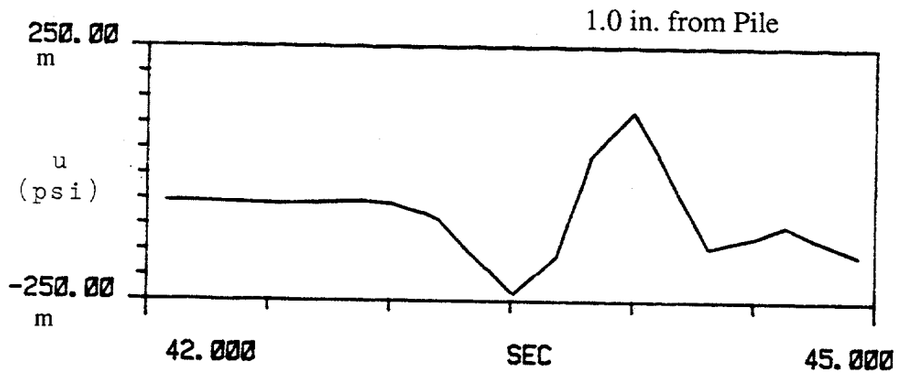

Fig. F.10. Time History Measurements of Pile Head Movement and Near Field Pore Water Pressure, Test I1, [m = milli].

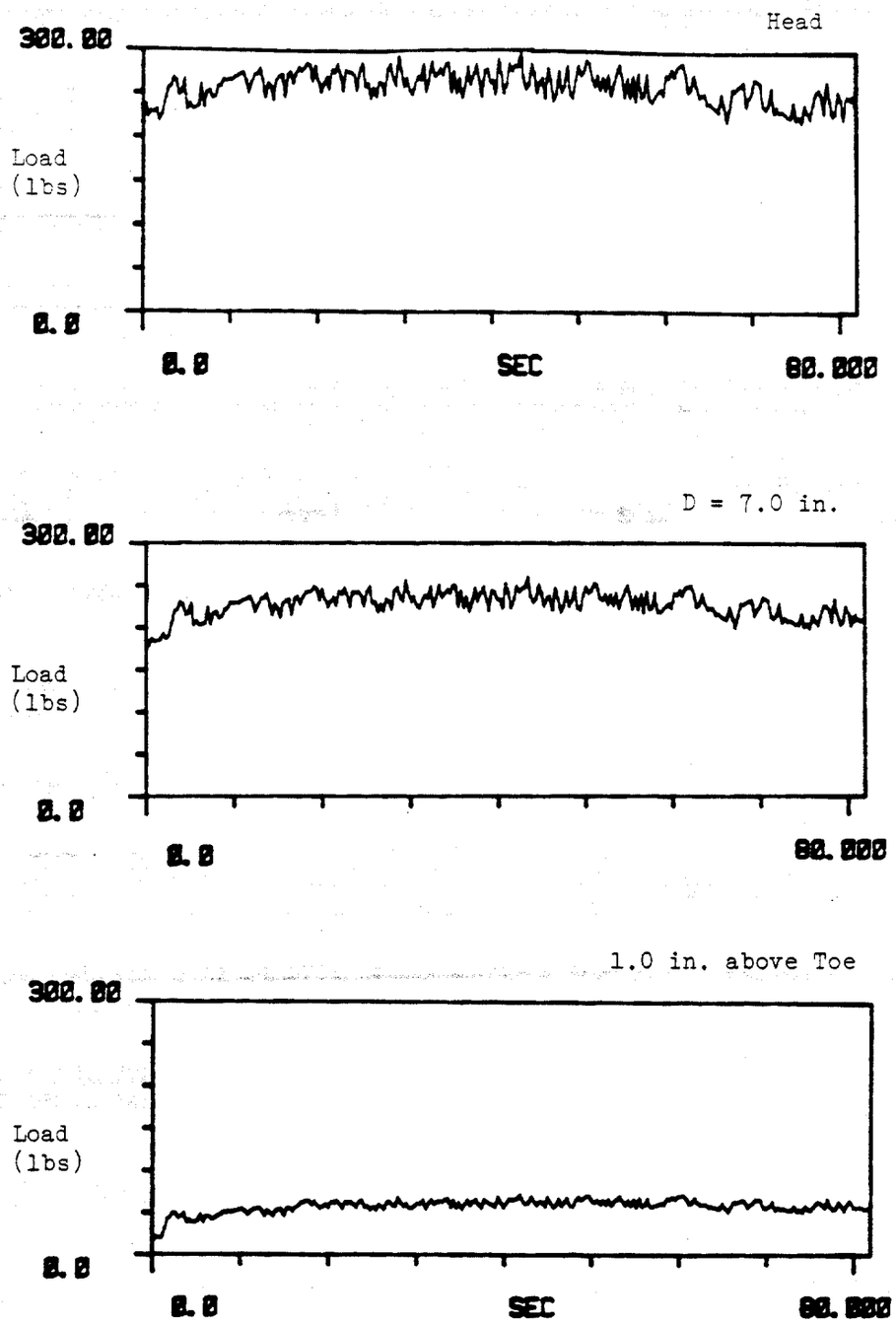

Fig. F.11. Time History Measurements of Dynamic Load on Pile, Test J.

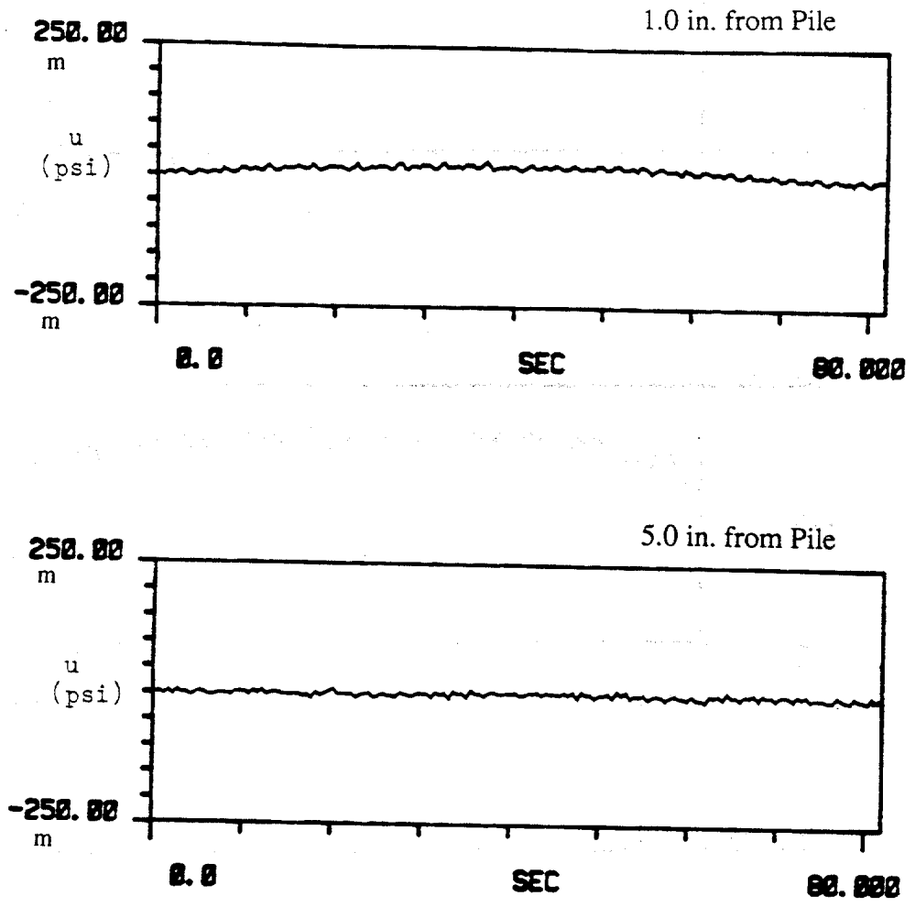

Fig. F.12. Time History Measurements of Near and Far Field Pore Water Pressures, Test J, [m = milli].

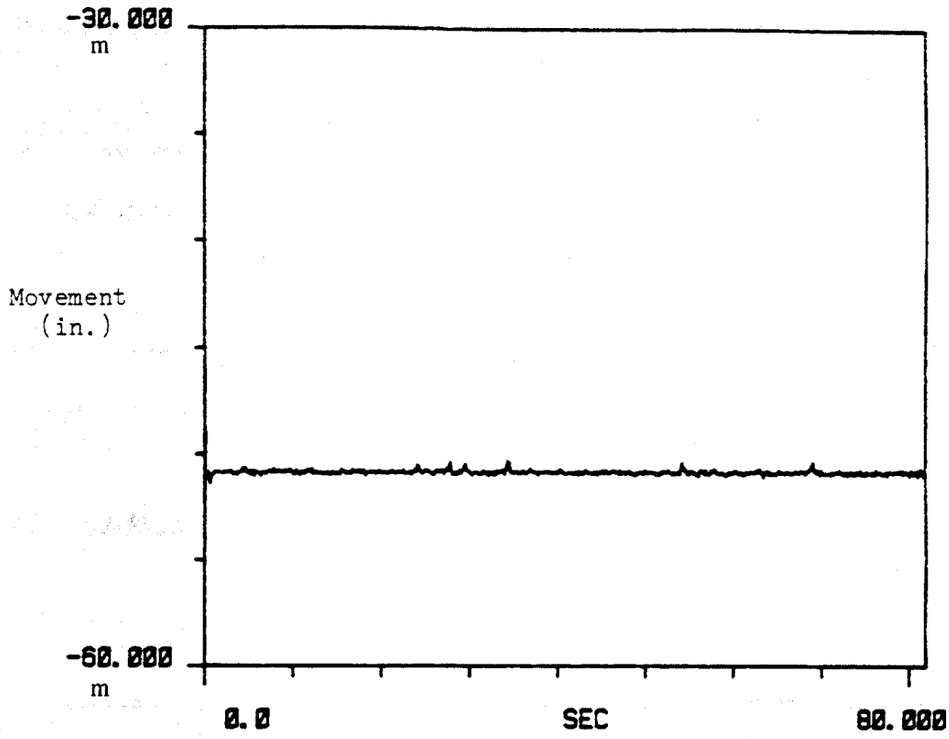

Fig. F.13. Time History Measurements of Pile Head Movement, Test J, [m = milli].

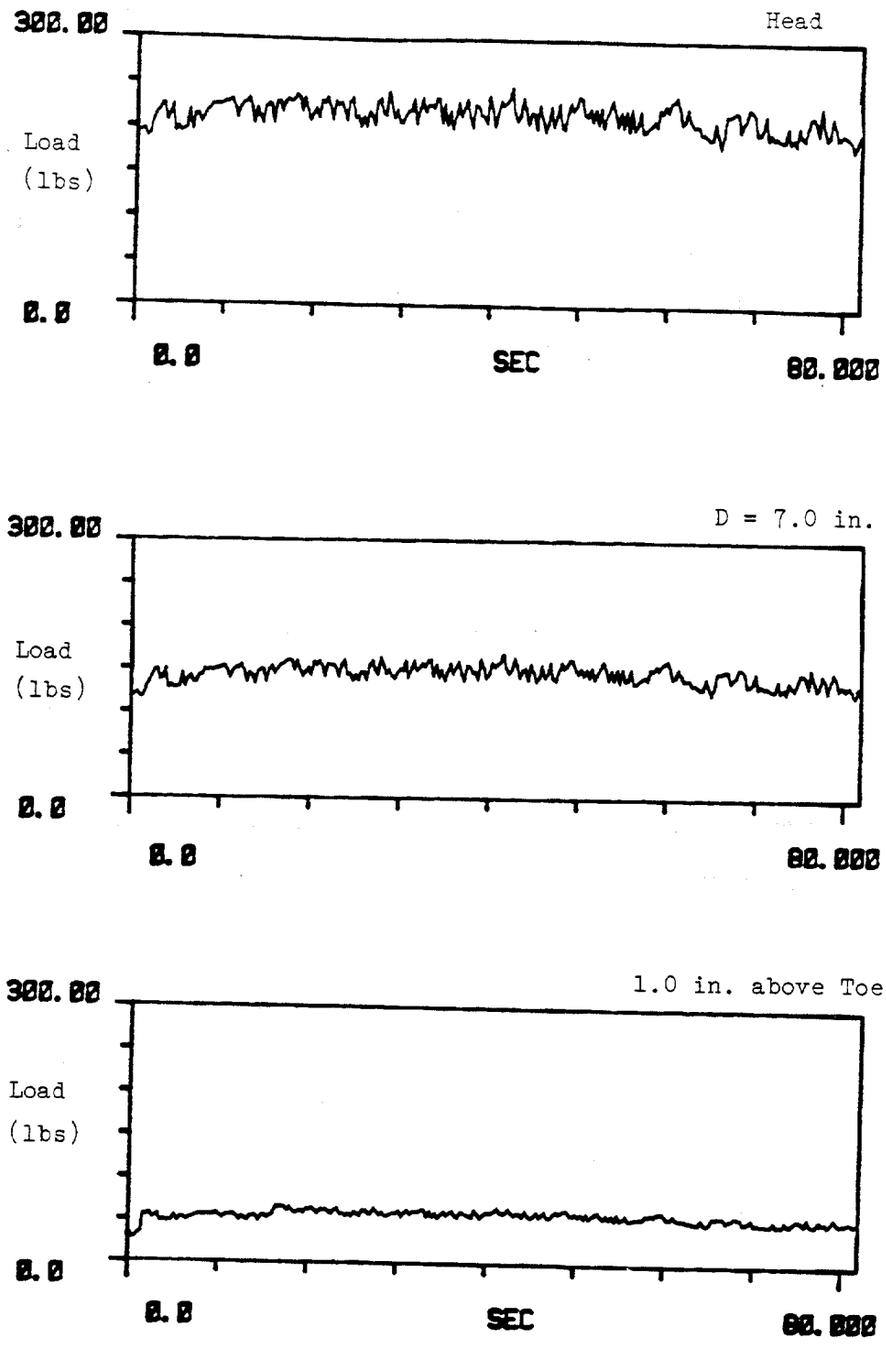

Fig. F.14. Time History Measurements of Dynamic Load on Pile, Test L1.

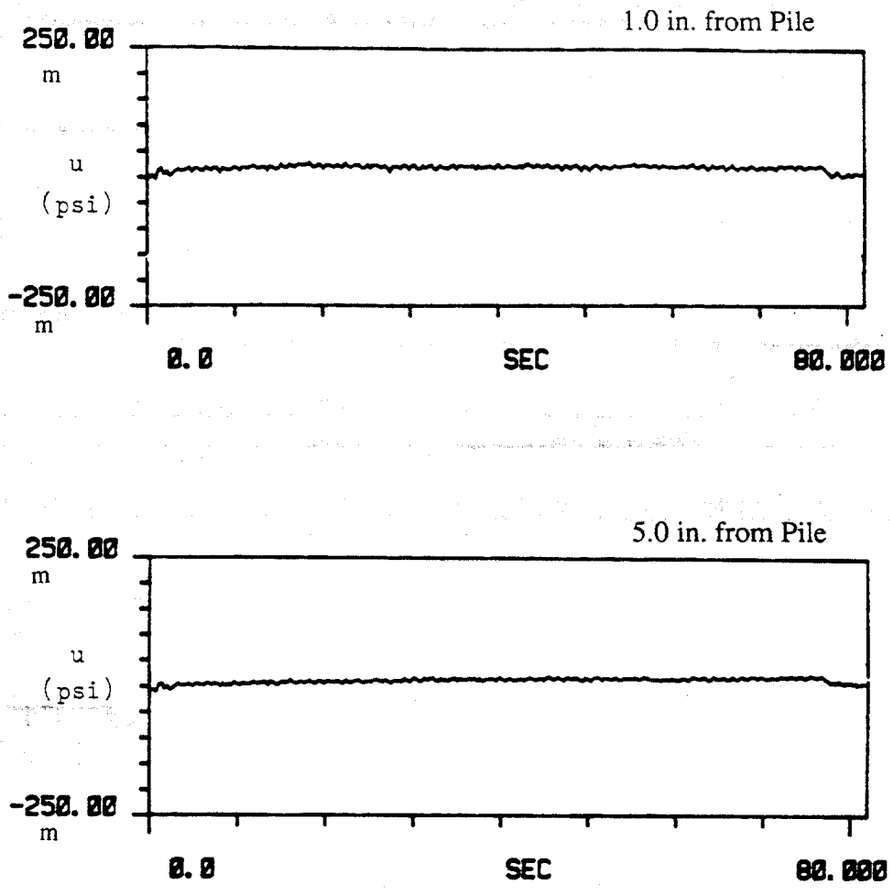

Fig. F.15. Time History Measurements of Near and Far Field Pore Water Pressures, Test L1, [m = milli].

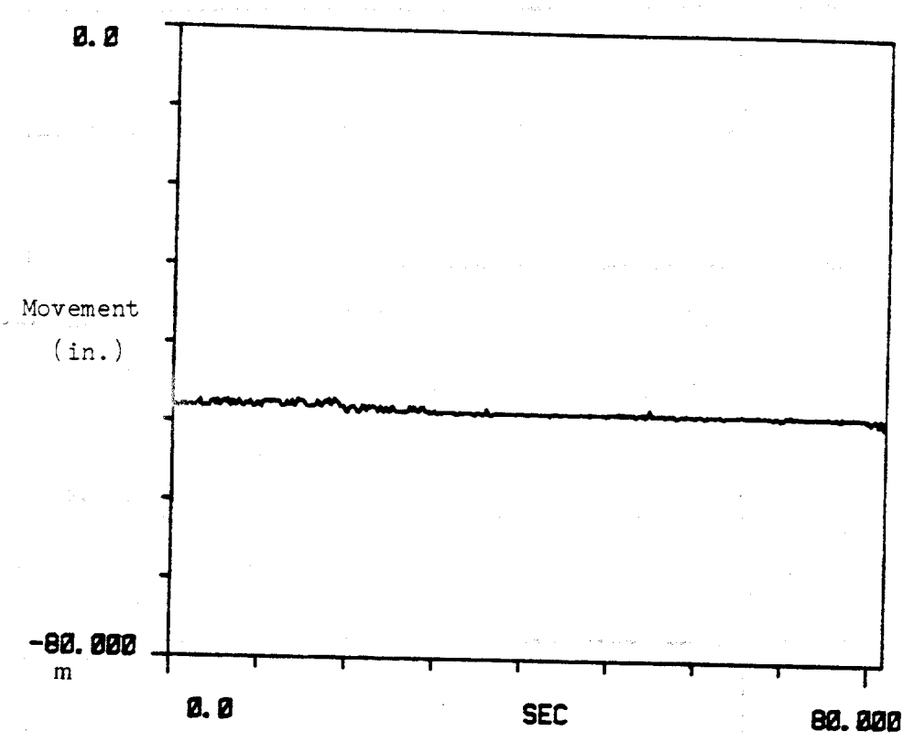

Fig. F.16. Time History Measurements of Pile Head Movement, Test J, [m = milli].

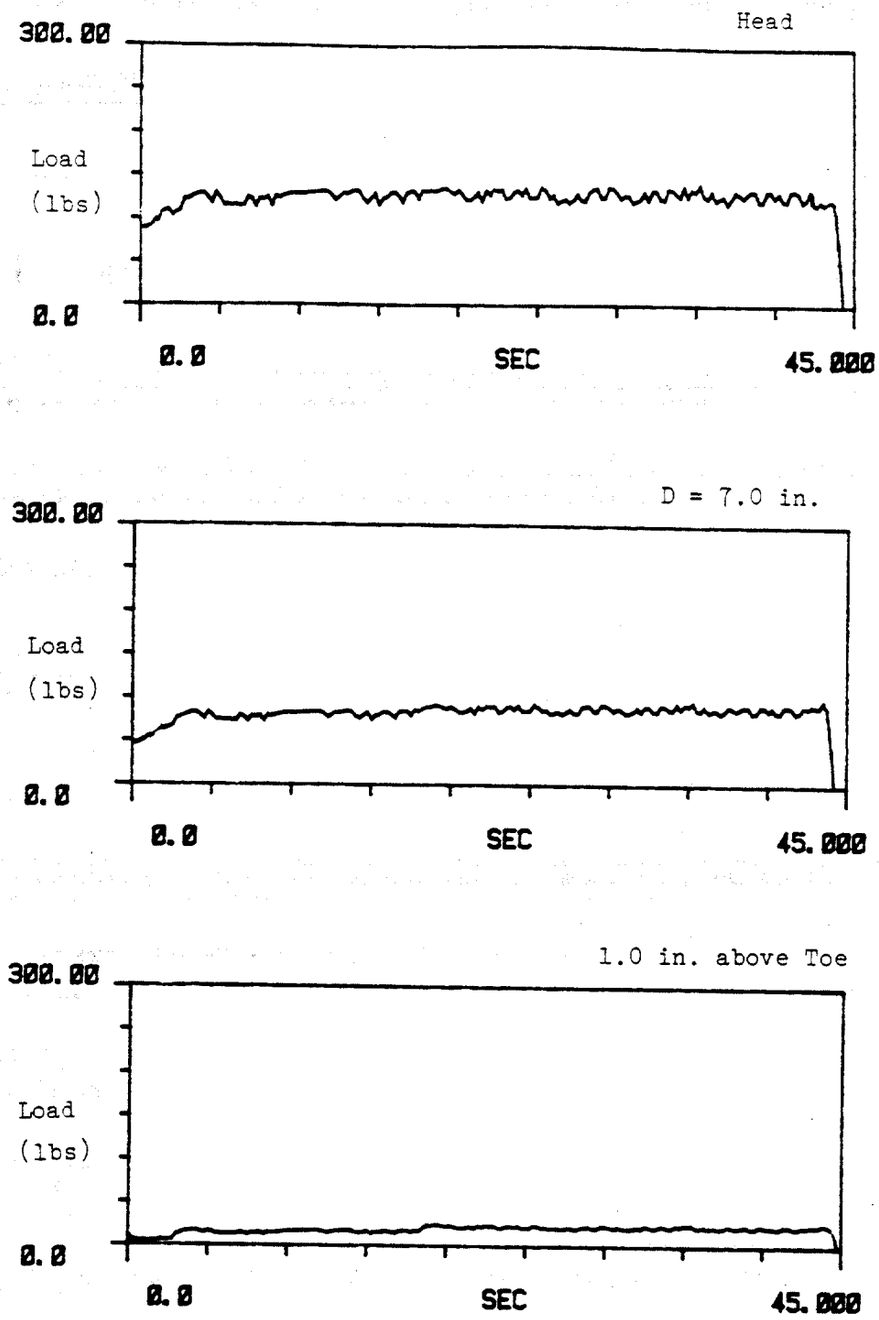

Fig. F.17. Time History Measurements of Dynamic Load on Pile, Test L2.

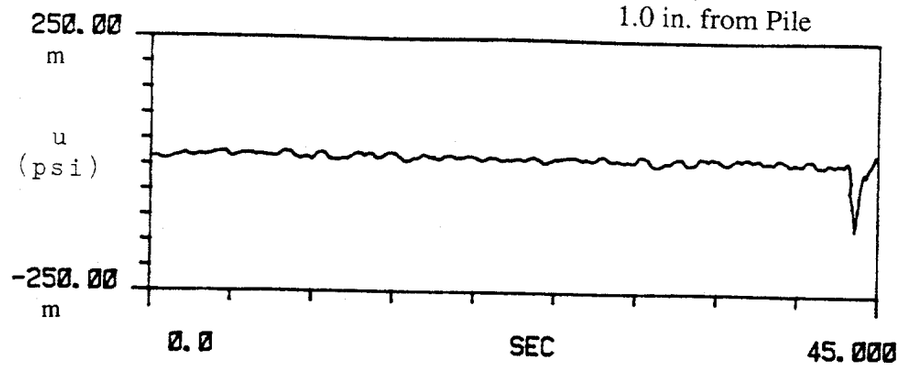

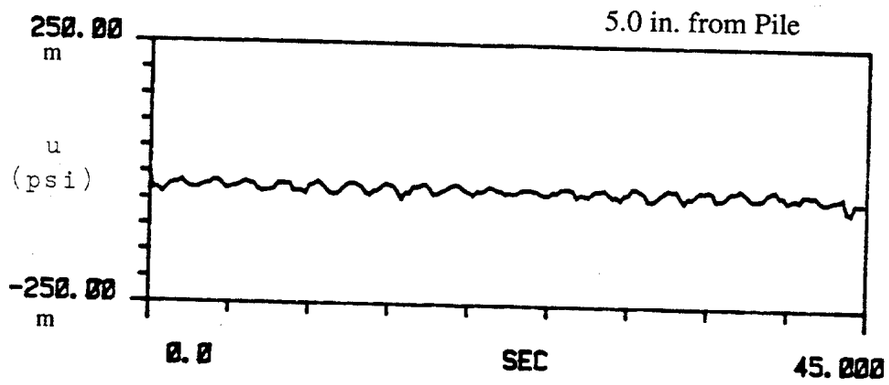

Fig. F.18. Time History Measurements of Near and Far Field Pore Water Pressures, Test L2, [m = milli].

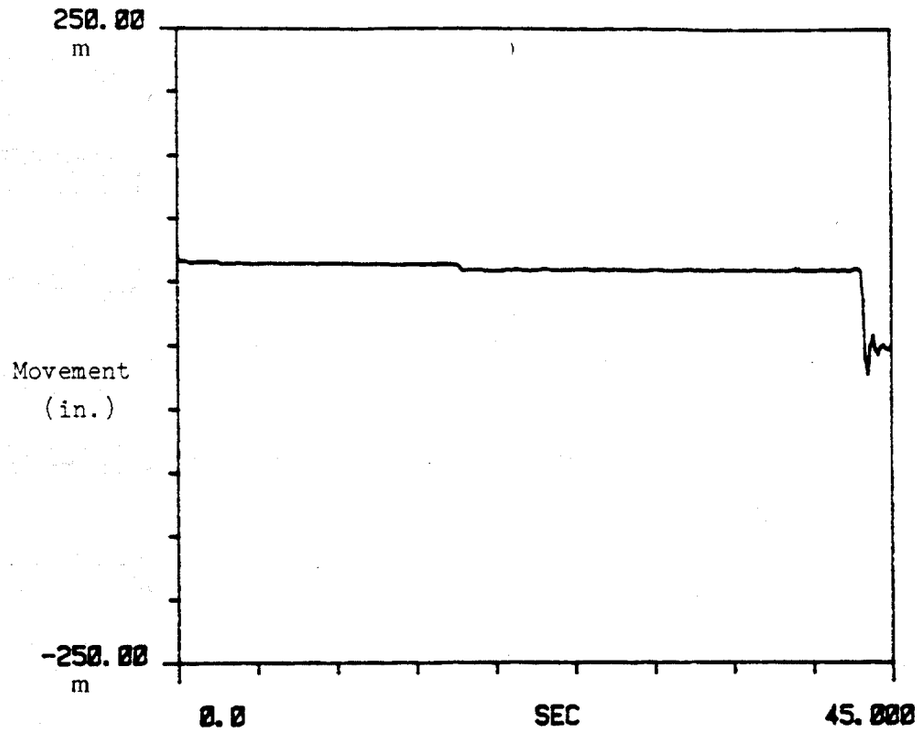

Fig. F.19. Time History Measurements of Pile Head Movement, Test L2, [m = milli].

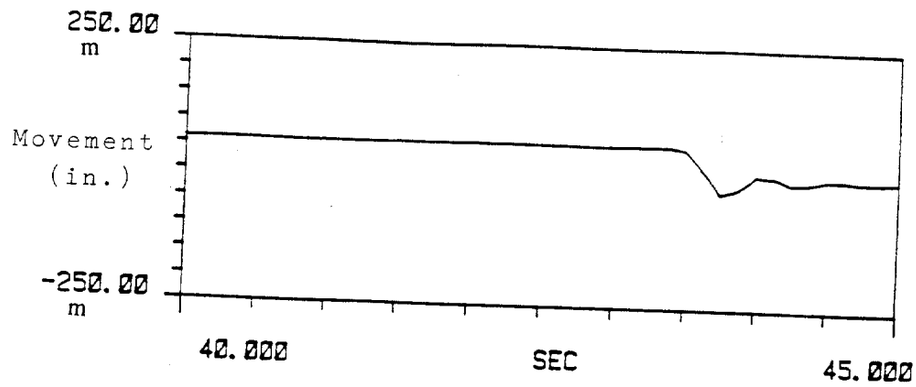

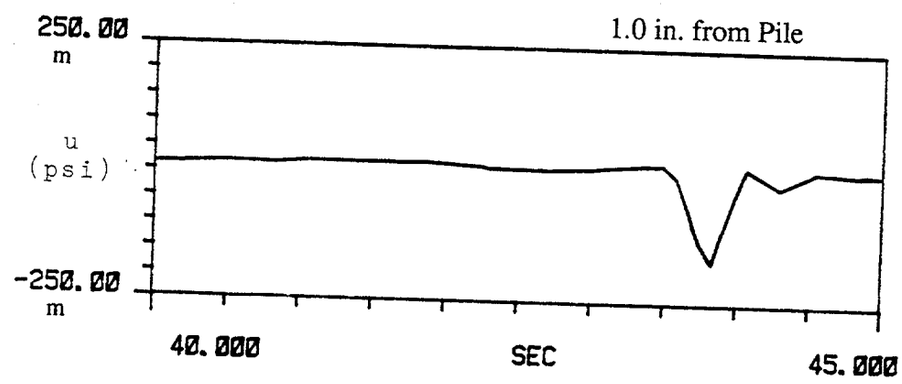

Fig. F.20. Time History Measurements of Pile Head Movement and Near Field Pore Water Pressure, Test L2, [m = milli].

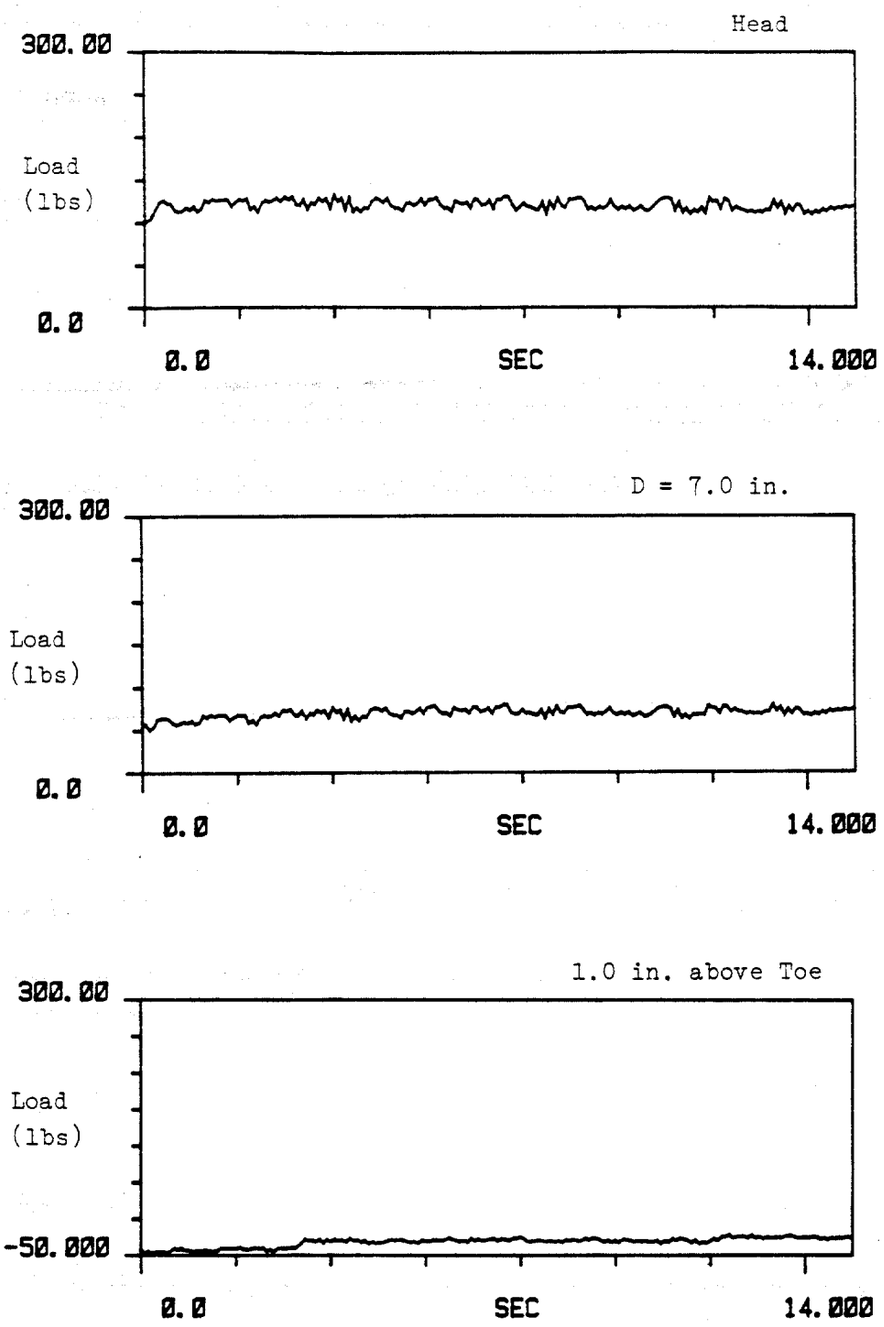

Fig. F.21. Time History Measurements of Dynamic Load on Pile, Test M1.

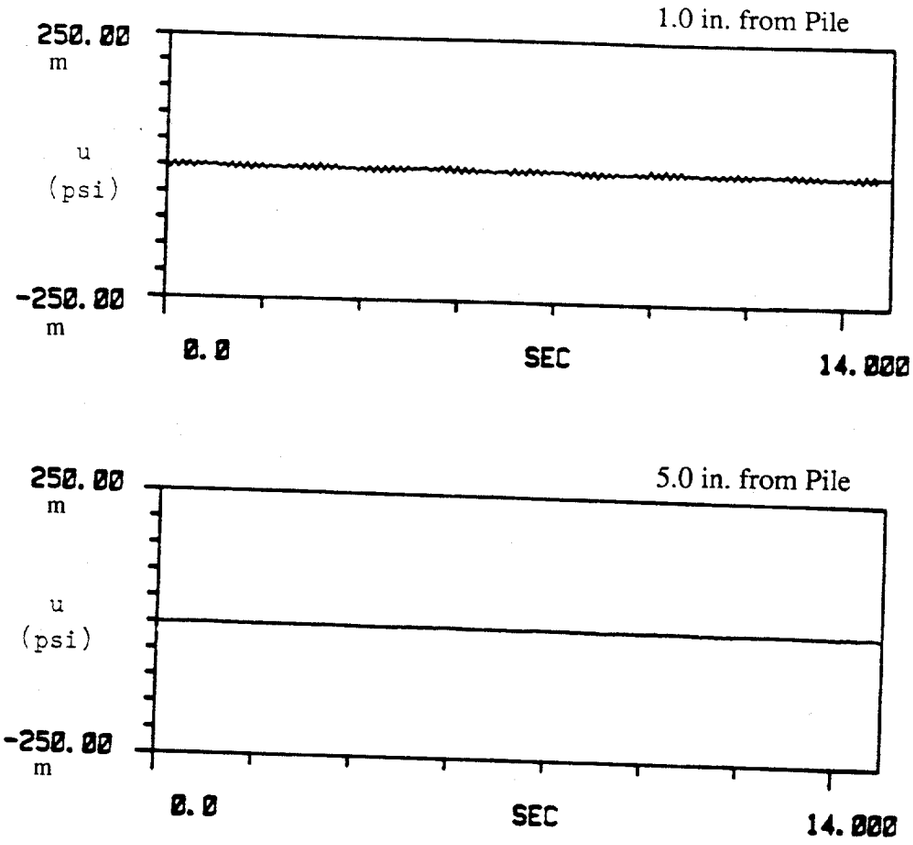

Fig. F.22. Time History Measurements of Near and Far Field Pore Water Pressures, Test M1, [m = milli].

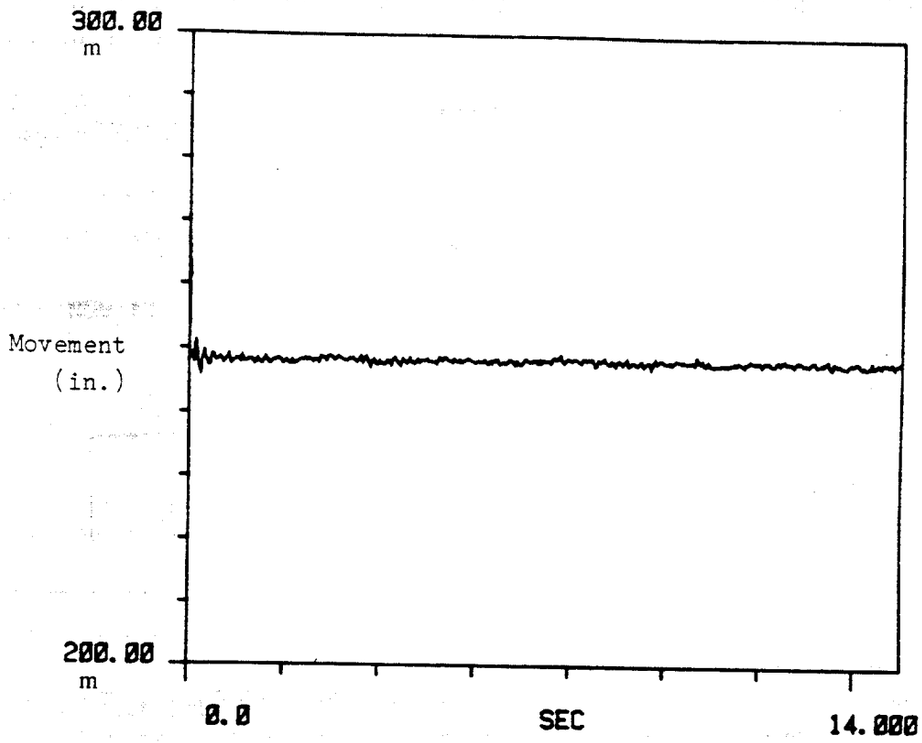

Fig. F.23. Time History Measurements of Pile Head Movement, Test M1, [m = milli].

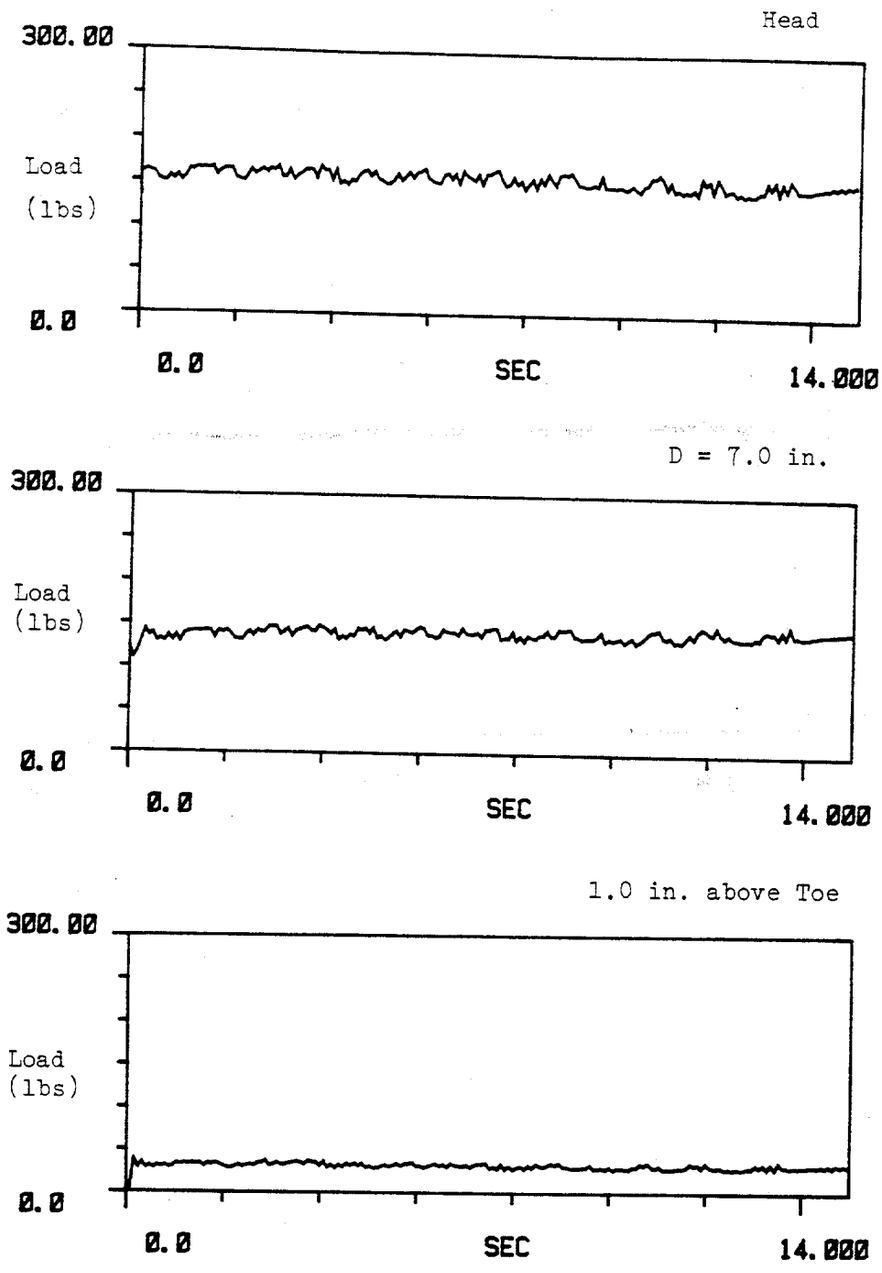

Fig. F.24. Time History Measurements of Dynamic Load on Pile, Test M2.

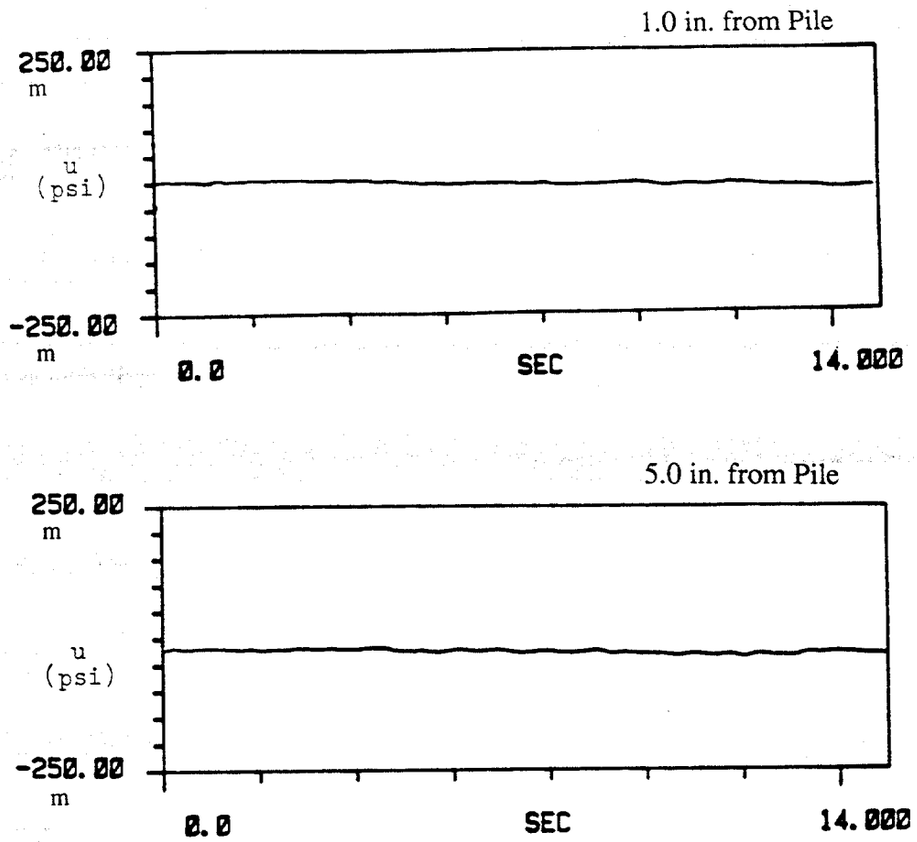

Fig. F.25. Time History Measurements of Near and Far Field Pore Water Pressures, Test M2, [m = milli].

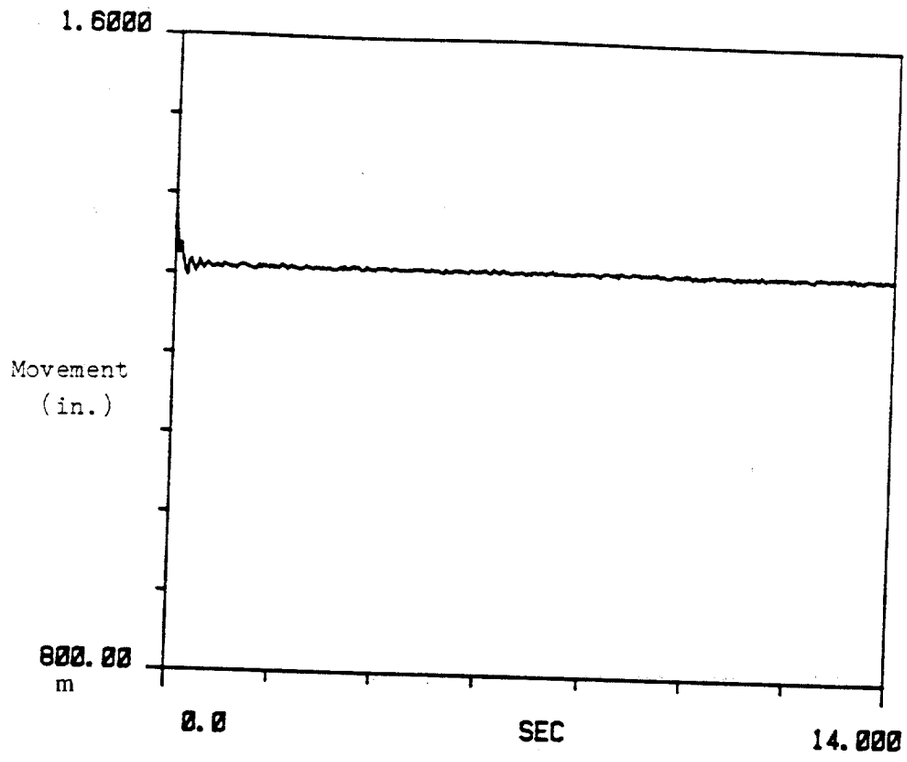

Fig. F.26. Time History Measurements of Pile Head Movement, Test M2, [m = milli].

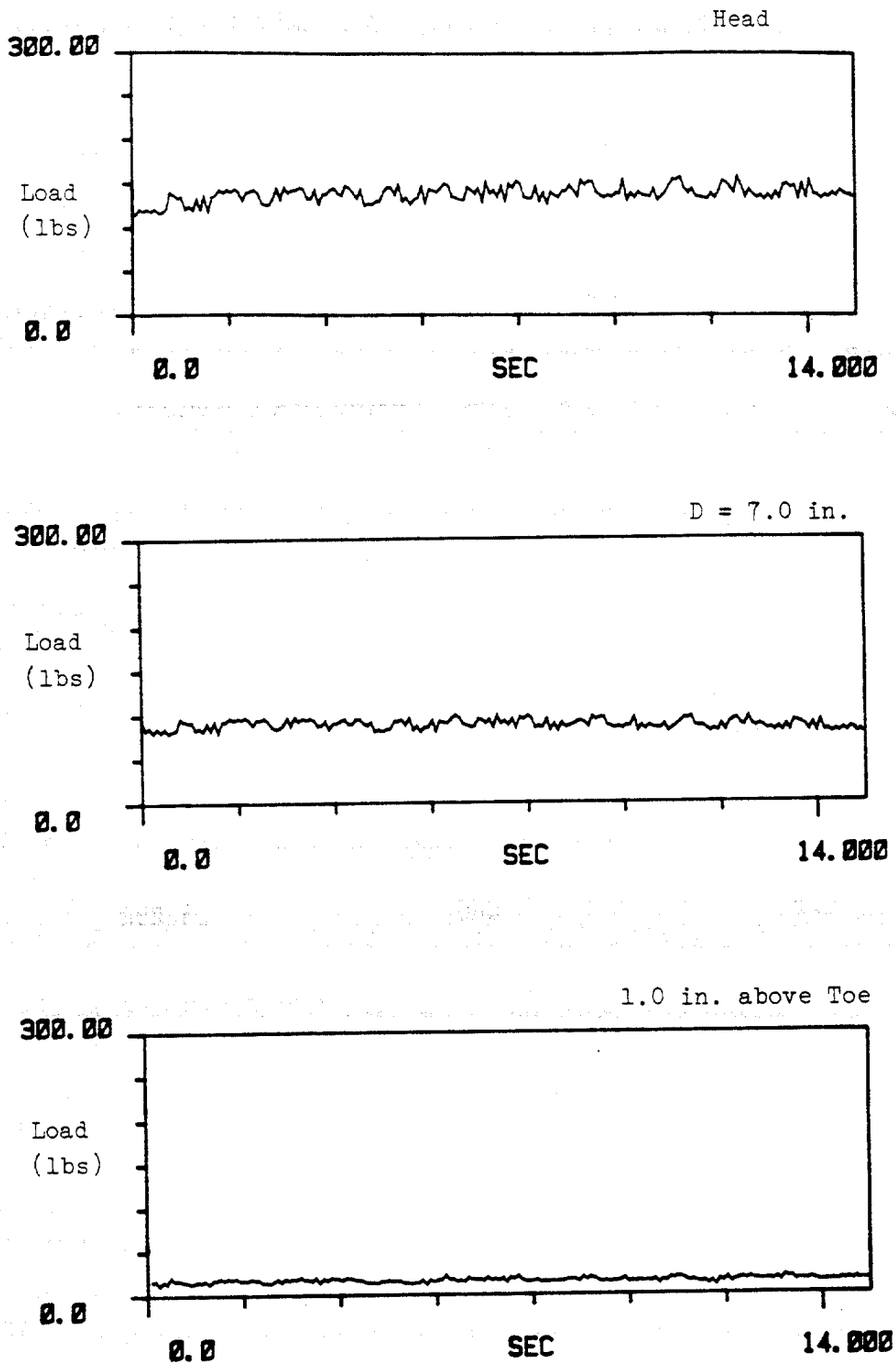

Fig. F.27. Time History Measurements of Dynamic Load on Pile, Test N1.

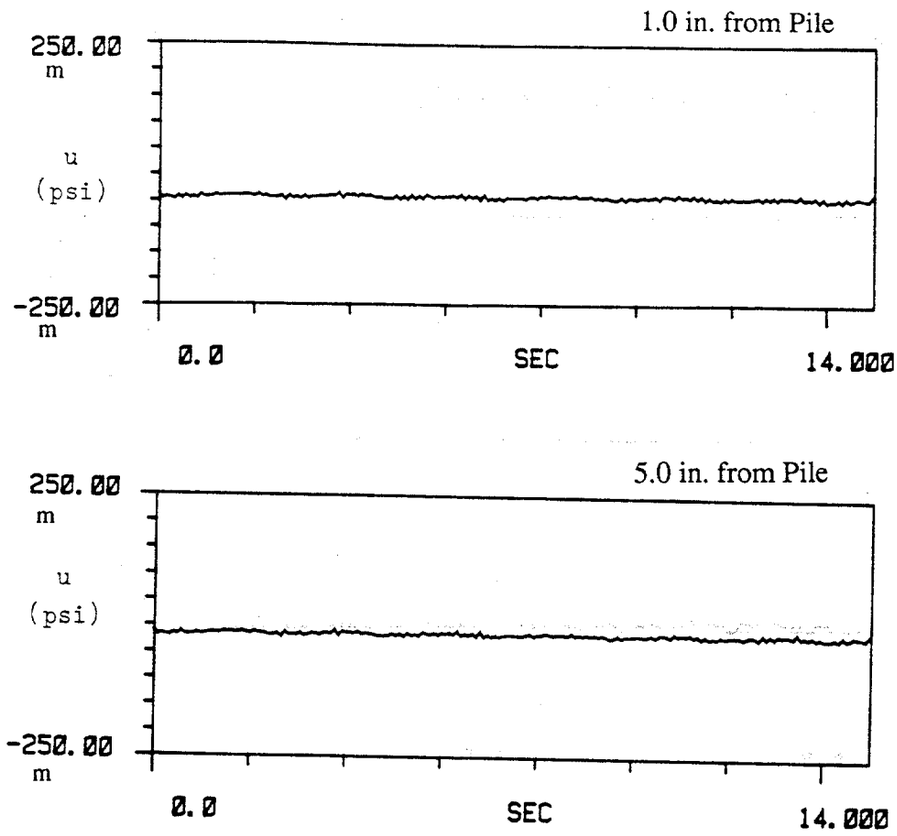

Fig. F.28. Time History Measurements of Near and Far Field Pore Water Pressures, Test N1, [m = milli].

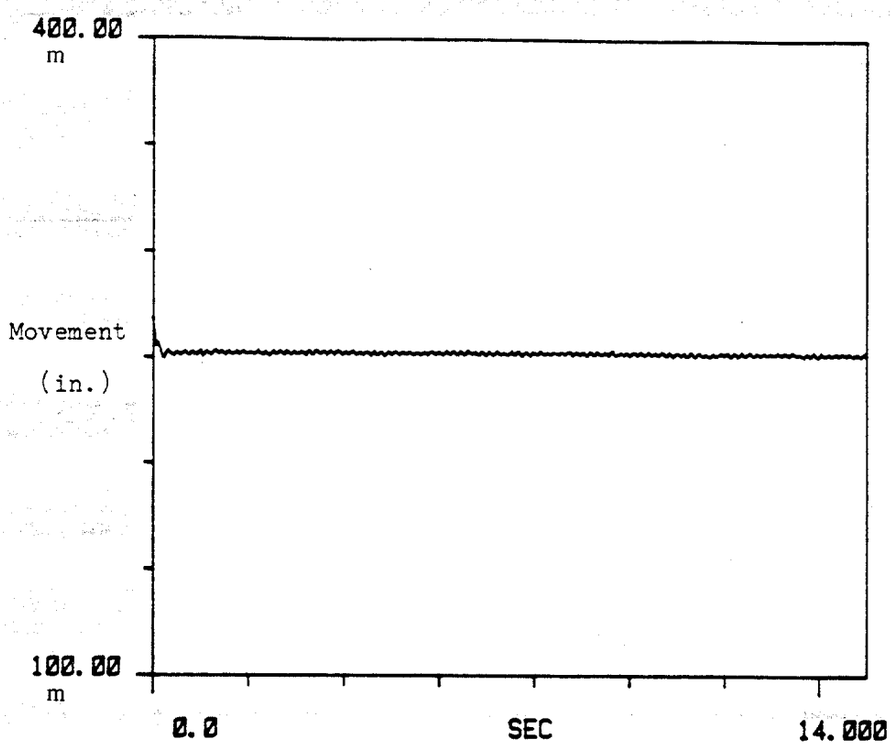

Fig. F.29. Time History Measurements of Pile Head Movement, Test N1, [m = milli].

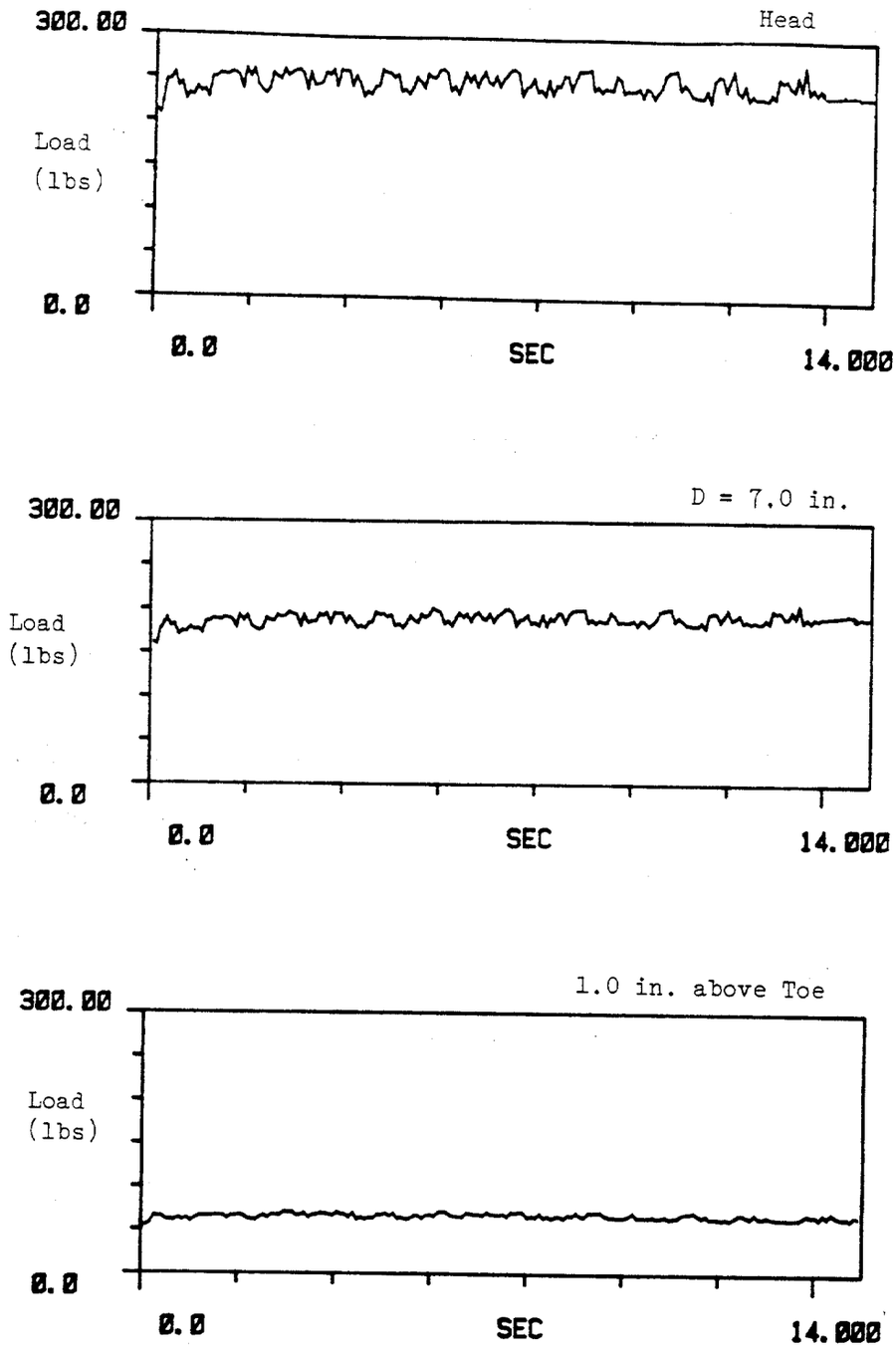

Fig. F.30. Time History Measurements of Dynamic Load on Pile, Test N2.

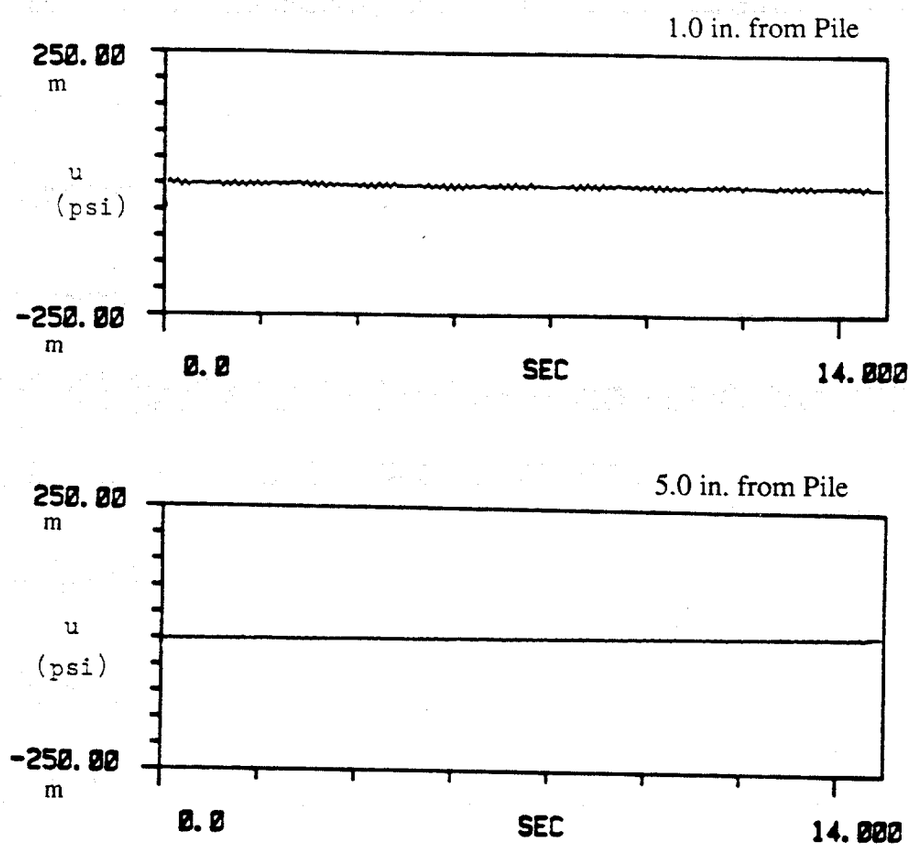

Fig. F.31. Time History Measurements of Near and Far Field Pore Water Pressures, Test N2, [m = milli].

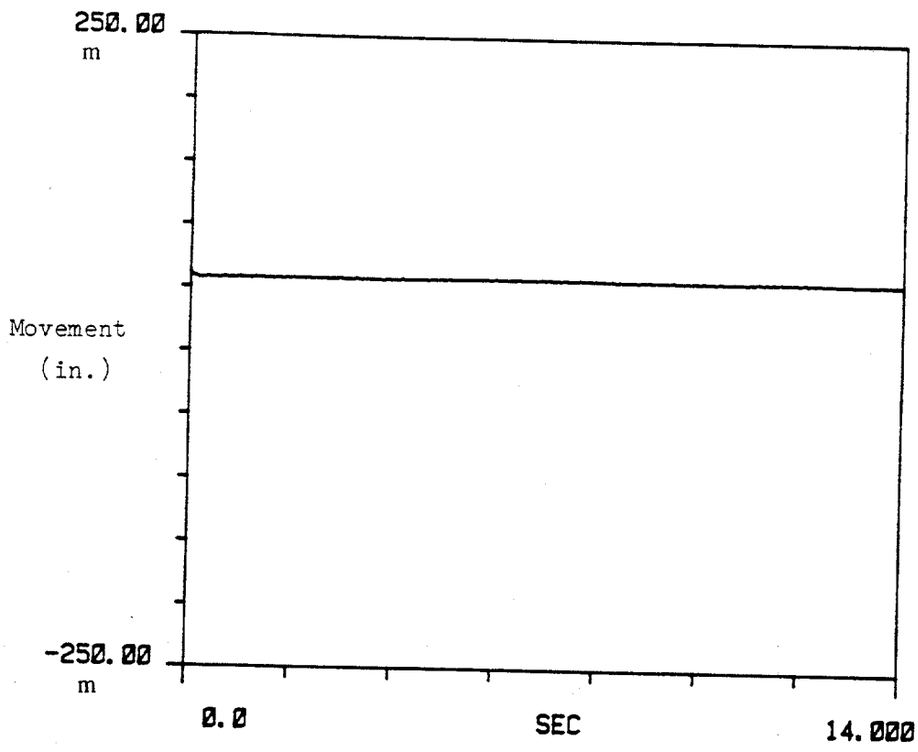

Fig. F.32. Time History Measurements of Pile Head Movement, Test N2, [m = milli].

APPENDIX G

Basic Axial Wave Propagation Analysis in a Finite Rod

For a prismatic member, that is, one with properties constant along the length, the equation of axial motion can be expressed as follows:

$$\frac{\partial^2 u\,(x,t)}{\partial x^2} = \frac{1}{c^2}\,\frac{\partial^2 u\,(x,t)}{\partial t^2} \qquad \text{(G.1)}$$

where

u = displacement along the axis x,
c = velocity of wave propagation,
t = time.

Let the soil column be represented by an elastic rod subjected to an exciting displacement function at one end and free at the other. The boundary conditions are given as follows:

$$(1)\ u\,(0,t) = U_o\,(t),$$
$$(2)\ \partial u/\partial x\,|_{x=L} = 0,$$

and the initial condition is: $u\,(x,0) = 0$.

The solution of Eq. G.1 can be obtained by separation of variables, assuming that the solution has the following form:

$$u\,(x,t) = Y(x)\,G(t)\,. \qquad \text{(G.2)}$$

Substituting Eq. G.2. into the governing differential equation (Eq. G.1) gives

$$Y''(x)\,G(t) = \frac{1}{c^2}\,Y(x)\,\ddot{G}(t), \quad \text{or} \quad \frac{Y''(x)}{Y(x)} - \frac{1}{c^2}\frac{\ddot{G}(t)}{G(t)} = 0\,. \qquad \text{(G.3)}$$

Because the first term in Eq. G.3 is a function of x only and the second term a function of t only, the equation can be satisfied for arbitrary x and t only if each other term is equal to a constant, that is

$$\frac{Y''(x)}{Y(x)} = \frac{G(t)}{c^2\,G(t)} = -\lambda^2\,.$$

Thus, two ordinary differential equations are obtained, one involves each variable. These two equations may be written as follows:

$$Y''(x) + \lambda^2\,Y(x) = 0\,, \text{ and} \qquad \text{(G.4)}$$

$$G(t) + c^2\,\lambda^2\,G(t) = 0\,. \qquad \text{(G.5)}$$

Let the solutions of Eqs. G.4 and G.5 be as follows:

$$Y(x) = A\cos(\lambda x) + B\sin(\lambda x)\,, \qquad \text{(G.6)}$$

and

$$G(t) = C\cos(c\lambda t) + D\sin(c\lambda t)\,. \qquad \text{(G.7)}$$

• As $u(x,0) = 0$, i.e., $Y(x)\,G(0) = 0$, it follows that (because $Y(x) \neq 0$), $G(0) = 0$. And, since $G(0) = c$, thus $c = 0$. Therefore,

$$G(t) = D\sin(c\lambda t)\,. \qquad \text{(G.8)}$$

• As $\partial u/\partial x\,|_{x=L} = 0$, $Y'(x)\,G(t)\,|_{x=L} = 0 \Rightarrow Y'(L) = 0$,

and

$$Y'(L) = -\lambda A\sin(\lambda L) + \lambda B\cos(\lambda L) = 0\,.$$

Therefore,

$$B = A\tan(\lambda L),$$

and

$$Y(x) = A\,[\cos(\lambda x) + \tan(\lambda L)\sin(\lambda x)]\ . \qquad (G.9)$$

• As $u(0,t) = Y(0)\,G(t) = A\,G(t) = U_o(t)$, thus,

$$G(t) = \frac{1}{A}\,Uo\,(t)\ .$$

If $U_o(t)$ is chosen as $U_o(t) = K \sin \omega t$, then

$$G(t) = D \sin(c\lambda t) = \frac{1}{A}\,Uo\,(t) = \frac{K}{A}\,\sin\omega t\ . \qquad (G.10)$$

The only possibility for Eq. G.10 to hold is that

$$D = \frac{1}{A},\ \text{and}\ c\lambda = \omega\ \left(\Rightarrow\ \lambda = \frac{\omega}{c}\right)\ . \qquad (G.11)$$

From Eqs. G.8, G.9 and G.11, it follows that

$u(x,t) = Y(x)\,G(t)$, or

$$u(x,t) = K \sin\omega t\,[\cos(\omega x/c) + \tan(\omega L/c)\sin(\omega x/c)]\ , \qquad (G.12)$$

and

$$\varepsilon = \partial u/\partial t = K(\omega/c)\sin(\omega t)\,[-\sin(\omega x/c) + \tan(\omega L/c)\cos(\omega x/c)]\ . \qquad (G.13)$$

The expression given in Eq. G.13 corresponds to the axial strain ε_{xx}. The derivation of an expression for the shearing strain γ_{xy} is as follows:

For small strain theory,

$$\varepsilon_{xx} = \partial u / \partial x,\ \text{in which}\ u = u(x), \qquad (G.14)$$

$$\varepsilon_{yy} = \partial v / \partial y,\ \text{in which}\ v = v\ (y), \qquad (G.15)$$

$$\gamma_{xy} = 2\varepsilon_{xy} = (\partial u / \partial y) + (\partial v / \partial x). \qquad (G.16)$$

Since u is independent of y (see Eq. G.12), then Eq. G.16 becomes

$$\gamma_{xy} = 2\varepsilon_{xy} = \partial v / \partial x\ . \qquad (G.17)$$

Also, since

$$\varepsilon_{yy} = \partial v / \partial y = -\nu\, \varepsilon_{xx} \text{ , in which } \nu = \text{Poisson's ratio,}$$

thus,

$$v = -\nu\, \varepsilon_{xx}\, y + \text{Constant.} \qquad \text{(G.18)}$$

Let the origin of the axes be at the bottom center of the soil column.
For $y = 0, \Rightarrow v = 0, \Rightarrow$ Constant = 0. Thus Eq. G.18 becomes

$$v = -\nu\, \varepsilon_{xx}\, y \text{ , and} \qquad \text{(G.19)}$$

$$\partial v / \partial x = -\nu\, y\, (\partial \varepsilon_{xx} / \partial x) \text{ .} \qquad \text{(G.20)}$$

Equating Eqs. G.17 and G.20, we get

$$\gamma_{xy} = 2\varepsilon_{xy} = -\nu\, y\, (\partial \varepsilon_{xx} / \partial x) = -\nu\, y\, (\partial^2 u / \partial x^2) \text{ .} \qquad \text{(G.21)}$$

Differentiating u twice with respect to x in Eq. G.12 , and substituting it into Eq. G.21, we finally get:

$$\gamma_{xy} = -\nu Y K \frac{\omega}{c} \sin\omega t \left[-\frac{\omega}{c} \cos\left(\frac{\omega x}{c}\right) - \frac{\omega}{c} \tan\left(\frac{\omega L}{c}\right) . \sin\left(\frac{\omega x}{c}\right) \right] \text{ .} \qquad \text{(G.22)}$$

Let the properties of the column of soil be:

E (Young's modulus) = 2000 psi (Fig. 4.2, σ_3 = 10 psi),

ρ (soil density) = 0.00016 lb-sec/in^4.

Thus

c (Velocity of wave propagation) = 3535 in/sec.

Also, for

L (length of test chamber) = 20 in.,

Y (radius of test chamber) = 10 in.,

ν (Poisson's ratio) = 0.25 .

For two signals (Fig. 5.13), one high-frequency (ω = 1 Hz = 6.28 rad/sec) low-displacement (K = 0.05 in.) signal, and one low-frequency (ω = 0.12 Hz= 0.766 rad/sec)

high-displacement (K = 0.73 in.) signal, the maximum shearing strain (γ_{xy}) computed in the soil column was in the order of 10^{-4}%.

Appendix H

Spectra, Acceleration, Velocity and Displacement Time Histories for Magnitudes 7.0 and 7.5 (Horizontal Motion)

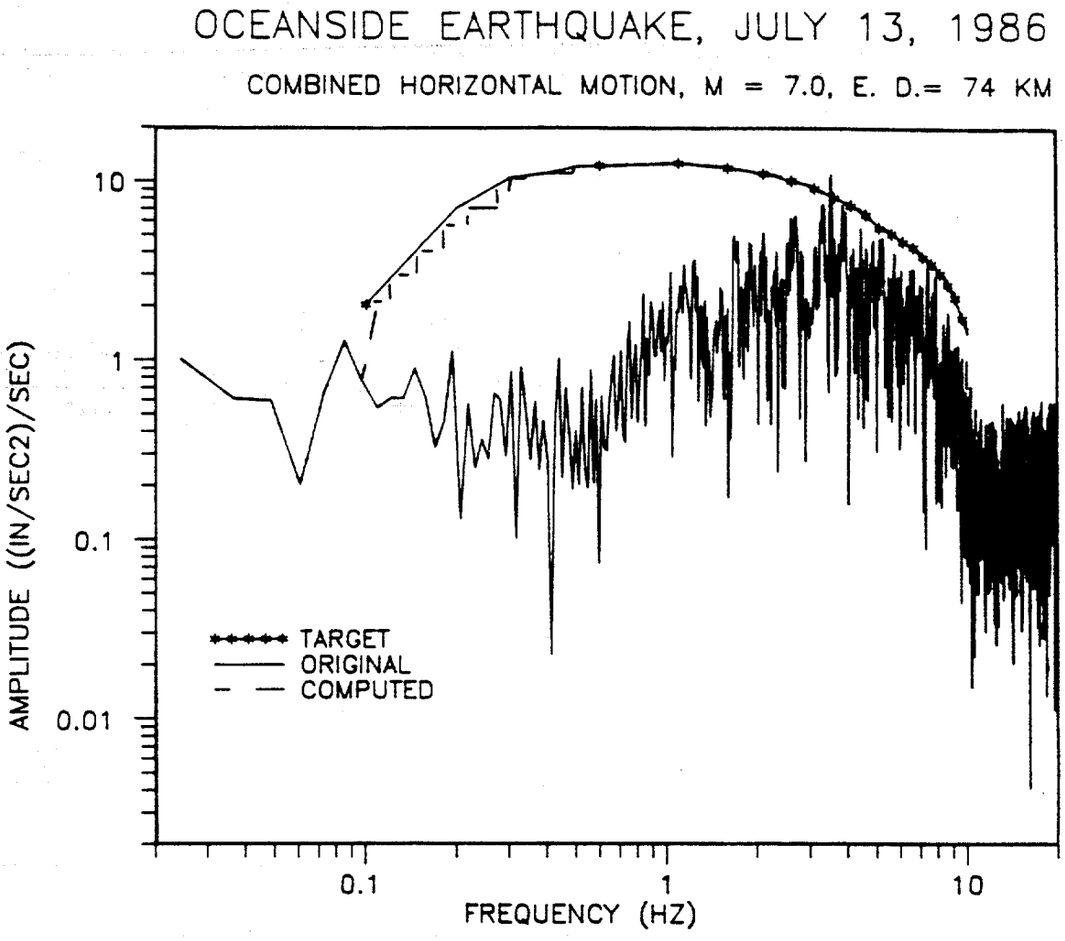

Fig. H.1. Original, Target and Computed (Scaled, M=7.0) Spectra (Horizontal Motion).

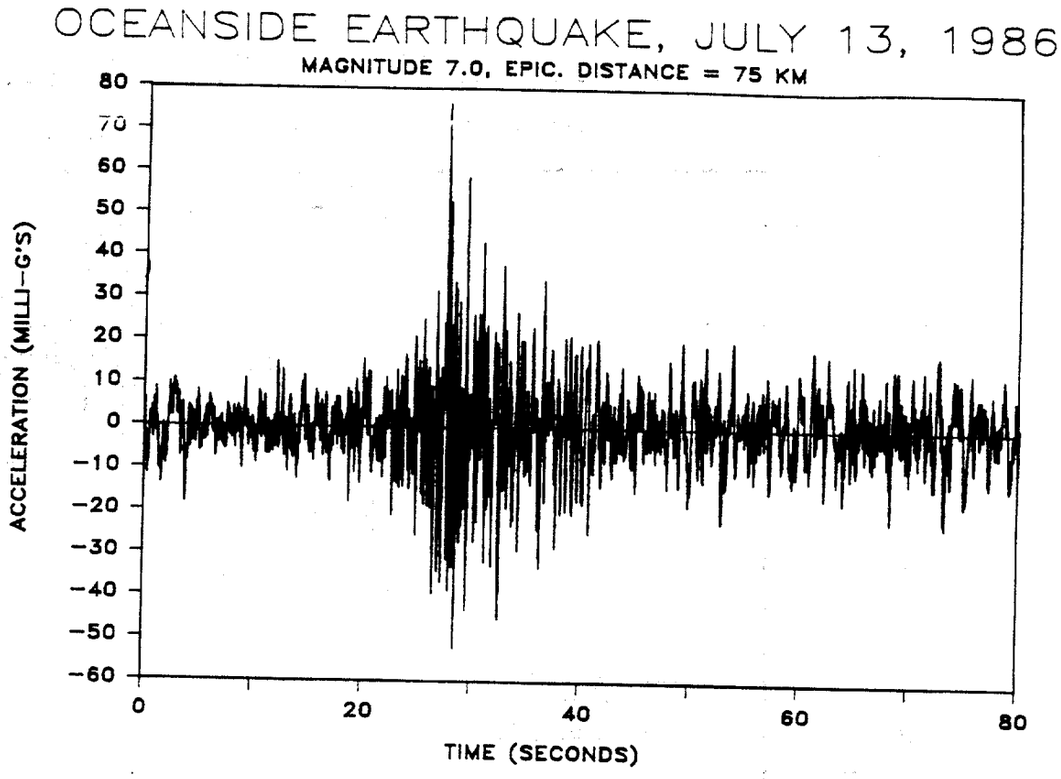

Fig. H.2. Combined Scaled (M=7.0) Horizontal Record of Oceanside Earthquake.

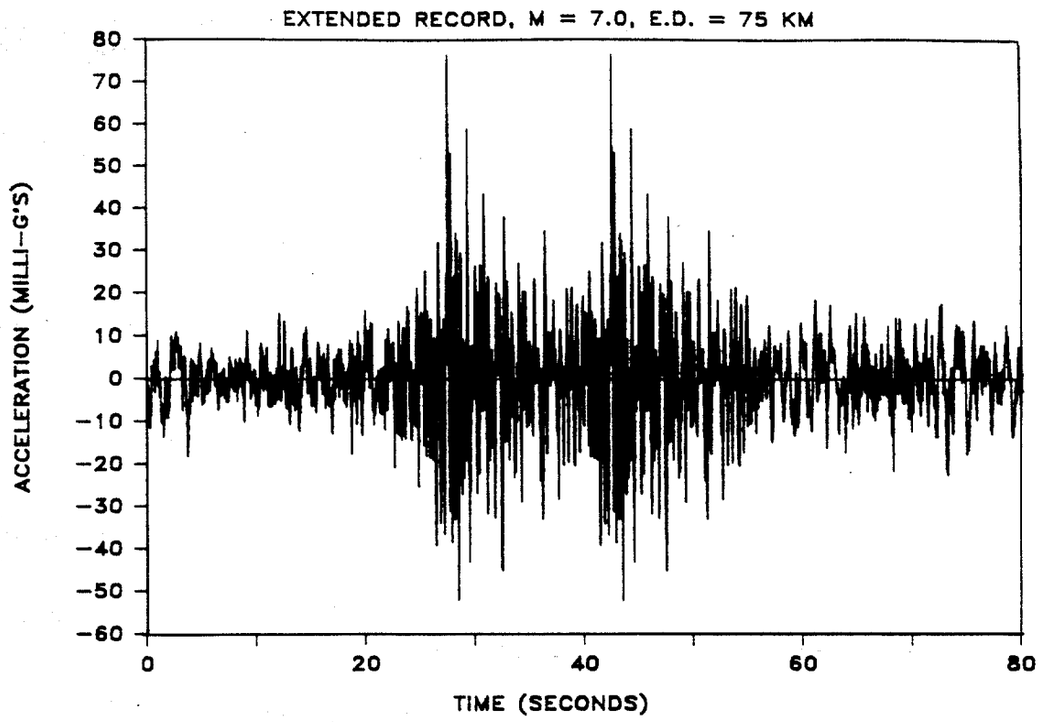

Fig. H.3. Extended Scaled (M=7.0) Horizontal Record of Oceanside Earthquake.

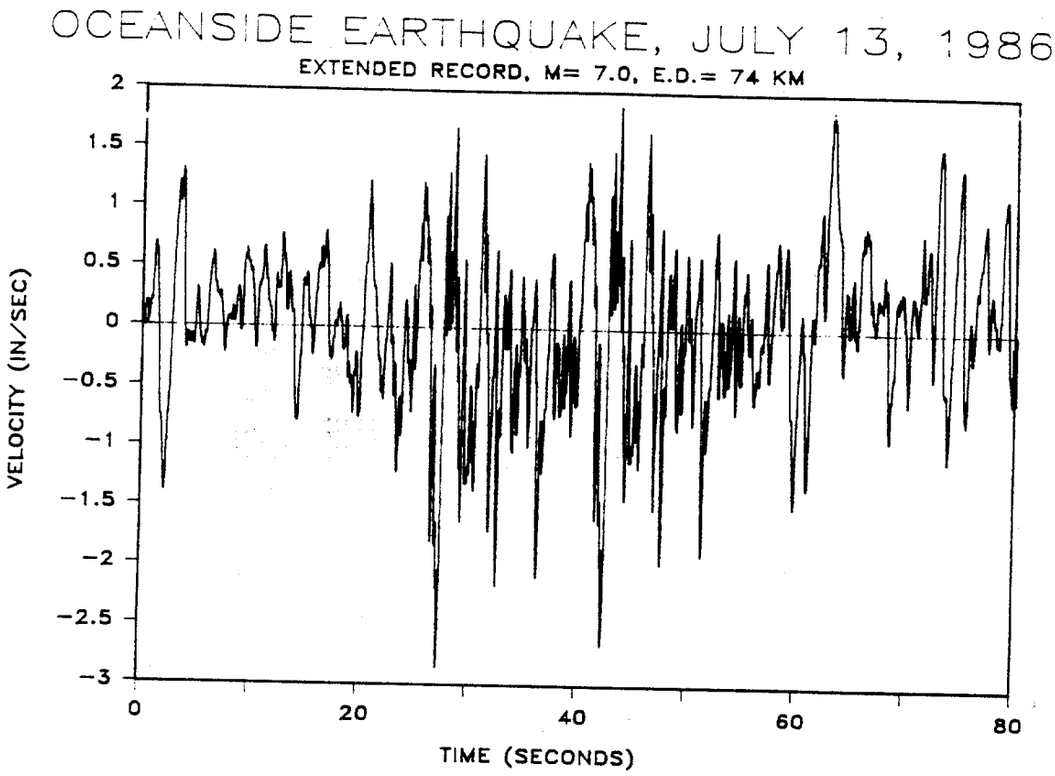

Fig. H.4. Velocity Time History of Extended and Scaled (M=7.0) Horizontal Component of Oceanside Earthquake.

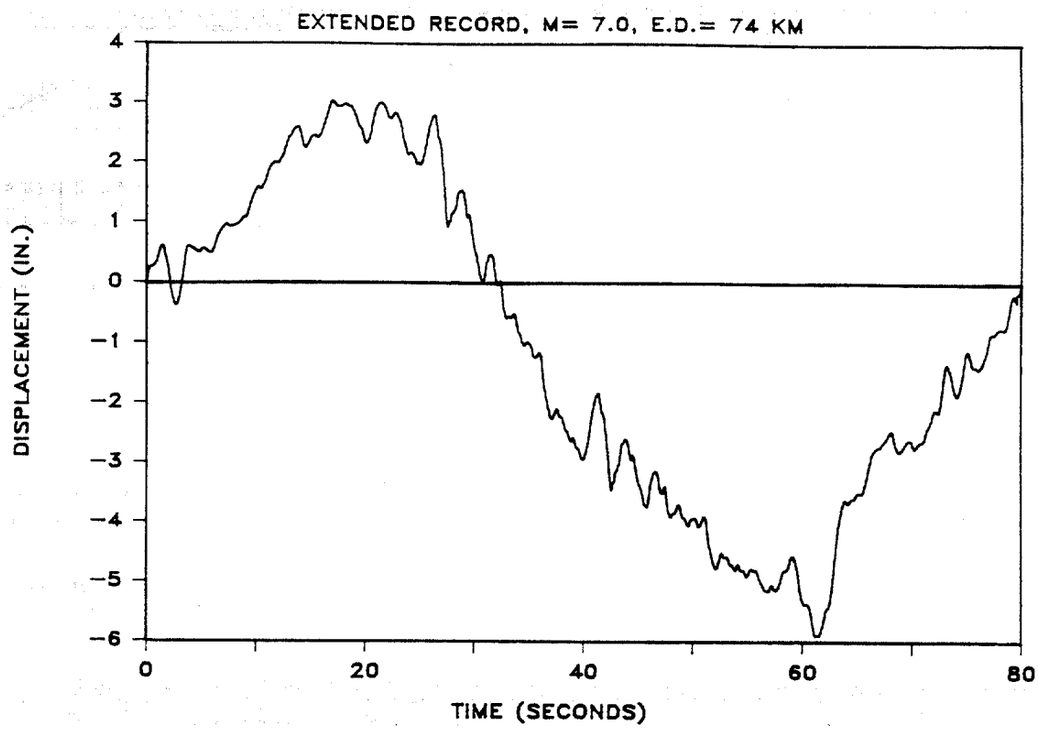

Fig. H.5. Displacement Time History of Extended and Scaled (M=7.0) Horizontal Component of Oceanside Earthquake.

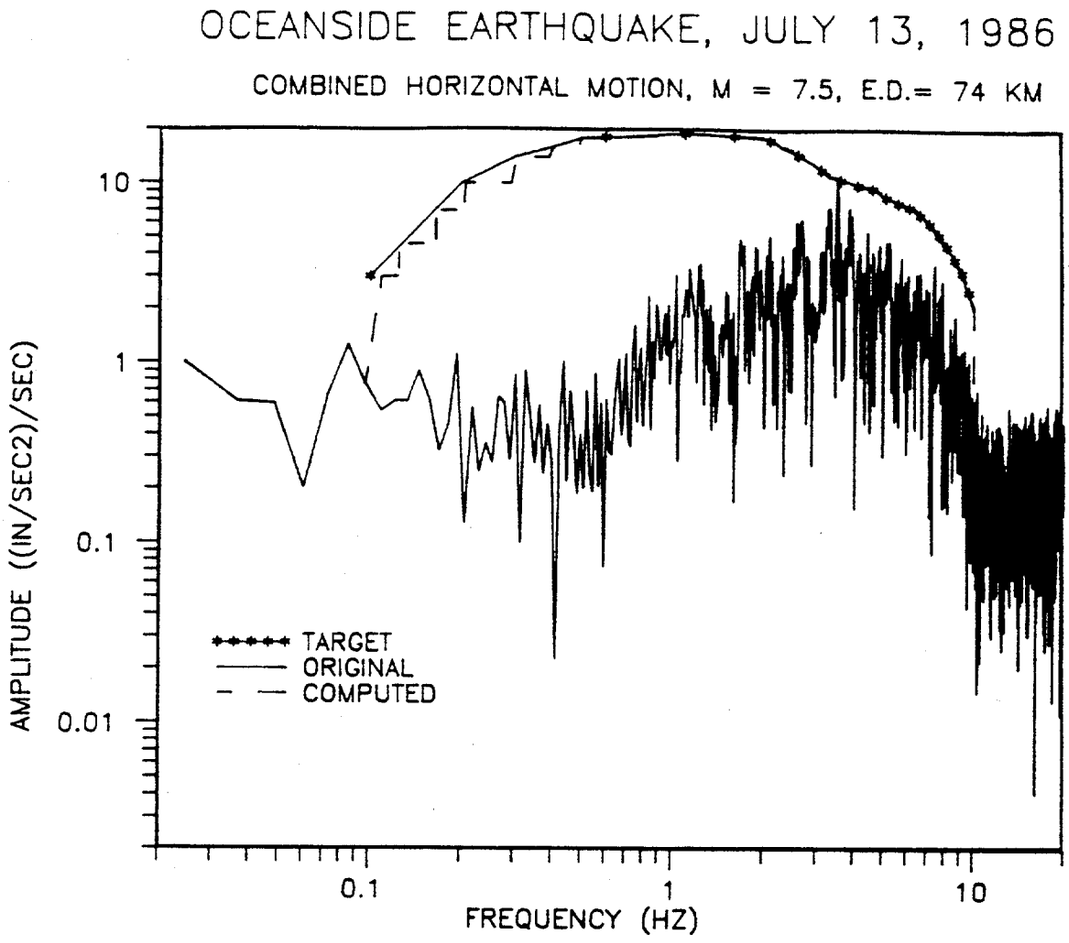

Fig. H.6. Original, Target and Computed (Scaled, M=7.5) Spectra (Horizontal Motion).

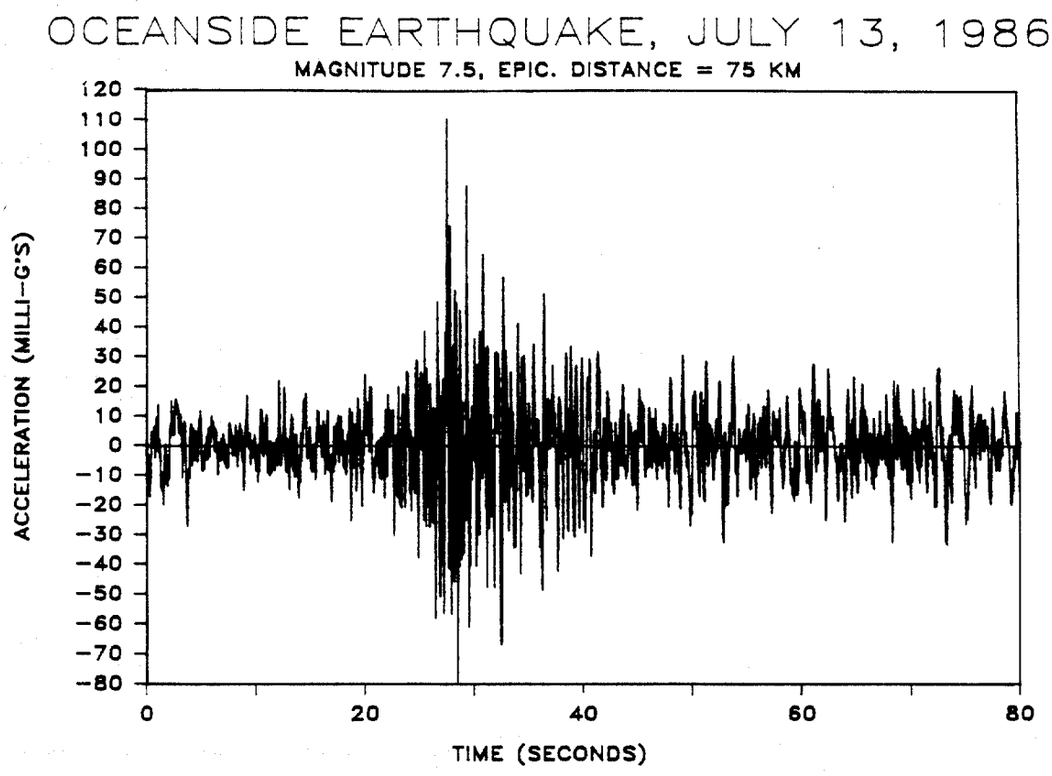

Fig. H.7. Combined Scaled (M=7.5) Horizontal Record of Oceanside Earthquake.

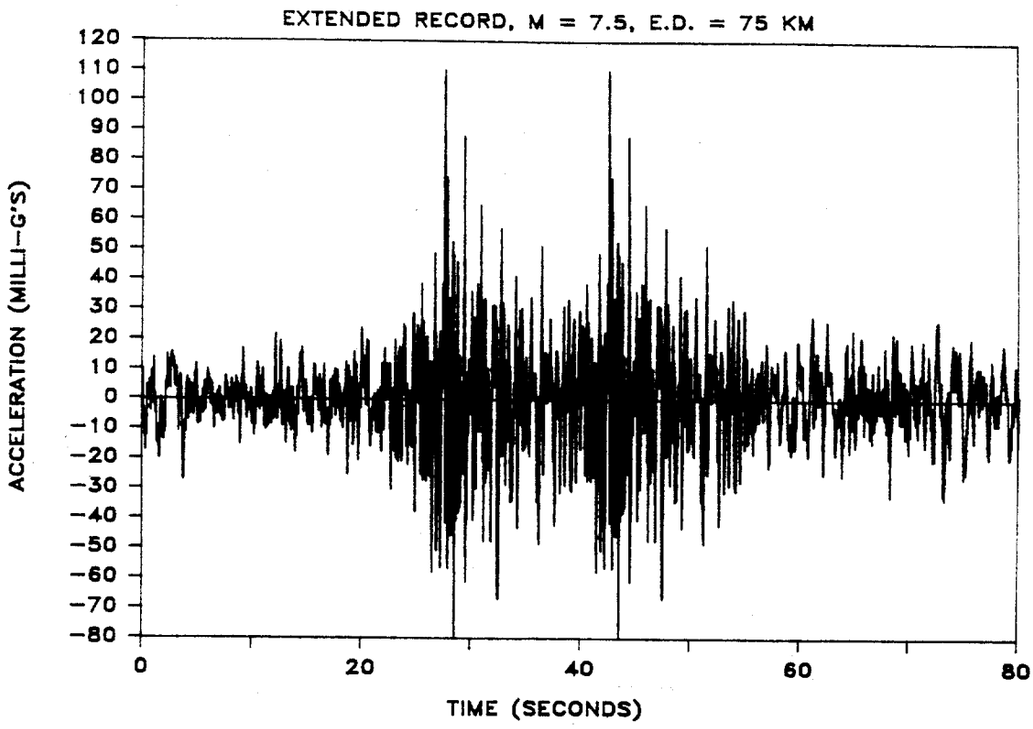

Fig. H.8. Extended Scaled (M=7.5) Horizontal Record of Oceanside Earthquake.

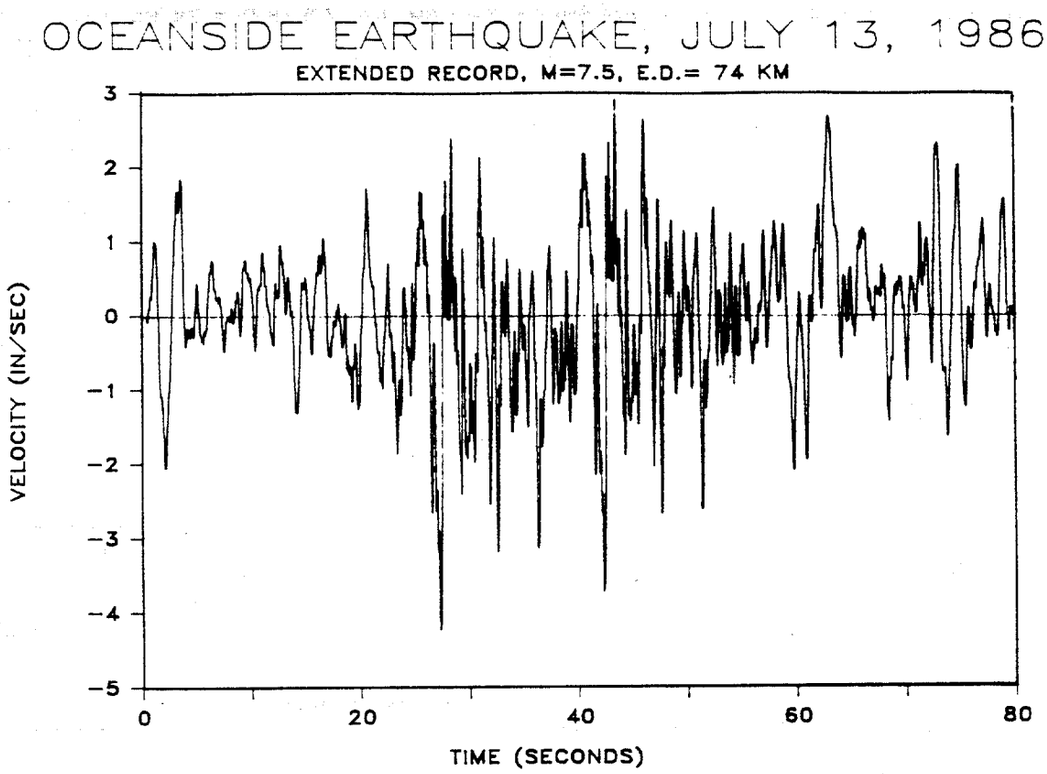

Fig. H.9. Velocity Time History of Extended and Scaled (M=7.5) Horizontal Component of Oceanside Earthquake.

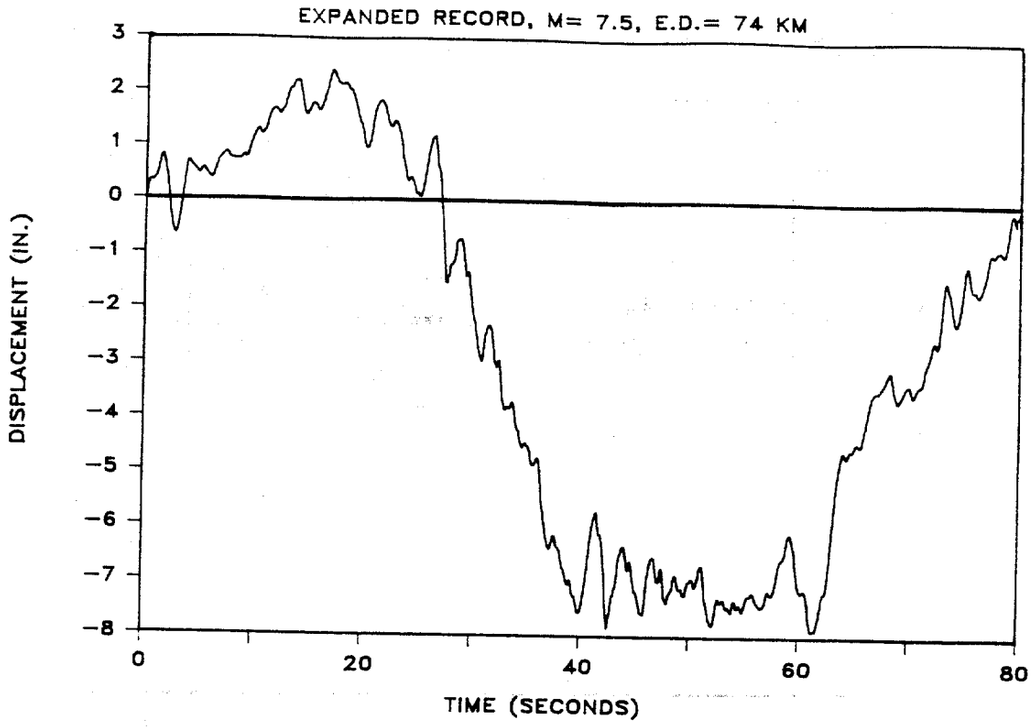

Fig. H.10. Displacement Time History of Extended and Scaled (M=7.5) Horizontal Component of Oceanside Earthquake.

Appendix I

Soil Properties for SHAKE Analysis

0'

Dr = 55% - 70%

-6'

Dr = 55% - 70% <----------Input Motion

-12'

S_u = 1.0 Ksf - 2.5 Ksf

-30'

Dr = 55% - 70%

-50'

Dr = 55% - 70%

-70'

Dr = 55% - 70%

-100'

S_u = 2.0 Ksf - 3.0 Ksf

-150'

S_u = 2.0 Ksf - 4.0 Ksf

-210'

Appendix J

Time History Measurements During Dynamic Tests, Horizontal Motion (Raw Data).

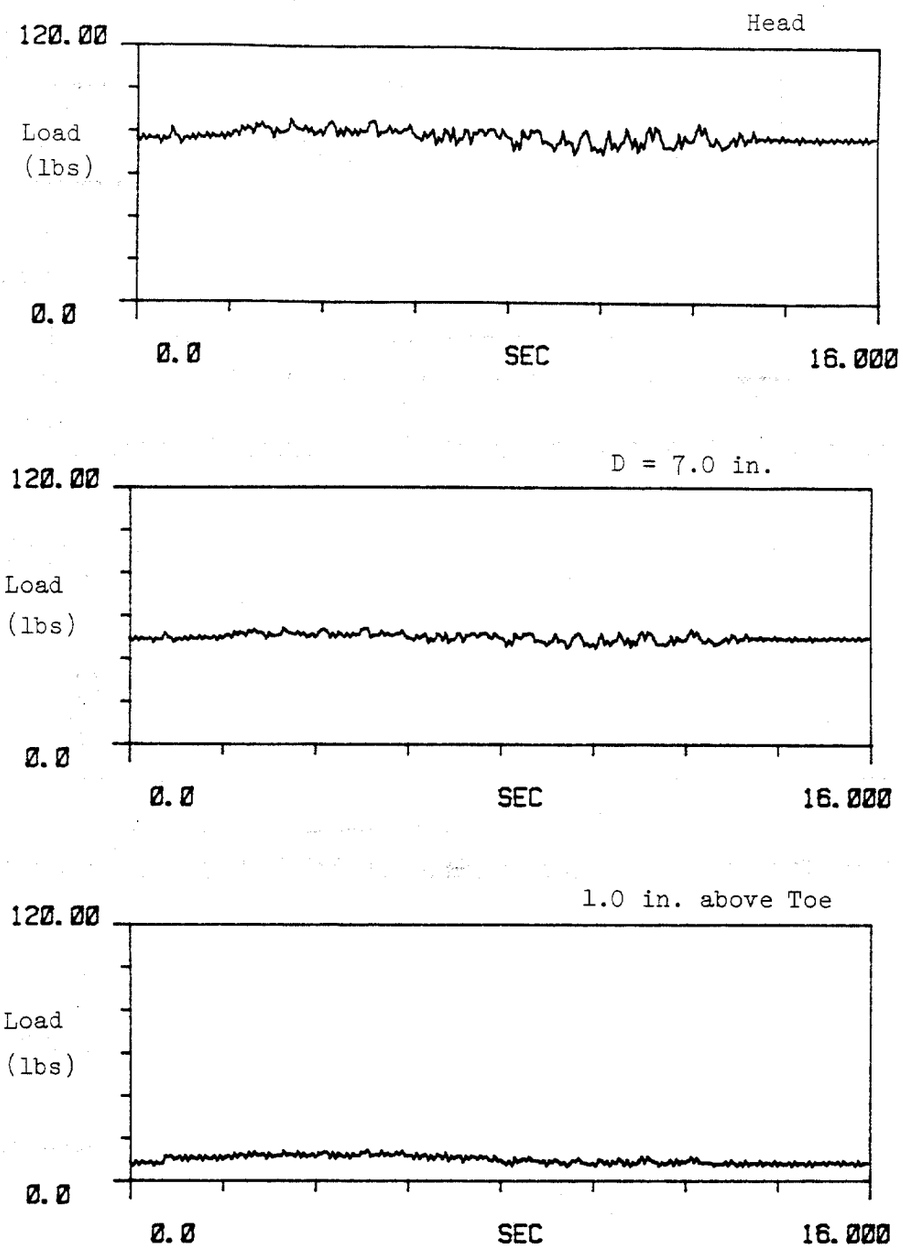

Fig. J.1. Time History Measurements of Dynamic Load on Pile, Test R1.

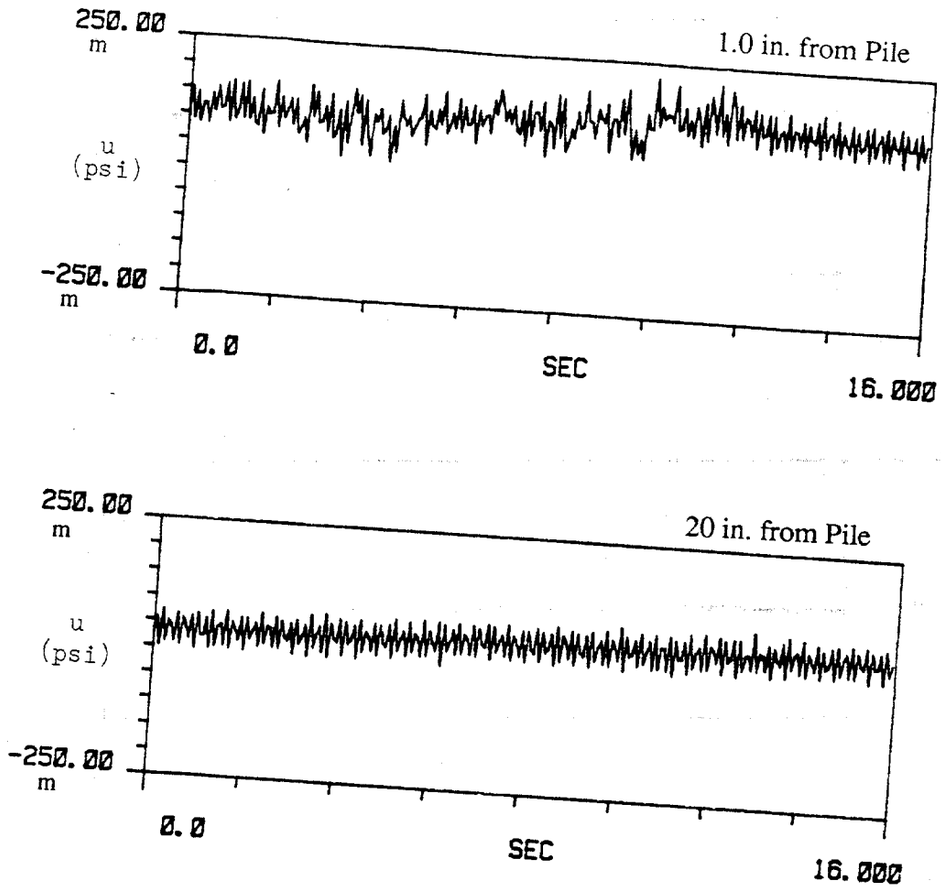

Fig. J.2. Time History Measurements of Near and Far Field Pore Water Pressures, Test R1, [m = milli].

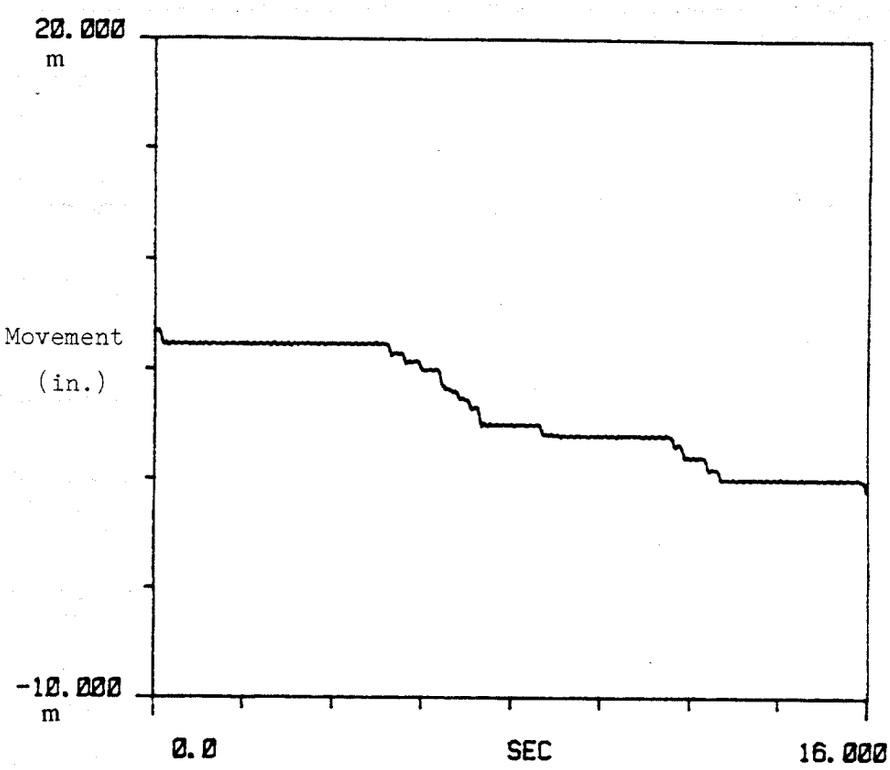

Fig. J.3. Time History Measurements of Pile Head Movement, Test R1. [m = milli].

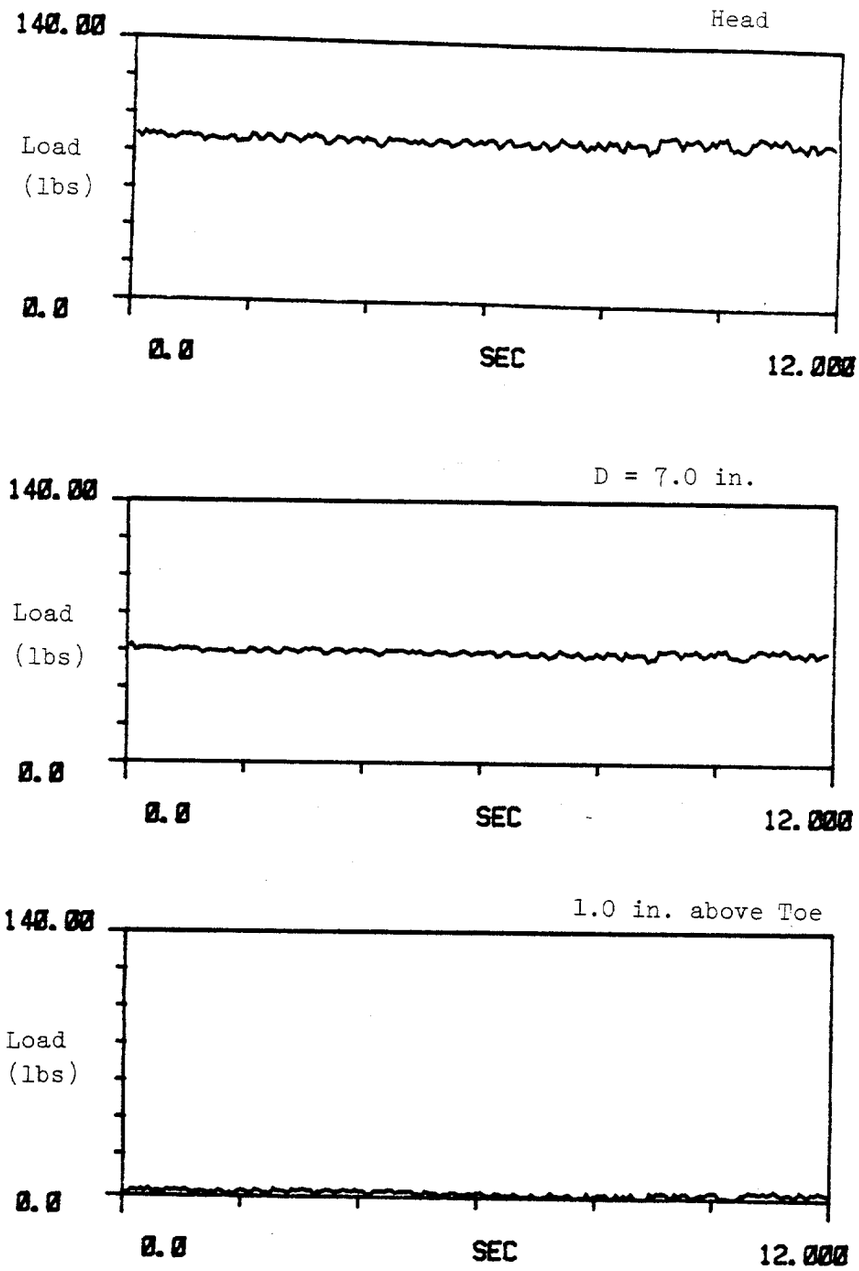

Fig. J.4. Time History Measurements of Dynamic Load on Pile, Test S1.

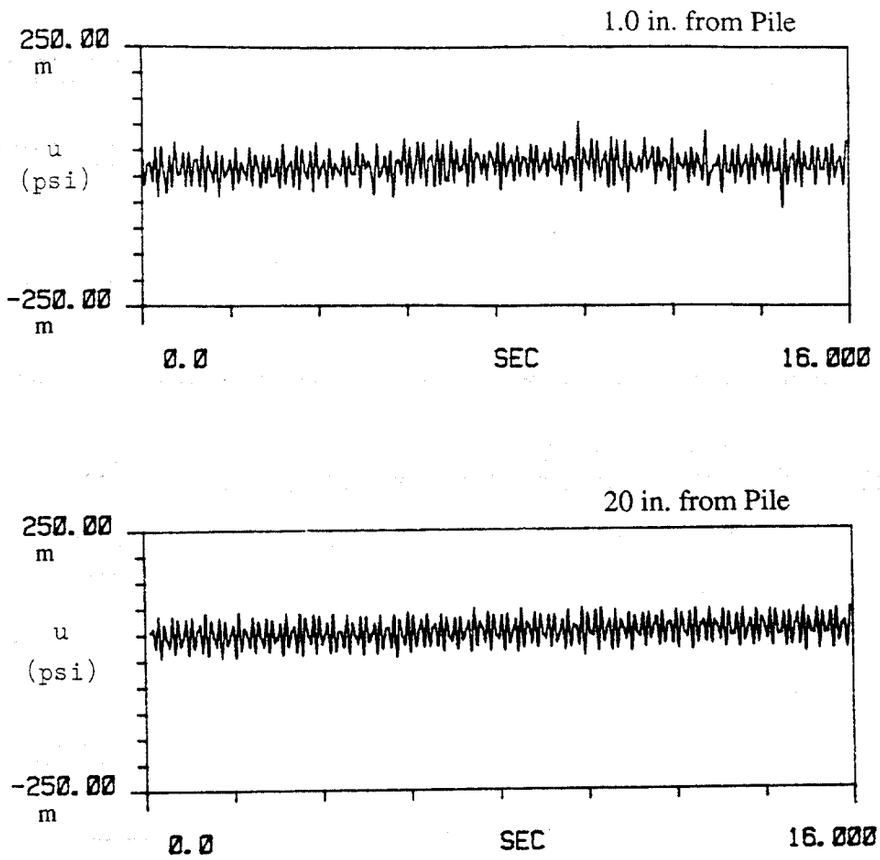

Fig. J.5. Time History Measurements of Near and Far Field Pore Water Pressures, Test S1, [m = milli].

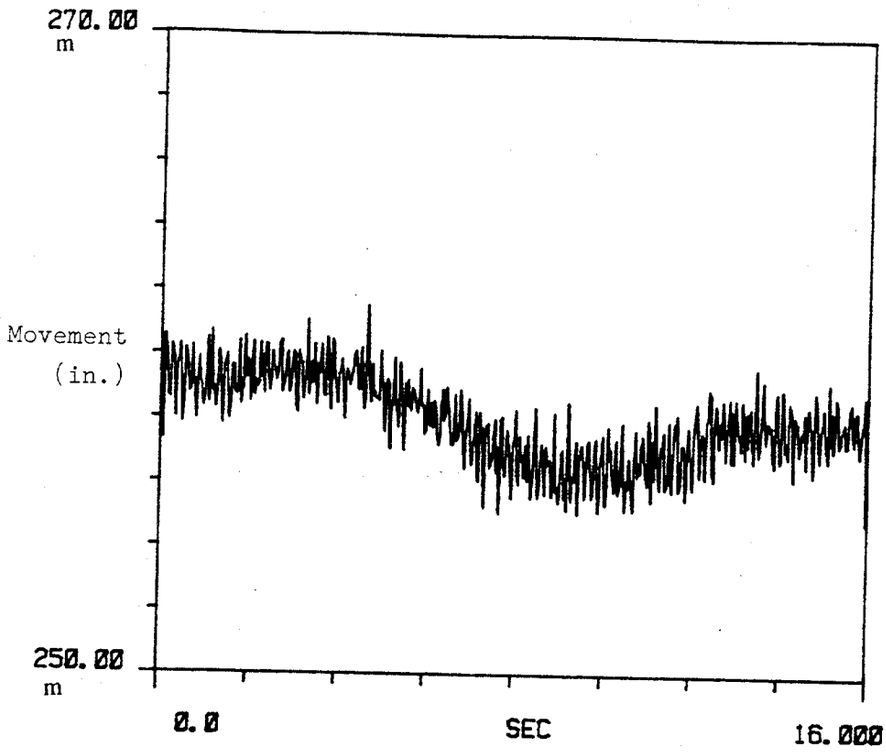

Fig. J.6. Time History Measurements of Pile Head Movement, Test S1, [m = milli].

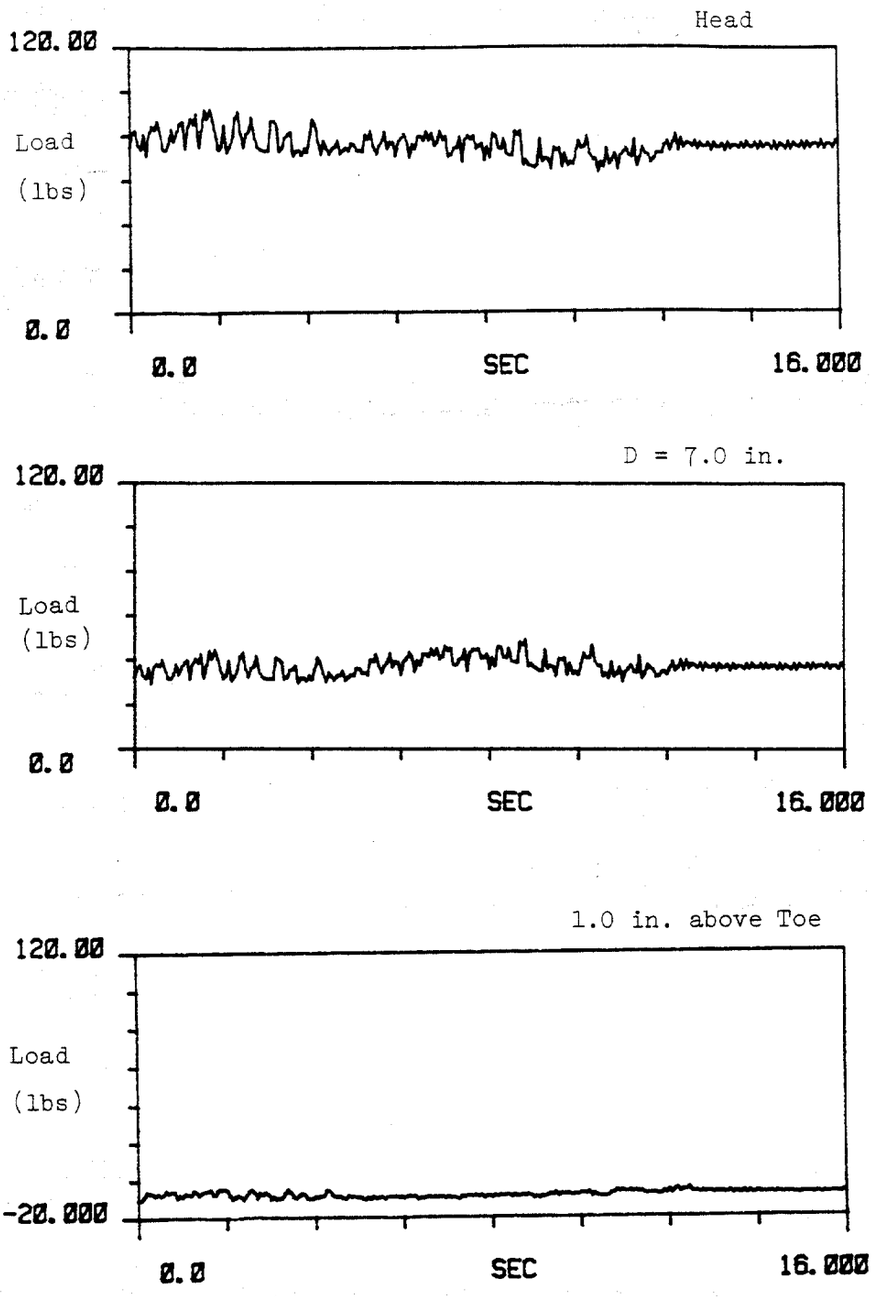

Fig. J.7. Time History Measurements of Dynamic Load on Pile, Test S2.

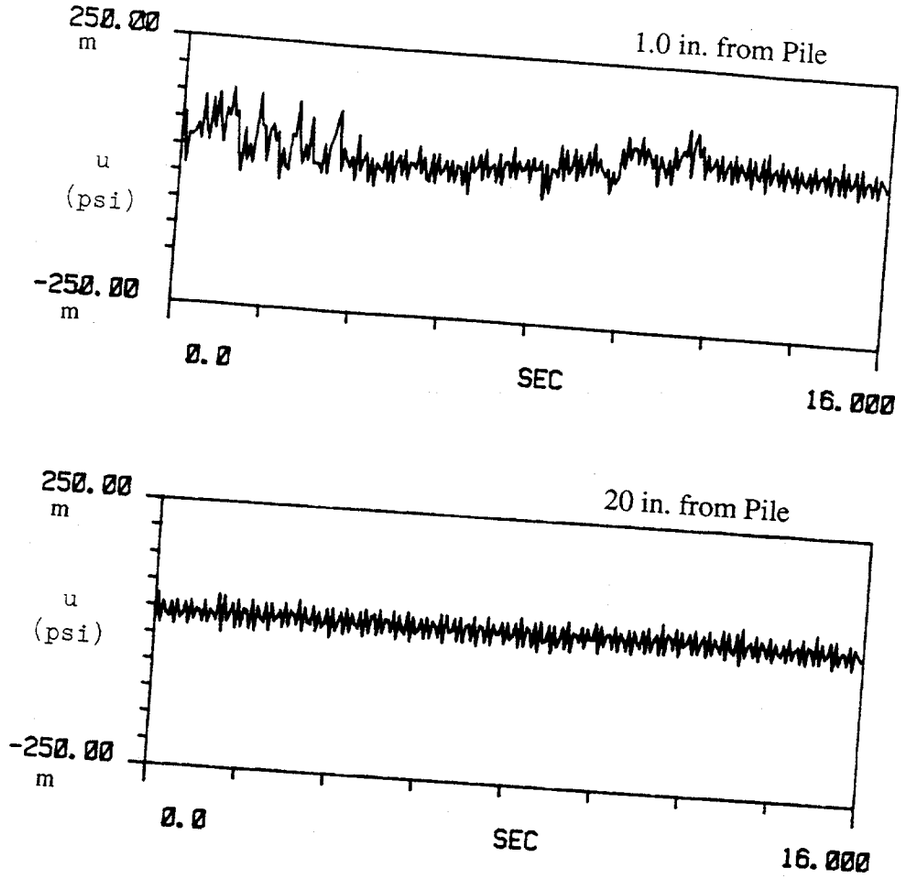

Fig. J.8. Time History Measurements of Near and Far Field Pore Water Pressures, Test S2, [m = milli].

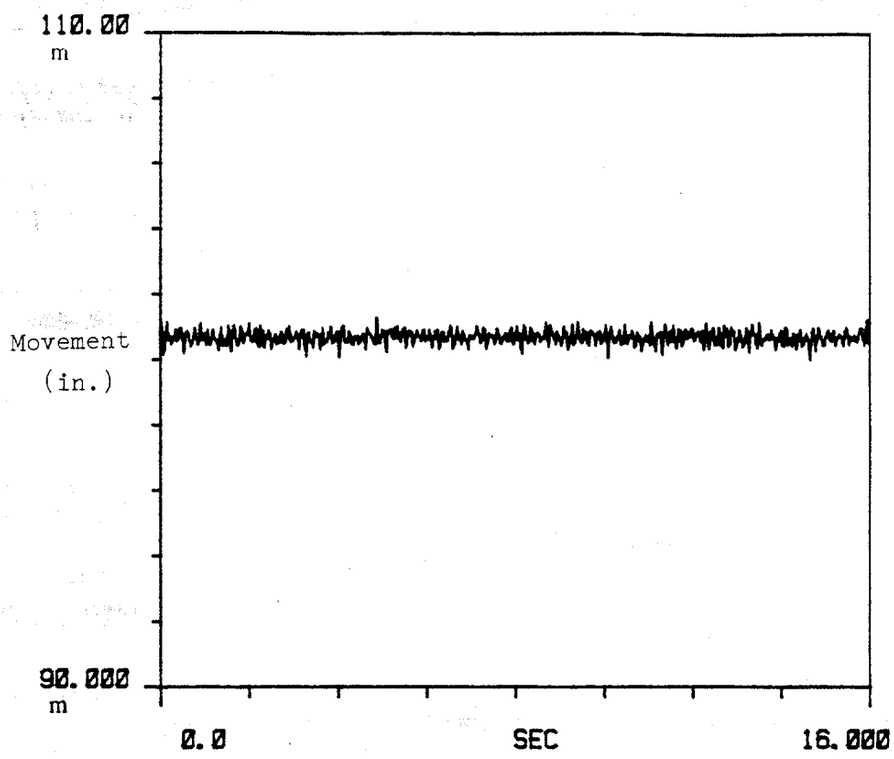

Fig. J.9. Time History Measurements of Pile Head Movement, Test S2, [m = milli].

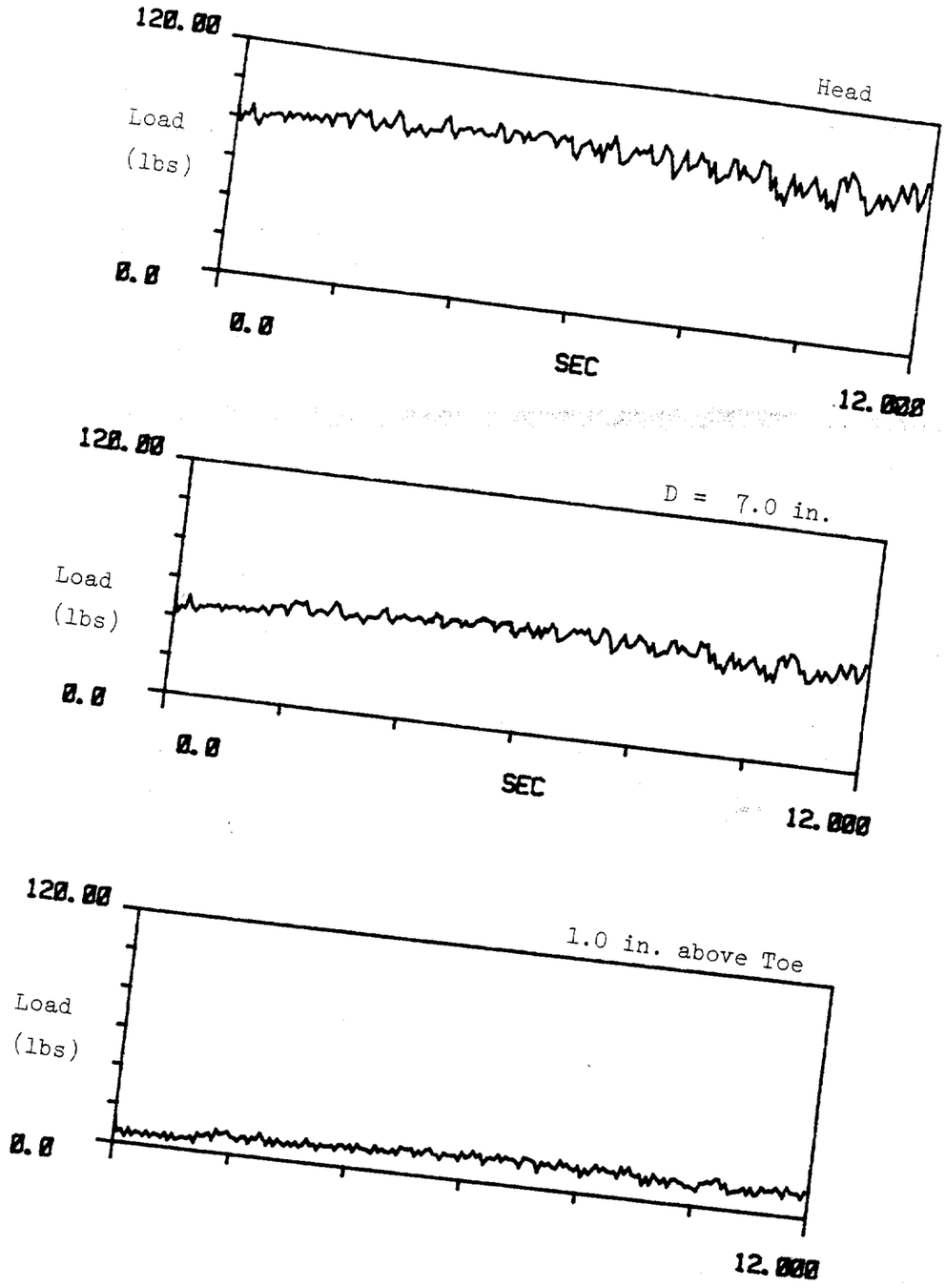

Fig. J.10. Time History Measurements of Dynamic Load on Pile, Test S3.

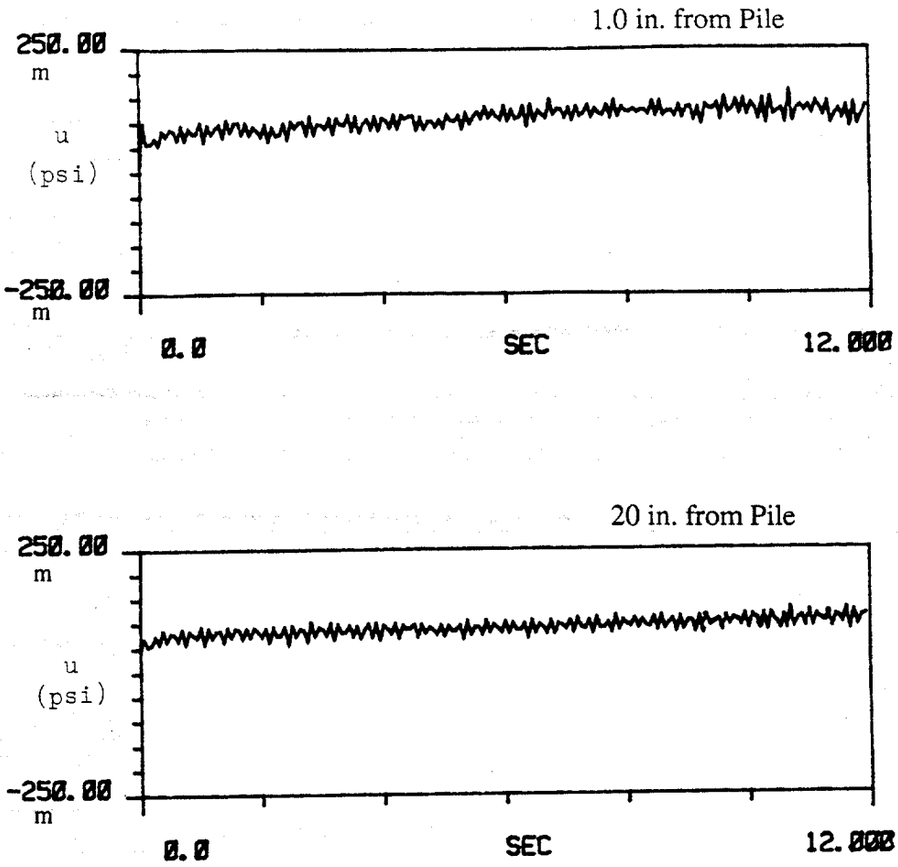

Fig. J.11. Time History Measurements of Near and Far Field Pore Water Pressures, Test S3, [m = milli].

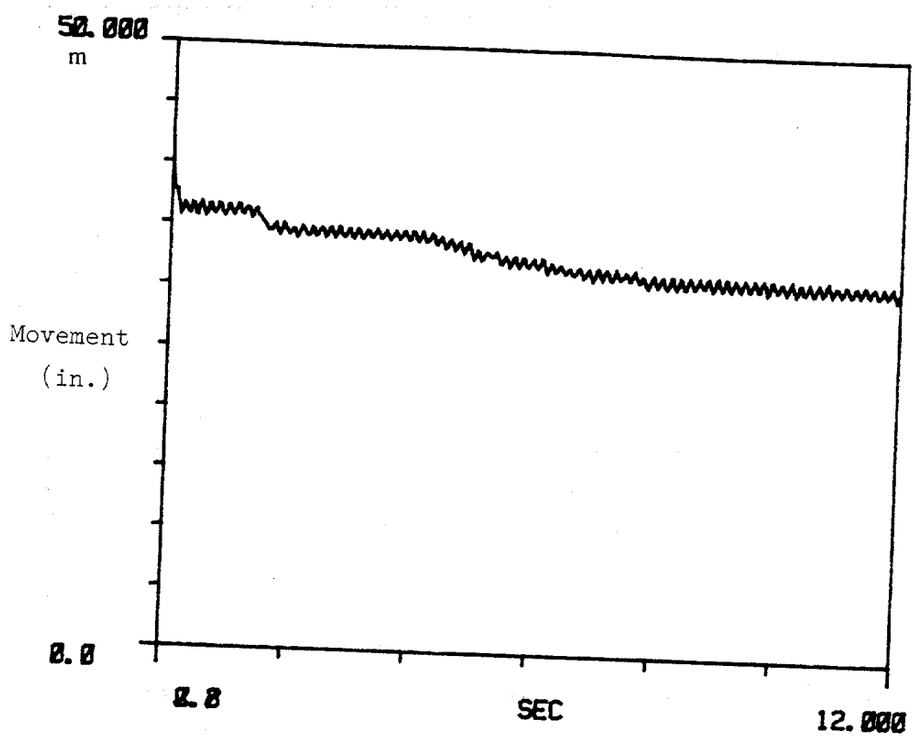

Fig. J.12. Time History Measurements of Pile Head Movement, Test S3, [m = milli].

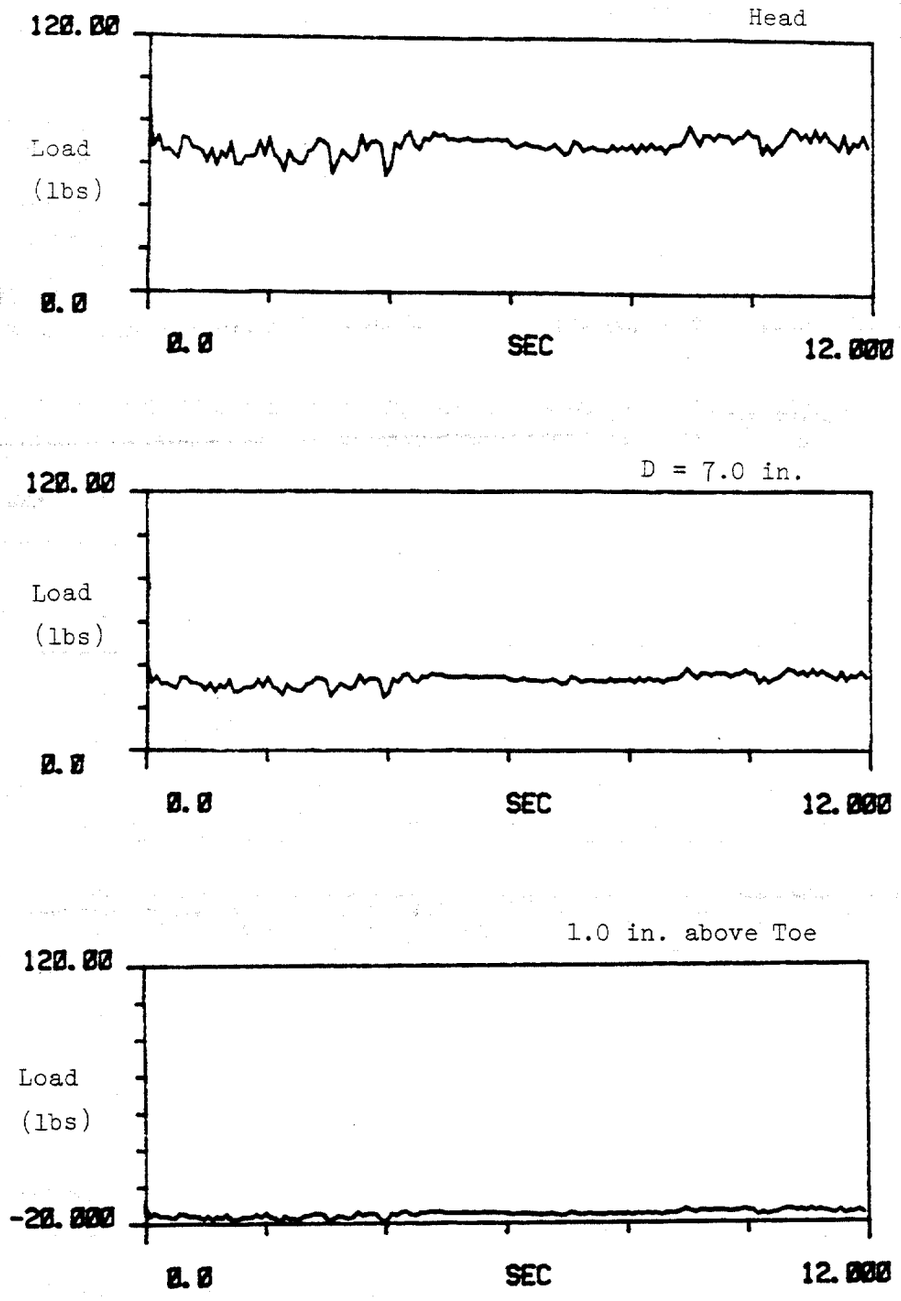

Fig. J.13. Time History Measurements of Dynamic Load on Pile, Test U2.

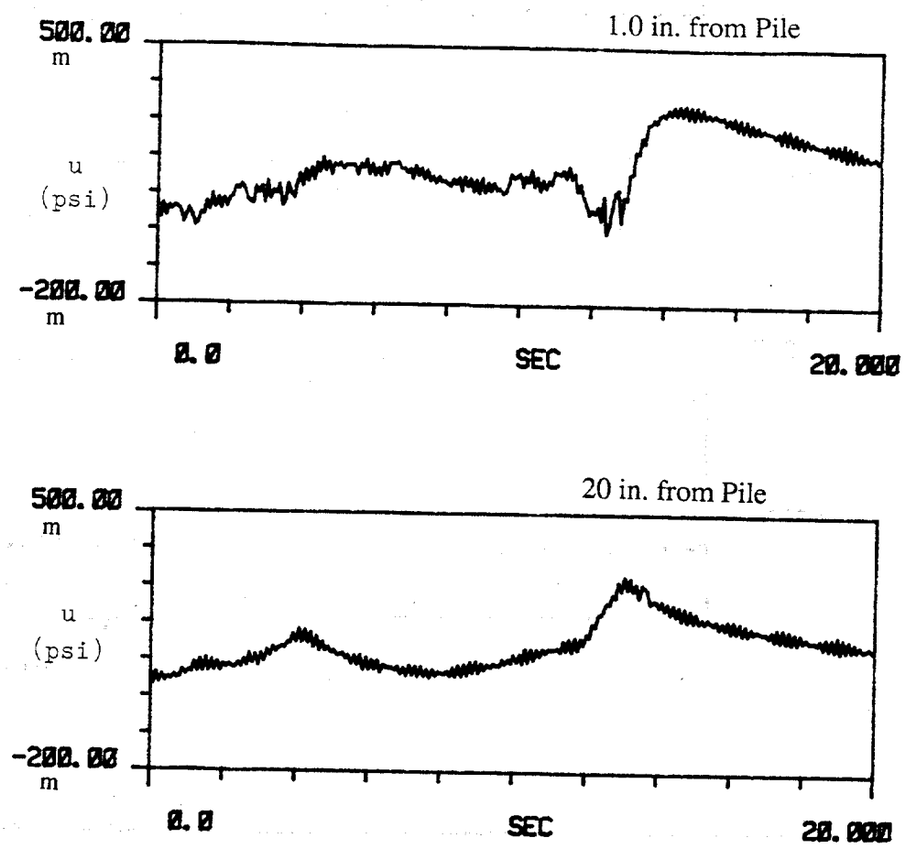

Fig. J.14. Time History Measurements of Near and Far Field Pore Water Pressures, Test U2, [m = milli].

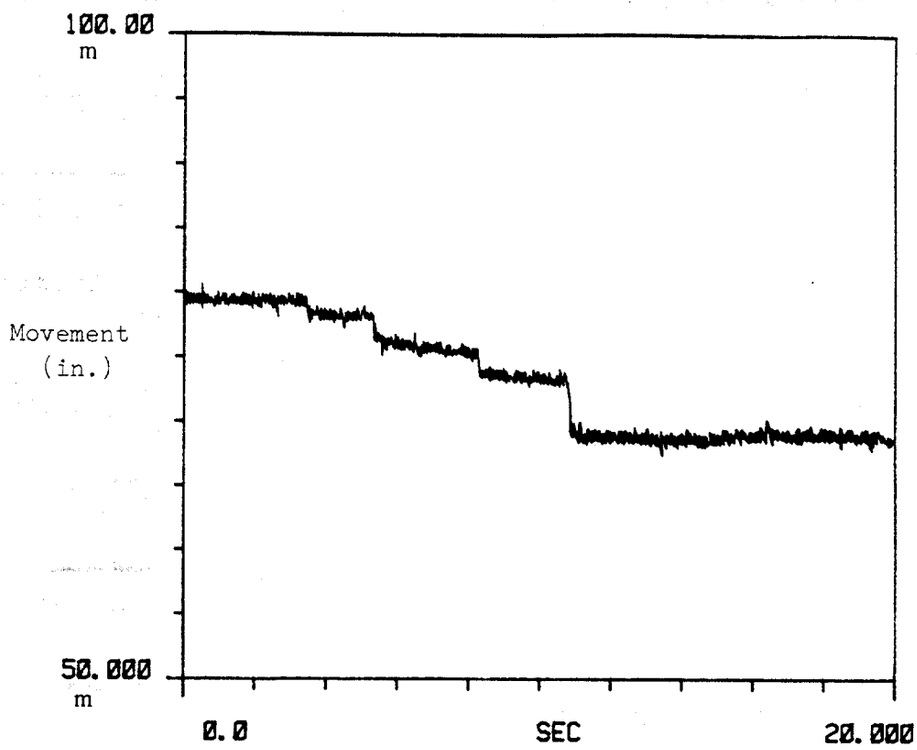

Fig. J.15. Time History Measurements of Pile Head Movement, Test U2, [m = milli].

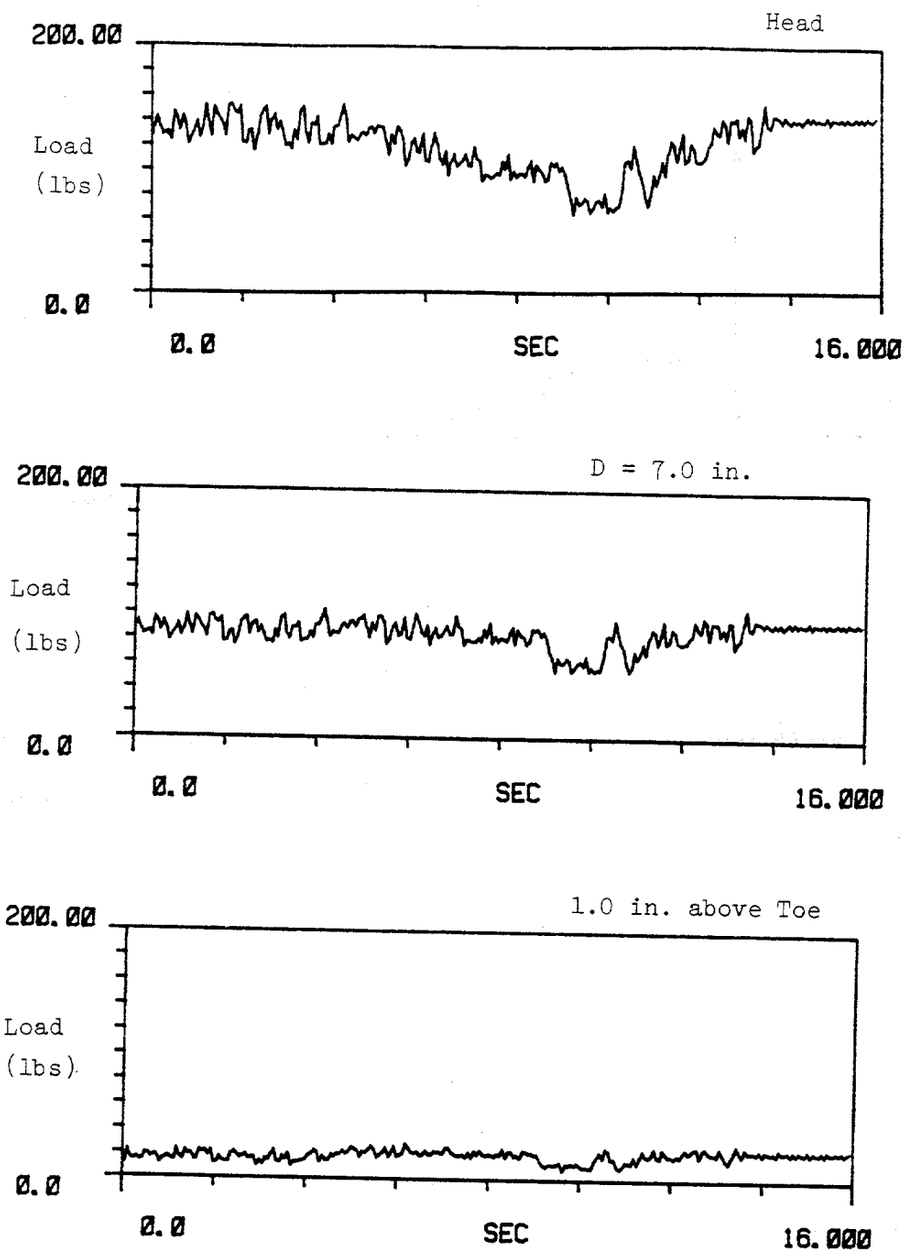

Fig. J.16. Time History Measurements of Dynamic Load on Pile, Test V1.

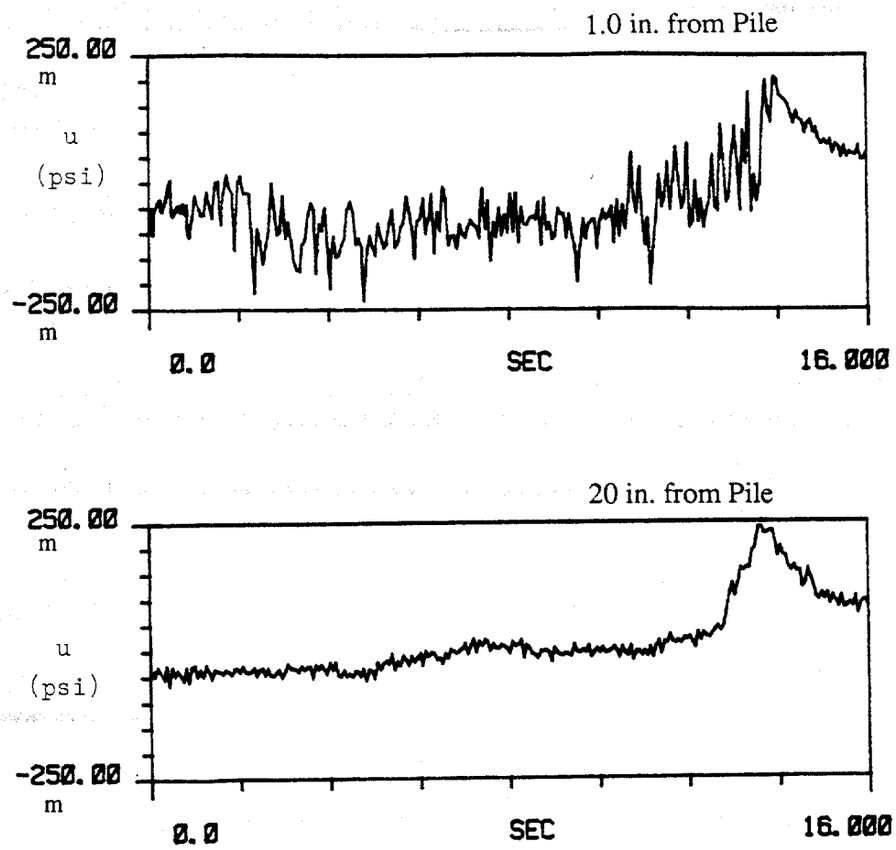

Fig. J.17. Time History Measurements of Near and Far Field Pore Water Pressures, Test V1, [m = milli].

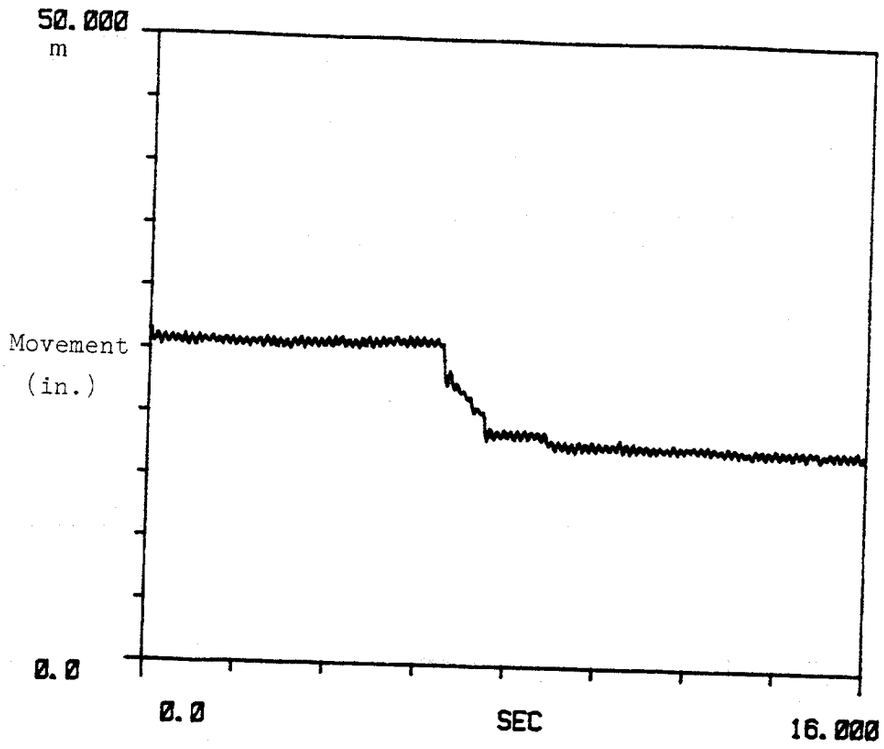

Fig. J.18. Time History Measurements of Pile Head Movement, Test V1, [m = milli].

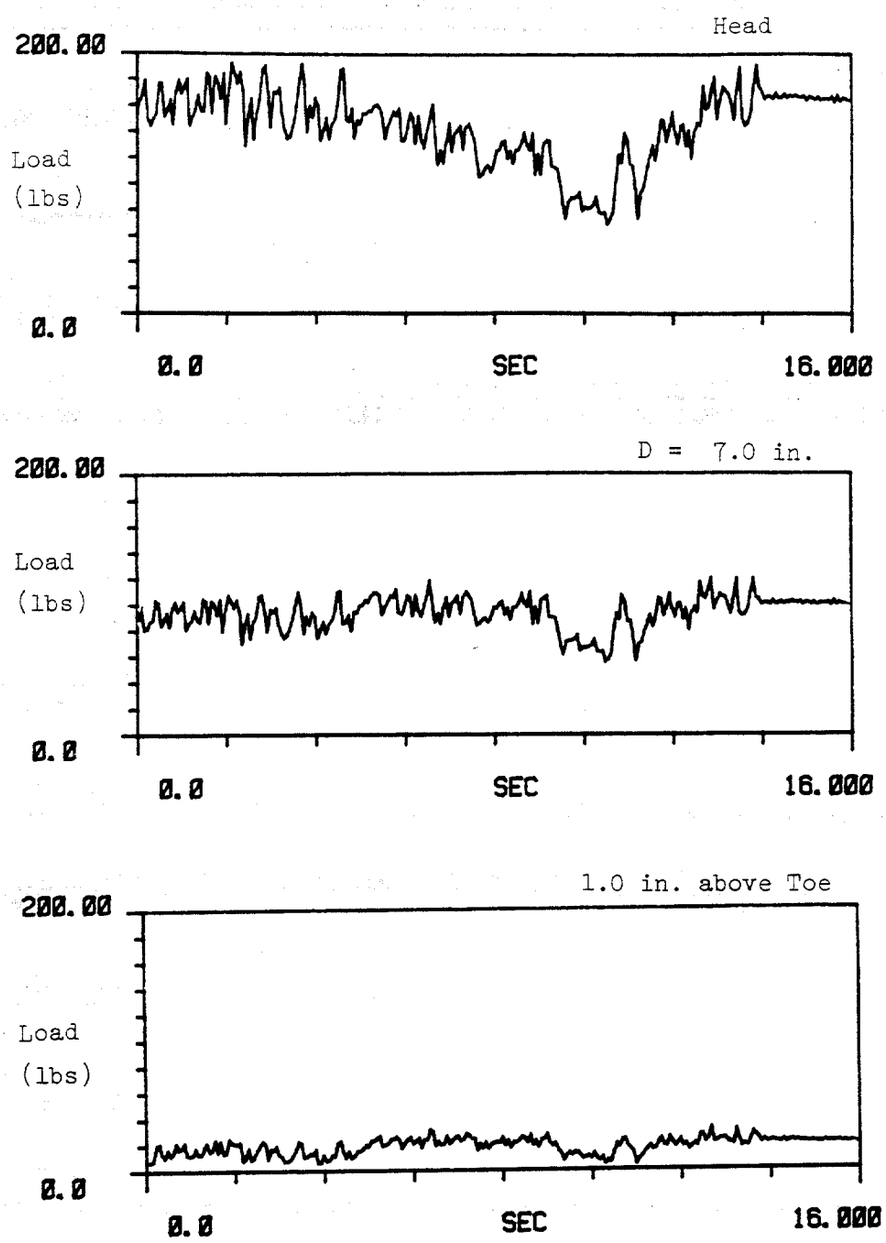

Fig. J.19. Time History Measurements of Dynamic Load on Pile, Test V2.

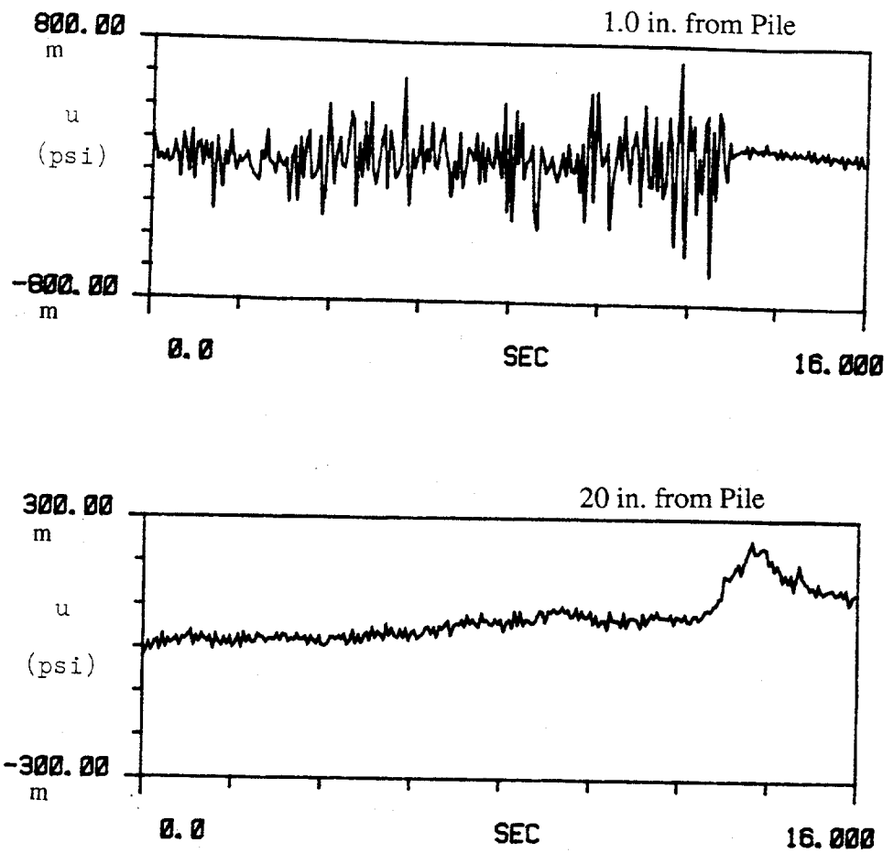

Fig. J.20. Time History Measurements of Near and Far Field Pore Water Pressures, Test V2, [m = milli].

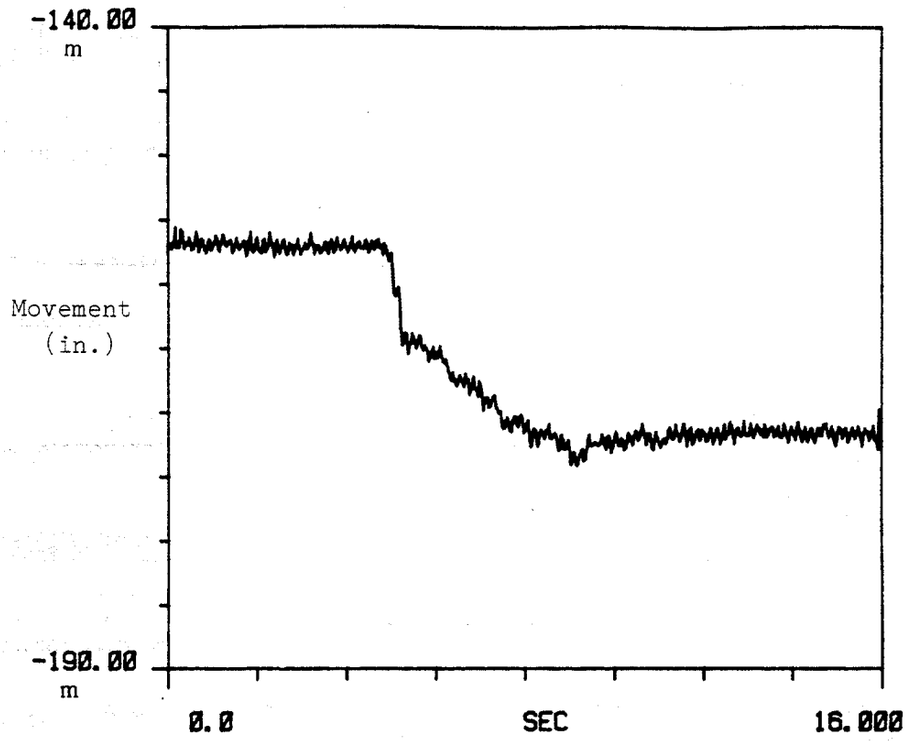

Fig. J.21. Time History Measurements of Pile Head Movement, Test V2, [m = milli].

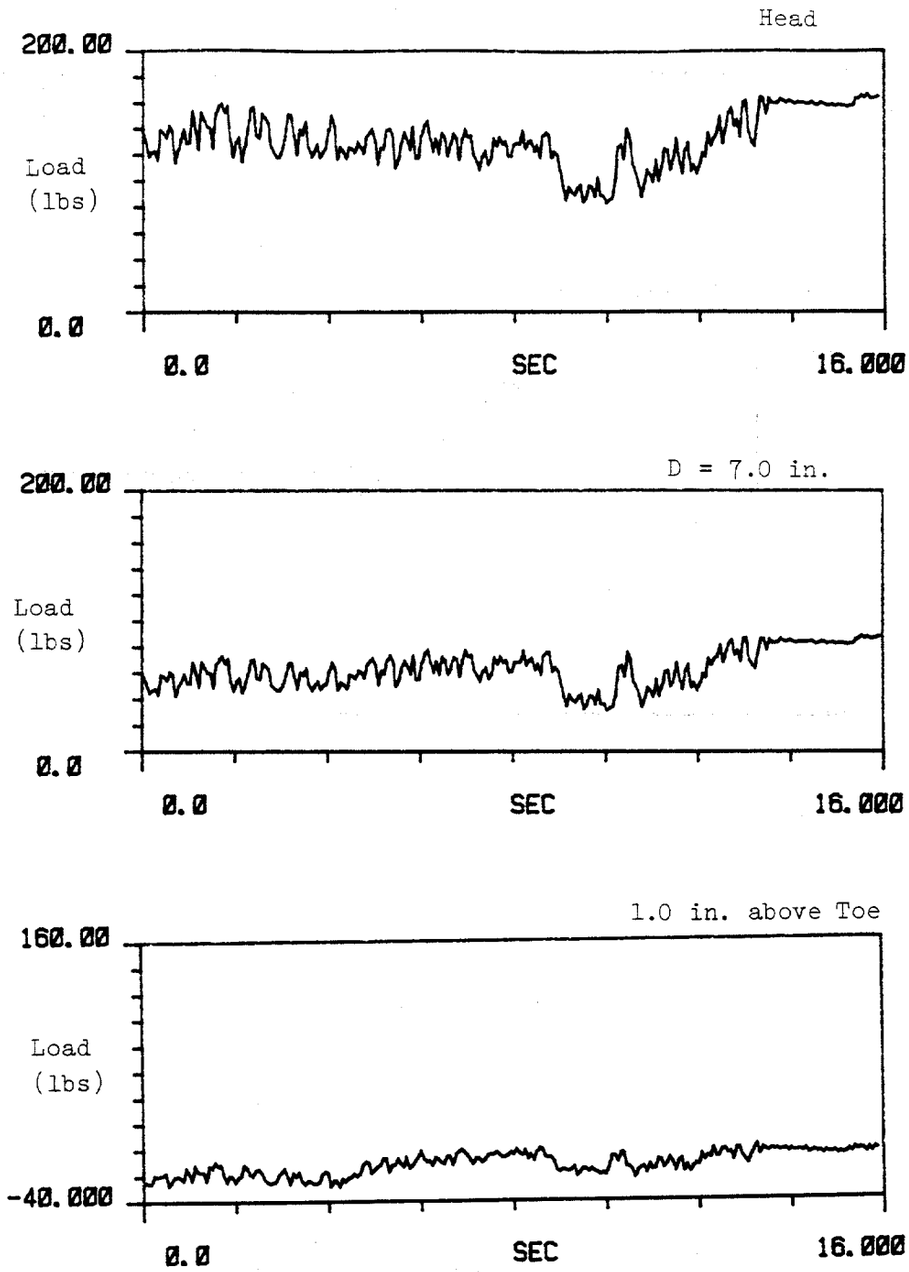

Fig. J.22. Time History Measurements of Dynamic Load on Pile, Test W1.

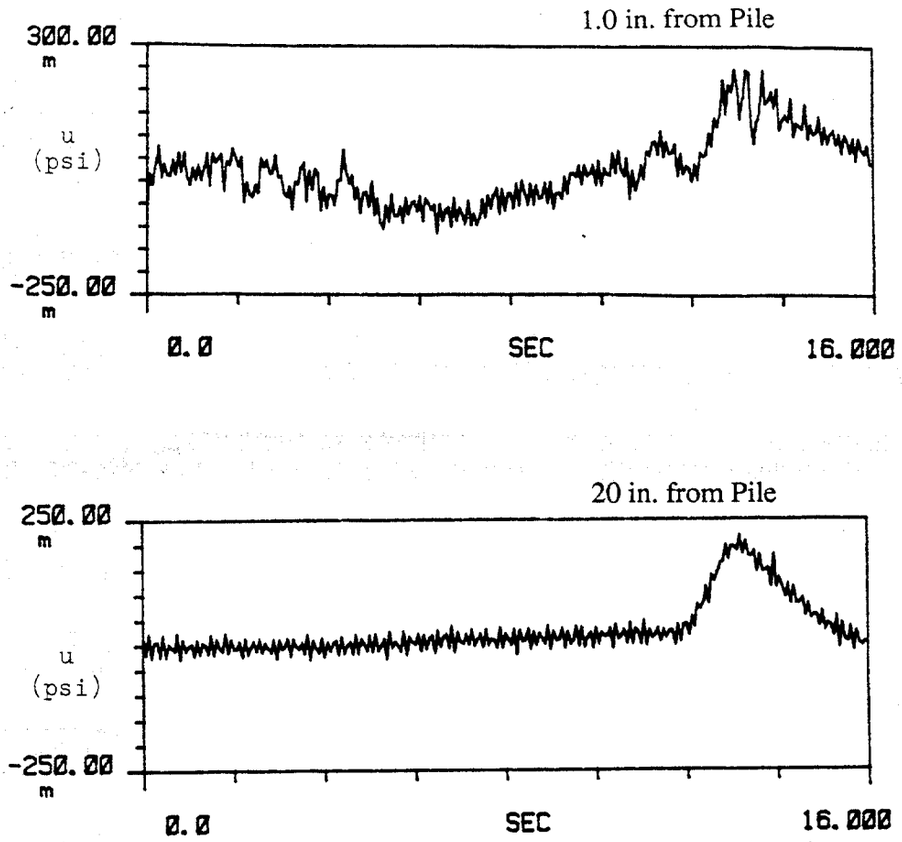

Fig. J.23. Time History Measurements of Near and Far Field Pore Water Pressures, Test W1, [m = milli].

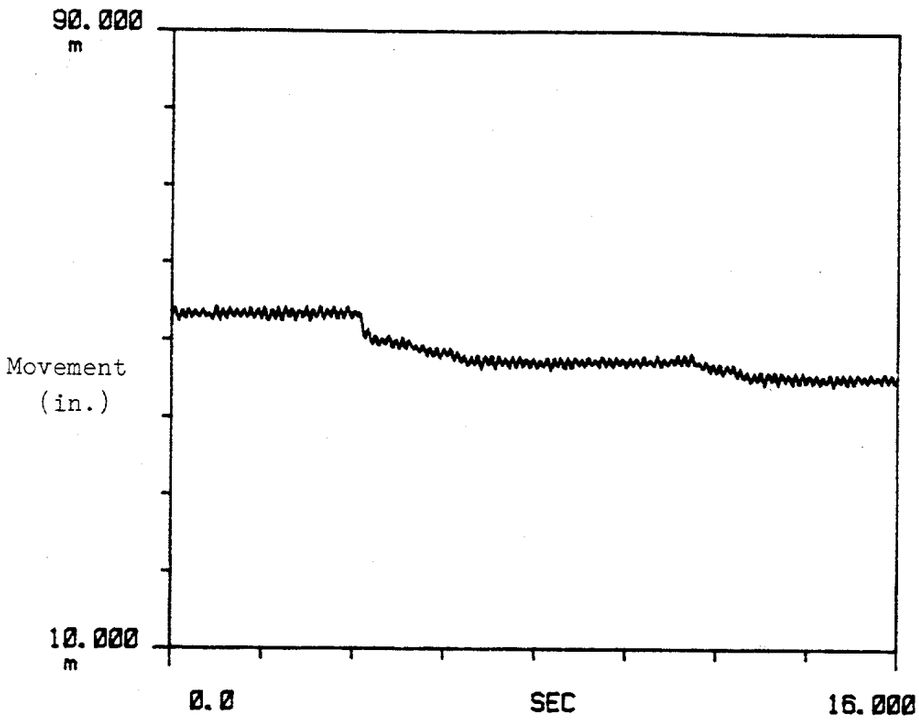

Fig. J.24. Time History Measurements of Pile Head Movement, Test W1, [m = milli].

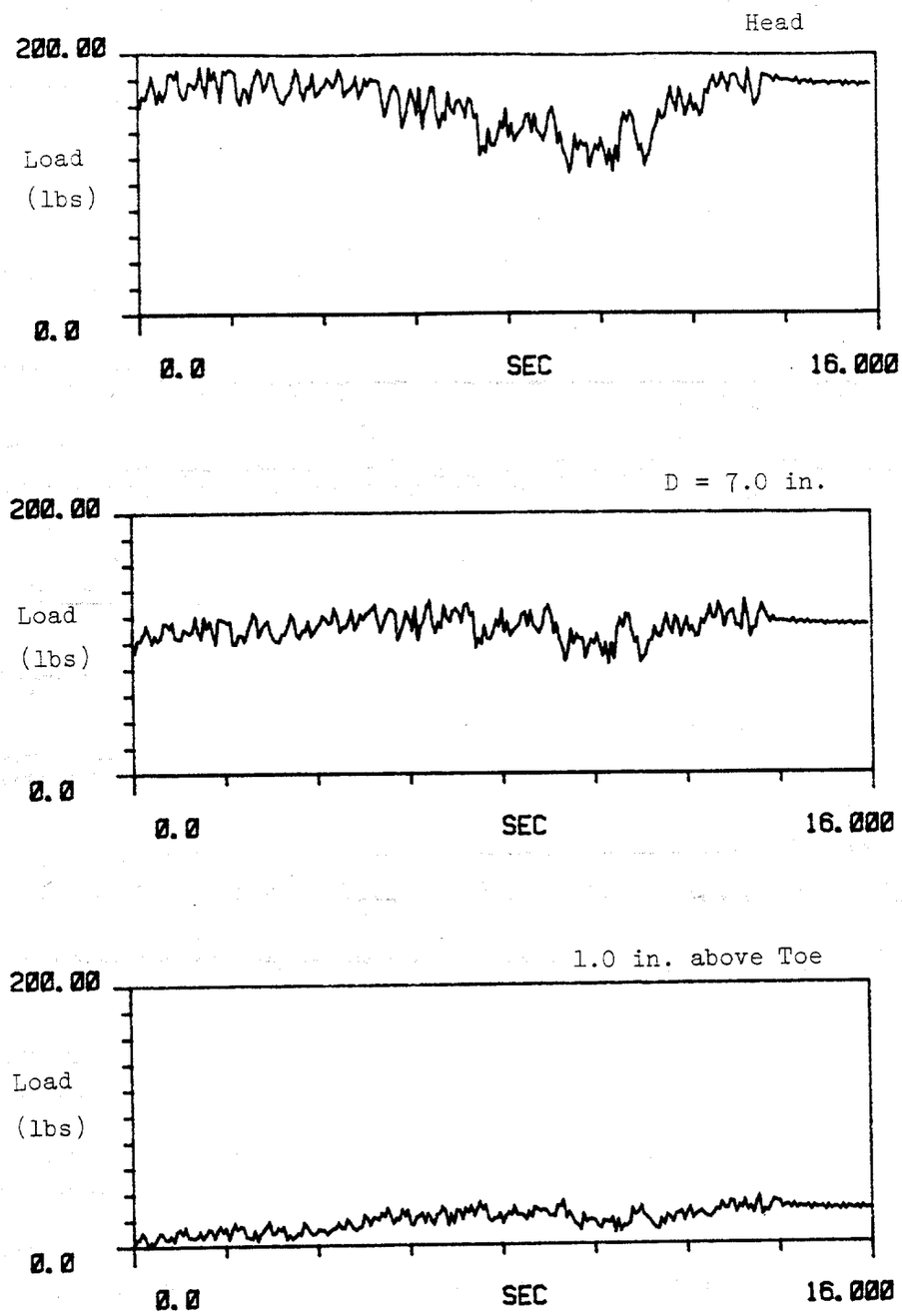

Fig. J.25. Time History Measurements of Dynamic Load on Pile, Test W2.

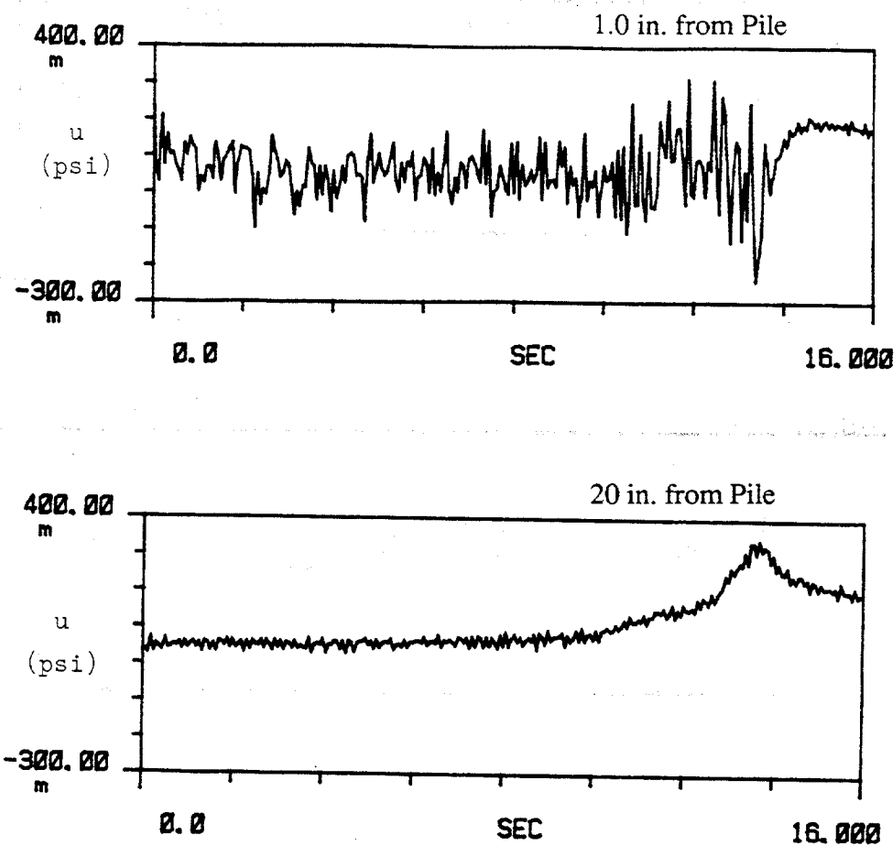

Fig. J.26. Time History Measurements of Near and Far Field Pore Water Pressures, Test W2, [m = milli].

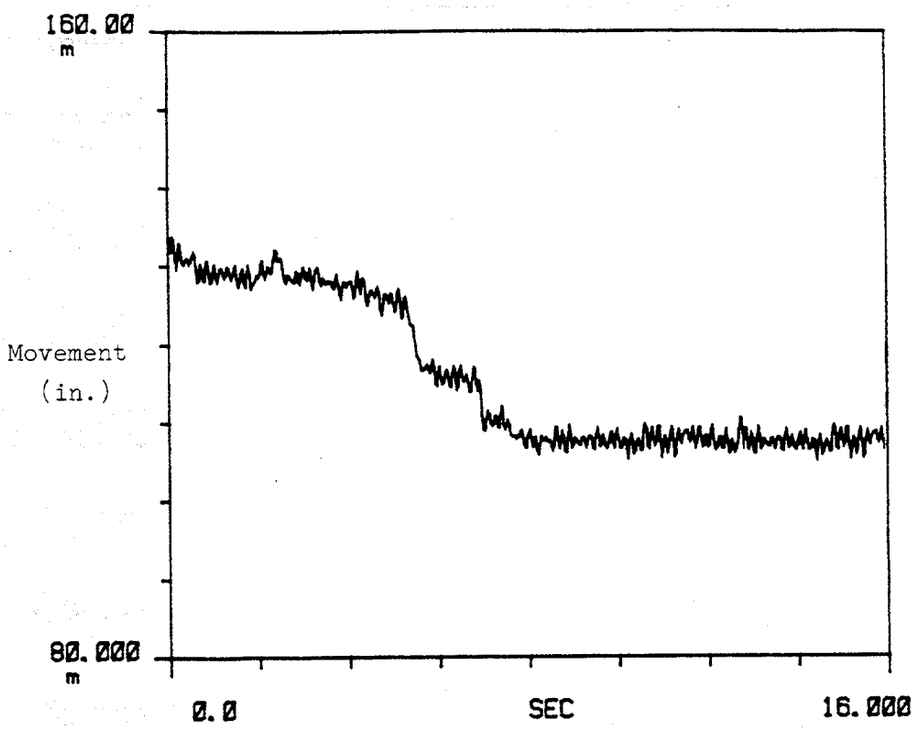

Fig. J.27. Time History Measurements of Pile Head Movement, Test W2, [m = milli].

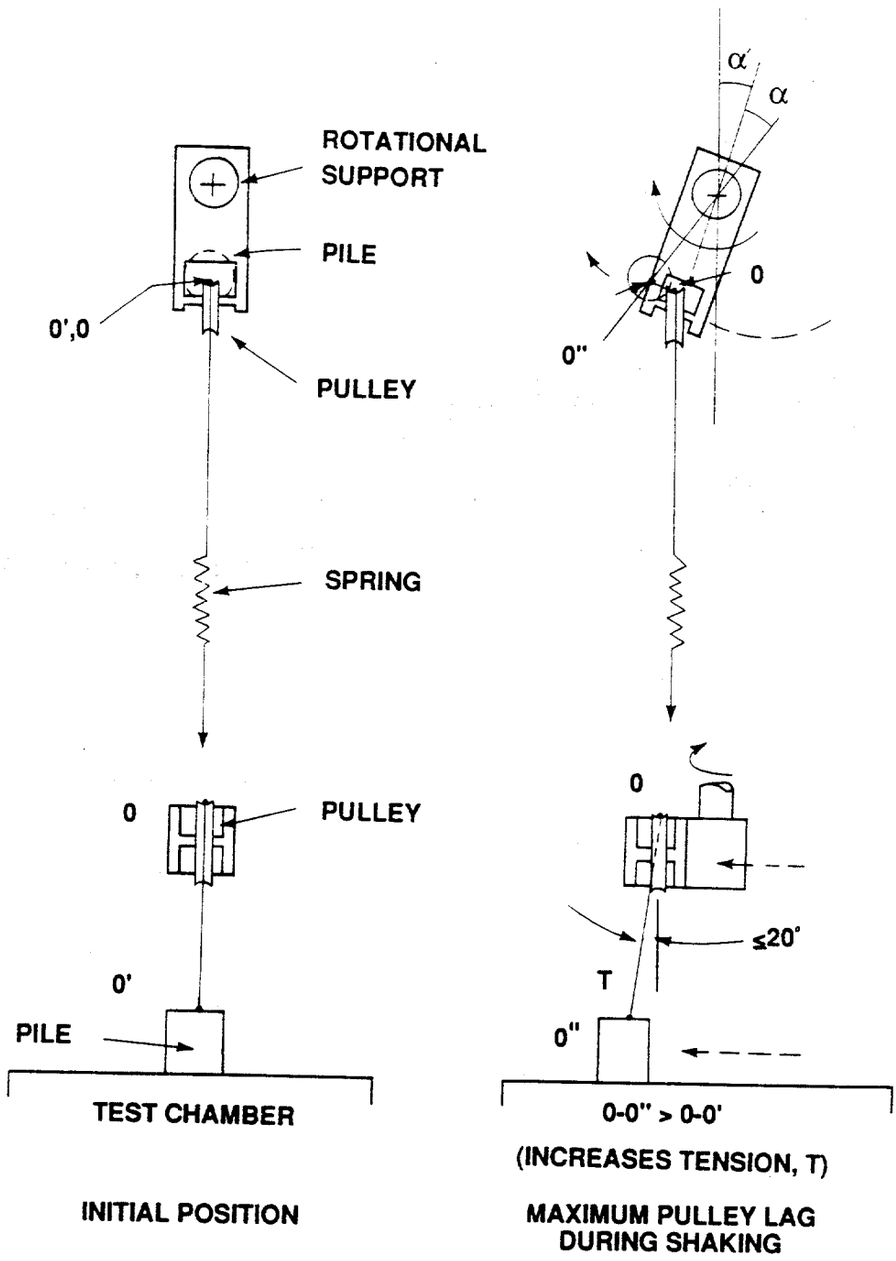

Fig. J.28. Illlustration of Effect of Pulley Lag on Axial Force on Pile During Horizontal Tests